CERIA-BASED SINGLE-ATOM CATALYSTS: FROM SIMPLIFIED MODELS TOWARDS REAL-WORLD COMPLEXITY

Julian Geiger

UNIVERSITAT ROVIRA i VIRGILI

Ceria-based Single-Atom Catalysts: From simplified models towards real-world complexity

Julian Geiger

DOCTORAL THESIS
2023

UNIVERSITAT ROVIRA I VIRGILI
CERIA-BASED SINGLE-ATOM CATALYSTS: FROM SIMPLIFIED MODELS TOWARDS REAL-WORLD COMPLEXITY
Julian Geiger

Julian Geiger

Ceria-based Single-Atom Catalysts: From simplified models towards real-world complexity

DOCTORAL THESIS

Supervised by
Prof. Núria López Alonso

Institute of Chemical Research of Catalonia (ICIQ)
and Rovira i Virgili University (URV)

Tarragona
2023

Institut Català d'Investigació Química
   Av. Països Catalans, 16
   43007 Tarragona. Spain

Prof. Núria López Alonso, group leader in the Institute of Chemical Research of Catalonia,

I STATE that the present study, entitled "**Ceria-based Single-Atom Catalysts: From simplified models towards real-world complexity**", presented by Julian Geiger for the award of the degree of Doctor of Chemical Science and Technology, has been carried out under my supervision at the Institut Català d'Investigació Química, ICIQ.

Tarragona, September 1st, 2023

Prof. Núria López Alonso

Sponsors

CERIA-BASED SINGLE-ATOM CATALYSTS: FROM SIMPLIFIED MODELS TOWARDS REAL-WORLD COMPLEXITY
Julian Geiger

Acknowledgements

I would like to express my sincere gratitude to Prof. Núria Lóez for giving me the opportunity to pursue my Ph.D. degree in her group. Throughout the last four years, I have learned and grown immensely, both professionally, and personally. I started as a student, and I leave as a scientist. I would further like to thank Dr. Nathan Daelman for assisting me on the beginning of this journey, for many long and fruitful scientific discussions, and for teaching me the craft of exploring oxidation state dynamics of ceria-based single-atom catalysts via DFT. I also thank Prof. Nicola Marzari for giving me the opportunity to join his group during my 3.5-month stay in Lausanne in early 2023. I have learned incredibly much from all the wonderful members of the THEOS lab. I also thank my collaborators, in particular Dr. Weiming Wan and Prof. Beatriz Roldan Cuenya, as well as Ivan Surin and Prof. Javier Pérez-Ramírez for the insightful and rewarding joint projects. The city of Tarragona and the ICIQ are both places full of beautiful people. To all the friends I have made here, you will always have a special place in my heart. Lastly, I would like to thank my parents, for giving me the beautiful gift that life is, and for their continued unconditional love and support throughout it.

Contents

List of Figures

List of Tables

Glossary

2O Two-fold oxygen coordination

3O Three-fold oxygen coordination

4O Four-fold oxygen coordination

AC Aberration corrector

AGI Artificial general intelligence

AI Artificial intelligence

AiiDA Automated interactive infrastructure and database for computational science

AIMD *Ab initio* molecular dynamics

ALD Atomic layer deposition

BE Binding energy

BH Born-Haber

BIC Bayesian information criterion

BLUE Best linear unbiased estimator

BMS Bayesian machine scientist

CLBE Core-level binding energy

CT Charge-transfer

CV Cross-validation

DFT Density-functional theory

EDX Energy-dispersive X-ray analysis

EDXS Energy dispersive X-ray spectroscopy

EMSI Electronic metal-support interaction

EN Elastic net

EPR Electron paramagnetic resonance

EXAFS Extended X-ray absorption fine structure

FCC Face-centered cubic

FT Fourier transformation

FTIR Fourier-transform infrared spectroscopy

GGA Generalized gradient approximation

GNN Graph neural network

GPT Generative pretrained transformer

HAADF High-angle annular dark-field

HRSTEM High-resolution scanning transmission electron microscopy

HSE Heyd-Scuseria-Ernzerhof

HT High-throughput

hyperparameter Parameter of a machine learning model that is not learned during the training process, but must be chosen/optimized beforehand.

IRAS Infrared reflection-absorption spectroscopy

IWI Incipient wetness impregnation

KFCV K-fold cross-validation

KS Kohn-Sham

Lasso Least absolute shrinkage and selection operator

LDA Local density approximation

LEED Low-energy electron diffraction

LLM Large language model

LOGOCV Leave-one-group-out cross-validation

LR Linear regression

MAE Mean absolute error

MCMC Markov chain monte carlo

MD Molecular dynamics

ML Machine learning

MOF Metal-organic framework

mOS Metal oxidation state

MS Mass spectrometry

MvK Mars-van Krevelen

NaN Not a number

NLP Natural language processing

NN Neural network

NN Nearest neighbor

NNN Next-nearest neighbor

NNP Neural network potential

NP Nanoparticle

NVT NVT

OLS Ordinary least squares

OQMD Open quantum materials database

OS Oxidation state

OSC Oxygen storage capacity

PAW Projector augmented wave

PBE Perdew-Burke-Ernzerhof

PCA Principal component analysis

PP Pseudopotential

PROX Preferential oxidation

RF Random forest

RFE Recursive feature elimination

RMSE Root-mean-square error

RSS Residual sum of squares

SA Single-atom

SAC Single-atom catalyst

SFS Sequential feature selection

SIE Self-interaction error

SMSI Strong metal-support interaction

SR Symbolic regression

SRPES Synchrotron radiation photoelectron spectroscopy

SS Subsurface

SSE Sum of squared errors

STEM Scanning transmission electron microscopy

STM Scanning tunneling microscopy

STY Space-time yield

TAP Temporal analysis of products

TEM Transmission electron microscopy

TM Transition metal

TPD Temperature programmed desorption

TS Transition state

TWC Three-way catalyst

UHV Ultra high vacuum

VASP Vienna Ab initio Simulation Package

WGS Water-gas shift

XANES X-ray absorption near edge spectroscopy

XAS X-ray adsorption spectroscopy

XPS X-ray photoelectron spectroscopy

List of publications

1. Highly Stable and Reactive Platinum Single Atoms on Oxygen Plasma-Functionalized CeO_2 Surfaces: Nanostructuring and Peroxo Effects. W. Wan, J. Geiger, N. Berdunov, M. L. Luna, S. W. Chee, N. Daelman, N. López, S. Shaikhutdinov, and B. R. Cuenya. *Angew. Chem. Int. Ed.*. **2022**, *61* (20), e202112640.

2. Coupling Metal and Support Redox Terms in Single-Atom Catalysts. J. Geiger, and N. López. *J. Phys. Chem. C* **2022**, *126* (32), 13698–13704.

3. Data-driven models for ground and excited states for Single Atoms on Ceria. J. Geiger, A. Sabadell-Rendón, N. Daelman, and N. López. *npj Comput. Mater.* **2022**, *8* (1), 171–178.

4. Low-Valent Manganese Atoms Stabilized on Ceria for Nitrous Oxide Synthesis. I. Surin, Z. Tang, J. Geiger, S. Damir, H. Eliasson, M. Agrachev, F. Krumeich, S. Mitchell, V. A. Kondratenko, E. V. Kondratenko, G. Jeschke, R. Erni, N. López, and J. Pérez-Ramírez. *Adv. Mater.* **2023**, *8* (1), e2211260.

Julian Geiger did the computational work of all publications. He is the main contributor to the machine learning analysis of publication 3 and the main author of publications 2 and 3. He contributed to the writing process of publications 1 and 4.

Abstract

In recent years, single atoms have emerged as a new paradigm in catalysis, promising numerous advantages over traditional approaches. Despite the growing potential for industrial application, the precise structure of the active site is often still poorly understood. In addition, at the atomic scale, dynamic effects become ubiquitous and influence reactivity. This thesis approaches these issues for ceria-based single-atom catalysts with various transition metals as active centers. Via Density Functional Theory modelling, atomic structures are resolved, local polaron distributions explored, and electron transfer dynamics between the isolated metal atoms and the surface investigated, proving their ubiquity in ceria-based systems. Moreover, the influence of surface reduction as the most common chemical modification of ceria, is addressed, showing how uncommon metal oxidation states can be made accessible via the electronic interaction with the support. The obtained wealth of data is further used to construct predictive machine learning models that provide additional physical insight into the metal-support interaction. In collaboration with experimental groups, surface peroxide as the origin of the exceptionally high stabilization capability of oxygen plasma pretreated ceria for atomically dispersed platinum, is revealed. Lastly, the reactivity landscape for ammonia oxidation to nitrous oxide is explored for a ceria-based manganese catalyst, allowing to rationalize its high catalytic performance via a thermodynamically favorable catalytic cycle. The results prove the pivotal role of ceria as a non-innocent support, influencing atomic structure, dynamic behavior, and reactivity. They present a further step towards atomically precise control in single-atom catalysts, desperately needed for industrial application.

Chapter 1

Introduction

The world is full of wonders, but they become more wonderful, not less wonderful when science looks at them.

David Attenborough

Science is not only compatible with spirituality; it is a profound source of spirituality.

Carl Sagan

Only when our clever brain and our human heart work together in harmony can we achieve our true potential.

Jane Goodall

1.1 Are we solving climate change?

In this community, in which we concern ourselves themselves with (computational) heterogeneous catalysis, the impact of human industrial activity and its contribution to anthropological climate change are frequently brought up topics[1,2]. With the amount of literature available, I do not think it makes sense to further discuss them in depth here. We should also all already be well-aware of them, as we start feeling the effects all around us, with temperature records being broken year after year, ice caps melting

Chapter 1. Introduction

at alarming rates, and standing witness to an unprecedented decimation of wildlife, already classifiable as the sixth mass-extinction[3–6]. Thus, restoring and conserving the delicate balances that enable life on our blue marble are undoubtedly among the most important undertakings of our time. It is for this reason that I deem the disingenuous use of such motives to fill introductory paragraphs of scientific articles in the pursuit of securing monetary funding rather questionable. I would therefore like to approach this topic in this thesis introduction in a rather different way.

It is often stated that we need more efficient catalytic processes to reduce the impact of industrial production. While this is certainly the case, I would argue that the currently prevailing practice of *planned obsolescence* all but obliterates any such improvements. What good does optimizing production do, when the resulting products are intentionally constructed to break early and be irreparable? Instead, the logical focus should be on durability and ease of reparation and/or recycling. Yet, such an approach is not desirable under a system that is predicated on infinite growth and values financial profit above everything else, human life included. It should come to no surprise that infinite growth on a finite planet is anything but sustainable. I would further argue that in the majority of cases, the average person's concern for climate change ends where personal comfort begins. This is particularly true for us citizens of highly developed countries, enjoying unprecedented prosperity at the expense of the natural world around us. As such, it stands to reason that the need for more efficient catalysts is vastly exceeded by the need for fundamental changes to our economic systems and societies.

1.2 The beauty of science

With such a bleak outlook, is all hope lost already? Fortunately, I would say quite the opposite. Since the widespread adaptation of the scientific method in Europe around the 16th century[7], its application has enabled us to achieve absolutely extraordinary progress. We now yield the technology of gods. And so, at least from the scientific perspective, many of the problems outlined above are already solved, or are, in principle, solvable. For instance, due to significant advances in the efficiency of agriculture, we currently produce enough food to feed ten billion people[8]. The fact that there still exists hunger in this world is of economical and societal origin— Science has already solved this problem. In accordance, the ability to split the atom, as well as decades of research on renewable energies, could provide us with sufficient sources of clean and safe energy (see Fig. 1.1). The prevailing pollution of our planet is of economical and societal origin—Science

has already solved this problem. Numerous additional examples could be included here, but I think the message should be clear.

I would further like to pose the question if science really needs to state ulterior motives to justify its practice. In my opinion, it does not. Its profound positive impact on the development of humanity needs no further discussion, and some examples have already been given above. And yet, many of its most important discoveries were made by chance, with their future impact being vastly underestimated. The "light amplification by stimulated emission of radiation", today commonly known as the laser, was dubbed "a solution in search of a problem" by its inventor, Theodore Harold Maiman, just to establish itself as one of the most important technologies of the 20th century[9]. Similarly, after discovering radio waves, Heinrich Hertz did "not think that the wireless waves I have discovered will have any practical application"[10]. Today, communication via radio waves is crucial for practically all electronic devices we use on a daily basis. And while Alexander Fleming "did not invent penicillin, but only discovered it by accident"[11], it became one of the most impactful discoveries in the field of medicine, saving an estimated 80 to 200 million lives up to this day[12]. These are just a few examples of the notorious difficulty to predict the impact of scientific discoveries—and the future in general. It is for this reason that I believe monetary funding, and with it, the ability to conduct scientific research, should not be predicated on pre-imagined ideas of their importance, as is often the case in the current publishing system. Nonetheless, it goes without saying that any serious scientist should have clear ideas in mind when carrying out their work.
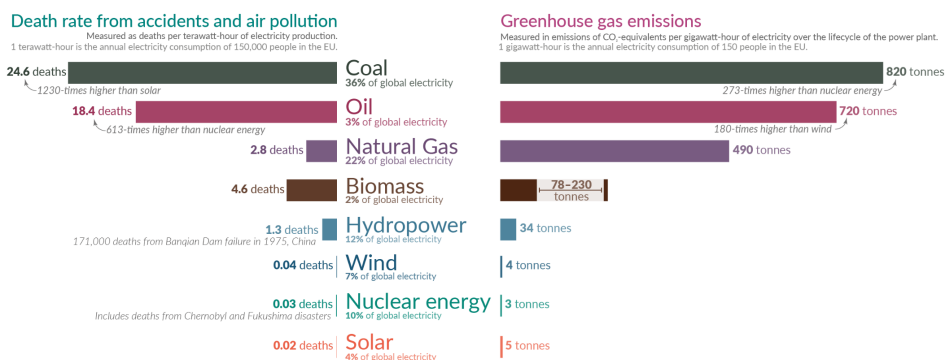
Figure 1.1: Safest and cleanest energy sources available today. Figure adapted from Ref. [13].

Chapter 1. Introduction

1.3 Single Atoms: A new frontier in catalysis

1.3.1 Industrial impact of catalysis

The above being said, there is no doubt that finding better and more efficient catalysts is a valuable undertaking for improving the production of the materials that provide the basis for our modern life. Around 90% (by volume) of produced chemicals rely on solid catalysts[14], generating global sales of around \$1.5 trillion in value[15]. The use of catalysts in a different phase (typically solid) than the reaction mixture (typically gas or liquid) is called heterogeneous catalysts. This approach provides various advantages, most importantly the facile separation of the catalyst from the reaction mixture, allowing for easy recycling, long durability, and high efficiency, thus making it the ideal choice for the industrial production of bulk chemicals. The efficiency of catalysts can be quantified via the E-factor, which is defined as waste, or "everything but the desired product" per kg of product, including solvent consumption, chemicals used during work-up, and related processes[16]. As shown in Table 1.1, with increasing tonnage of product, the E-factor generally decreases. Notably, oil refining and bulk chemical production, which rely practically exclusively on heterogeneous catalysts, achieve very low E-values. On the other hand, the production of high-value fine chemicals and pharmaceuticals relies on processes that generate excessive amounts of waste, often far exceeding the product quantity. The reason for this is that these products are usually complex organic molecules whose synthesis requires precise control of the active catalyst site and the resulting reactivity, usually only achievable with homogeneous transition metal complexes. However, the presence of the catalyst in the same phase as the reaction mixture thus complicates separation and work-up.

Table 1.1: E-factors of different sectors of the chemical industry. Table adapted from Ref. [16].

Industry segment	Product tonnage (p/a)	E-factor (kgs waste/kg product)
Oil refining	$10^6 - 10^8$	< 0.1
Bulk chemicals	$10^4 - 10^6$	$< 1 - 5$
Fine chemicals	$10^2 - 10^4$	$5 - 50$
Pharmaceuticals	$10 - 10^3$	$25 - > 100$

1.3.2   How SACs bridge the catalysis gap

It is at this divide between the homogeneous and heterogeneous approaches, where single-atom catalysts (SACs) hold the promise of unification in the field of catalysis. Typically, the embedding of the catalytically active, isolated metal atoms is achieved in solid matrices like other metals[17], metal-organic frameworks (MOFs)[18], doped carbons[19], or metal oxides[20]. Hence, easy separation from the reaction mixture, one of the main advantages of heterogeneous catalysts, is achieved. On the other hand, atomically precise control of the metal atom's chemical state and environment, commonly termed the "speciation"[1], allows for fine-tuning of the catalytic center, similar to homogeneous transition metal complexes. Furthermore, as every metal atom functions as an active site, SACs provide perfect atom utilization, particularly important when scarce and precious metals are being used.

The proposition of isolated atoms as catalytically active sites dates back all the way to 1999, when atomically dispersed Pt embedded in a MgO surface was identified as an active catalyst for propane combustion[21]. In addition, in their seminal work of 2003, Fu and coworkers proposed single atoms of gold and platinum anchored on ceria as active species in the water-gas shift (WGS) reaction[22]. The term single-atom catalyst (SAC), however, was first coined in literature in 2011 for a Pt_1/FeO_x system with exceptional activity in CO oxidation[23]. Importantly, it presented the first case in which the atomic dispersion of the active metal was proven unambiguously. Ever since, the field of single-atom catalysis has grown significantly, with applications emerging for thermal, electrochemical and photo-catalytic transformations[19,20,24–29]. Fig. 1.2 compiles a number of hallmark developments from the last two decades, with advancements being made in the synthesis, characterization, and application of SACs, which typically go hand in hand.

1.3.3   Synthesis of SACs

The first challenge towards the application of SACs lies in the controlled preparation of materials that expose isolated, active, and stable metal atoms. This feat is everything but simple and has only become possible in recent years[19,30,31]. As metal particle size decreases, the fraction of low-coordinated sites increases, and with it the relative surface energy. At the complete absence of metal-metal bonds, it reaches its maximum, making isolated metal atoms inherently unstable. Thus, there is a great thermodynamic driving force for metal agglomeration (also called sintering) by which

---

[1]Speciation refers to the local coordination environment of the isolated metal atom, as well as its electronic structure, most importantly its oxidation state.

Chapter 1. Introduction
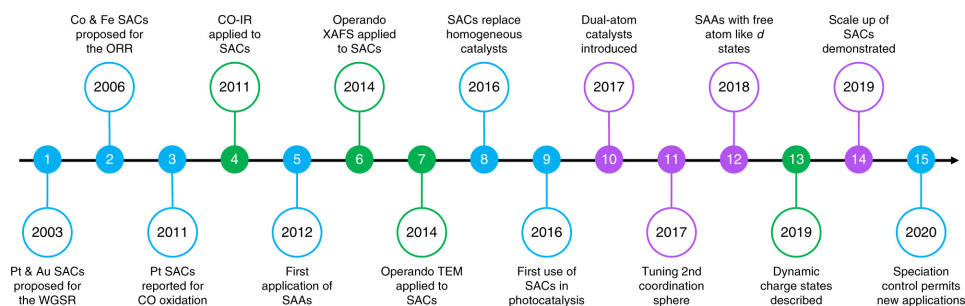
Figure 1.2: Timeline of important developments in the field of single-atom catalysis throughout the last two decades, grouped by synthesis (purple), characterization (green), and application (blue). Figure taken from Ref. [28].

catalytically active metal centers are lost in the bulk of growing nanoparticles (NPs), a fate which commonly leading to the deactivation of heterogeneous catalysts based on small metal NPs. Therefore, great care must be taken in achieving metal separation during synthesis, e.g. via low rates of metal deposition and by providing sufficient (but not deactivating) stabilization on the support.

Today, there exist a variety of techniques that have successfully been used for the synthesis of SACs[19,30,31]. The most suited preparation method naturally depends on the combination of carrier and metal. It can broadly be classified into bottom-up and top-down approaches. In the former case, the target single-atom (SA) metal is dispersed and stabilized already during the synthesis of the support material, while in the latter case, it is introduced on a pre-prepared host. Examples for bottom-up approaches are co-precipitation from a precursor solution, containing the minority metal, often in spatially isolated sites[32]. Another example is the pyrolysis of carbon and/or nitrogen-rich compounds, which has been widely used for the preparation of SACs based on metal-organic frameworks (MOFs) and carbonaceous support materials. Top-down approaches are for instance, direct deposition of the metal from the gas phase, atomic layer deposition (ALD), and incipient wetness impregnation (IWI)[19]. Despite the difficulties in their preparation, the last two decades have seen great progress, and modern, advanced synthesis protocols have achieved the preparation of SACs with impressive metal loadings up to $16\,wt\%$[33] and $23\,wt\%$[34], approaching industrial maturity[29].

In addition to the widespread carbonaceous structures mentioned above, (reducible) metal oxides are among the most commonly used support materials for the synthesis of SACs[20,24,25]. Indeed, it was for Pt_1/FeO_x for

30

UNIVERSITAT ROVIRA I VIRGILI
CERIA-BASED SINGLE-ATOM CATALYSTS: FROM SIMPLIFIED MODELS TOWARDS REAL-WORLD COMPLEXITY
Julian Geiger

1.3. Single Atoms: A new frontier in catalysis

which the term "single-atom catalyst" first emerged in literature[23]. Here, stabilization of isolated metal sites is usually achieved by a strong bonding between the metal and the carrier, with the effect originally discovered for metal NPs and termed strong metal-support interaction (SMSIs)[35,36]. If the interaction is further accompanied by significant charge transfer, it is often referred to as electronic metal-support interaction (EMSI)[2], a term first coined by Campbell[37]. In the case of ceria, the reducible oxide host material for all SACs discussed in this thesis, the strong electronic interaction was first noted upon the realization that very small silver nanoparticles are significantly more stabilized on ceria than on non-reducible MgO[38]. Furthermore, the effect was shown to be responsible for the increased water dissociation ability of ceria-supported Pt_8 particles[39]. It is this strong (electronic) interaction, that allows for the stabilization of metals in the form of isolated atoms on ceria. Until today, stable ceria-based SACs of the group 10 metals[40–43], gold[44], copper[45], rhodium[46] and manganese[47] could sucessfully be prepared, and will be discussed in more detail in Section 2.3.

1.3.4   Characterizing SACs

In addition to the delicate preparation of SACs, their thorough characterization presents another hurdle on the way to becoming a widely adapted technology. Due to the miniscule size of individual atoms, this presents a formidable challenge. Nonetheless, the first direct visualization of uranium atoms anchored on a carbon-based support dates back as far as 1970[48], and was achieved via transmission electron microscopy (TEM). However, the exceptionally high atomic number (Z) contrast that made it possible is typically not a given for most catalysts of practical interest. Since then, significant improvements have been made, and high-angle annular dark-field (HAADF) detectors, as well as aberration correctors (ACs) have made the visualization of individual metal atoms almost routine[49]. And yet, the speciation of the active site of SACs is often still poorly understood. In addition, microscopy only enables the visualization of a small fraction of the surface, thus raising the question of its representativeness of the entire catalyst.

Instead, indirect probing methods can provide more comprehensive data on the system under study. Here, techniques based on X-rays have proven to be particularly useful[50]. For instance, X-ray photoelectron spectroscopy (XPS) can be used to assign oxidation states (OS) of both, the isolated metal atoms, as well as the species that make up the support material,

---

[2]While both terms, strong and electronic metal-support interaction were initially coined for metal nanoparticles, I would argue that they can be equally applied for the interaction between isolated, single atoms and the support, and I will use them accordingly.

Chapter 1. Introduction

while energy-dispersive X-ray analysis (EDX) yields information about the distribution of the different elements over the sample, reaching atomic resolution. Furthermore, X-ray absorption near edge spectroscopy (XANES) and extended X-ray absorption fine structure (EXAFS) analysis can provide additional information about the electronic structure and local coordination environment of the isolated metal atoms, such as the nature and distance of bonding partners. Absence of metal-metal bonds at typical bulk distances can therefore yield indirect proof of the absence of metal particles, indicative of atomic dispersion. Similarly, the presence of hyperfine splitting in electron paramagnetic resonance (EPR) experiments can provide evidence for the atomic nature of the metal species[51], as agglomeration to particles would broaden out the signal[52]. The last class of indirect analytical techniques I'd like to include here, relies on probe molecules to extract information about the species of interest. Infrared spectroscopy, such as Fourier-transform infrared spectroscopy (FTIR) and infrared reflection-absorption spectroscopy (IRAS) are common examples. For instance, from the vibrational frequency of adsorbed CO, information of the adsorption site can be inferred[43,53]. Similarly, the location of the desorption peak during temperature programmed desorption (TPD) experiments provides the strength of the interaction between the adsorbate molecule and the active site, from which the nature of the latter can be inferred.

In summary, there exists a large toolbox of different analytical techniques, which provide varied, and often complementary, information about the systems under study. As such, many works combine multiple techniques in an effort to achieve a comprehensive characterization of the samples. However, experimental restrictions frequently arise. For instance, electron microscopy requires conducting probes and ultra-high vacuum (UHV) conditions (1×10^{-7} - 1×10^{-12} bar). And while indirect techniques can give information at the atomic level, they often do so averaged over mesoscopic or even macroscopic areas of the samples. Similarly, in the temporal domain, results are typically averaged over data acquisition times. Furthermore, the use of UHV, common in analytical surface science is many orders of magnitude away from the elevated pressures often used in real catalytic converters, a discrepancy well-known as the so-called pressure gap[54]. The fact that catalysts frequently exhibit dynamic behavior during operation further complicates the situation[55–58]. Strides have been made to acquire data during catalyst operation, using *operando* or *in-situ* techniques[59–61], however, their application is still far from routine.

1.3.5   The role of computational modelling

In recent years, computational modelling, in particular based on density functional theory (DFT), has established itself as a valuable element in the chemical analytics toolbox outlined above[62,63]. Its success can be attributed to significant increases in computing power, allowing for the simulation of ever larger systems, with ever higher accuracy. Despite these advances, real catalysts still present an overwhelming amount of complexity, covering length scales from the atomic to the macroscopic. Thus, the construction of simplified model systems, e.g. based on extended low-index facets or idealized nanoparticles, is still necessary[63]. Nonetheless, insights derived from simulations on said model systems can be of high value and aid in the analysis of experimental results. This is particularly the case for information that is often not directly accessible to experiment, such as details of the electronic structure, metastable or transition states (TS), as well as dynamic phenomena. For instance, in a study combining STM, XPS, synchrotron radiation photoelectron spectroscopy (SRPES), and DFT simulations, the amount of charge transfer from platinum NPs to a $CeO_2(111)$ support, and therefore the extent of EMSI, could be quantified[64]. In other works, it could further be shown that for many catalysts, the active center is far from static, but better described by an ensemble of interconverting geometrically distinct, metastable structures that are responsible for the observed reactivity[56]. Such fluxionality remains elusive to direct experimental observation. In extreme cases, the disintegration of metal NPs via surface diffusion of individual metal atoms[55,65], or the formation volatile species[41] was observed, and could even be used for the synthesis of SACs[31]. Again, tracking dynamics at the atomic scale can benefit greatly from the support of *ab initio* simulations[61].

With active catalytic centers reaching the sub-Ångström domain, discerning the actual atomic structure of the catalytic center (i.e. the metal atom and its coordination sphere) becomes ever more challenging. Here, X-ray adsorption spectroscopy (XAS) methods, like XANES or EXAFS are particularly valuable[61]. In particular, comparison between experimental and simulated spectra (based on plausible structural models) can resolve the atomic structure of the catalyst. And even before the synthesis of the first stable Pt_1/CeO_2 SACs in 2016[40,41], the square-planar nano-pocket available on ceria nanoparticles (NPs) and (111) step edges was proposed as favorable site to stabilize single-atom platinum by DFT simulations[66]. In addition, with decreasing size of the catalytic center, the prevalence of dynamic effects may further increase. For example, on restructured $CeO_2(100)$, surface diffusion of labile oxygen[67], as well as dynamic charge-transfer (CT) between the oxide and adsorbed single-atom platinum[68] could be identified. In such

Chapter 1. Introduction

cases, the required length and time scales become increasingly inaccessible to experimental techniques.

1.4 High-throughput and machine learning

In addition to assisting experimental characterization, computational techniques have now reached a degree of sophistication that even enables them to guide experiments and catalyst design. For instance, as various descriptors for near arbitrary materials can be accurately predicted at low cost, volcano plots[3], a hallmark of heterogeneous catalysis research, can now be constructed based purely on computational data. This allows for promising materials to be identified even before their actual synthesis[69–71].

Similarly, the increased amount of computing power has also allowed for the advent of so-called high-throughput (HT) simulations, which take the approach introduced in the previous paragraph a step further. Here, the idea is that large bodies of (computed) data are created, which can then be quickly and easily screened for desired catalysts/materials, given that suitable descriptors of the target property are known[75]. This approach has been used for example in the prediction of novel and stable binary alloys[76], the search for easily exfoliable 2D materials[77], and even to verify the accuracy of common computational methods[78]. Furthermore, by combining thousands of HT DFT simulations, Hegde and coworkers could create the "phase stability network of all inorganic materials", a network of 21,000 thermodynamically stable compounds linked by 41 million edges which define stable two-phase equilibria between most elements of the periodic table[79].

However, as shown in Fig. 1.3, raw data still requires refinement and analysis before it can provide insight, eventually leading to societal impact. This data-driven approach is often called the 4th paradigm of science (Fig. 1.4). However, the ever-growing amounts and generation rates of data already far exceed our human cognitive abilities, limiting us to manually discern only a fraction of the true richness hidden in the data. Instead, in recent years, machine learning (ML) has firmly established itself in the natural sciences and proven more than capable of overcoming such human

---

[3]Volcano plots emerge from Sabatier's principle, which states that the interaction between a catalyst and its substrate should be "just right"[72,73]. If it is too weak, the catalyst cannot bind the substrate sufficiently to enable the reaction. If it is too strong, product release after the reaction might be inhibited, with both effects lowering the reaction rate. Thus, plotting the relative activity of various catalysts against the binding energy of the substrate leads to an inverted parabolic shape, often called a volcano, indicating that there is an optimal region of highest activity. Since its original formulation, similar relations have been found for a variety of descriptors among different types of catalytic processes[74] and the volcano has established itself as a fundamental concept in heterogeneous catalysis.

Figure 1.3: The flow from data to wisdom and impact. Figure taken from Ref. [80].

limitations[80–84]. For instance, Tshitoyan and coworkers trained an unsupervised natural language processing (NLP) model on 3.3 million scientific abstracts published throughout the last century[85]. With their model, the scientists could extract latent, hidden knowledge from the dataset, in particular, showing that future discoveries are largely already contained within past publications[85]. In another work, a neural network (NN) was trained on materials contained in the open quantum materials database (OQMD)[78] to capture interactions and similarities between different elements, allowing for the prediction of physical properties at high speed and without manual human input[86]. The resulting model could then be used to scan a vast chemical space of 450 million hypothetical materials of the composition $A_wB_xC_yD_z$ involving 86 possible elements, and to predict novel, stable materials based on the ML-predicted formation energy. Thus, it could therefore well be that during the 4th paradigm of science, the importance of human cognition will quickly diminish and make way for advanced AI, as schematically shown in Fig. 1.4.

Beyond the capability of discovering hidden knowledge in raw data, the computational efficiency of trained ML models, holds the promise to bridge the length- and time-scale problems inherent to *ab initio* modelling of chemical systems. One common application of ML in the field, lies in the generation of neural network potentials (NNPs)[80,88,89]. These are, in effect,

Chapter 1. Introduction
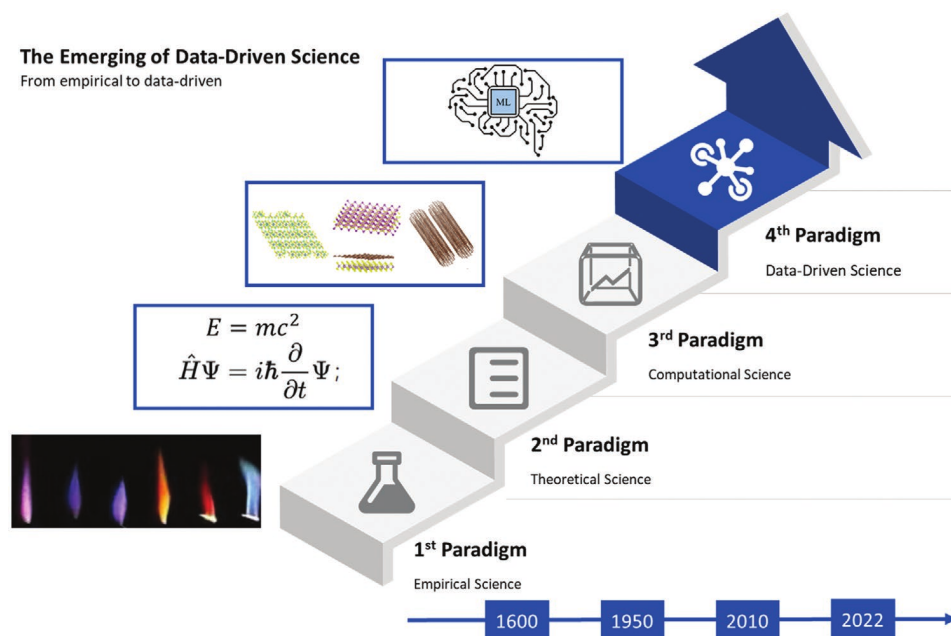
Figure 1.4: The four paradigms of science. From empirical to theoretical to computational to data-driven in the 21st century. Figure taken from Ref. [87].

NN-based force fields trained on DFT data, thus providing *ab initio* accuracy at the speed of empirical methods. This allows for the simulation of much larger systems for much longer time scales at high accuracy. For instance, simulations of systems with up to a billion atoms and hundreds of millions of time steps[90–94], have been reported, bringing the simulation of previously inaccessible chemical phenomena into reach. In principle, NNPs circumvent the need for expensive DFT evaluations at each step along the trajectory, as ML-predicted energies and forces are used to drive atomic motion according Newton's equations instead. Similarly, efforts have been undertaken to circumvent the expensive *ab initio* evaluation of energies on entirely novel structures, as well. Of particular importance in the field of heterogeneous catalysis is the prediction of adsorption energies, as it would allow for the rapid screening of catalysts and construction of reaction networks, among others. Here, graph-based representations of atomic structures, used in graph neural networks (GNNs) have proven particularly suited. The approach was successfully applied for the accurate adsorption energy prediction of organic molecules on metal surfaces in the open catalyst project and the GAME-Net model[95,96].

Lastly, I would like to highlight a few examples from the broader ap-

1.4. High-throughput and machine learning

plication of ML in science and technology. For one, researchers at Google
DeepMind could develop a NN-based density functional, DM21, that solves
the fractional electron problem[97], as well as AlphaFold, a protein structure
prediction algorithm, that solves the protein folding problem[98]. Further-
more, in recent months, the large language models (LLMs) based on the
generative pretrained transformer (GPT) architecture[99] released by Ope-
nAI[100], have conquered the world by storm. ChatGPT has become the
fastest growing app in the history of the web, crossing the 100 million user
mark after only 2 months[101]. And the capabilities of GPT-4 go as far as to
"show sparks of AGI"[102], with AGI, or artificial general intelligence, possi-
bly being the last invention humans will ever make.

Productivity Soars, Wages Stagnate

Percent growth in U.S. productivity and hourly compensation, 1950-2018

Net productivity — Hourly compensation

252.9%
115.6%
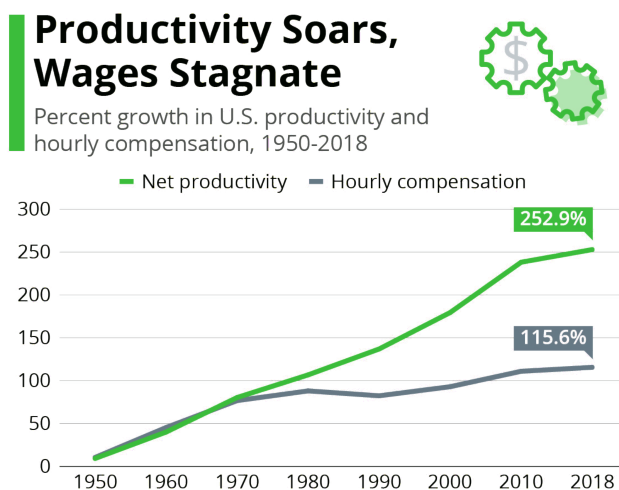
Figure 1.5: United States wage development drastically falling behind in-
creases in worker productivity over the past 50 years. Figure adapted from
Ref. [103].

Only time will tell if the last statement of the previous paragraph will be
a curse or a blessing. The current AI revolution has the potential to generate
the most prosperous and productive period of human existence. I do hope
that this time the people will reap the benefits, contrary to what has been
the general trend of the last decades (see Fig. 1.5). However, I think few of
us can even truly begin to imagine how fundamental the impact of advanced
AI will be on our species. Already at current-day sophistication, GPT-4 is
in the top 10% in the bar exam, the United States juridical examination,
which takes the average person around seven years of higher education to
reach, while in the advanced AP Chemistry exam, GPT-4 outperforms 70%
of human contenders[100]. According to Sam Altman, CEO of OpenAI, this
could drive the "cost of intelligence near zero"[104], while providing possible

Chapter 1. Introduction

---

financial gains up to \$100 trillion to whoever invents true AGI[105]. Together with the likely assumption that generative AI will advance in other fields, such as image or video generation, just as rapidly[106–108], this will likely render humans obsolete, even in the domains, in which we pride ourselves most, from intellect, to creativity. And while astronomical discoveries of the past have gradually diminished our role in the cosmic play, advanced AI will do the same yet again.

1.5 Objectives

The main objective of this thesis is to gain an in-depth understanding of various aspects of ceria-based single-atom catalysts (SACs) by density functional theory (DFT) simulations and machine learning methods. This will include exploring the prevalence and nature of dynamic charge-transfer between various single metal atoms and $CeO_2(100)$ supports, including the influence of surface reduction for the common Pt_1/CeO_2 system. The nature of the metal-support interaction will further be investigated by machine learning models that aim to reproduce the metal adsorption energies, based on readily available descriptors that do not require prior *ab initio* evaluation. Moreover, it will be shown how physical insight into the electronic interaction can be derived from these predictive models. Using the obtained insights, further computational modelling will be used to elucidate the atomic structure, stability and catalytic reactivity of two experimentally prepared, ceria-based SACs, containing platinum and manganese as the active metal center.

I will begin Chapter 3 with an exploration of the well-known Pt_1/CeO_2 catalyst, for which the dynamic oxidation state behavior was first identified. Based on this system, the correlation between local polaron structure and oxidation state dynamics will then be introduced. Before widening the scope to other metals of the periodic table, I will elucidate the influence of surface reduction on the assumed oxidation state of the platinum atom and its dynamic behavior. Then, I will address the question if local and restructured $CeO_2(100)$ facets can stabilize isolated atoms of the group 9–11 metals to identify promising systems. Via an extensive sampling of local polaron distributions, electronic ensembles of ground and excited states for each metal will be explored, allowing to discern for which metals dynamic oxidation state behavior is feasible. The actual absence/presence of the effect at finite temperatures is finally confirmed by *ab initio* molecular dynamics simulations.

I will then use the dataset of local polaron distributions obtained from the exploration of ceria-based SACs to construct a machine learning model that can predict metal adsorption energies without the need for explicit DFT evaluation. The first hurdle in this pursuit is the search for a suitable feature space of easily accessible descriptors. Then, the algorithm has to be chosen, its hyperparameters tuned, and the resulting model evaluated. After overcoming these challenges, I will derive physical insight from the predictive model by analyzing the influence of the individual features. Identifying the main contributions to the electronic interaction, allows for their disentanglement via a symbolic regression model, that further yields an analytical expression to estimate the adsorption energies.

Chapter 1. Introduction

Lastly, in Chapter 5, I will make use of computational modelling to obtain insight and understanding for two experimentally prepared ceria-based SACs, starting with single-atom platinum on oxygen-plasma pre-treated ceria. First, the synthesis of the catalyst, as well as reference samples, will be summarized, with a particular focus on the unique modifications achieved by the oxygen plasma treatment. Then, I will show how I could assign a previously unknown oxygen signal in the XPS spectrum to surface peroxide species, and how their presence alters the adsorption behavior of deposited platinum atoms. It will further be outlined how the combined effect of nanostructuring and surface peroxide achieve the exceptionally high stabilization of single-atom Pt enabled by the plasma treatment. The second system under study is given by isolated manganese on a ceria support. Following a more simple synthesis method, the speciation of the metal atom was experimentally not know and had to be addressed by simulations. With representative catalyst models available, I then explored the reactivity landscape of ammonia oxidation to nitrous oxide, for which the system showed exceptional activity and selectivity.

Chapter 2

Theory

The underlying physical laws necessary for the mathematical theory of a large part of physics and the whole of chemistry are thus completely known, and the difficulty is only that the exact application of these laws leads to equations much too complicated to be soluble. It therefore becomes desirable that approximate practical methods of applying quantum mechanics should be developed, which can lead to an explanation of the main features of complex atomic systems without too much computation.

Paul Dirac

2.1   Density Functional Theory

Density Functional Theory (DFT) presents the workhorse of modern-day computational research in chemistry, catalysis and materials science[109]. Its popularity can be attributed to the fact that it offers high accuracy at reasonable computational cost. In this section, I will outline the foundations of this very successful theory, starting from the Born-Oppenheimer approximation, which decouples the motion of electrons and nuclei. This is followed by the first Hohenberg-Kohn theorem, which states that all properties of an electronic system are uniquely defined by the ground state electron density. The second Hohenberg-Kohn theorem then uses the variational principle to show that the electron density that minimizes the energy of the total functional is the true electron density corresponding to the complete solutions of the Schrödinger equation.

However, the Hohenberg-Kohn theorem is a pure uniqueness theorem, so it does not provide a solution to the quantum many-body problem. It

41

Chapter 2.   Theory

---

was Kohn and Sham who then showed that a system of hypothetical, non-interacting electrons produces the same density as the real interacting electron system, thus allowing for approximate solutions to be found. While the Kohn-Sham method is in principle exact, the form of the exchange-correlation functional is not known. Thus, common approximations will be discussed in the following subsection, which will be followed by the so-called Hubbard correction, can improve the description of the electronic structure at low computational cost. Lastly, the special treatment of periodic systems motivated by Bloch's theorem, and the introduction of pseudopotentials (PPs) and the projector augmented wave (PAW) method will conclude the required foundations underlying the simulations presented in this work.

2.1.1   Born-Oppenheimer approximation

The fundamental quantity underlying all of quantum mechanics is the wave-function. For the quantum many-body problem, it has the general form:

$$\Psi\left(\boldsymbol{x}, \boldsymbol{X}\right) \tag{2.1}$$

where

$$
\begin{aligned}
\boldsymbol{x} &:= (\boldsymbol{x}_1, \ldots, \boldsymbol{x}_N) = (\boldsymbol{r}_1, \sigma_1, \ldots, \boldsymbol{r}_N, \sigma_N) \\
\boldsymbol{X} &:= (\boldsymbol{X}_1, \ldots, \boldsymbol{X}_\mathrm{M}) = (\boldsymbol{R}_1, \Sigma_1, \ldots, \boldsymbol{R}_\mathrm{M}, \Sigma_\mathrm{M})
\end{aligned}
\tag{2.2}
$$

denote the spatial $(\boldsymbol{r}, \boldsymbol{R})$ and spin (σ, Σ) coordinates of the N electrons and M nuclei, respectively. The total energy of the system is then given by the time-independent Schrödinger equation[110]:

$$\hat{H}\Psi(\boldsymbol{X}, \boldsymbol{x}) = E\Psi(\boldsymbol{X}, \boldsymbol{x}). \tag{2.3}$$

with the non-relativistic Hamiltonian:

$$\hat{H} = \hat{T}_n + \hat{T}_e + \hat{V}_{nn} + \hat{V}_{ne} + \hat{V}_{ee} \tag{2.4}$$

composed of the kinetic energy operators $\hat{T}_n$ and $\hat{T}_e$ for the nuclei and the electrons, respectively, as well as the potential energy operators, $\hat{V}_{nn}$, $\hat{V}_{ne}$,

UNIVERSITAT ROVIRA I VIRGILI
CERIA-BASED SINGLE-ATOM CATALYSTS: FROM SIMPLIFIED MODELS TOWARDS REAL-WORLD COMPLEXITY
Julian Geiger

2.1. Density Functional Theory

and $\hat{V}_{ee}$ for the corresponding interactions, in atomic units:

$$\hat{T}_n = -\sum_{A=1}^{M} \frac{1}{2m_A} \boldsymbol{\nabla}_A^2 \tag{2.5}$$

$$\hat{T}_e = -\sum_{i=1}^{N} \frac{1}{2} \boldsymbol{\nabla}_i^2 \tag{2.6}$$

$$\hat{V}_{nn} = -\sum_{i=1}^{N} \sum_{A=1}^{M} \frac{Z_A}{r_{Ai}} \tag{2.7}$$

$$\hat{V}_{ne} = \sum_{i=1}^{N} \sum_{j>i}^{N} \frac{1}{r_{ij}} \tag{2.8}$$

$$\hat{V}_{ee} = \sum_{A=1}^{M} \sum_{B>A}^{M} \frac{Z_A Z_B}{R_{AB}} \tag{2.9}$$

$$\tag{2.10}$$

Now, given the significantly greater mass of nuclei compared to electrons, we assume their movement to be much slower and treat their positions as stationary[111]. This allows us to factorize the wavefunction Eq. 2.1 into a nuclear and electronic part, where the former only depends on the atomic coordinates, while they enter parametrically in the latter:

$$\Psi(\boldsymbol{X}, \boldsymbol{x}) = \Psi_n(\boldsymbol{X})\Psi_e(\boldsymbol{X}, \boldsymbol{x}). \tag{2.11}$$

Substituting the product of Eq. 2.11 in the original Schrödinger equation, subtracting the nuclear terms on both sides, and dividing by the total wavefunction gives:

$$\frac{\left(\hat{T}_e + \hat{V}_{ee} + \hat{V}_{ne}\right) \Psi_e(\boldsymbol{X}, \boldsymbol{x})}{\Psi_e(\boldsymbol{X}, \boldsymbol{x})} = E - \frac{\left(\hat{T}_n + \hat{V}_{nn}\right) \Psi_n(\boldsymbol{X})}{\Psi_n(\boldsymbol{X})} \tag{2.12}$$

Hence, the right-hand side of Eq. 2.12 depends solely on the nuclear coordinates, and we can therefore collate the terms as $E_e(\boldsymbol{X})$. Now, multiplication on both sides by the electronic wavefunction yields the electronic Schrödinger equation:

$$\left(\hat{T}_e + \hat{V}_{ee} + \hat{V}_{ne}\right) \Psi_e(\boldsymbol{X}, \boldsymbol{x}) = E_e(\boldsymbol{X})\Psi_e(\boldsymbol{X}, \boldsymbol{x}) \tag{2.13}$$

2.1.2 Hohenberg-Kohn theorems

Although the Born-Oppenheimer approximation achieves a significant simplification of the quantum many-body problem, the wavefunction still depends on $4N$ coordinates (three spatial and one spin coordinate for each

Chapter 2. Theory

electron), thus making the treatment of larger system computationally prohibitive. Fortunately, however, as shown by the first Hohenberg-Kohn theorem[112], a system of electrons with all its properties is completely determined by the electron density ϱ_0 of the ground state. This allows for a reduction of the dimensionality to only the three spatial variables of the electron density (spin shall not be considered explicitly in the following). I will prove this via contradiction by showing that two electronic systems with the same number of electrons as given by:

$$N = \int d\boldsymbol{r}\, \varrho_0(\boldsymbol{r}) = \int d\boldsymbol{r}\, \varrho_0'(\boldsymbol{r}), \tag{2.14}$$

but with external potentials v and v' (which differ by more than an additive constant) cannot have the same ground state electron density ϱ_0. For this, we define the two Hamiltonians $\hat{H} = \hat{T} + \hat{V}_{ee} + \hat{v}$ and $\hat{H}' = \hat{T} + \hat{V}_{ee} + \hat{v}'$, where the local multiplicative potentials have the form: $\hat{v} = \sum_{i=1}^{N} v(\boldsymbol{r}_i)$, and the corresponding two ground state wavefunctions Ψ_0 and Ψ_0'. From the variational principle, it then follows that:

$$\left\langle \Psi_0 \left| \hat{T} + \hat{V}_{ee} + \hat{v} \right| \Psi_0 \right\rangle < \left\langle \Psi_0' \left| \hat{T} + \hat{V}_{ee} + \hat{v} \right| \Psi_0' \right\rangle \tag{2.15}$$

and

$$\left\langle \Psi_0' \left| \hat{T} + \hat{V}_{ee} + \hat{v}' \right| \Psi_0' \right\rangle < \left\langle \Psi_0 \left| \hat{T} + \hat{V}_{ee} + \hat{v}' \right| \Psi_0 \right\rangle. \tag{2.16}$$

Adding both inequalities yields:

$$\langle \Psi_0 | \hat{v} | \Psi_0 \rangle + \left\langle \Psi_0' \left| \hat{v}' \right| \Psi_0' \right\rangle < \left\langle \Psi_0' | \hat{v} | \Psi_0' \right\rangle + \left\langle \Psi_0 \left| \hat{v}' \right| \Psi_0 \right\rangle. \tag{2.17}$$

Since $\hat{v}$ is a local, multiplicative potential, we can substitute:

$$\langle \Psi_0 | \hat{v} | \Psi_0 \rangle = \int d\boldsymbol{r}\, v(\boldsymbol{r}) \varrho_0(\boldsymbol{r}) \tag{2.18}$$

and the inequality of Eq. 2.15 becomes:

$$\int d\boldsymbol{r}\, v(\boldsymbol{r})\varrho_0(\boldsymbol{r}) + \int d\boldsymbol{r}\, v'(\boldsymbol{r})\varrho_0'(\boldsymbol{r}) < \int d\boldsymbol{r}\, v(\boldsymbol{r})\varrho_0'(\boldsymbol{r}) + \int d\boldsymbol{r}\, v'(\boldsymbol{r})\varrho_0(\boldsymbol{r}). \tag{2.19}$$

With our initial assumption that $\varrho_0(\boldsymbol{r}) = \varrho_0'(\boldsymbol{r})$ this leads to the contradiction:

$$\int d\boldsymbol{r}\, v(\boldsymbol{r})\varrho_0(\boldsymbol{r}) + \int d\boldsymbol{r}\, v'(\boldsymbol{r})\varrho_0(\boldsymbol{r}) < \int d\boldsymbol{r}\, v(\boldsymbol{r})\varrho_0(\boldsymbol{r}) + \int d\boldsymbol{r}\, v'(\boldsymbol{r})\varrho_0(\boldsymbol{r}) \tag{2.20}$$

concluding the proof.

UNIVERSITAT ROVIRA I VIRGILI
CERIA-BASED SINGLE-ATOM CATALYSTS: FROM SIMPLIFIED MODELS TOWARDS REAL-WORLD COMPLEXITY
Julian Geiger

2.1. Density Functional Theory

The second Hohenberg-Kohn theorem now states that any trial electron density that integrates to the correct number of electrons, will lead to an energy that is greater than or equal to the true ground-state energy. To derive this, I will follow a constrained search approach for the ground state energy E_0 of an electronic system with N electrons:

$$
\begin{aligned}
E_0 &= \min_{\Psi \to N} \left\{ \left\langle \Psi \left| \hat{T} + \hat{V}_{ee} + \hat{v} \right| \Psi \right\rangle \right\} \\
&= \min_{\varrho \to N} \left\{ \min_{\Psi \to \varrho} \left\{ \left\langle \Psi \left| \hat{T} + \hat{V}_{ee} + \hat{v} \right| \Psi \right\rangle \right\} \right\} \\
&= \min_{\varrho \to N} \left\{ \min_{\Psi \to \varrho} \left\{ \left\langle \Psi \left| \hat{T} + \hat{V}_{ee} \right| \Psi \right\rangle + \langle \Psi | \hat{v} | \Psi \rangle \right\} \right\} \\
&= \min_{\varrho \to N} \left\{ \min_{\Psi \to \varrho} \left\{ \left\langle \Psi \left| \hat{T} + \hat{V}_{ee} \right| \Psi \right\rangle + \int d\boldsymbol{r} v(\boldsymbol{r}) \varrho(\boldsymbol{r}) \right\} \right\} \\
&= \min_{\varrho \to N} \left\{ \min_{\Psi \to \varrho} \left\{ \left\langle \Psi \left| \hat{T} + \hat{V}_{ee} \right| \Psi \right\rangle \right\} + \int d\boldsymbol{r} v(\boldsymbol{r}) \varrho(\boldsymbol{r}) \right\} \\
&= \min_{\varrho \to N} \left\{ F[\varrho] + \int d\boldsymbol{r} v(\boldsymbol{r}) \varrho(\boldsymbol{r}) \right\}
\end{aligned}
\tag{2.21}
$$

Here, the condition $\min_{\Psi \to N}$ denotes that we are carrying out a *constrained search* over all wavefunctions that define an N-electron system. Then, all wavefunctions yielding a certain electron density are grouped together and within each of these groups the one is sought which minimizes the energy. In the third line of Eq. 2.21, the local multiplicative potential $\hat{v}$ can then be taken out of the bra-ket and expressed as an integral over the electron density (see Eq. 2.18). Importantly, for a given electron density, this integral is fully determined, and it can therefore be taken out of the inner *constrained search*. Finally, the remaining inner *constrained search* defines the Hohenberg-Kohn functional $F[\varrho]$ of the electron density. Thus, the electron density ϱ_0 that fulfills the minimization in the last line of Eq. 2.21 is the ground state electron density. Consequently, the ground state wavefunction is the wavefunction that minimizes the Hohenberg-Kohn functional:

$$
F[\varrho] = \min_{\Psi \to \varrho_0} \left\langle \Psi \left| \hat{T} + \hat{V}_{ee} \right| \Psi \right\rangle ,
\tag{2.22}
$$

which can finally be expressed as:

$$
\Psi_0 = \Psi[\varrho_0] .
\tag{2.23}
$$

2.1.3 Kohn-Sham formalism

Although the Hohenberg-Kohn theorems enable us to consider the much simpler electron density rather than the complex wavefunction as the fundamental quantity, except for the simplest of systems, the remaining quantum

Chapter 2. Theory

many-body problem still cannot be solved analytically. The root of this lies in the electron-electron interaction operator, thus in the Kohn-Sham (KS) formalism[113], a model system of hypothetical, non-interacting electrons, which we assume to produce the same electron density as the real electronic system, is introduced. The Hamiltonian of such a system of non-interacting electrons under the influence of a local multiplicative potential, $\hat{v}_s$ is given by:

$$\left[\hat{T} + \hat{v}_s\right]\Phi_0 = E_{s,0}\Phi_0 \tag{2.24}$$

with

$$\hat{v}_s = \sum_{i=1}^{N} V_s\left(\boldsymbol{r}_i\right) \tag{2.25}$$

Following a similar *constrained search* approach as in the derivation of the second HK theorem we obtain in equivalence to the HK functional:

$$T_s[\varrho] = \min_{\Psi \to \varrho}\{\langle\Psi|\hat{T}|\Psi\rangle\} \tag{2.26}$$

with the wavefunction that fulfills the minimization in Eq. 2.26 as $\Phi[\varrho]$. Now, taking the functional derivative leads to the Euler equation:

$$\frac{\delta\left\{T_s[\varrho] + \int d\boldsymbol{r}v_s(\boldsymbol{r})\varrho(\boldsymbol{r})\right\}}{\delta\varrho(\boldsymbol{r})} = \frac{\delta T_s[\varrho]}{\delta\varrho(\boldsymbol{r})} + v_s(\boldsymbol{r}) = \mu. \tag{2.27}$$

Despite the fact that E_0 corresponds to the minimum of this functional, we set its derivative is a constant, μ, instead of 0, as the constraint:

$$\int d\boldsymbol{r}\delta\varrho(\boldsymbol{r}) = 0 \tag{2.28}$$

must be fulfilled (however, a constant does not change the functional derivative). Eq. 2.27 therefore defines the Kohn-Sham potential:

$$v_s(\boldsymbol{r}) = -\left.\frac{\delta T_s[\varrho]}{\delta\varrho(\boldsymbol{r})}\right|_{\varrho=\varrho_0} + \mu \tag{2.29}$$

with the ground-state KS wavefunction:

$$\Phi_0 = \Phi\left[\varrho_0\right]. \tag{2.30}$$

From this we can formally define the exchange and correlation energy functionals as:

$$E_x[\varrho] = \left\langle\Phi[\varrho]\left|\hat{V}_{ee}\right|\Phi[\varrho]\right\rangle - \frac{1}{2}\int d\boldsymbol{r}d\boldsymbol{r}'\frac{\varrho(\boldsymbol{r})\varrho\left(\boldsymbol{r}'\right)}{|\boldsymbol{r}-\boldsymbol{r}'|} \tag{2.31}$$

and

$$E_c[\varrho] = \left\langle \Psi[\varrho] \left| \hat{T} + \hat{V}_{ee} \right| \Psi[\varrho] \right\rangle - \left\langle \Phi[\varrho] \left| \hat{T} + \hat{V}_{ee} \right| \Phi[\varrho] \right\rangle, \qquad (2.32)$$

respectively. From this, we can now reconstruct the original HK functional as:

$$F[\varrho] = T_s[\varrho] + U[\varrho] + E_x[\varrho] + E_c[\varrho] \qquad (2.33)$$

which, when substituted into Euler's equation, Eq. 2.29, leads to:

$$v_s(\boldsymbol{r}) = v(\boldsymbol{r}) + v_H([\varrho_0]) + v_x([\varrho_0]) + v_c([\varrho_0]) \qquad (2.34)$$

where we have replaced the functional derivatives of the energy terms by their respective potentials. Eq. 2.34 therefore provides us with a formal definition of the KS potential, from which the many-body KS equation:

$$\left[\hat{T} + \hat{v} + \hat{v}_H + \hat{v}_x + \hat{v}_c \right] \Phi_0 = E_{s,0} \Phi_0 \qquad (2.35)$$

can be constructed. As no electron-electron interaction is present in Eq. 2.35, it can be decoupled into the one-electron KS equations:

$$\left[-\frac{1}{2} \boldsymbol{\nabla}^2 + v(\boldsymbol{r}) + v_H(\boldsymbol{r}) + v_x(\boldsymbol{r}) + v_c(\boldsymbol{r}) \right] \varphi_i(\boldsymbol{r}) = \epsilon_i \varphi_i(\boldsymbol{r}) \qquad (2.36)$$

2.1.4 Density functional approximations

The theoretical foundations of KS-DFT outlined up to this point are, in principle, exact. However, we are now faced with the problem that the exchange and correlation functionals are actually unknown, and approximations must be introduced. Thus, we present here conceptually important and widely used approaches, following the so-called *Jacob's ladder* classification, Fig. 2.1, which orders them by increasing accuracy[114]. The simplest approximation (first rung) is given by the local-density approximation (LDA)[113], for which the exchange-correlation energy takes the general form:

$$E_{xc}^{LDA}[\varrho] = \int \varrho(\boldsymbol{r}) \epsilon_{xc}(\varrho(\boldsymbol{r})) d\boldsymbol{r}, \qquad (2.37)$$

and only involves the electron density. It is motivated by the fact that for the homogeneous electron gas, the exchange functional is known to be[113]:

$$E_x^{LDA}[\varrho] = c \int d\boldsymbol{r} \varrho^{\frac{4}{3}}(\boldsymbol{r}). \qquad (2.38)$$

However, as the correlation functional cannot be derived exactly, it must be obtained numerically, e.g. via Quantum Monte Carlo sampling. Due to

Chapter 2.   Theory
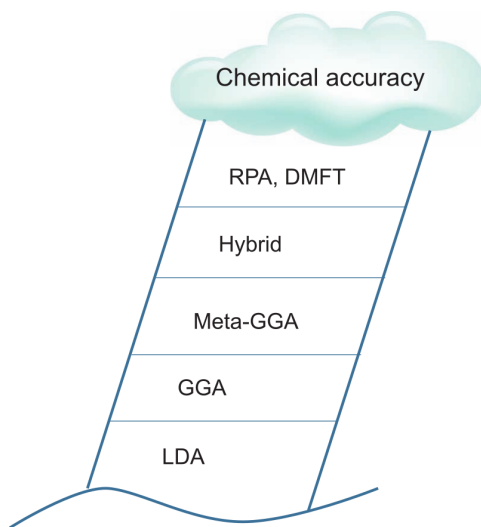
Figure 2.1: Jacob's ladder of density functional approximations. Taken from [114].

its foundation in the homogeneous electron gas, LDA works reasonably well for systems with slowly changing electron densities, such as bulk materials, however, its accuracy quickly degrades for systems with rapidly changing electron densities, such as molecules or surfaces.

Hence, a natural extension is the inclusion of the gradient of the electron density in the functional, leading to the generalized-gradient approxima-tion (GGA)[115,116] class of functionals (second rung), where the exchange-correlation energy taking the general form:

$$E_{xc}^{GGA}[\varrho] = \int d\boldsymbol{r}\epsilon_{xc}^{GGA}(\varrho(\boldsymbol{r}); \boldsymbol{\nabla}\varrho(\boldsymbol{r}))\varrho(\boldsymbol{r}). \qquad (2.39)$$

Various parametrizations have been proposed that aim to reproduce exper-imental results or meet fundamental theoretical constraints. The resulting functionals are often named after the initials of their constructors, for in-stance the PBE functional, developed by Perdew, Burke, and Ernzerhof[116], which forms the basis for the simulations presented in this work.

Following the same line of reasoning, including higher-order derivatives can further improve the accuracy of density functional approximations. For instance, so-called meta-GGA functionals (third rung) also include the Laplacian of the electron density. Nonetheless, this approach quickly pro-vides diminishing returns, as DFT-inherent shortcomings are not resolved. For instance, one such shortcoming is the so-called self-interaction error (SIE). It arises due to the fact that the Hartree energy is computed as the

Coulomb interaction between every electron and the average density created by all electrons, meaning that the electron is artificially interacting with itself. Although common exchange-correlation approximations aim to cancel out this nonphysical self-interaction, the removal is usually insufficient. Practically, this can lead to erroneous geometries and energies, as well as solutions with over-delocalized electrons.

One possibility to alleviate this issue is to mix in a fraction of the exact Hartree-Fock exchange energy, to obtain so-called hybrid functionals (fourth rung). As obtaining the exact Hartree-Fock exchange is rather expensive, it is common practice to only use it for short-range interactions, and the DFT exchange for long-range interactions, allowing for smoother convergence. One popular range-separated hybrid functional developed by Heyd, Scuseria, and Ernzerhof (HSE) takes the general form:

$$E_{xc}^{HSE} = \alpha E_x^{HF,SR}(\omega) + (1-\alpha)E_x^{PBE,SR}(\omega) + E_x^{PBE,LR}(\omega) + E_c^{PBE} \quad (2.40)$$

where 25% of Hartree Fock exchange is usually used ($\alpha = 0.25$), and typical choices for the range-separation parameter ω are $0.2 \, \text{Å}^{-1}$ (HSE06) or $0.3 \, \text{Å}^{-1}$ (HSE03)[117–119].

2.1.5   Hubbard correction

While hybrid functionals provide a better description of the electronic structure than GGA functionals, calculation of the exact Fock exchange is computationally expensive, thus limiting the size of systems that can be studied. An alternative approach is given by the so-called Hubbard U correction[120–123]. Here, an *ad-hoc* energy correction is added to the approximate DFT energy, E_{DFT}. In the rotationally invariant formulation[124] it takes the form:

$$E_{\text{DFT+U}} = E_{\text{DFT}} + \frac{U_{\text{eff}}}{2} \sum_{\sigma} \left[\sum_m \rho_{mm}^{\sigma} - \sum_{m,m'} \rho_{mm'}^{\sigma} \rho_{m'm}^{\sigma} \right], \qquad (2.41)$$

where U_{eff} determines the overall strength of the correction, and $\rho_{mm'}^{\sigma}$ is the spin orbital density matrix of the orbitals to which it is applied. The latter is obtained via:

$$\rho_{mm'}^{\sigma} = \sum_{i,\sigma} f_i^{\sigma} \langle \phi_i^{\sigma} | \hat{P}_{mm'}^I | \phi_i^{\sigma} \rangle, \qquad (2.42)$$

with the occupancy number f_i^{σ} of the ϕ_i^{σ} quasiparticle orbital and $\hat{P}_{mm'}^I$ the projector operator of the atom at site I and m, m' the magnetic quantum numbers of the orbitals to which the correction is applied.

Chapter 2. Theory

In effect, Eq. (2.41) causes an energy penalty for partially occupied states, pushing the system towards either fully occupied or unoccupied orbitals. It therefore counteracts the excessive electron delocalization caused by the self-interaction error (SIE) inherent to local and semi-local functionals. It is therefore particularly useful for the description of strongly correlated materials and materials containing highly localized d or f electrons. Lastly, it restores the derivative discontinuity at integer electron numbers (see Fig. 2.2), which is a known property of the true functional.
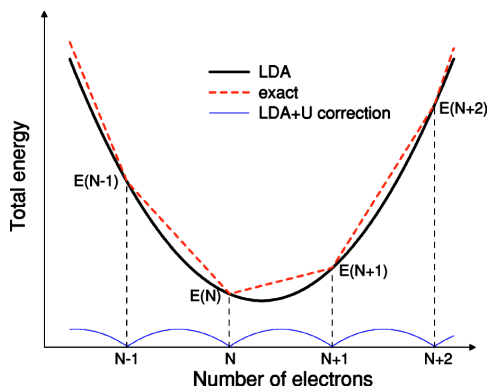
Figure 2.2: Restoration of piecewise linearity of the total energy w.r.t. the number of electrons by the Hubbard U correction. Taken from[125].

2.1.6   Periodic systems: Bloch's theorem and plane waves

I will now outline the treatment of the special case of a periodic potential with translational symmetry, $v(\boldsymbol{r})$ for which $v(\boldsymbol{r} + \boldsymbol{R}) = v(\boldsymbol{r})$. Such a potential is formed, for instance, by the atomic nuclei in a crystalline lattice, with the lattice vectors $\boldsymbol{R}$:

$$\boldsymbol{R} = n_1\boldsymbol{a_1} + n_2\boldsymbol{a_2} + n_3\boldsymbol{a_3} \tag{2.43}$$

where n_1, n_2, n_3 are integers and $\boldsymbol{a_1}, \boldsymbol{a_2}, \boldsymbol{a_3}$ are the primitive vectors that span the crystal lattice. In this case, the solution to the Schrödinger equation is given by Bloch's theorem, which states that the electron wavefunctions can be written as the product of a plane wave, $e^{i\boldsymbol{g}\cdot\boldsymbol{r}}$, and a function, $u_{\boldsymbol{g}}(\boldsymbol{r})$, with the same periodicity as the lattice[126,127]:

$$\psi_{\boldsymbol{g}}(\boldsymbol{r}) = u_{\boldsymbol{g}}(\boldsymbol{r})e^{i\boldsymbol{g}\cdot\boldsymbol{r}}. \tag{2.44}$$

Here, $\boldsymbol{g}$ is a general reciprocal vector that can be expressed as the sum of a reciprocal lattice vector $\boldsymbol{G}$ and a vector of the first Brillouin zone $\boldsymbol{k}$:

$$\boldsymbol{g} = \boldsymbol{G} + \boldsymbol{k}. \tag{2.45}$$

with:

$$\boldsymbol{k} = k_1\boldsymbol{b_1} + k_2\boldsymbol{b_2} + k_3\boldsymbol{b_3}, \tag{2.46}$$

and

$$\begin{aligned}
\boldsymbol{b_1} &= 2\pi\frac{\boldsymbol{a_2} \times \boldsymbol{a_3}}{\boldsymbol{a_1} \cdot (\boldsymbol{a_2} \times \boldsymbol{a_3})} \\
\boldsymbol{b_2} &= 2\pi\frac{\boldsymbol{a_3} \times \boldsymbol{a_1}}{\boldsymbol{a_2} \cdot (\boldsymbol{a_3} \times \boldsymbol{a_1})} \\
\boldsymbol{b_3} &= 2\pi\frac{\boldsymbol{a_1} \times \boldsymbol{a_2}}{\boldsymbol{a_3} \cdot (\boldsymbol{a_1} \times \boldsymbol{a_2})}.
\end{aligned} \tag{2.47}$$

With this, we can now rewrite Eq. 2.44 as:

$$\psi_{\boldsymbol{g}}(\boldsymbol{r}) = \left(u_{\boldsymbol{g}}(\boldsymbol{r})e^{i\boldsymbol{G}\cdot\boldsymbol{r}}\right)e^{i\boldsymbol{k}\cdot\boldsymbol{r}} = u_{n\boldsymbol{k}}(\boldsymbol{r})e^{i\boldsymbol{k}\cdot\boldsymbol{r}}, \tag{2.48}$$

where we have introduced the so-called *band index, n*[128]. Given that $e^{i\boldsymbol{G}\cdot\boldsymbol{r}}$ and $u_{\boldsymbol{g}}(\boldsymbol{r})$ are periodic over the lattice, $u_{n\boldsymbol{k}}(\boldsymbol{r})$ is as well. Consequently, the KS orbitals can be divided into a plane wave $e^{i\boldsymbol{k}\cdot\boldsymbol{r}}$ and a periodic function $u_{n\boldsymbol{k}}(\boldsymbol{r})$, where $\boldsymbol{k}$ is a wave vector located in the first Brillouin zone.

As the KS one-electron equations cannot be solved analytically (except for the simplest of systems), for practical applications, they must be expanded in a basis set, and transformed into a form that can be handled by computers. To this end, we make use of the Fourier transform (FT), which allows representation of any function as a linear combination of sinusoidal functions. In addition, as we have just shown, the eigenfunctions of the Schrödinger equation for a periodic potential can be expressed as the product of a plane wave and a lattice-periodic function. Thus, Bloch's theorem motivates the use of plane waves as a natural basis set choice for crystalline solids. In theory, the FT would require an infinite number of basis function, in practice, however, only plane waves up to a certain energy, given by:

$$|\boldsymbol{G} + \boldsymbol{k}| < \boldsymbol{G}_{\text{cut}} \text{ with } E_{\text{cut}} = \frac{\hbar^2}{2m}\boldsymbol{G}_{\text{cut}}^2 \tag{2.49}$$

are used. As eigenfunctions of the FT, plane waves further lend themselves naturally to transformations between real and reciprocal space, allowing reduction of computational cost by the use of the highly efficient fast Fourier transform (FFT). Lastly, plane waves naturally respect periodic boundary conditions, which are used to simulate infinitely extending crystals/surfaces.

2.1.7 Pseudopotentials and the PAW method

As outlined in the previous section, plane waves are generally a good basis set choice for crystalline materials. However, one shortcoming is that accurately describing the rapid oscillations of wavefunctions near the atomic nucleus would require such high energy cutoffs that exceed any practical limit.

Chapter 2. Theory

In addition, for most problems in chemistry, materials science, and catalysis, only the valence electrons are of interest, while it is usually sufficient to treat the core electrons as static and inert (frozen core approximation). This approach has the additional advantage that it reduces the number of electrons in the system that must be treated explicitly. In practice, it is achieved by replacing the nuclear potential by a so-called *pseudopotential* (PP)[129]. An illustration is provided in Fig. 2.3. There exist various different
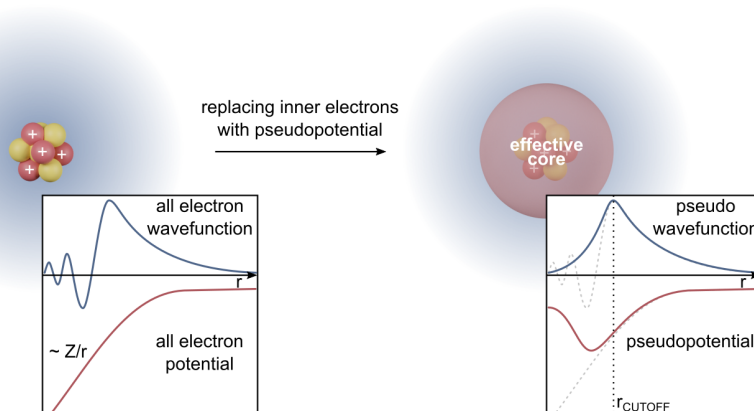
Figure 2.3: Pseudopotential replacing oscillatory all electron potential, resulting in smoother pseudo-wavefunction. Taken from [130].

ways of constructing PPs, which will be outlined shortly in the following:

1. **Norm-conserving PPs** ensure that the valence electron wavefunction derived from the pseudopotential matches the "real" (all electron) wavefunction outside of a certain cutoff radius. This preserves the norm (i.e., the total probability of finding the electron) of the wavefunction.

2. **Ultrasoft PPs** relax the norm-conservation requirement, allowing for smoother pseudo-wavefunctions, thus further reducing computational cost. However, this comes at the cost of a higher requirement for nonlocality in the potential[131].

3. **Projector Augmented-Wave (PAW) method**[132,133] retains some of the information on the full electron wavefunction, thus providing a compromise between, all electron and PP methods. It therefore provides a more accurate description of the electron density near the nucleus, however, also incurs a slightly higher computational cost.

As the PAW method is implemented in the Vienna Ab initio Simulation Package VASP[134–136] (used throughout this thesis), we shall have a closer

UNIVERSITAT ROVIRA I VIRGILI
CERIA-BASED SINGLE-ATOM CATALYSTS: FROM SIMPLIFIED MODELS TOWARDS REAL-WORLD COMPLEXITY
Julian Geiger

2.2. Machine Learning

look at its mathematical formulation. Just like with PP-based methods, our goal is to replace the KS wavefunction $\psi_n(\boldsymbol{r})$ by a smoother pseudo-wavefunction $\tilde{\psi}_n(\boldsymbol{r})$, see Fig. 2.3. We can state the problem as:

$$\psi_n(\boldsymbol{r}) = \underbrace{\left(1 + \sum_a T^a\right)}_{T} \tilde{\psi}_n(\boldsymbol{r}), \tag{2.50}$$

where we have formally introduced the transformation operators T. These transform the pseudo-wavefunction within the *augmentation spheres* (index a), i.e. core regions of the atoms, into the all electron wavefunction, while outside, the KS and pseudo-wavefunctions shall be equal. In the PAW method, these transformation operators are constructed as:

$$T^a = \sum_i (\underbrace{\phi_i^a(\boldsymbol{r})}_{1} - \underbrace{\tilde{\phi}_i^a(\boldsymbol{r})}_{2}) \underbrace{\langle \tilde{p}_i^a}_{3} \mid \tag{2.51}$$

with 1. the *all electron partial waves*, which are basis functions in which the all electron wavefunction can be expanded within the augmentation sphere (usually the radial solutions to the Schrödinger equation for the free atom), 2. the *pseudo partial waves* outside the augmentation spheres, which are chosen identical to the all electron partial waves, and 3. the *projector functions*, or *pseudo partial waves* inside the augmentation spheres, which are chosen such that they form a basis for the pseudo-wavefunction with the augmentation sphere. Plugging Eq. 2.51 into Eq. 2.50 leads to:

$$\begin{aligned}
\psi_n(\boldsymbol{r}) &= \tilde{\psi}_n(\boldsymbol{r}) + \sum_a \sum_i (\phi_i^a(\boldsymbol{r}) - \tilde{\phi}_i^a(\boldsymbol{r})) \langle \tilde{p}_i^a \mid \tilde{\psi}_n \rangle \\
&= \tilde{\psi}_n(\boldsymbol{r}) + \sum_a \psi_n^a(\boldsymbol{r}) - \sum_a \tilde{\psi}_n^a(\boldsymbol{r}),
\end{aligned} \tag{2.52}$$

where in the second line the three components that reproduce the KS wavefunction in the PAW method can be identified clearly. They are given by a pseudo-wavefunction that remains smooth throughout, to which a sharp function, specifically defined within each augmentation sphere is added, and, lastly, a smooth function, existing solely within the spheres is subtracted, counteracting the first term.

2.2 Machine Learning

Having laid the necessary groundwork, I shall now raise the question, how efficient DFT *really* is? It is generally agreed upon that DFT has a scaling of around $O(N^3)$. That means, a doubling of system size leads to an eightfold

Chapter 2. Theory

increase in computing time. Increase system size by an order of magnitude, and a simulation that was previously finished in a day takes almost 3 years. Thus, it becomes clear why the accurate quantum mechanical treatment of atomic systems, despite the vast computational improvements of the last decades, is still limited to small systems of up to a few hundred atoms, and time scales in the picosecond range.

In recent years, Machine Learning (ML) has emerged as a promising avenue to overcome this challenge[80,83,137–139]. Trained on data generated from DFT calculations, ML algorithms can learn complex correlations, and subsequently predict properties of new systems at a significantly reduced computational cost. For example, ML algorithms have been employed to explore potential energy surfaces[140–142], construct new density functionals[97,143] predict adsorption energies of molecules on surfaces[95,144], and to quickly screen millions of materials for specific properties, vastly accelerating the rate of discovery[145,146], just to name a few examples. Thus, the integration of DFT and ML holds great promise for catalyzing scientific discoveries and technological advancements in a cost-effective and efficient manner.

I will begin this chapter with a discussion of linear regression which serves as fundamental building block for more complex algorithms. Then, I will introduce regularization and show how it can improve predictions, simplify models, and improve their interpretability. Then, the linearity constraint imposed by the former models will be lifted, and symbolic regression will be introduced as a method to derive closed-form mathematical expressions from data. Lastly, I will introduce ensemble methods, using the Random Forest (RF) as a popular example.

2.2.1 Regularized linear models

We begin with Linear Regression (LR) as the conceptually simplest model to predict a response y from a set of independent variables, $\boldsymbol{X}$. It can be formulated as:

$$\boldsymbol{y} = \boldsymbol{X}\boldsymbol{\beta} + \boldsymbol{\epsilon}. \tag{2.53}$$

where $\boldsymbol{\beta}$ are the unknown parameters or coefficients, and $\boldsymbol{\epsilon}$ is the noise of the measurement. Minimizing the residual sum of squares (RSS) as loss function:

$$\hat{\beta} = \underset{\boldsymbol{\beta}}{\operatorname{argmin}} \|\boldsymbol{y} - \boldsymbol{X}\boldsymbol{\beta}\|^2 \tag{2.54}$$

leads to the ordinary least squares (OLS) estimator:

$$\hat{\beta} = \left(\boldsymbol{X}^{\top}\boldsymbol{X}\right)^{-1}\boldsymbol{X}^{\top}\boldsymbol{y}. \tag{2.55}$$

The Gauss-Markov theorem now states that this estimator is the best linear unbiased estimator (BLUE) under the assumption of independently and identically distributed errors with zero mean and constant variance (which is typically given in applications where LR is suitable). It can thus be stated that the OLS estimator has the smallest variance among all linear unbiased estimates.

However, it might be desirable to sacrifice some variance to introduce a certain amount of bias, for instance to mitigate overfitting or to reduce the number of retained predictors, thus simplifying the model. This can generally be achieved by introducing a penalty term on the magnitude of the parameters $\boldsymbol{\beta}$ in the loss function, also known as regularization. Depending on the mathematical form of the penalty term, one obtains the well-known Ridge, Lasso, and Elastic Net (EN) estimators:

$$\hat{\beta}_{\text{Ridge}} = \underset{\boldsymbol{\beta}}{\operatorname{argmin}} \left\{ \|\boldsymbol{y} - \boldsymbol{X}\boldsymbol{\beta}\|^2 + \lambda\|\boldsymbol{\beta}\|^2 \right\} \tag{2.56}$$

$$\hat{\beta}_{\text{Lasso}} = \underset{\boldsymbol{\beta}}{\operatorname{argmin}} \left\{ \|\boldsymbol{y} - \boldsymbol{X}\boldsymbol{\beta}\|^2 + \lambda\|\boldsymbol{\beta}\| \right\} \tag{2.57}$$

$$\hat{\beta}_{\text{EN}} = \underset{\boldsymbol{\beta}}{\operatorname{argmin}} \left\{ \|\boldsymbol{y} - \boldsymbol{X}\boldsymbol{\beta}\|^2 + \lambda_1\|\boldsymbol{\beta}\|^2 + \lambda_2\|\boldsymbol{\beta}\| \right\} \tag{2.58}$$

where λ determines the amount of regularization applied. We can see that in the case of Ridge, the parameters $\boldsymbol{\beta}$ enter quadratically, as a so-called "L2 penalty", for Lasso with their absolute magnitude, as "L1 penalty", and for the EN as a linear combination of both. With the Ridge Regression loss, one obtains the following analytical solution:

$$\hat{\beta}_{\text{ridge}} = \left(\boldsymbol{X}^{\top}\boldsymbol{X} + \boldsymbol{\lambda}\boldsymbol{I} \right)^{-1} \boldsymbol{X}^{\top}\boldsymbol{y}. \tag{2.59}$$

Due to the non-differentiability of the absolute (L1) term, this is not the case for Lasso and EN, so here iterative approaches like Coordinate Descent typically used.

Ridge, Lasso, and EN achieve, in effect, the same modification of the initial LR model, that is, a shrinking of the feature coefficients which leads to a reduction in model complexity. One important difference, however, is the fact that with increasing regularization using the "L1 penalty", individual feature coefficients will vanish, while with the "L2 penalty", they will get arbitrarily close to zero, but never reach it exactly.

Hence, in addition to providing predictions, regularized linear models can also be used to extract information about relative feature importances. As the resulting models are simple weighted linear combinations of the features, they are easily interpretable. However, this linearity also limits their ability to capture more complex data relations. One way to alleviate this

Chapter 2. Theory
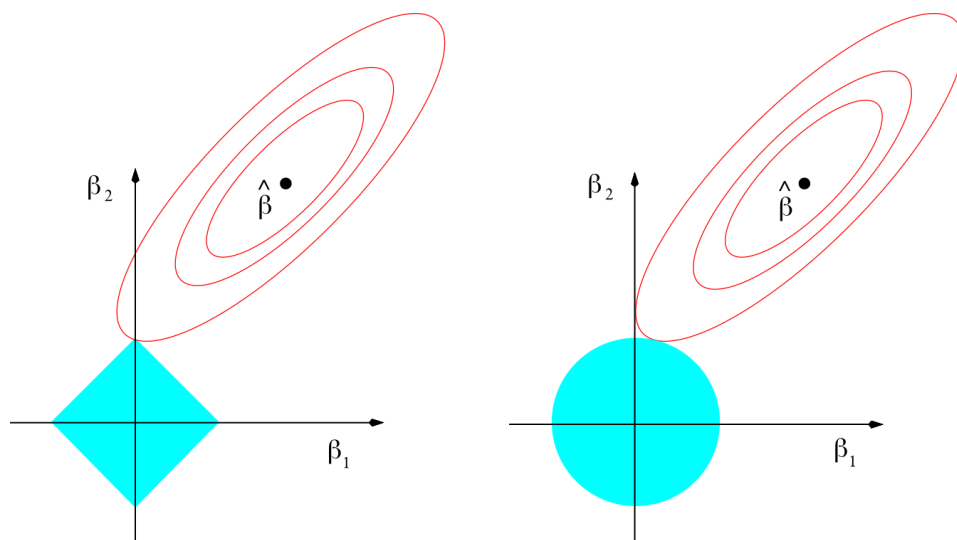
Figure 2.4: Contours of the errror (red lines) and constraint (blue shapes) functions for the Lasso (left) and Ridge (right) estimators. Taken from [147].

shortcoming is by constructing more complex, higher-order feature spaces via mathematical combinations of the primary set. Here, in-place modifications of individual features, such as exponentiation or taking the inverse, but also ratios, differences, summations, or multiplications involving any number of features, can be created. Although this indeed leads to higher model flexibility, the artificially constructed feature spaces grow rapidly and at the expense of interpretability.

2.2.2 Symbolic Regression

An alternative approach more akin to the classical discovery of physical laws is given by Symbolic Regression (SR). It is a type of regression analysis that seeks to discover the most suitable mathematical relationship to fit a given dataset. While traditional regression techniques as outlined in the previous section require a predetermined expression and optimize a set of coefficients, symbolic regression focuses on finding the optimal model structure itself. It yields an interpretable mathematical expression that explains the relationship between variables. SR is particularly suited when the theoretical relations underpinning a dataset are not known or when new relationships or insights in the data are sought after. The resulting models therefore offer more than mere prediction capabilities, but also allow for the understanding of the relationship and interactions among the variables.

UNIVERSITAT ROVIRA I VIRGILI
CERIA-BASED SINGLE-ATOM CATALYSTS: FROM SIMPLIFIED MODELS TOWARDS REAL-WORLD COMPLEXITY
Julian Geiger

2.2. Machine Learning

One such technique is the Bayesian Machine Scientist (BMS) developed by Guimera et al.[148] Given a dataset, the BMS explores the space of closed-form mathematical models, balancing goodness of fit and model complexity. Conceptually, this is achieved by representing mathematical expressions as trees where the internal nodes correspond to mathematical operations, and the leaves, to variables and parameters. This is schematically shown in Fig. 2.5. To obtain an initial starting guess for the exploration, the authors scraped (a total of 4080) named scientific equations from Wikipedia, converted them into the respective trees, and carried out a statistical analysis on, among other properties, the average number of each operations per expression, and number of variables/parameters. From this, a statistically plausible initial equation can be generated, given a set of input properties. Subsequently, the mathematical space is explored by applying modifications to the initial formula applying a Markov chain Monte Carlo (MCMC) sampling. The resulting models are evaluated based on the Sum of Squared Errors (SSE) and the Bayesian Information Criterion (BIC). The goal here is to fit the data as accurately as possible, while model complexity is penalized. The following modifications are applied during the sampling:

1. Elementary tree replacement, where an elementary tree is defined by containing at most one operation (50%)

2. Node replacement, where a node can be a function, a variable, or a parameter (45%)

3. Addition/removal of the root of the tree (5%)

Note that the relative probabilities for these modifications should not affect the equilibrium distribution, but might well alter the convergence speed.
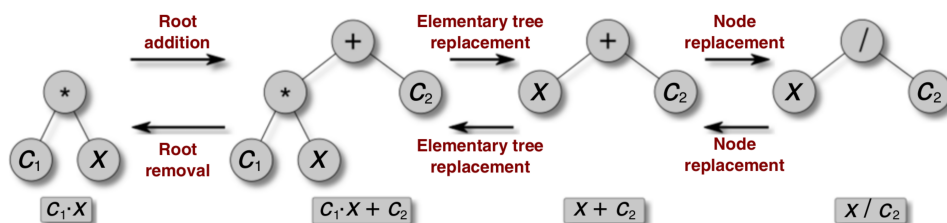
Figure 2.5: General tree structure used in the BMS to represent equations and modifications that are applied to explore the mathematical space. Taken from [148].

Chapter 2.   Theory

2.2.3   Ensemble Methods

While regularized linear models, such as the EN, and Symbolic Regression, like the BMS, yield closed-form expressions that can be written down as equations, this is not the case for so-called ensemble methods. This makes them highly versatile and able to reproduce arbitrarily complex data relations, however, their interpretation is usually also less straightforward. I will focus in this section on the Random Forest (RF) as a representative example.

Its fundamental building block, the Decision Tree is a flowchart-like structure in which each internal node represents a "test" on an independent variable, (e.g., is Feature A greater than a certain value?), each branch represents the outcome of the test, and each leaf node represents a predicted numerical outcome, typically the average target value of the training samples that reach that leaf. This is schematically shown in Fig. 2.6. During the construction of the tree, the choice for the best feature to split on is based on reducing standard deviation or minimizing the SSE in the target variable. This decision is made in a *greedy* fashion, meaning the locally optimal choice is made at each step with the assumption that this will eventually yield the global minimum (rather than trying to directly trying to find a global minimum). When making a prediction, the Decision Tree traverses the decision nodes starting from the root, testing the appropriate condition at each node, and following the branch corresponding to the outcome. This is repeated until a leaf node is reached, and the value associated with that leaf node is returned as the prediction.
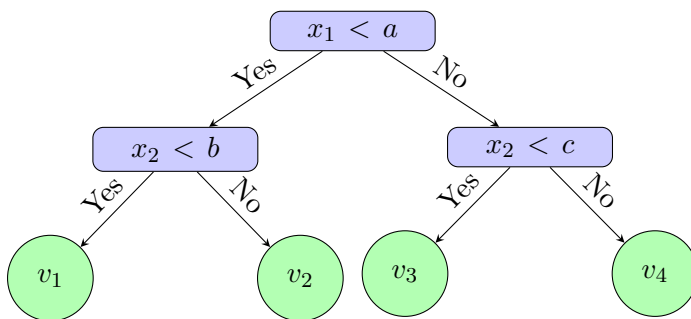
Figure 2.6: Schematic representation of a Decision Tree, where the two variables x_1 and x_2 are evaluated based on the thresholds, a, b, and c, yielding the final predictions v (image generated by GPT4 in `TikZ`.)

However, individual Decision Trees suffer from various shortcomings. Most importantly, they tend to overfit the training data, especially when being grown to arbitrary depth. Thus, the Random Forest implements vari-

UNIVERSITAT ROVIRA I VIRGILI
CERIA-BASED SINGLE-ATOM CATALYSTS: FROM SIMPLIFIED MODELS TOWARDS REAL-WORLD COMPLEXITY
Julian Geiger

2.3. The chemistry of ceria

ous modifications to alleviate these shortcomings. For one, it is constructed as an ensemble of many Decision Trees. Each tree then uses a random sample of the training data, which is drawn with replacement, meaning that individual points can be contained more than once. In that way, slightly different artifical training sets are generated for each tree, with the overall procedure called *Bootstrap Aggregating (Bagging)*. In addition, at each split in the Decision Tree, only a random subset of the features is considered. Both of these techniques help to decorrelate the individual Decision Trees, by introducing randomness in the model, thus reducing its overall variance while retaining the low bias. The final predictions are then obtained by averaging over the results obtained from each tree:

$$\hat{f}_{\text{RF}}^B(x) = \frac{1}{B} \sum_{b=1}^{B} T(x; \Theta_b), \qquad (2.60)$$

where Θ_b denotes the nth decision tree. These modifications allow RF to perform generally well on a wide variety of regression tasks[149].

2.3 The chemistry of ceria

In this section, I shall briefly introduce the material that the chemical systems discussed in this work are based on. Cerium oxide, CeO_2, crystallizes in a fluorite structure with the space group $Fm\overline{3}m$, in which the cerium (oxygen) ions occupy the regular (interstitial) sites of a face-centered cubic (FCC) lattice, with an experimental lattice parameter of 5.41 Å[150]. In this structure, the cerium centers adapt an oxidation state (OS) of 4+ at an electron configuration of $[Xe]4f^0$, meaning a complete depletion of the 4f orbitals. While the other stable, more reduced cerium oxide polymorph, Ce_2O_3, is well-known and studied, it will not be treated in this work, and will therefore not be discussed further. Astonishingly, despite being classified as a rare-earth metal, there is actually more cerium (66.5 ppm) in earth's crust than copper (60.0 ppm)[151], making it the most abundant of all lanthanides. Thus, ceria is a relatively common and cheap material, showing a long history of industrial use. Its main applications are the treatment of gaseous emissions, in particular as part of the three-way catalyst (TWC), the oxidative treatment of liquid waste, as well as in solid oxide fuel cells[152–155]. In recent years, it has attracted further attention for a variety of additional chemical transformation, among others, the water-gas shift (WGS) reaction[22,156,157], halogen production via oxidation of hydrohalogenes in the Deacon process[158], and hydrogenation reactions, where it facilitates the activation of hydrogen as key step[159].

Chapter 2. Theory

The catalytic versatility of ceria can be traced back to its rich chemistry, showing both, acid-base and redox-activity, facile oxygen transport, easy oxygen vacancy formation, and a large oxygen-storage capacity (OSC)[159]. In particular the latter properties make ceria an exceptional support material in oxidation reactions, as it can provide reactive oxygen directly from the lattice, rather than requiring prior dissociation of gas-phase O_2, which, instead heals the resulting vacancies. This reaction sequence is known as the Mars-van Krevelen (MvK) mechanism and is frequently proposed in ceria-assisted chemical transformations[160], for instance in CO oxidation to CO_2. As the expulsion of neutral oxygen leaves behind excess electrons in the material, their facile stabilization is crucial for the feasibility of this process.

In ceria, such excess electrons can be readily accommodated due to the easy interconversion of the Ce^{4+}/Ce^{3+} redox couple and the formation of small polarons in the material[68,161–163]. A polaron is a quasi-particle composed of an excess charge carrier (i.e. an electron or an electron hole) and the accompanying lattice distortions, as presented in Fig. 2.7 a. The distortions arise due to attractive/repulsive interaction of the localized charge with the surrounding ions, forming a self-generated potential well that traps the charge. Thus, an electron polaron leads to an additional occupied electronic state in the band gap, below the Fermi level, as opposed to the delocalization in the conduction band, typical for metals (see Fig. 2.7 b). The lattice distortions around the localized charge can be considered virtual phonons (that is, lattice vibrations) which follow the charge carrier through the material. Similarly, the propagation of lattice vibrations through a crystal can drive the movement of the localized charge. Though, in the absence of sufficiently strong lattice vibrations (i.e. the polaron hopping barrier for ceria is approximately $0.4\,eV$[164]), its localized nature gives rise to a local polaron structure — which will be one of the main concerns of this work.

Naturally, oxygen expulsion (and all other observed catalytic activity for that matter) must occur at the surface of the material, thus influencing reactivity[165]. The commonly exposed low-index surfaces of ceria are (111), (110), and (100), with computed surface (vacancy formation) energies of $0.70\,J\,m^{-2}$ ($1.68\,eV$), $1.06\,J\,m^{-2}$ ($1.17\,eV$), and $1.46\,J\,m^{-2}$ ($1.57\,eV$)[159,166]. On the respective facets, the cerium (oxygen) atoms are seven (three), six (two), and six (two) fold coordinated. All have been observed experimentally and nanocrystals exposing each surface can be achieved by specific, targeted synthesis protocols (see Fig. 2.8)[159]. While (111) as the most stable surface is the majority facet exposed on commercially available ceria powder, it is the least reactive. On the other hand, $CeO_2(100)$ is especially intriguing due to its polar nature after bulk cleavage, which leads to significant oxygen expulsion, making the resulting surface very dynamic[67].

UNIVERSITAT ROVIRA I VIRGILI
CERIA-BASED SINGLE-ATOM CATALYSTS: FROM SIMPLIFIED MODELS TOWARDS REAL-WORLD COMPLEXITY
Julian Geiger

2.3. The chemistry of ceria
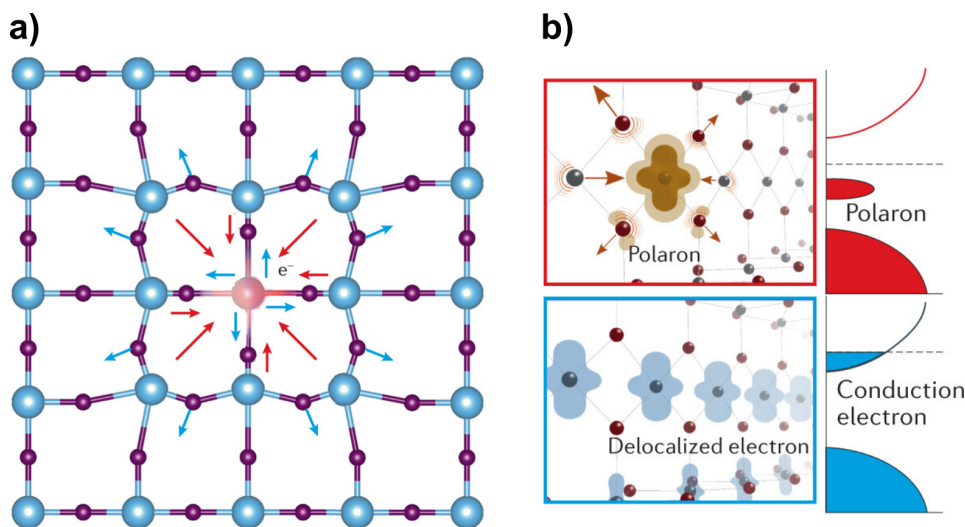
Figure 2.7: Geometric and electronic effect of small polarons. a) Lattice distortions leading to charge self-trapping. b) Formation of a localized electronic state above the valence band, below the Fermi energy, as opposed to a delocalized electron in the conduction band, as would be observed for metals, for instance. Figure adapted from Ref. [163].

In addition to the extended low-index surfaces, nanostructuring can give rise to local specific facets[67], the most prominent of which is a (100)-like motif present at (111) step edges and the corners of octahedral nanoparticles[66]. It provides a square-planar anchoring site involving four oxygen atoms, particularly favorable for stabilizing certain isolated metal atoms[167].

It was indeed this structural motif which enabled the synthesis of the first ceria-based single-atom catalysts (SACs) in 2016 by Dvořák and coworkers, and Jones and coworkers, who achieved this feat via the methods of atom trapping and surface step decoration, respectively[40,41]. Since then, lots of work on the topic of ceria-based single-atom catalysts has been carried out, and stable systems of the other group 10 metals[42], gold[44], copper[45], rhodium[46] and manganese[47] have been prepared, with promising applications ranging from preferential oxidation (PROX) of CO[44], to NO abatement[46], and the water-gas shift (WGS) reaction. Thus, ceria has established itself as one of the most versatile, promising and widely applied support materials for the synthetic preparation of SACs. In addition, its unique chemistry is also of fundamental theoretical interest[168,169]. As mentioned above, the formation of localized polarons (e.g. from excess electrons after oxygen expulsion) gives rise to local polaron distributions. In the case of SACs, however, the presence of the isolated metal atom presents an additional

Chapter 2. Theory
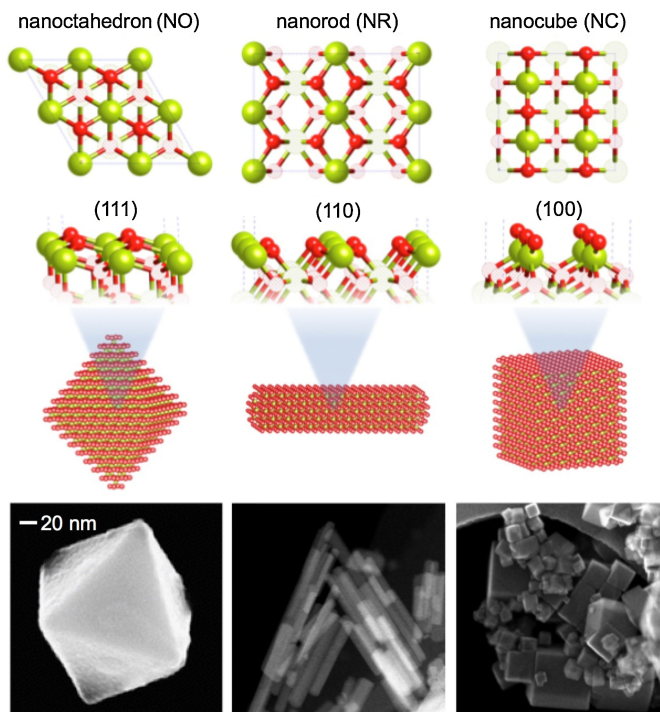
Figure 2.8: Atomic structures of low-index ceria facets and micrographs of nanocrystals with targeted surfaces. Figure taken from Ref. [159].

source of electrons that can transfer charge to the support[167,170,171]. Importantly, as was shown by Daelman and coworkers for the common Pt_1/CeO_2 system, the amount of charge-transfer is variable and dynamic, meaning that through the interaction with the support, the metal atom can adapt various oxidation states[68]. The origin of this effect, its implications, and generalizability present the contents of Chapter 3 and shall therefore not be further discussed here.

2.4 Computational setup

2.4.1 Structural models

All ceria structural models were derived from optimized CeO_2-bulk in the fluorite structure with the space group Fm$\bar{3}$m and a theoretical lattice parameter of 5.491 Å (experimental value: 5.41 Å)[150]. Slab models for the (111), (110), and (100), low-index surfaces were constructed as (3×3), (2×2), and (3×3) supercells, extending nine, six, and nine atomic layers along the z-direction, with the bottom three, four, and three fixed at the

UNIVERSITAT ROVIRA I VIRGILI
CERIA-BASED SINGLE-ATOM CATALYSTS: FROM SIMPLIFIED MODELS TOWARDS REAL-WORLD COMPLEXITY
Julian Geiger

2.4. Computational setup

optimized bulk positions, respectively (see Fig. 2.9). To resolve the dipole of oxygen-terminated $CeO_2(100)$ after bulk cleavage[67], I moved half of the surface oxygen atoms to the bottom of the slab in a checkerboard-like manner. For the molecular dynamics (MD) simulations of the (100)-based SAC structures with iridium, copper, cobalt and rhodium, the lateral slab extent was reduced to (2×2). At least 10 Å of vacuum were added on top of the surfaces to avoid non-physical interactions between periodic images. The oxygen plasma was modelled as isolated oxygen atoms (radicals).
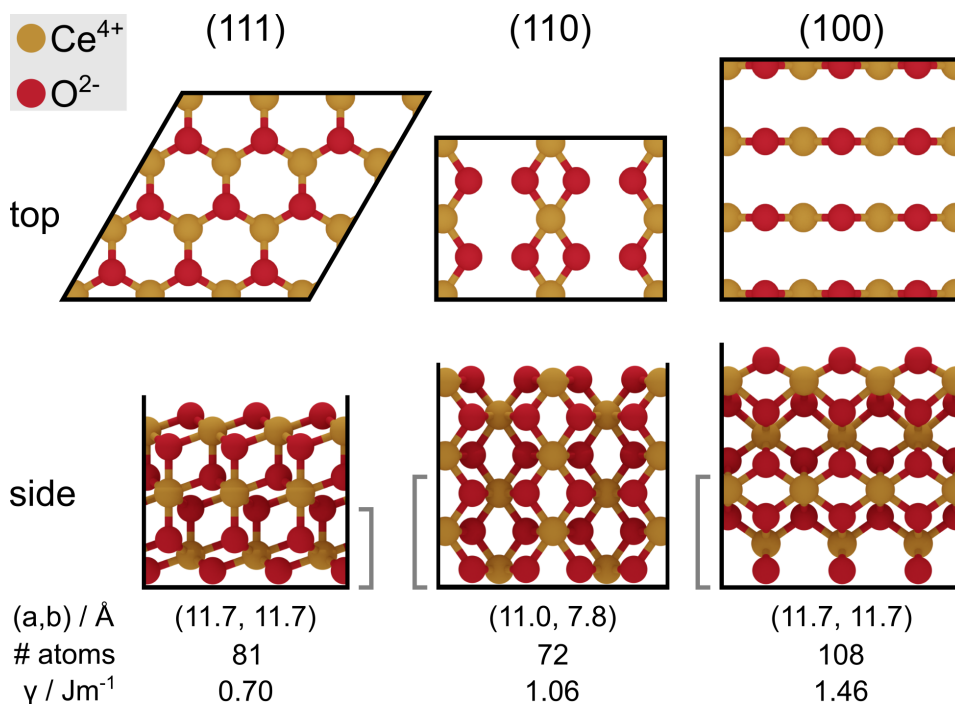
Figure 2.9: Top and side views of the structural models used for the ceria low-index surfaces. The lateral extent, a and b, of the (3×3), (2×2), and (3×3) supercells used for the (111), (110), and (100) facets, respectively, as well as the total number of atoms in the 9, 6, and 9 high atomic layer high slabs, and the pristine surface energies, γ, are indicated in the bottom row.

2.4.2 VASP settings

DFT simulations were performed with the Vienna Ab Initio Simulation Package (VASP, versions 5.4.4 and 6.3.0)[135] using the Perdew-Burke-Ernzerhof (PBE) generalized gradient (GGA) functional[116]. Core electrons were treated with the projector augmented wave (PAW) method[172,173] using PAW-PBE pseudopotentials, while valence electrons were expanded with

Chapter 2. Theory

plane waves up to a basis set cutoff of 500 eV. An effective on-site Hubbard U correction[121] of $U_{\text{eff}} = 4.5$ eV was applied on the cerium 4f manifolds, following Dudarev's formulism and previous work[68,122,174]. The electronic convergence threshold was set to 1×10^{-6} eV, and atomic positions were converged until absolute residual forces fell below 0.015 eV Å^{-1}. Spin polarization and dipole correction were applied when necessary. Bader charge analysis was carried out using the code developed by Henkelman and coworkers[175–178].

For slabs of a lateral extent of at least (3×3) unit cells, total energies were evaluated at the Gamma point (validation with a 3×3×1 k-point sampling was carried out in Ref. [166]), while for smaller models, the density of the Γ-centered grid was increased accordingly (apart from the MD simulations, where the computational cost required a Γ-point only sampling of the Brillouin zone). Formal oxidation states of metal single-atoms were assigned by counting the localized magnetic moments of reduced Ce^{3+} centers, applying a threshold of 0.8 μ_{B}[68]. The entire methodology was extensively validated in prior works[67,68,122,170].

Ceria vacancy formation energies (E_{vac}^{pris}), SAC formation energies for adsorbed (E_{ads}^{M}) and substitional (E_{sub}^{M}), as well as peroxide formation energies (E_{ads}^{O}) were calculated via:

$$E_{\text{vac}}^{\text{pris}} = E_{\text{DFT}} - E_{\text{surf}} + 0.5 \cdot E_{O_2} \tag{2.61}$$

$$E_{\text{ads}}^{M} = E_{\text{DFT}} - E_{\text{surf}} - E_{\text{M}}^{\text{bulk}} \tag{2.62}$$

$$E_{\text{sub}}^{M} = E_{\text{DFT}} - E_{\text{surf}} - E_{\text{M}}^{\text{bulk}} + E_{\text{CeO}_2}^{\text{bulk}} - E_{O_2} \tag{2.63}$$

$$E_{\text{ads}}^{O} = E_{\text{DFT}} - E_{\text{surf}} - 0.5 \cdot E_{O_2} \tag{2.64}$$

using the total DFT energy of the optimized systems (E_{DFT}) the energies of the respective pristine surfaces (E_{surf}), the energy of the metal atom in bulk (E_{M}^{bulk}–in the most stable polymorph, α-Mn in the case of manganese), the energy of a CeO_2 formula unit ($E_{CeO_2}^{bulk}$), and the energy of diatomic gas-phase oxygen (E_{O_2}). Adsorption energies of reaction intermediates were calculated using Eq. 2.62, referencing by the energy of the gas-phase molecule, accordingly.

Ab initio molecular dynamics (AIMD) simulations were conducted with the canonical NVT ensemble (constant number of particles, volume and temperature) [179]. An average temperature of 600 K was ensured using the Nosé-Hoover thermostat [180]. The 10 ps and 12 ps trajectories were sampled with time steps of one and three fs, respectively. For selected structures, I further used the HSE03–13 hybrid functional to refine the energies at the fixed PBE+U optimized geometries[181]. In view of the significantly higher computational cost of HSE03–13, the threshold for electronic convergence was lowered to 1×10^{-4} eV. Core-level binding energies (CLBEs)

were evaluated following the final-state approximation[182–184]. CLBEs for the O 1s level of surface and peroxide oxygen were referenced to the signal of lattice oxygen in a ceria bulk ($2\times2\times2$), while for the Mn 3d signal a 29-atom supercell of α-Mn was used.

2.4.3 Sampling of local polaron distributions

For the sampling of local polaron distributions on (100)-based SACs, I applied a two-step optimization procedure. In the initial geometery optimization, the Ce^{3+} pseudopotentials (PPs) available in VASP, were used for cerium centers at the proposed polaron localizations. Due to this, the final structures contain the geometric distortions that would be caused by small polarons at the proposed positions. Then, in the second step, the standard PPs were used, and the structures fully relaxed. Irrespective if the initial polaron distribution was retained, the final structures were then included in the primary dataset. An alternative approach for initially enforcing a desired polaron distribution is given by occupation matrix control[185], however, due to its availability and simplicity, we chose the PP-approach. After the second optimization, polarons are identified via their magnetic moment, as outlined above.

As will be shown in Chapter 3, for $CeO_2(100)$-based SACs of the group 9–11 transition metals (TMs), as well as structures with a defective support, up to four polarons were obtained. Nonetheless, I deemed the exhaustive sampling of up to two polarons sufficient, due to the combinatorial growth of the number of possible distributions, and as it is not crucial to obtain every individual state within the ensemble for the intended purposes. It further occurred frequently that alternative polaron distributions than the initially proposed were obtained. Thus, sampling exhaustively by also including, in principle, symmetry-equivalent structures provides the highest chance of finding all distributions for a given number of polarons. And while the combinatorial explosion could be counteracted by the use of specialized algorithms (rather than a in-house Python script) which account for symmetry-equivalence, like the structure enumeration module of the `icet` library[186], or the `disorder` algorithm[187,188], the symmetry of CeO_2-based structures is quickly lowered upon restructuring of the coordination sphere and/or vacancy introduction. Thus, to summarize important considerations from the applied methodology:

1. There is no guarantee that a proposed Ce^{3+} distribution is retained during the structural optimization. If convergence to a different distribution is reached, the result is still considered as valid.

2. In cases where the same Ce^{3+} distribution is obtained from different

Chapter 2.   Theory

initial structures, I selected the lowest-energy result.

3. If the optimization led to the transfer of more than two electrons to the ceria surface, the resulting structures were also included in the dataset.

4. Cases where electrons localized in the subsurface layer were discarded.

As such, the approach presents a reasonable compromise between completeness of the structural sampling and computational feasibility.

2.4.4   Statistical techniques

For the statistical tasks, I made heavy use of the `scikit-learn` (`sklearn`) Python library[189]. All the data follows FAIR principles (findable, accessible, interoperable, and reusable)[190], with data and code accessible on Git-Lab[191] and raw simulation data uploaded to ioChem-BD[192]. Predictive ML models were evaluated using K-fold cross-validation (KFCV) with a 5-fold data split, as well as leave-one-group-out cross-validation (LOGOCV). Data centering and standardization were applied when necessary. To simplify and streamline the evaluation of different `sklearn` predictors, using different data partitioning schemes, feature sets, target variables, as well as visualization, feature selection, etc., I wrote the publicly available `sklwrap` Python library[193]. Reported error measures (R2, RMSE, MAE) were evaluated on the testing data, and are averaged over the different train-test splits, with standard deviations indicated. For the Bayesian Machine scientist (BMS)[148], the number of steps was limited to 10,000, of which the first 1000 were discarded. The maximum depth was set to 100 iterations per step. At each step, the following BMS outputs were examined: (i) the current function and its complexity, (ii) the Bayesian Information Criterion (BIC), (iii) the sum of squared errors (SSE), and (iv) the values of all the fitting constants. Functions were evaluated by mathematical analysis, focusing on accuracy and simplicity.

2.4.5   Other tools of the trade

Lastly, I also made heavy use of the atomic simulation environment (`ase`)[194] and `pymatgen` Python libraries[195], both of which implement classes to work with (peridodic) atomistic structures. Data handling and manipulation was achieved with `pandas`[196], while plots were created with the Python Plotly library[197], and structural renders with the Blender 3D modelling software[198]. I further made use of the "automated interactive infrastructure and database for computational science" (AiiDA) for driving the VASP simulations. AiiDA enables the construction of automated workflows, has a strong focus

on provenance and reproducibility, and implements efficient data storage via a PostgreSQL database[199–201]. In addition, all raw simulation data was uploaded to the ioChem-BD online repository[192].

Chapter 2. Theory

Chapter 3

Oxidation state dynamics of ceria-based SACs

In the world of the very small, where particle and wave aspects of reality are equally significant, things do not behave in any way that we can understand from our experience of the everyday world . . . all pictures are false, and there is no physical analogy we can make to understand what goes on inside atoms. Atoms behave like atoms, nothing else.

John Gribbin

3.1 Charge-transfer at the Pt/CeO$_2$ interface

As the typical system used in the three-way catalyst (TWC) of car exhaust converters, Pt/CeO$_2$ records a long history of commercial use. Here, the ceria support acts as an oxygen buffer, with lattice oxygen being consumed (replenished) under oxygen-lean (rich) reaction conditions[202,203]. In addition, it was shown that the formation and consumption of oxygen vacancies is directly coupled to the presence of reduced Ce^{3+} centers, (small polarons)[162], which matched CO conversion rates stoichiometrically[204]. These are formed when lattice oxygen is consumed during CO oxidation, and the remaining excess electrons are accepted by the reducible ceria support.

However, oxygen vacancies do not present the only possible origin of reduced Ce^{3+} centers in the ceria support. Alternately, they can be formed by electron transfer from an adsorbed metal particle. The effect was first noted by Bruix et. al through an unexpected 20-fold increase in the rate of the water-gas shift (WGS) reaction by Pt/CeO$_2$[39]. Campbell coined the

69

Chapter 3. Oxidation state dynamics of ceria-based SACs

term Electronic Metal-Support Interaction (EMSI) for the effect, reminiscent to the well-known Strong Metal-Support Interaction (SMSI)[37]. The amount of charge-transfer (CT) was quantified by Lykhach and co-workers, who showed that 17% surface reduction presents the maximum for the (111) surface[64]. Similarly, Pt-NPs composed of around 50 atoms lead to the highest relative amount of CT of ≈1 electron per 10 Pt atoms. Interestingly, the study found that for very small particles, CT was suppressed. The authors attributed this observation to the fact that nucleation of metal particles likely occurs at surface vacancy sites, where the underlying partially reduced facet has a lower tendency of accepting electrons from the metal particle.

In the same year, however, the first two ceria-supported Pt-SACs were reported, which painted a rather different picture. These systems were synthesized by the groups of Jones and Dvořák via atom trapping and surface step decoration, respectively[40,41]. Again, surface defects were identified as the likely sites for the stabilization of platinum. However, rather than nucleation of metal particles at oxygen vacancies, the authors observed stabilization of isolated atoms on steps between (111) facets. Since then, experimental data, such as XPS measurements, as well as computational studies have shown that SA-Pt assumes a metal oxidation state (mOS) of 2+[66,205], much higher than the CT limit observed for NPs by Lykhach and coworkers.

3.1.1 Local polaron structure and OS dynamics

The origin of the charged state of SA-Pt lies in the spontaneous charge-transfer (CT) upon metal deposition, oxidizing the platinum atom while reducing the ceria support. Daelman and coworkers could show that the effect is possible due to the band alignment between the empty Ce 4f states of the ceria surface and the filled states of the single metal atom[68]. In contrast to a metal substrate in which electron density would be distributed throughout the material, the excess electrons reduce Ce^{4+} centers, forming small, localized polarons. Due to their localized nature, geometrically distinct geometric polaron distributions emerge in the ceria support, and lead to closely spaced energy states. I will henceforth refer to such a set of states, composed of the ground state, and low-lying excited states corresponding to the different CT locations, for a SAC at a given mOS as an electronic ensemble.

Furthermore, the number of electrons transferred from the metal atom to the ceria support might vary, depending on the coordination environment (*vide infra*). Fig. 3.1 shows the electronic ensembles for SA-Pt, stabilized on the $CeO_2(100)$ facet, denoted Pt-2O due to the two-fold oxygen coordination. This coordination pattern allows for the presence of Pt^0, Pt^{1+},

and Pt^{2+}, which span a total range of adsorption energies of $\approx 0.5\,eV$. The electronic ensembles for different mOS are significantly overlapping, and, interestingly, Pt^{1+} presents the ground state, slightly below Pt^{2+} and Pt^0, the least stable species.
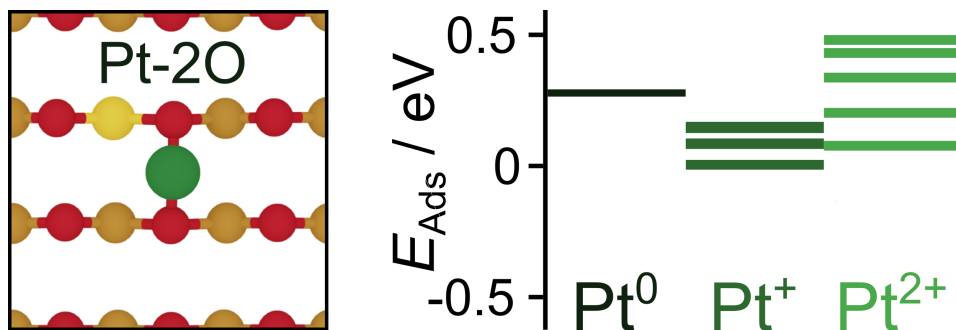
Figure 3.1: Global minimum structure and adsorption energies for distinct states of the Pt-2O SAC.

At elevated temperatures, polaron hopping events start occuring within ceria and cause structural transformations within the electronic ensembles[206]. In addition, given small enough energy differences between states with different mOS, CT between the Pt atom and the support becomes possible and the mOS takes on a dynamic character[68]. Fig. 3.2 shows the evolution of the Pt-2O SAC, during a $600\,K$ *ab initio* molecular dynamics (AIMD) trajectory in the (3×3) supercell. The metal resides mainly in the 1+ and 2+ oxidation states, with approximately equal overall lifetimes of $5.7\,ps$ and $6.2\,ps$ (or 48% and 52%), respectively. Only one short-lived ($\approx$ $100\,fs$) Pt^0 species is observed. These results are in line with the relative stabilities and distributions of states obtained from the static DFT simulations compiled in Fig. 3.1. Notably, small polarons are exclusively located at the nearest neighbor (NN) positions to the Pt atom, with no farther or subsurface (SS) states observed. In the case of Pt^{2+}, the two Ce^{3+} centers are located diagonally to each other around the Pt atom. In total, approximately 48 polaron hopping events and 40 mOS changes occur during the $12\,ps$ trajectory.

Chapter 3. Oxidation state dynamics of ceria-based SACs
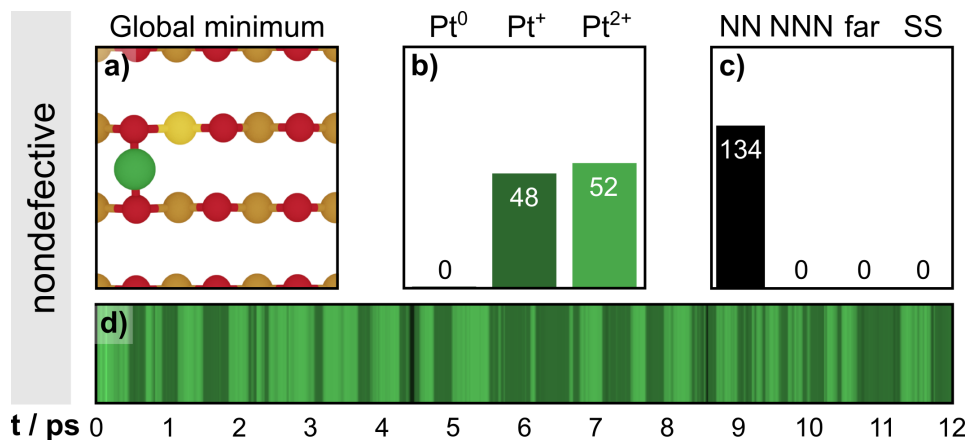
Figure 3.2: Dynamic mOS behavior of the $Pt_1/CeO_2(100)$ SAC.

3.1.2 Influence of surface reduction

As outlined in the previous sections, upon single-metal adsorption, the ceria support can be reduced by accepting electrons via CT. However, on experimental samples, some degree of surface reduction is usually already present prior to metal deposition[207,208]. Thus, I next investigated how the presence of a vacancy and the resulting polarons would influence the electronic ensembles and mOS dynamics. For the pristine (100)-2O and reconstructed (100)-4O facets prior to metal deposition, the defective structures, representative polaron distributions, and energy distributions are shown in Fig. 3.3. In the latter case, the vacancy was placed in the bottom Ce-O-Ce row to decouple the effect of the reconstruction from the effect of surface reduction. On both surfaces, the ensembles span almost 1 eV in energy. Due to symmetry-breaking, a higher total number of states is available for the reconstructed (100)-4O structure. Overall, individual energies are determined by the interplay of a few geometric factors, namely (i) the degree to which the lattice can adjust for the more spacious polarons (ii) the repulsion between them, and, lastly, (iii) the accommodation of oxygen distortions toward the newly formed empty site. These effects rationalize the global minimum structure for the (100)-2O surface, in which both reduced Ce^{3+} centers are at a nearest neighbor (NN) to the surface vacancy.

The effect of surface reduction on the behavior of the Pt-2O catalyst is shown in Fig. 3.4. The two additional polarons and symmetry breaking cause a significant increase in the number of distinct, accessible states, as seen in panel **b**. Additionally, the ratio of Pt^{2+} to Pt^+ changes in favor of the latter, as the surface it is less prone to accept electrons from the metal center[64]. Accordingly, Pt^+ becomes the majority species during the
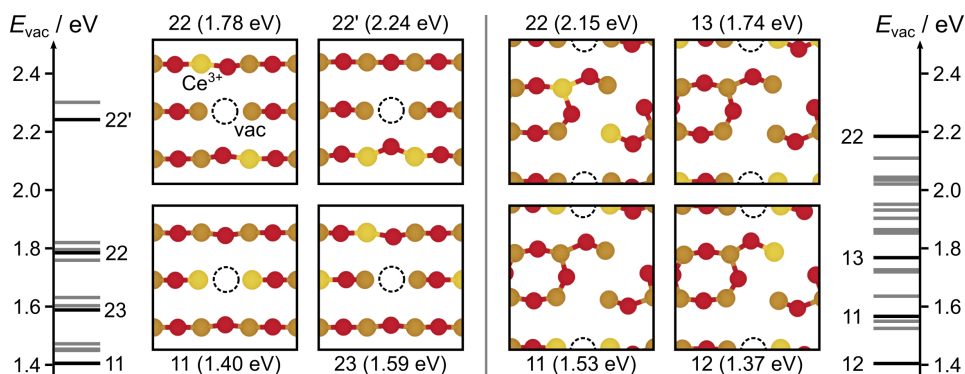
Figure 3.3: Ensemble of vacancy formation energies for various surface polaron distributions on pristine CeO$_2$(100)-2O and CeO$_2$(100)-4O, obtained at a 3×3×1 k-point sampling. Individual distributions are denoted by the set of indices (n,m), where 1, 2, and 3 correspond to nearest neighbor (NN), next-nearest neighbor (NNN), and further positions. Individual states within the energy distributions are shown in grey, and in black for the presented structures.

AIMD trajectory (panel **d**), making up 86% of the SAC lifetime, while Pt^{2+} is only present for a total of 13%, or 10.2 ps and 1.6 ps, respectively. Furthermore, despite an increased number of around 54 polaron hopping events, mOS changes of SA-Pt occur less frequently ($\approx$ 19 times) than for the nondefective support (48 and 40 on the nondefective CeO$_2$(100)-2O support, respectively). Thus, by controlling the degree of surface reduction, unusual metal charge states, such as Pt$^+$, can be stabilized.

Chapter 3. Oxidation state dynamics of ceria-based SACs
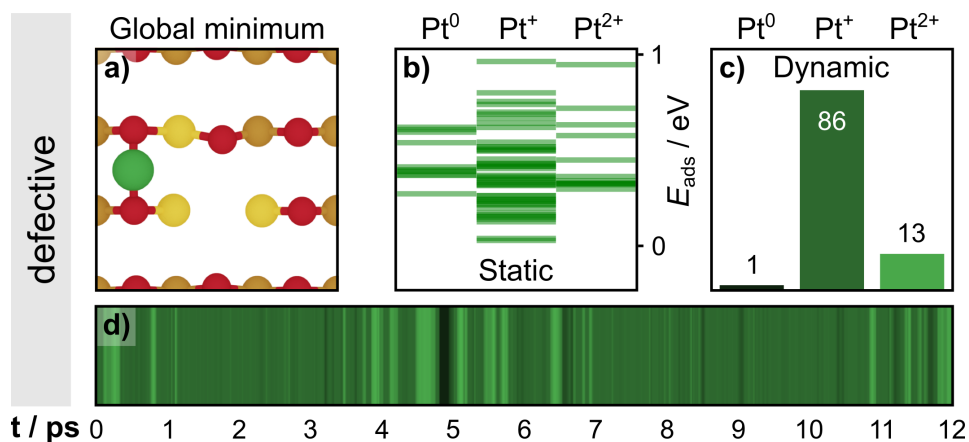
Figure 3.4: Alterations to the global minimum (a), electronic ensembles (b), and mOS dynamics (c & d) to the Pt-2O SAC caused by the introduction of a vacancy.

3.2 OS dynamics across the periodic table

Since the works of Jones and Dvořák[40,41], Pt_1/CeO_2 remains the most extensively studied ceria-based SAC[20,209]. However, ceria-based catalysts of the other group 10 TMs[42,210–212], as well as gold[213,214], copper[215], and rhodium[216] have also been synthesized, and the library of known SACs grows further when other (reducible) oxide supports, such as FeOx and TiO_2 are taken into account[20,53]. Thus, the question arises whether the emergence of electronic ensembles and mOS dynamics is possible due to a particular electronic alignment between SA-Pt and ceria, or if the facile formation of small polarons in the support allows for the same dynamic interaction with other isolated metal atoms.

3.2.1 Stabilizing isolated metal atoms on ceria

To answer this question, I extended the database of SA species to the full set of group 9–11 TMs, namely cobalt, rhodium, iridium, nickel, palladium, platinum, copper, silver, and gold, as well as the common low-index facets of ceria, (111), (110), and (100). Overall, possible adsorption sites are on-top, bridge, and three-fold hollow. The former two are accessible on all facets, either involving cerium/oxygen, or a mix of both, while the latter motif is only accessible on the (111) facet. In addition, metal atoms can be stabilized within ceria/oxygen vacancies, thus taking substitutional positions[213], and even a dynamic formation mechanism has been proposed[55]. The actual adsorption site depends on the type of the metal, the preparation of the

UNIVERSITAT ROVIRA I VIRGILI
CERIA-BASED SINGLE-ATOM CATALYSTS: FROM SIMPLIFIED MODELS TOWARDS REAL-WORLD COMPLEXITY
Julian Geiger

3.2. OS dynamics across the periodic table

catalyst, and is often still under debate.

In the following, I will focus on the stabilization of the chosen TMs coordinated to lattice oxygen of the ceria support. An overview of the considered sites is presented in Fig. 3.5, and the obtained ground state adsorption energies (referenced to the bulk metal) are listed in Table 3.1. Here, I found that only the coordination motifs provided by (100) can stabilize isolated metal atoms, with the only exceptions being cobalt and nickel on (110), for which adsorption is slightly exothermic. Silver and gold are not stable on any of the facets due to their nobility.
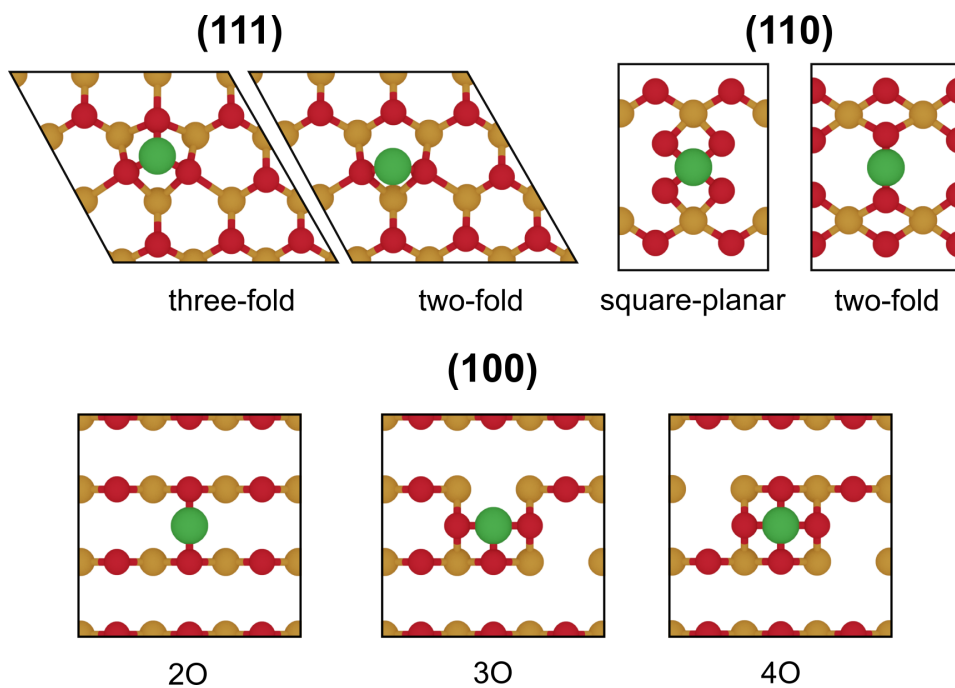
Figure 3.5: Common adsorption sites on ceria low-index facets.

The surface trends can be attributed to the oxygen atoms having a higher degree of saturation (that is, bonds to three neighboring Ce) on the (111) and (110) facets, than the (100) facet (only two bonds to neighboring Ce). On the latter facet, surface oxygen are therefore more accessible for the formation of strong bonds with adsorbed, isolated metal atoms. Additionally, the spacing between parallel Ce-O-Ce rows is smaller on the (110) facet (2.88 Å) than on (100) (3.88 Å). Thus, the lower degree of coordinative saturation, as well as its more open nature, make the (100) facet the most suitable for stabilizing single metal atoms. Recall, however, that the (100) surface acts as a surrogate model for (111) step edges and local facets of nanostructured ceria, while ceria cubes exposing (100) at a macroscopic

Chapter 3.   Oxidation state dynamics of ceria-based SACs

scale are generally not suited to stabilize SA metals[41]. This is likely due to the higher degree of surface reduction present on nanostructures that expose mainly (100)[217,218], such that no electrons can be transferred from the metal, which therefore remains in its metallic state, prone to agglomeration.

Table 3.1: DFT (PBE+U) adsorption energies (all values in units of eV) for the considered group 9–11 transition metals on the common low-index surfaces of ceria, obtained via $E_{Ads} = E_{total} - E_{surface} - E_{bulk\ metal}$. Metal adsorption energies are always referenced against the corresponding pristine surface (in the case of (100), unreconstructed (100)-2O) and the bulk metal. The oxidation state of the adsorbed single metal atom is indicated in brackets. For the three coordination environments provided by the (100) surface, an extensive sampling procedure of local polaron distributions has been performed and the ground state energies and mOS are tabulated here.

M	(111)	(110)	(100)-2O	(100)-3O	(100)-4O
Co	1.15 (2+)	−0.01 (3+)	−0.76 (2+)	−1.01 (3+)	−1.25 (3+)
Rh	2.73 (1+)	0.70 (2+)	0.51 (2+)	0.63 (3+)	−0.15 (3+)
Ir	3.03 (2+)	1.12 (2+)	0.48 (2+)	0.70 (3+)	−0.17 (4+)
Ni	1.24 (2+)	−0.13 (2+)	−0.74 (2+)	−0.50 (2+)	−1.03 (2+)
Pd	1.93 (0)	1.35 (0)	0.16 (1+)	0.73 (1+)	−0.43 (2+)
Pt	2.79 (0)	0.33 (2+)	0.03 (1+)	0.54 (2+)	−0.34 (2+)
Cu	0.91 (1+)	0.29 (1+)	−0.78 (1+)	−0.39 (1+)	−0.29 (2+)
Ag	1.03 (1+)	0.99 (1+)	−0.12 (1+)	0.31 (1+)	0.55 (1+)
Au	1.96 (1+)	0.59 (1+)	−0.28 (1+)	0.17 (1+)	0.51 (3+)

3.2.2   Ubiquity of OS dynamics

Motivated by the intriguing results for platinum outlined above, I further explored the electronic ensembles for the full set of group 9–11 TMs on the three coordination environments provided by the $CeO_2(100)$ facet up to a mOS of 2+. The resulting database consists of 701 symmetry-inequivalent structures, which were obtained from 1242 initial distributions via a two-step optimization procedure (further details are outlined in Sec. 2.4.3). The results are presented in Fig. 3.6.

Each metal presents at least one state in one of the three considered coordination environments where adsorption is exothermic w.r.t. to the bulk metal. As we traverse the rows of the periodic table downwards, overall stability tends to decrease. This can be attributed to the greater spatial

UNIVERSITAT ROVIRA I VIRGILI
CERIA-BASED SINGLE-ATOM CATALYSTS: FROM SIMPLIFIED MODELS TOWARDS REAL-WORLD COMPLEXITY
Julian Geiger

3.2. OS dynamics across the periodic table

requirement of the metal atoms confined within the small surface pockets. For the group 9 and 10 metals, 4O coordination presents the ground state, 2O an intermediate, and 3O the least stable state. On the other hand, for the more noble group 11 metals, stability generally decreases with coordination number. Overall, as metal valency increases, so does the propensity towards higher oxidation states. The group 9 metals show the largest mOS variability throughout the set, ranging from 0 (+1) to +4 for rhodium and iridium (cobalt). Interestingly, the mOS variability of Ir collapses in the 4O coordination, similar to the group 10 metals, which are only observed in a mOS of 2+. Lastly, the 1+/3+ redox couple for gold, known from coordination chemistry, is well reproduced in the Au-4O system.
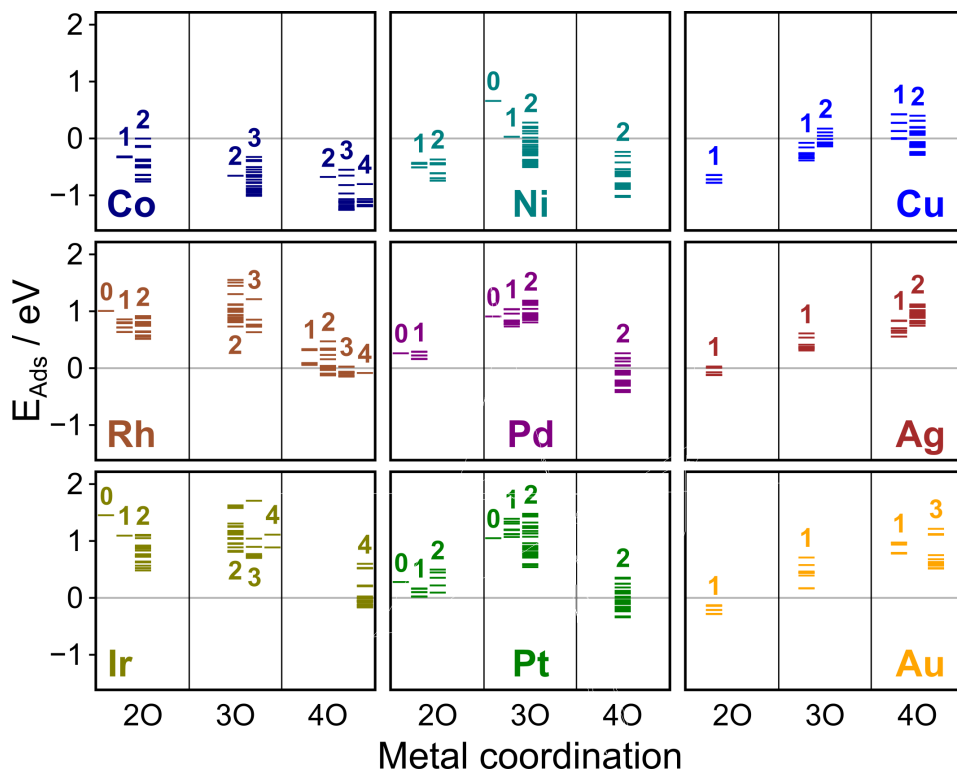
Figure 3.6: Adsorption energies of the electronic ensembles of $CeO_2(100)$-based group 9–11 TM SACs. Each TM is represented by one panel. The 2O, 3O, and 4O coordination environments are shown in Fig. 3.5. mOS values are annotated above/below the respective energy distributions.

Based on these results, we then selected the group 9 metals, cobalt, rhodium, and iridium, as well as copper as the most stable group 11 representative, in 4O coordination to investigate their dynamic behavior at

Chapter 3. Oxidation state dynamics of ceria-based SACs

elevated temperatures (600 K) with AIMD. The results are presented in
Fig. 3.7. It should be noted here that in order to make the simulations com-
putationally feasible, the supercell size was decreased from (3×3) to (2×2).
In addition, mOS deviations persisting for up to 10 fs (10 time steps at an
MD sampling rate of 1 fs) are considered to be short artifacts, rather than
stable, persistent species. In all cases, the majority species observed in the
dynamic simulation corresponds to the ground state of the static sampling,
Fig. 3.6.
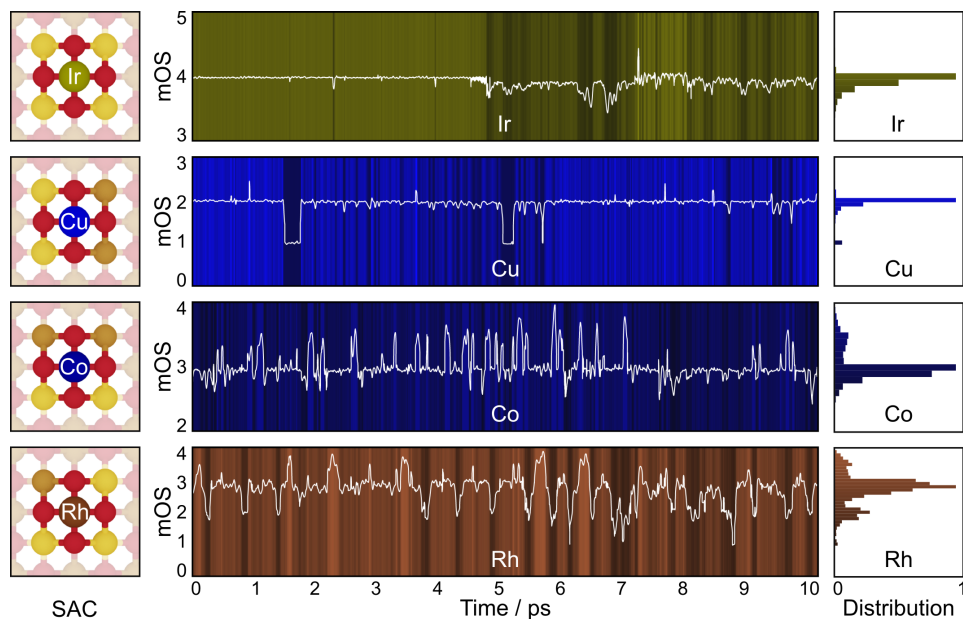
Figure 3.7: Molecular Dynamics of selected $CeO_2(100)$-4O based SACs in-
vestigated for mOS dynamics at 600 K (supercells reduced to (2×2) as com-
pared to the results presented in Fig. 3.2 and 3.4). The left panels show
surface views of the initial, unoptimized SAC structures, with ground state
Ce^{3+} distributions indicated (one subsurface polaron for Co-4O). The center
panels depict the continuous mOS progressions during the 10 ps trajecto-
ries, as indicated via the white lines and background color gradients, where
brighter (darker) color corresponds to higher (lower) mOS values. Distri-
butions of states at mOS increments of 0.1 are shown in the right panels.

As expected from the absence of any accessible states at an mOS other
than 4+, iridium remains in this state throughout the full trajectory. Inter-
estingly, this corresponds to the reduction of every surface cerium atom in
the smaller supercell. Consequently, as seen in Fig. 3.8, after around 7 ps,
two polarons get transferred to the subsurface, thus reducing the strain in
the surface layer. This state lasts for about 1 ps, and afterwards one po-

laron remains in the subsurface, while the other three remain in the topmost layer. Thus, population of the subsurface Ce^{4+} centers incurs a lower energy penalty than reduction of the iridium atom, for which only the 4+ state is accessible in the square-planar 4O coordination.

For the other two group 9 metals, rhodium and cobalt, on the other hand, a variety of oxidation states are available (see Fig. 3.6) and get populated along the trajectory (see Fig. 3.7). Overall, cobalt remains in the 3+ ground state for the majority of the simulation, however, deviations to Co^{4+} that last up to 70 fs appear frequently. This high mOS state is likely promoted by the localization of one polaron in the subsurface layer of the slab throughout the simulation. In line with the close energetic spacing of the different electronic ensembles, Fig. 3.6, the trajectory for rhodium is similarly dynamic, with Rh^{2+} and Rh^{4+} states frequently appearing. Indeed, the longest lifetime of the Rh-4O system in the 3+ ground state remains below 600 fs. Lastly, copper presents a rather stable trajectory with only two relatively long-lived (200 fs) 1+ deviations from its 2+ ground state.
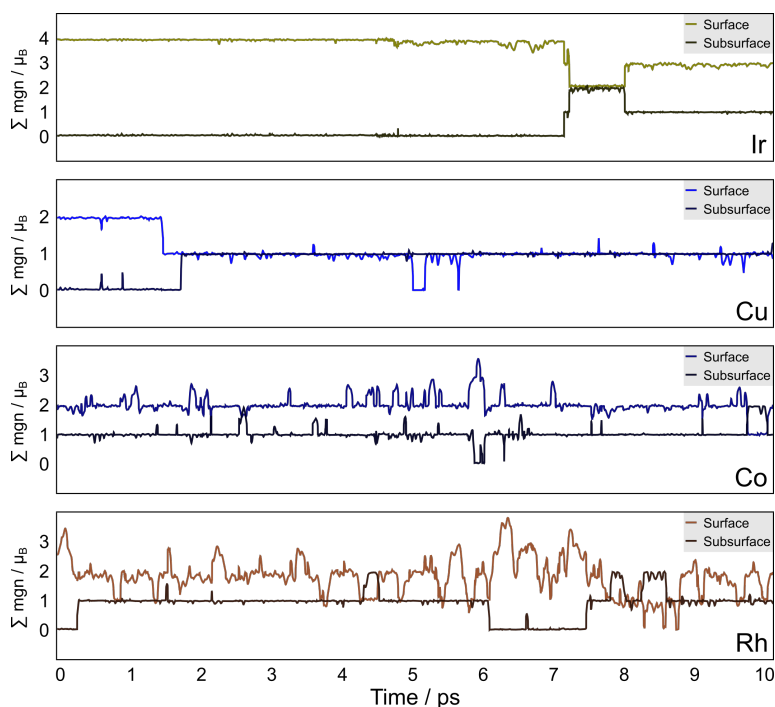
Figure 3.8: Relative magnetizations (mgn) of surface and subsurface cerium centers in units of Bohr magnetons (μ_B) during the AIMD trajectories of $CeO_2(100)$-based SACs of iridium, copper, cobalt and rhodium.

Chapter 3.   Oxidation state dynamics of ceria-based SACs

Chapter 4

Data-driven models for the M_1/CeO_2 interaction

Forget artificial intelligence — in the brave new world of big data, it's artificial idiocy we should be looking out for.

Tom Chatfield

With four parameters I can fit an elephant, and with five I can make him wiggle his trunk.

John von Neumann

In the previous chapter, I have outlined how the formation of small polarons in the ceria support leads to the emergence of electronic ensembles of SACs, and, in turn, mOS dynamics at finite temperatures. This phenomenon can be beneficial for catalysis, as it allows the metal center to adapt its electronic structure during a reaction sequence[68]. However, it also introduces an additional electronic degree of freedom that should be considered in the simulations, thus significantly increasing their complexity. Without taking local polaron structure into account, the 1242 two-step optimizations performed in Ref. [166] and analyzed in the previous chapter, would collapse to only 27 simulations (one per combination of metal and coordination). However, in that case, one has no guarantee of finding the global ground state, neither in terms of the mOS, nor the local polaron

Chapter 4. Data-driven models for the M_1/CeO_2 interaction

distribution. As such, this uncertainty now has to either be accepted, or the computational resources have to be ramped up significantly to obtain the full picture. Fortunately, machine learning (ML) promises to provide a remedy to this conundrum[219]. In the present chapter, I will thus outline how I constructed an interpretable, data-driven model to predict adsorption energies of ceria-based SACs.

4.1 Feature engineering

Often called the "gold of the 21ˢᵗ century", the first and most crucial ingredient to any machine learning endeavor is data. Thus, prior to constructing predictive models, it is worth exploring the set at hand. In total, it is composed of 701 DFT (PBE+U)-simulated adsorption energies of symmetry-inequivalent electronic states of the group 9–11 metals in three coordination environments available on local $CeO_2(100)$ facets, as presented in Fig. 3.6. Thus, it should first be noted that the data does not originate from a continuous distribution, but is rather composed of individual classes. The most important distinctions can be made for the metal species, its oxidation state, and the coordination environment, which are, however, somewhat interrelated. For one, higher coordination generally promotes higher mOS. In addition, the higher the mOS adapted by the metal, the higher the number of possible local polaron distributions, and the more data points of the respective metal are contained in the full set. Overall, the most well-represented metals are rhodium with 112 data points, followed by iridium and platinum, with 95 and 90, respectively, and gold, as the noblest metal, being the least well-represented with only 36 states. Additionally, oxygen restructuring in the different coordination motifs leads to symmetry lowering (in the order of 2O>4O>3O) and different amounts of symmetry-inequivalent local polaron distributions. Overall, the combination of both effects leads to a total of 233, 171, and 297 structures for 2O, 3O and 4O, respectively, while the most commonly assumed mOS throughout the full set 2+ with 443 data points.

Next, suitable descriptors, or commonly referred to as *features* (the terms will be used interchangeably), of the system that influence the target property must be identified, and encoded in a form that can be used in computer algorithms. For the task of adsorption energy prediction, the feature set must include relevant geometric and electronic properties that influence the relative stabilities of the final structures, accounting for local polaron distributions. Taking inspiration from literature[220–222], I compiled an extensive set of primary descriptors. A schematic overview of the final, selected features is presented in Fig. 4.2, while the full list of all initial candidates is given in Table 7.1.

4.1. Feature engineering

The first subset are atomic descriptors of the SA metals, which are directly available from literature tables[223], and are independent of the actual SAC structure. Among others, these are the atomic number, Z, electronegativity, χ, and orbital levels/radii of the isolated metal atoms, as well as thermodynamic properties of the metal-metal and metal-oxygen interactions[223], such as bond enthalpies of the metal-metal, $\Delta G^{\text{M-M}}$, and metal-oxygen bonds, $\Delta G^{\text{M-O}}$, for the diatomic species and bulk systems.

It is important to note here that for many of these physical properties, there exist multiple related numerical representations. For instance, electronegativity, defined as the tendency of an atom in a chemical compound to attract electron density, can be expressed in Pauling's, Mulliken's, or Martynov-Batsanov's scale. In such cases, I found that the inclusion of a measure of the underlying physical property in the feature set is more important than its actual numerical representation, as model parameters can adapt to different numerical input during training[4]. However, including multiple descriptors of the same physical property should be avoided, as this might introduce feature correlations that can be detrimental to model performance.

The second feature subset is composed of metal descriptors that depend on the SAC structure at hand, namely the coordination number of the metal atom, N_{O}, its oxidation state, mOS, and the cumulative ionization energy up to the adapted mOS, IP. As I have outlined in Chapter 3, the mOS increases with the coordination number and so does the cumulative ionization energy. Hence, these descriptors are somewhat correlated, however, I ensured that the numerical correlation is sufficiently weak to not pose any problem for the ML models, as evident from the correlation heatmap for the full primary feature set, Fig. 4.1.

Up to now, the features have only been concerned with the SA-metal. To account for local polaron structure, I therefore added geometric descriptors of the ceria surface to the primary feature space. In particular, I evaluated the number of surface oxygen bound to the Ce^{3+} centers (denoted ϵ), indicative of surface strain, the M–Ce^{3+} distances, and the Ce^{3+}–Ce^{3+} distances. I also investigated the influence of including descriptors based on M–O and Ce^{3+}–O bond lengths, however, these did not lead to noticeable improvements in model performance. In addition, they did not satisfy important considerations for constructing suitable features from interatomic distances that emerged during the conception of the models and will be presented in the following paragraph.

---

[4]This is different from the *descriptors* commonly used for the construction of neural network potentials (NNPs). Here, the term refers to the mathematical representation of the 3D structure of an atomic system (rather than its emergent physical properties), and presents one of the most crucial components for the success of the method[224,225].

Chapter 4.   Data-driven models for the M_1/CeO_2 interaction
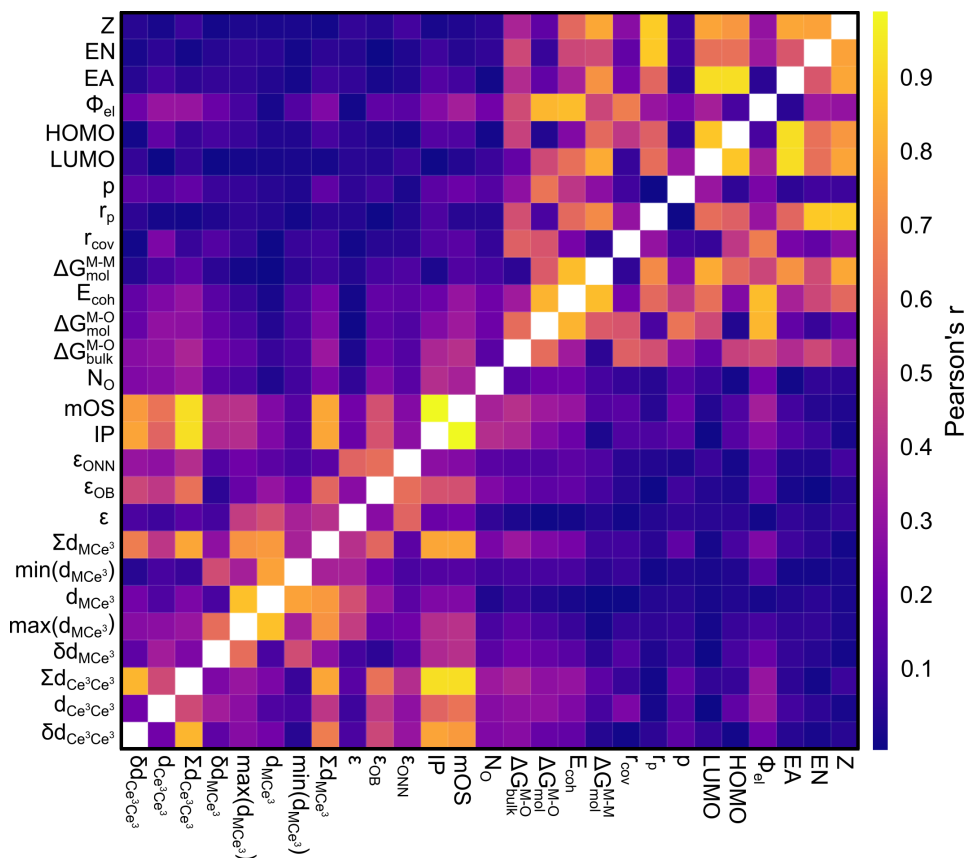
Figure 4.1: Correlation heatmap of the full primary feature space.

First, to obtain the numeric values of the selected interatomic distances, DFT-optimized structures should not be used as their evaluation would require previous expensive *ab initio* simulations, thus defeating the purpose of constructing the ML model. Instead, one can assess the positions of the localized polarons in the optimized structures, but evaluate the respective distances based on the pristine ceria slabs, prior to SA addition, thus alleviating the need for prior structural optimization of the SAC structure. Furthermore, in VASP (as well as other simulation codes) atomic coordinates are usually represented with a significant number of digits[5], posing the question to which point they still encode chemically relevant information and where numerical noise begins. I chose a threshold of 1×10^{-2} Å here.

Furthermore, rather than evaluating the absolute distances, I evaluated the relative distances in units of primitive lattice vectors of the unit cell. While this, in principle, still requires knowledge of the final polaron distri-

UNIVERSITAT ROVIRA I VIRGILI
CERIA-BASED SINGLE-ATOM CATALYSTS: FROM SIMPLIFIED MODELS TOWARDS REAL-WORLD COMPLEXITY
Julian Geiger

4.1. Feature engineering

butions (which might differ from the initially proposed one), it allows for the preparation of an artificial distribution without optimization, followed by the generation of the corresponding distance descriptors and their use as inputs in the ML models.

Additionally, as the SAC structures assume different mOS, depending on the metal identity and the coordination environment, the number of polarons in the ceria support, and, accordingly, the number of distances to be evaluated, varies throughout the data set. For instance, the number of distinct M–Ce^{3+} (Ce^{3+}–Ce^{3+}) distances varies between 0 and 4 (6). However, in order to be used in the ML models, the features must be well-defined for the entire data set and must not contain any missing values. Thus, to remove the inherent inhomogeneity within the data set I calculated statistical measures, namely, the sum, mean, minimum, maximum, and standard deviation for each group of distance features, and used those in the ML models, rather than the primitive, individual values. During that process, I defaulted missing entries (*i.e.* Ce^{3+}–Ce^{3+} distances for structures with mOS=0/1) to so-called "Not a Number" (NaN) values, which are simply ignored when calculating the statistical functions with the `numpy` Python library[226]. Lastly, since the interatomic distances account for the ionic (rather than the covalent) portion of the metal-support interaction, I used the inverse values of the distances to construct the features to better reflect the inverse dependency of the electrostatic force on distance (as given by Coulomb's law). The considerations and procedures outlined in the preceding paragraphs remain equivalent.
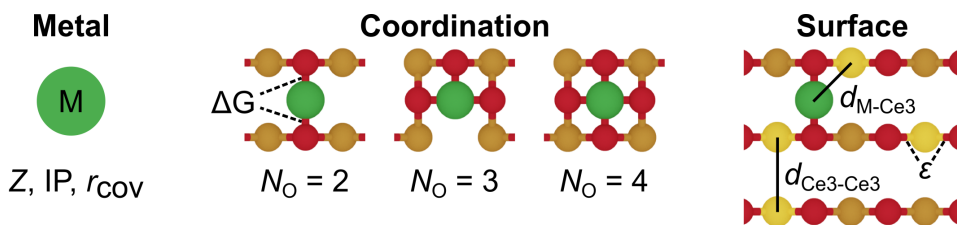
Figure 4.2: Schematic representation of primary features derived from the isolated metal, the coordination motif of the SAC structure, and the local polaron distribution in the support (the symbols are explained in the main text).

---

[5] *e.g.* 16 digits in a typical POSCAR/CONTCAR VASP structure file

Chapter 4. Data-driven models for the M_1/CeO_2 interaction

4.2 Construction of predictive models

Having constructed a suitable primary feature space that captures the dominant physical interactions at play in the SACs, I then turned my attention towards the exploration of predictive ML algorithms. Following Occam's Razor, I began with linear regression (LR) as the simplest, non-parametric regression model. The obtained results are presented in Fig. 4.3. Rather unsurprisingly, when only metal features are used and local polaron structure is not accounted for, each distinct combination of metal, mOS and coordination yields a cluster of values at the average DFT adsorption energy (panel **a** of Fig. 4.3). Adding descriptors for local polaron structure, these clusters start getting untangled, however, they are still widely spread around the ideal fit line, and the model has low predictive power. I attribute this to the linearity constraint of LR, which allows it to only poorly fit the given data.
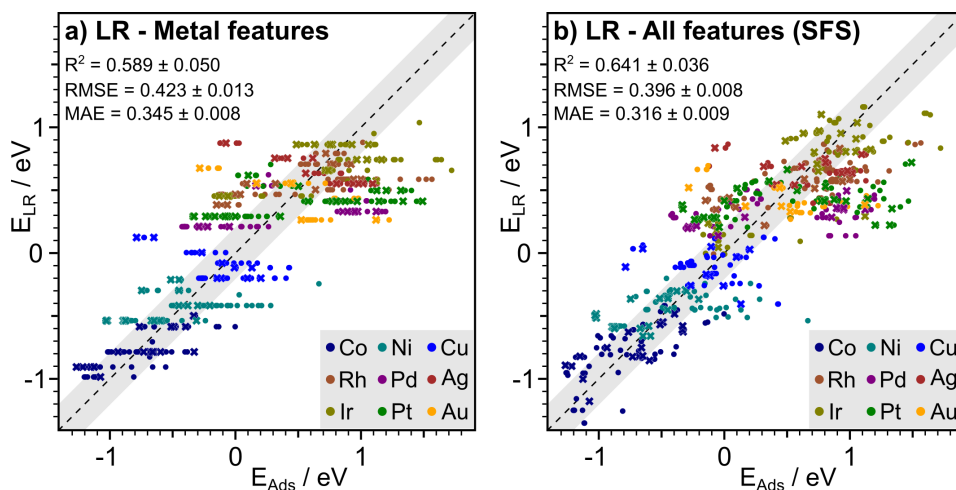
Figure 4.3: Performances of a linear regression (LR) model on the dataset of group 9–11 SACs presented in Fig. 3.6, using only metal descriptors (panel **a**), and the full set of primary features (panel **b**).

To remove this linearity constraint, I constructed a 2D feature space, obtained via mathematical combinations (products and ratios) of the primary features. As the set now contains about 871 descriptors, regularization becomes essential to avoid overfitting. Thus, I evaluated the Ridge, Lasso, and Elastic Net (EN) algorithms, which differ in the penalty functions they implement (see Sec. 2.2.1 for further details). Since EN combines both L1 and L2 regularization, whose ratio and overall strength can be tuned, it provides the highest degree of control and was therefore chosen as the

4.2.   Construction of predictive models

production algorithm for further model optimization.

Fig. 4.4 shows the influence of varying the overall degree of regularization (α), as well as the ratio of the L1 and L2 penalties (`l1_ratio`) on the predictive performance (panel **a**) and the retained number of features (panel **b**)[6]. This process of optimizing internal model parameters, aside from the actual training process, is typically referred to as hyperparameter optimization. From panel **a** of Fig. 4.4 it can be seen that the best performance, that is, the lowest root-mean-squared error (RMSE) on the testing set of about $0.15\,\text{eV}$ is achieved if the total amount of regularization, α is kept below about 0.01. Within the range of considered α values of 1×10^{-3} to 1×10^{-1}, the RMSE remains below the value for the LR model ($0.4\,\text{eV}$). Interestingly, at fixed $\alpha = 1 \times 10^{-3}$, the performance of the model stays relatively consistent across the range of considered `l1_ratio` values (0.1-0.999), ranging from 0.155 to $0.183\,\text{eV}$. However, as the `l1_ratio` increases, so does the amount of the applied L1 penalty and, consequently, the number of retained features shrinks from 181 to 48 (the origin of this behavior is explained in Sec. 2.2.1). Lastly, when α is increased beyond a value of about 0.01, model performance generally decreases, with higher `l1_ratio` leading to a faster decay.

Thus, to obtain a desired minimum performance, for example an RMSE of, say, $0.2\,\text{eV}$, a minimum number of features is required. At an α-value of 0.015 this error is achieved with an `l1_ratio` of 0.01, resulting in a model that contains 117 features, while at a higher alpha value of 0.005, the `l1_ratio` can be increased to 0.5, such that the resulting model contains only 41 features. Going forward, I chose the second option of low overall regularization and high ratio of L1 to obtain a simpler and easier interpretable model.

While the construction of a 2D feature space allows introducing nonlinearity in the EN model, predictions are still obtained via weighted linear combinations of those features, providing a rather restricted functional form. In the Random Forest (RF) model, on the other hand, no linearity constraint (see Sec. 2.2.3) is present, allowing the algorithm to fit arbitrarily complex data relations[147,149]. This allows direct use of the simpler primary feature set. Just like EN, the RF model contains various hyperparameter that should be tuned for optimal performance, most importantly, the number of trees that the ensemble is composed of, the depth to which those trees are grown, and the feature subset size that is considered at each split.

The influence of varying each hyperparameter on model performance (while keeping the others at the default values) is presented in Fig. 4.5. As

---

[6]α and `l1_ratio` and are the parameters for controlling the total amount of regularization and the ratio of the L1 to L2 penalties in the implementation of the Python library `scikit-learn`[189] which was used for all ML algorithms.

Chapter 4. *Data-driven models for the M_1/CeO_2 interaction*
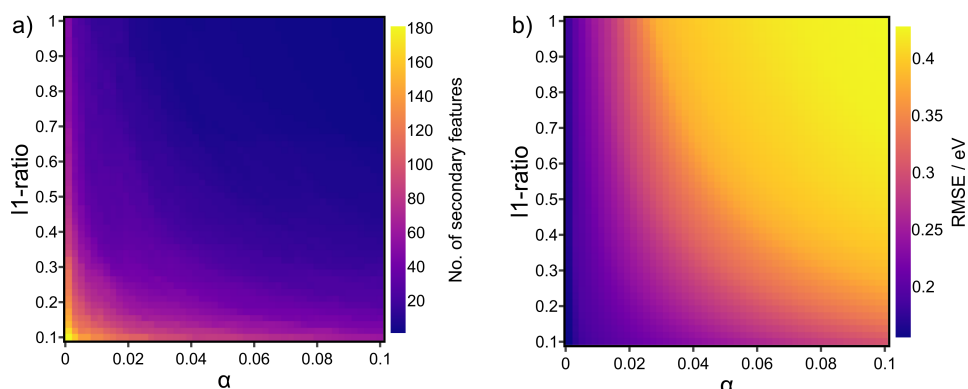
Figure 4.4: Hyperparameter tuning of Elastic Net model

the number of trees is increased, panel **a**, performance converges, at which point a further increase only adds computational overhead. I therefore set this parameter to 128, a value where convergence is reached, and which is divisible by the number of CPU cores of my workstation (8 in that case). This allows for efficient parallelization during training, as trees are grown fully independently, allowing for ideal parallelization. Next, I optimized the tree depth. If growth is unrestricted (as is the default in the `sklearn` implementation) trees are grown until the final leaves are *pure*, meaning they contain only a single training data point. For an individual decision tree, this situation would mean significant overfitting, however, the various decorrelation techniques implemented in the RF (see Sec. 2.2.3) can largely alleviate this issue. Nonetheless, I set this parameter to a value of 8, at which the testing errors are largely converged (as evident from panel **b** of Fig. 4.5) and the trees of the RF are composed of $2^8 = 256$ final leaves, each of which contains about two training data points (4/5 of the 701 total points ≈ 561). Thus, some averaging is applied when obtaining the final predictions on the testing data. Moreover, it can be seen that when the tree depth is increased further, mainly the training errors decrease, increasing the discrepancy between training and testing performance, indicative of overfitting. Lastly, as evident from panel **c**, model performance increases and eventually converges with increasing feature subset size. I set this parameter to a value of 0.5, which again helps with decorrelation, as different random feature subsets are chosen at each split.

Using the respective primary (for RF) and secondary (for EN) feature sets, and fine-tuning the algorithms as outlined above, I obtained models with predictive powers approaching DFT accuracy, as presented in Fig. 4.6. Testing RMSE (MAE) values are about 0.19 eV (0.14 eV) and 0.15 eV (0.11 eV) for the EN and RF models, respectively. In addition,

4.2. Construction of predictive models
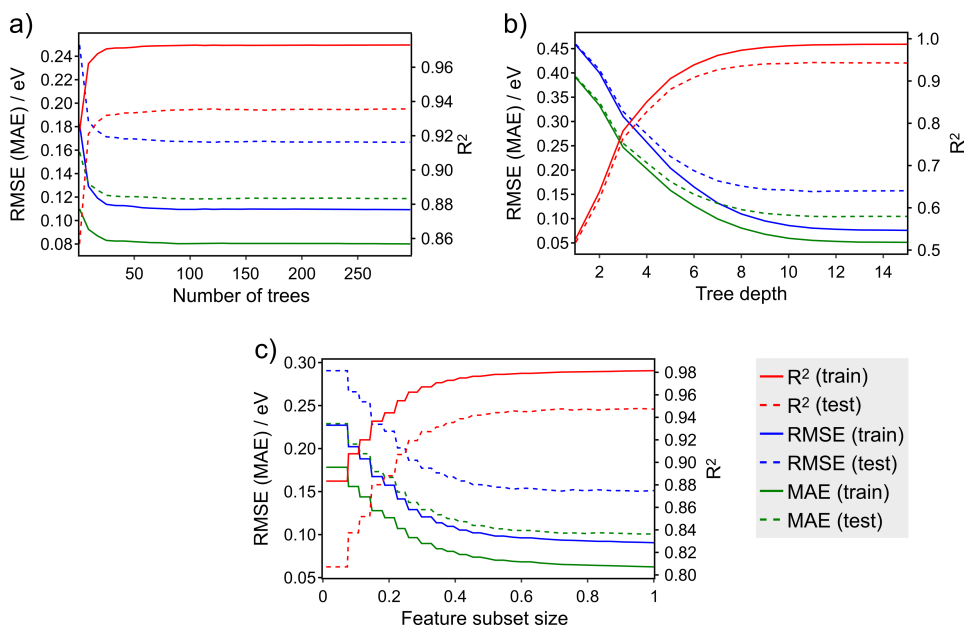
Figure 4.5: Hyperparameter optimization of the Random Forest (RF) model.

standard deviations of the predictions across the different splits of the 5-fold cross-validation procedure are in the order of $0.01\,\text{eV}$, therefore showing the high consistency of the predictions throughout the full dataset.

89

Chapter 4. Data-driven models for the M_1/CeO_2 interaction
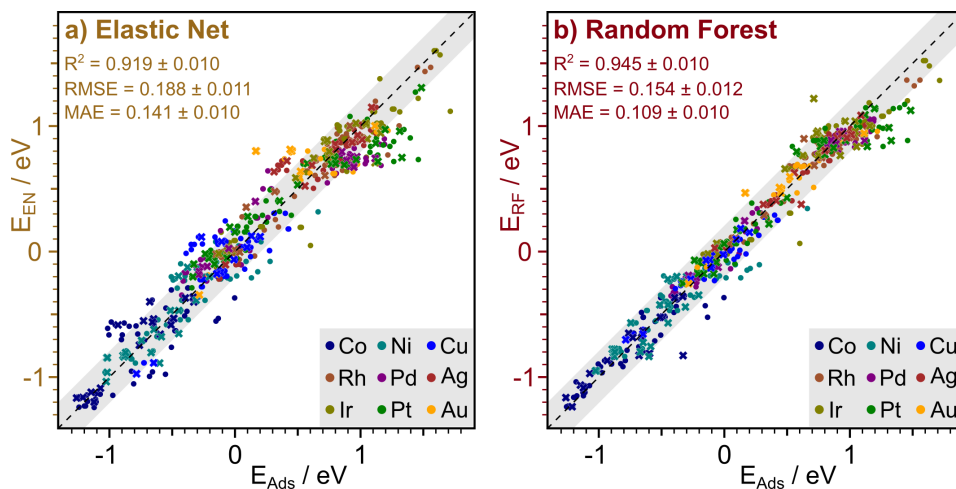
Figure 4.6: Best-performing elastic net (EN) and random forest (RF) model under 5-fold cross-validation using the full feature space.

4.3 Model evaluation

To test if the trained models could also achieve reasonable predictions on data classes entirely outside the training set, I further tested their performance via leave-one-group-out cross-validation (LOGOCV). Here, I partitioned the data based on the metal species, with the model being trained on all metals, except the initially excluded one, which is then used to evaluate the testing errors. This approach is different form KFCV, where the testing data is, in principle, also unseen, however, data points for each metal are contained in the training set according to their statistical distribution. Under LOGOCV, the RF model performed rather poorly (RMSE > 0.35 eV and MAE > 0.3 eV), which I attribute to the fact that its predictions are entirely constrained to the range of values used for training. In addition, as outlined in Sec. 4.1, the whole data set is rather inhomogeneous, therefore by excluding the subset of one metal, the RF is missing crucial data for the construction of the decision trees during training. On the other hand, the EN model generates a more continuous mapping from the input (feature) to the output (target) space and can better interpolate the missing data points during LOGOCV, leading to a better performance. As evident from Fig. 4.7, the general trends are reproduced, but predictions are notably worse than when KFCV is used. This showcases the high importance of creating balanced and representative datasets for the training of ML models. Nonetheless, each panel of Fig. 4.7, in principle, avoids performing up to ≈ 100 expensive two-step DFT simulations. It remains up to

the reader to decide if the reduction in computational effort outweighs the loss in accuracy.

Having achieved high predictive accuracy, I then turned my attention towards the task of model simplification, aiming to extract the most important features. Here, numerous approaches can be used, among others, the direct extraction of relative feature coefficients (or, in the case of RF, feature importances[7]), dimensionality reduction techniques like principal component analysis PCA, as well as *greedy* algorithms like recursive feature elimination (RFE) and sequential feature selection (SFS), with the former two being discussed in more detail in the following.

So-called *greedy* algorithms are based on the hope that making the locally optimal choice at each stage will eventually lead to the global minimum. In RFE and *backward* SFS, that means sequentially removing features from the initial set until a desired target accuracy and/or number of features is obtained. The difference between the two algorithms is that in RFE, the selection is based on an importance metric initially evaluated on the full-rank model, while in SFS, the effect of the removal of each feature is evaluated at each step of the procedure, with the feature removed that leads to the smallest decrease (or largest increase) in accuracy. Backward SFS therefore avoids possible ambiguities caused by the initial importance assignment. However, this comes at the price of a higher computational cost, as at each step of the procedure, as many models need to be trained as there are features contained in the subset. Due to the short training times of the EN and RF models of a few seconds on a desktop workstation, I chose SFS as the primary feature selection algorithm. During *backward* SFS, for both models errors initially decreased upon feature removal and stayed relatively constant until feature numbers as low as ten, indicative of a slight over-determination of the primary set.

---

[7]However, for RF, the obtained values may be unreliable, particularly in the presence of high-cardinality features. Here, the so-called *permutation importance* or usage of *out-of-bag* samples may provide better alternatives.

Chapter 4. Data-driven models for the M_1/CeO_2 interaction
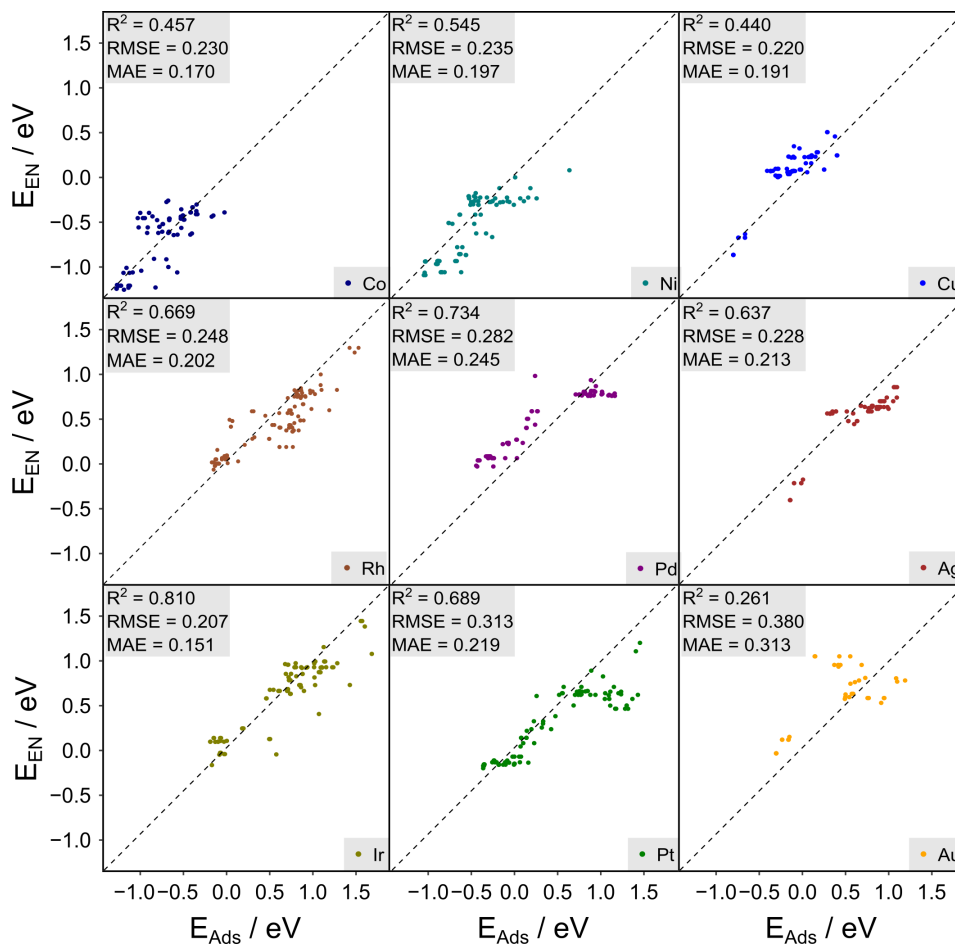
Figure 4.7: Performance of the elastic net (EN) model under leave-one-group-out cross-validation (LOGOCV). Presented performances for each metal were obtained by a model that was trained on data which fully excluded the respective metal.

This result provided a motivation for then changing the direction of the algorithm to *forward* SFS, where instead the descriptor set is built from the ground up. Thus, starting from an empty set, I added features individually, retaining the one that leads to the best performance improvement until a given threshold is met. It should be noted that neither method is exhaustive (both are *greedy*), as to obtain the globally optimal n-feature subset of a given initial size N feature pool, one would have to evaluate all $C(N,n) = \frac{N!}{(N-n)! \cdot n!}$ possible subsets for each subset size n. This presents a computationally intractable problem for the data at hand, and I remain doubtful about the magnitude of the performance increase this could actually provide.

The results of running the forward SFS for the elastic net (EN) and random forest (RF) models under the two applied data partitioning schemes (KFCV and LOGOCV), are presented in Fig. 4.8, Overall, model performances converge quickly, and reasonable results can be obtained with just a few features. It should be noted that the exact selected subset varies with model choice and CV procedure (see Table 7.2). In addition, as the EN model requires a 2D feature space to achieve reasonable performances, I fixed the cumulative ionization potential, IP, as the first primary feature, following the physical insight of the Born-Haber cycle in which it was identified as a main contributing term. The respective combined 2D feature spaces were then constructed for each added descriptor. As such, the actual number of features used in the EN model ranges from two to 92, and was obtained by generating the 2D combinations of the two to eight selected primary features (still presenting a drastic reduction from the initial 871 features in the secondary space). This also presents the origin of the missing entry for a single primary feature in the EN bar plot of Fig. 4.8.

Chapter 4. Data-driven models for the M_1/CeO_2 interaction
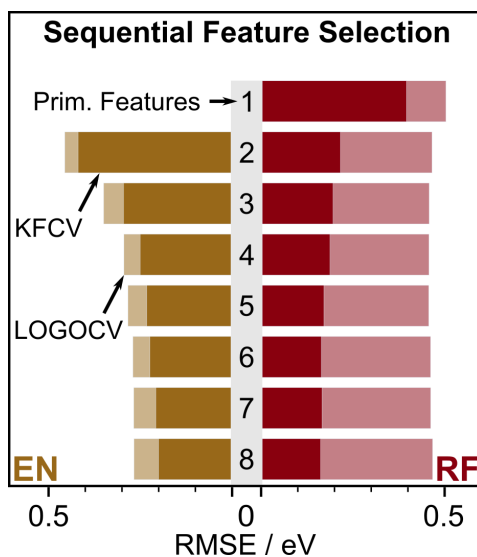
Figure 4.8: Performances (testing-RMSEs) for the elastic net (EN) and random forest (RF) models during sequential feature selection (SFS) under K-fold cross-validation (KFCV) and leave-one-group-out cross-validation (LO-GOCV) up to the inclusion of eight primary features.

4.4 From black-box to physical models

Despite the feature space simplifications presented in the previous section, deriving physical insight from the predictive models remains non-trivial. This is due to the fact that the EN still requires dozens of higher-order features to provide accurate predictions, while the many decorrelation techniques implemented in the RF obscure the decision-making process (see Subsection 2.2.3). However, as shown by SFS, as little as eight features can be sufficient to obtain accurate predictions. The small size of such a reduced feature space thus allows for the application of the BMS algorithm, a symbolic regression technique that searches closed-form equations to fit the data[148]. The prior feature space reduction is necessary due to the rapid growth of the functional search space. The method provides the advantage that the resulting equations are directly accessible for physical interpretation.

The final set of physical properties and corresponding features (schematically already shown in Fig. 4.2) chosen as input variables for the BMS algorithm are (i) the metal species, Z; (ii) the ionization potential to the adapted charge state, IP; (iii) its size, r_{cov}; (iv) the coordination environment, N_O; (v) the covalent contribution of the metal-oxygen bonds, $\Delta G_{bulk}^{\text{M-O}}$;

UNIVERSITAT ROVIRA I VIRGILI
CERIA-BASED SINGLE-ATOM CATALYSTS: FROM SIMPLIFIED MODELS TOWARDS REAL-WORLD COMPLEXITY
Julian Geiger

4.4. From black-box to physical models

(vi) surface strain and distortion, ϵ; (vii) Coulomb interactions between the metal and the support, $\min(d_{\text{M-Ce3}})$; and lastly (viii) Coulomb interactions between Ce^{3+} centers, $\text{avg}(d_{\text{Ce3-Ce3}})$. The choice for the minimum and average statistical measures for the last two descriptors is motivated by the assumption that the shortest $M-Ce^{3+}$ interaction is the most decisive, while the influence of multiple polarons is then captured by their average distance from each other.

In addition, the feature set accounts for all interactions that were previously used in a Born-Haber (BH) model to rationalize the metal-support interaction in a ceria-based Pt-SAC[68], which is schematically presented in Fig. 4.9. The main energetic contributions that were taken into account for this model were the ionization energy of the metal atom, IP, covalent interactions with the surface oxygen, E_{Cov}, surface distortion E_{Dist}, and Coulomb interactions between the metal atom and the support, as well as within the support E_{Coul}. While in the BH model, all terms were evaluated explicitly using known physical formulae, my data-driven approach uses physical descriptors, with the functional form being searched by the BMS algorithm. Its higher flexibility thus enables extension to the nine metals, three coordination environments, mOS states ranging from zero to four, and various local polaron distributions contained in the dataset. Further generalization, e.g. to other oxide supports is conceivable, given that suitable descriptors can be found.
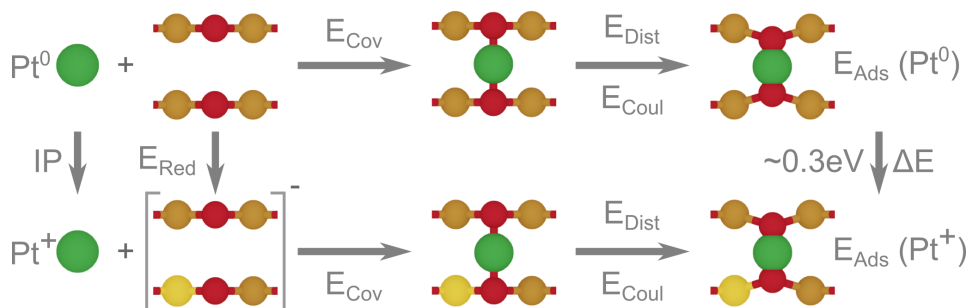
Figure 4.9: Schematic of Born-Haber model used to rationalize the small energy difference between the Pt^0 and Pt^+ states of a ceria-based Pt-SAC. Figure adapted from Ref. [68].

However, even with the reduced set of eight primary features, during initial model runs with the BMS algorithm, only metal features were retained. This can be attributed to the larger energy differences between structures with different metal atoms, than within the electronic ensembles, which only differ in their local polaron distribution. As such, due to the penalty on model complexity implemented in BMS, the geometric de-

Chapter 4. Data-driven models for the M_1/CeO_2 interaction

scriptors were lost during the optimization process, and, consequently, the capability of the method to reproduce the electronic ensembles. Thus, we further decomposed the primary set into metal features (the five first of the list above), and oxide features (the latter three). A first BMS model was then trained with only the metal descriptors, correctly positioning each respective electronic ensemble in the approximate region of the energy spectrum. The obtained values were then subtracted from the DFT-calculated data to obtain the remaining oxide contributions. A second BMS model was then trained on the residuals, using only the three oxide features. Lastly, the predictions of both models were then summed via:

$$E_{\text{Ads}} = E_{\text{Ads}}^{\text{M}} + E_{\text{Ads}}^{\text{Ox}} \approx E_{\text{BMS}}^{\text{M}} + E_{\text{BMS}}^{\text{Ox}} = E_{\text{BMS}}. \qquad (4.1)$$

Overall the BMS provides slightly lower accuracy than the previous EN and RF models, with an RMSE (MAE) of $0.20\,\text{eV}$ ($0.15\,\text{eV}$). Fig. 4.10 shows the final BMS predictions with the distributions of the electronic ensembles as obtained by DFT indicated as transparent background for easy comparison. It can be seen that the overall agreement is reasonable. The global mOS minima and energy differences between electronic ensembles are accurately reproduced in various cases. However, they occupy narrower ranges in the energy spectrum than the values obtained by DFT. Possible interpretations and remedies are provided in Chapter. 6.
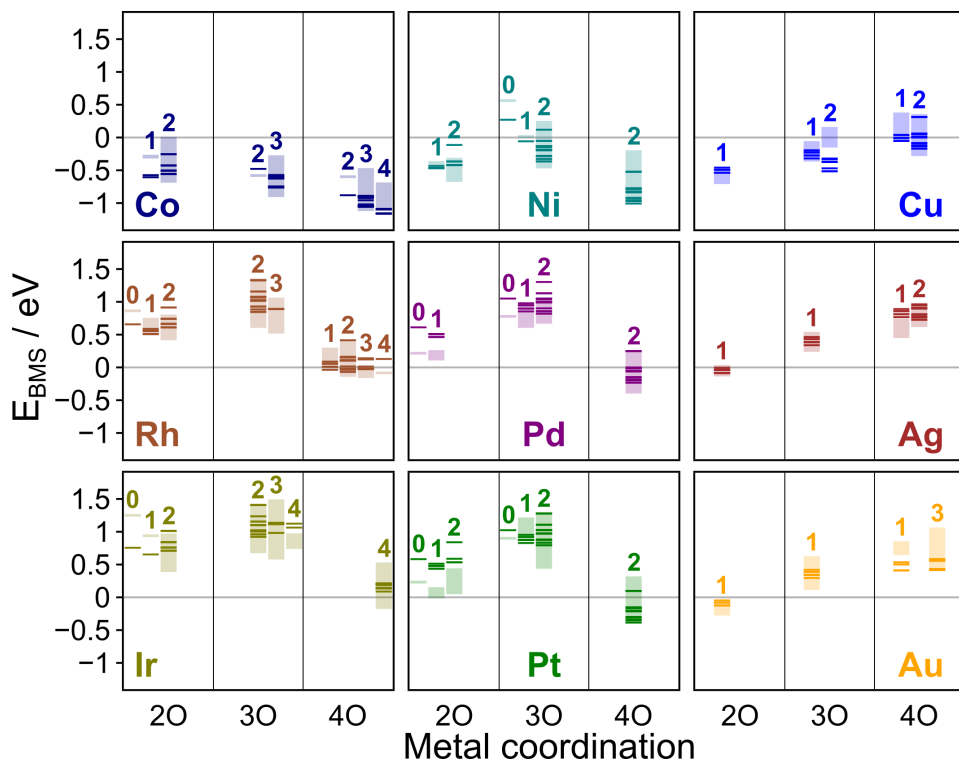
Figure 4.10: Predictions of the BMS model for the full dataset. The energy ranges of the electronic ensembles as obtained by DFT are indicated via transparent background colors.

The BMS provides slightly lower predictive accuracy than the EN and RF models, however, it yields the closed-form mathematical expression that is used by the algorithm to make the predictions. For the best-performing model, I obtained for the metal part the following equation:

$$E_{\mathrm{BMS}}^{\mathrm{M}} = \overbrace{\boldsymbol{N}_{\mathrm{O}} c_3 + \Delta\mathbf{G}^2}^{(i)} + \overbrace{\boldsymbol{N}_{\mathbf{O}} c_1 \left(\boldsymbol{\Delta\mathbf{G}} + c_2\right)^{\boldsymbol{N}_{\mathrm{O}}} \cos\left(\boldsymbol{r}\right)}^{(ii)}$$

$$- \overbrace{\frac{\boldsymbol{N}_{\mathbf{O}} r^2 \left(\mathbf{IP} + \mathbf{Z}\right)^{-c_2 - \boldsymbol{N}_{\mathbf{O}}}}{c_4 \left(\boldsymbol{\Delta\mathbf{G}} + c_5\right)^2 \left(\boldsymbol{\Delta\mathbf{G}} \cdot \left(\mathbf{IP} + \mathbf{Z}\right)^{-c_2 - \boldsymbol{N}_{\mathbf{O}}} + c_4\right) \left(\boldsymbol{r} + \cos\left(\frac{c_6 \boldsymbol{r}}{c_4}\right)\right)^2}}^{(iii)} \tag{4.2}$$

As the expressions are rather lengthy, I shortened some descriptor symbols

Chapter 4. Data-driven models for the M_1/CeO_2 interaction

from the previous notation ($r_{cov} \rightarrow r$; $\Delta G_{bulk}^{M\text{-}O} \rightarrow \Delta G$; $\min(d_{M\text{-}Ce3}) \rightarrow d_{MC}$; $\text{avg}(d_{Ce3\text{-}Ce3}) \rightarrow d_{CC}$) and typeset them in bold to distinguish them from the coefficients, c_i. For easier interpretability, I further ordered the individual terms of the linear combination of Eq. 4.2 in the order of increasing number of features. In addition, a visualization of the predicted value for each term is provided in Fig. 4.11. It should be noted that, as these are only the constituent metal terms, no local polaron structure enters at this stage. Furthermore, interpretations of the individual terms will be based on the observed positioning of the metal data points in the energy spectrum, as well as their functional form. The ranges of the input metal features are given in Table 4.1 and the coefficients of the BMS equations in Table 7.3.
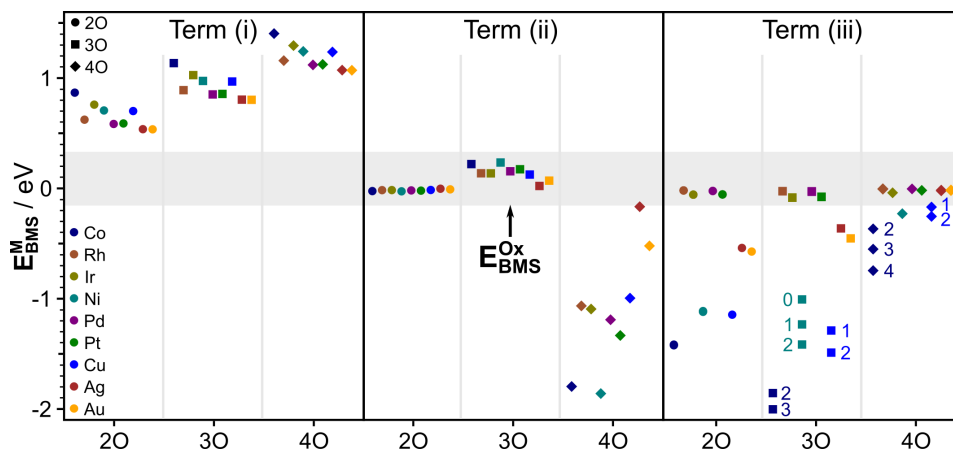
Figure 4.11: Predictions given by the individual terms of the metal-part of the trained BMS model.

Term (i) of Eq. 4.2 spans a positive range of 0.54 to 1.40 eV. As it depends only on the coordination number, N_O, and the metal-oxygen bond strength, ΔG, we attribute it mainly to distortion effects. Due to the positive value of c_3 (see Table 7.3), higher coordination leads to a more destabilizing effect. The three coordination environments are thus placed on separate levels. In addition, the term ΔG^2 is always positive and leads to a distinction between the metal atoms instead, albeit within a rather small range of 0.00 to 0.35 eV. The overall values obtained for term (ii) are between -1.86 and 0.24 eV. It has an almost negligible influence on metal atoms in 2O coordination, slightly destabilizes 3O coordination, and is highly exothermic for 4O coordination. Mathematically, this is mainly due to the $c_2^{N_O}$ term, which amounts to approximately $-5^{(2 \text{ to } 4)}$ (only slightly modified by ΔG), thus also providing an alternating effect on stability based on coordination. Lastly, the $\cos(r)$ term is largest for small atoms, thus

particularly stabilizing these species in higher coordination, in line with the DFT predictions. The rather convoluted form of term (iii) makes a straight-forward, mathematical interpretation challenging. It contains all five metal features and spans a range of -2.00 to $0.00\,\text{eV}$, therefore having a stabilizing effect independent of metal species and coordination environment. As it contains the ionization potential, IP, it introduces a first distinction by metal oxidation states (mOS), albeit the difference is not significant for all structures. Overall, the largest effects are again observed for the first row metals, as the term approaches zero for large atomic numbers and large covalent radii.

Table 4.1: Values of the input features used for the metal-terms of the final BMS model (as selected from Table 7.1). The comma-separated values of the (cumulative) ionization potential, $\boldsymbol{IP}$, correspond to the accessible mOS states for each respective metal. $\boldsymbol{\Delta G}$ and IP are given in units of eV, $\mathbf{r}$ in units of Å.

M	Z	$\boldsymbol{\Delta G}$ / eV	r / Å	IP / eV
Co	27	-0.58	1.26	7.88, 17.08, 33.50, 51.20
Rh	45	-0.30	1.35	0.00, 7.46, 18.08, 31.06, 42.00
Ir	77	-0.47	1.37	0.00, 8.97, 17.00, 28.00, 40.00
Ni	28	-0.41	1.21	0.00, 7.64, 18.17
Pd	46	-0.22	1.31	0.00, 8.34, 19.43
Pt	78	-0.23	1.28	0.00, 8.96, 18.56
Cu	29	-0.41	1.38	7.73, 20.29
Ag	47	-0.04	1.53	7.58, 21.48
Au	79	-0.02	1.44	9.23, 30.00

Lastly, the remaining oxide term:

$$E_{\text{BMS}}^{\text{Ox}} = \frac{1}{c_1}\left(\boldsymbol{d_{\text{CC}}} + \frac{\boldsymbol{d_{\text{MC}}}}{c_2^2\boldsymbol{d_{\text{MC}}} - c_2\boldsymbol{d_{\text{CC}}}}\cos\left(c_1\left(c_1\boldsymbol{\epsilon}\left(c_1 + c_2\right) + \boldsymbol{\epsilon}^2\right)\right)\right) \quad (4.3)$$

contains the three surface descriptors (see above) and accounts for Coulomb interactions between the metal atoms and polarons, as well as the polarons themselves, and their incurred surface strain. It again takes a rather complex mathematical form that makes direct interpretation challenging. It spans a range of -0.15 to $0.33\,\text{eV}$, which is indicated by the gray background in Fig. 4.11, thus with a similar magnitude as polaron hopping barriers in ceria[164]. It provides the final disentanglement of the metal clusters, based on the mOS and local polaron structure.

Chapter 4. Data-driven models for the M_1/CeO_2 interaction

Chapter 5

Theory meets experiment

We confuse the world as talked about, described, and measured with the world which actually is. We are sick with a fascination for the useful tools of names and numbers, of symbols, signs, conceptions and ideas.

The greater the scientist, the more he is impressed with his ignorance of reality, and the more he realizes that his laws and labels, descriptions and definitions, are the products of his own thought. They help him to use the world for purposes of his own devising rather than understand and explain it.

Alan Watts

In the last two chapters, I have showcased the inherent complexity of ceria-based SACs that arises due to local polaron structure, as well as how machine-learning can aid in reducing the computational effort in their accurate treatment and provide additional physical insight. Having laid this groundwork, I will now outline how I could assist in the study of real-world experimental catalytic systems by computational modelling. The two examples that will serve this purpose are high-density SA platinum on oxygen-plasma pre-treated ceria, active in the CO oxidation reaction, and SA manganese on a ceria powder support, showing high activity and selectivity in ammonia oxidation to N_2O.

Chapter 5. Theory meets experiment

5.1 Fabrication of high-density Pt_1/CeO_2

5.1.1 Synthesis and characterization

The first system was prepared by Dr. Weiming Wan, Prof. Beatriz Roldán Cuenya, and coworkers at the Fritz-Haber Institute in Berlin, who treated commercially available ceria powder, exposing mainly the (111) facet, with oxygen plasma[43]. The resulting system was found to stabilize isolated SA-Pt up to an impressive nominal metal loading of 0.2 ML ($1.6 \times 10^{14}\,cm^{-2}$) and to be active and resistant against sintering in the CO oxidation reaction at near atmospheric pressure. While the catalytic activity was intriguing, the main focus on the project was on the synthetic preparation via oxygen-plasma treatment, which holds promise to establish itself as a general strategy for the preparation of SACs with high metal loading.

Hence, to elucidate the effect of other, well-known surface modifications on Pt adsorption, the experimentalists prepared catalysts based on a variety of differently pre-treated supports. Namely, these are (i) the unmodified, commercial ceria sample, used as a reference system [$Pt/CeO_2(111)$], (ii) a partially reduced surface, obtained via annealing in UHV, and used to probe the effect of oxygen vacancies (Pt/CeO_2-red), and, lastly, (iii) a sample with an increased surface step density, prepared via literature procedures (Pt/CeO_2-step)[40]. As evidenced by LEED [Fig. 5.1 a)], in all three reference systems the hexagonal long-range symmetry typical for $CeO_2(111)$ is retained, however, for the oxygen-plasma treated sample it is completely lost. This is indicative of a significant amount of surface restructuring, which could be confirmed by STM measurements [Fig. 5.1 b-d)], showing an extremely rugged surface with ceria nanoparticles of up to 2 nm in width and exceeding 1 nm in height. On all samples, platinum was then deposited from a metallic rod at room temperature with a low flux of 0.03 ML/min ($2.4 \times 10^{13}\,cm^{-2}$) to minimize metal aggregation[43]. Aberration-corrected STEM even made the visualization of isolated platinum atoms on the oxygen-plasma treated sample possible (Fig. 5.1 e), thus confirming atomic dispersion. After metal deposition, the samples were then subjected to a thermal flash at 523 K, followed by 5 min of annealing at the same temperature to ensure the separation of purely thermal from reaction-induced steps. Lastly, the catalysts were exposed to the ambient-pressure CO-oxidation reaction mixture to measure their performance in CO oxidation.
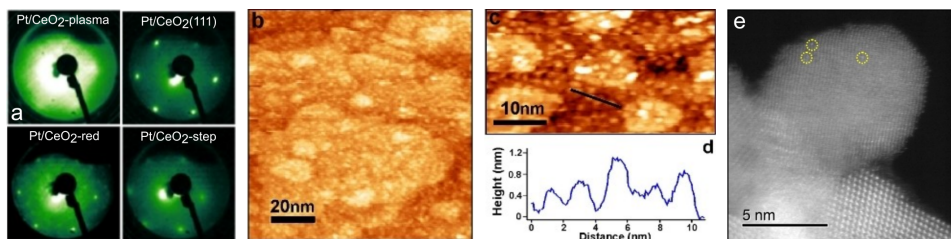
Figure 5.1: Experimental characterization carried out for the Pt/CeO_2-plasma and the reference samples. **a)** LEED showing the presence (absence) of long-range hexagonal symmetry, **b)** STM of the highly nanostructured plasma-treated sample, **c)** Higher-resolution STM scan, **d)** Height profile along the black line indicated in c), **e)** Aberration-corrected STEM in which SA-Pt anchored on a ceria nanoparticle become visible. Figure adapted from Ref. [43].

In addition, XPS was used to gain further insight into the catalytic systems, in particular, oxidation states. It allows assigning the platinum mOS, and identifying novel oxygen species, via the respective 4f and 1s core-level binding energies (CLBEs). The XPS results for the catalytic systems based on the commercial and oxygen-plasma pre-treated supports at the different synthesis stages and after use in the CO oxidation are presented in Fig. 5.2. For the $Pt/CeO_2(111)$ sample, upon deposition, platinum species show a binding energy (BE) of $71.8\,eV$, characteristic for metallic particles[8]. During heating, this peak shifts towards lower BE ($71.4\,eV$), indicative of sintering. After exposure to the reaction mixture, two new peaks appear at $72.7\,eV$ and $74.2\,eV$, which can be assigned to Pt^{2+} and Pt^{4+}, respectively, and which are obtained by the oxidation of the platinum particles.

For the Pt/CeO_2-plasma sample, Fig. 5.2 b), on the other hand, only a single peak at around $72.6\,eV$ is observed, and assigned to Pt^{2+}. As opposed to the oxidation of metallic particles, which occurred on the $Pt/CeO_2(111)$ sample, platinum is present in this oxidized state right after deposition, and remains so throughout the whole life cycle of the catalyst. In addition, no signal for metallic nanoparticles was found, providing strong evidence that platinum is indeed mainly present as isolated atoms on the Pt/CeO_2-plasma sample. A likely candidate for stable atomic dispersion are highly favorable square-planar coordination environments on local restructured (100) facets, which also promote the observed mOS (see Sec. 3.1)[40,68].

---

[8]In reality, an additional peak at a BE of about $75.2\,eV$ is observed. This is due to spin-orbit coupling which leads to a splitting of the degenerate 4f state, resulting in two distinct electron transitions, termed $4f_{7/2}$ and $4f_{5/2}$, with the former corresponding to the main signal used for analysis (see annotation in Fig. 5.2 b).

Chapter 5.   Theory meets experiment

The O 1s XPS spectra for both samples (Fig. 5.2) show a main peak at about 529.2 eV, originating from lattice oxygen of the upper layers of the ceria support (see Sec. **??**). After exposure to the reaction mixture, an additional signal appears at 531.8 eV (531.4 eV) for Pt/CeO_2 (Pt/CeO_2-plasma), which is usually assigned to surface hydroxyl groups formed with residual water in the gas mixture, and/or surface carbonates formed during the reaction. Interestingly, however, the Pt/CeO_2-plasma system is the only sample that shows another peak at 530.8 eV already after metal deposition. It persists the thermal flash, but vanishes during annealing, indicating a metastable species. In addition, its relative intensity grows upon grazing angle measurement[43] confirming its location near the surface. Via computational modelling, I could assign this peak to peroxo-species, which further turned out to be crucial for the exceptional performance of the catalyst (*vide infra*).
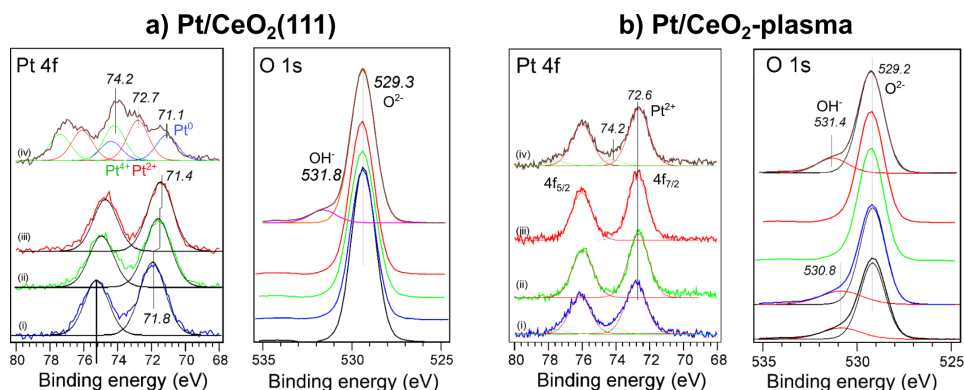
Figure 5.2: Pt 4f and O 1s XPS spectra of the Pt/CeO_2(111) and Pt/CeO_2-plasma samples: (i) as deposited at 300 K; (ii) after thermal flash to 523 K; (iii) after annealing at 523 K for 5 min; (iv) after CO oxidation. Figure adapted from Ref. [43].

5.1.2   Identification and role of peroxide

Due to the presence of the novel O 1s peak at 530.8 eV before exposure to the reaction mixture, as well as the fact that the signal is obtained after oxygen pre-treatment, I deemed it likely that it originates from reactive surface oxygen species. These can be formed either by direct reaction of atomic oxygen radicals of the plasma with lattice oxygen, or, alternatively, by the adsorption of O_2 in the oxygen vacancies formed via preferential sputtering by the high-velocity plasma particles. In the latter case, depending on the number of electrons being transferred upon integration of

O_2 into the vacancy site, either superoxide, $O_2^{\bullet-}$ or peroxide, O_2^{2-}, can be formed. In the high-energy plasma environment, there likely exists a mixture of various species, however, their easy interconversion should result in the transformation to the most stable product until the time of metal deposition. Furthermore, relative stabilities depend on the exposed facet, and, due to the significant nanostructuring observed in the STM measurements, all low-index (and possibly also high-energy stepped facets) should be exposed. Previous literature reports indicate that the formation of peroxides is generally accompanied by a larger formation energy[227,228], thus I chose them as the representative structural element.

Hence, Fig. 5.3 shows the most stable optimized peroxide structures on the three ceria low-index facets in the (2×2) supercells. The structures were obtained by adding an oxygen radical to a lattice oxygen of the pristine surface, resulting in the desired nominal O_2^{2-} species. I evaluated peroxide surface coverages up to a full monolayer, ML, with the formation energies listed in Table 5.1. It can be seen that on the (111) facet, the additional oxygen atom adapts a bridging position between two cerium atoms, slightly above the original lattice oxygen, while on the (110) facet, it is sticking up, as it cannot be effectively integrated into the surface layer. Nonetheless, the adsorption energy of the oxygen atom is higher in the latter case, $-2.87\,\text{eV}$ vs. $-2.68\,\text{eV}$, likely due to the fact that lattice oxygen is more coordinatively unsaturated on the (110) facet, being bound to only two cerium atoms, as opposed to three for the (111) facet. The highest formation energy, $-3.36\,\text{eV}$, is obtained for the most reactive (100) surface. Due to its open nature[67], the peroxide species can be fully integrated into the surface layer. The same trend continues up to full monolayer coverage, with (100) providing the highest reaction energy for peroxide formation from lattice oxygen.

Chapter 5. Theory meets experiment
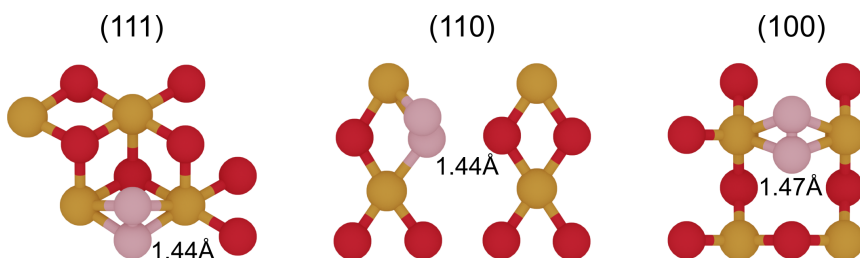
Figure 5.3: Top views of the structures of peroxide species formed by the reaction with oxygen radicals on the low-index ceria surfaces. As annotated, the peroxide groups can be identified by their O–O bond length of about 1.4 Å. The (100) surface can ideally accommodate the second oxygen atom within its surface layer, while a bridging position is adopted on (111) and it is considerably protruding outwards on (110).

Table 5.1: Peroxide formation energies for the low-index surfaces of ceria at different coverages, (coverages given relative to the number of surface cerium atoms). All values are in units of eV and are referenced to the energy of the pristine surface and the total energy of the adsorbed oxygen radicals: $\Delta E = E_{\text{total}} - E_{\text{pris}} - N_0 E_O$. The values in parenthesis denote relative changes of the peroxide formation energies for incremental increases in coverage. For 0.5 ML, two different geometric arrangements of the peroxide groups [diagonal (d) and row-wise (r)] were considered.

Surface	Θ_{peroxide} / ML				
	0.25	0.5–d	0.5–r	0.75	1.0
(111)	-2.68	-5.22 (-2.55)	-5.33 (-2.66)	-7.73 (-2.40)	-10.09 (-2.36)
(110)	-2.87	-5.68 (-2.81)	-5.72 (-2.85)	-8.35 (-2.63)	-11.00 (-2.65)
(100)	-3.36	-6.73 (-3.37)	-6.56 (-3.20)	-9.69 (-2.96)	-12.67 (-2.98)

To evaluate the validity of my proposal of peroxide presence on the oxygen-plasma treated sample, I then simulated core-level binding energies (CLBEs) to compare with the observed XPS signal, applying the final state approximation[184]. While XPS is generally considered a surface-sensitive technique, it still has a penetration depth of a few nm[229], corresponding to numerous atomic layers, making the main signal bulk-like. Hence, I used the O^{2-} signal of ceria bulk in a 2×2×2 supercell as a reference. Table 5.2 lists the average obtained relative CLBEs for surface lattice oxygen, as well as the peroxide groups. The signal for surface lattice oxygen is slightly redshifted by approximately -0.8 eV for (111) and (110), and by -1.2 eV for (100). This can be rationalized by the fact that surface oxygen atoms have fewer bonds to cerium atoms and therefore possess a higher valence electron

density, which partially shields the nuclear charge for the core electrons, thus reducing their binding energy. Despite this, typically no extra signal for the surface layer is observed in XPS, as the effect is averaged out as deeper subsurface layers are gradually probed until, after a few atomic layers, the species are fully bulk-like.

For the peroxide groups, on the other hand, clear blueshifts of the signals of around $1.6\,\text{eV}$, $1.3\,\text{eV}$, and $1.4\,\text{eV}$, for the respective (111), (110), and (100) facet are observed. Following the same reasoning as above, the shift can be attributed to the lower valence electron density in the O_2^{2-} than the O^{2-} motif. Experimentally, the signal will likely be observed at slightly higher values due to the aforementioned averaging over the upper atomic layers. As seen in Fig. 5.2, in the Pt/CeO_2-plasma sample, the novel peak is indeed blueshifted by around $1.6\,\text{eV}$ relative to the main signal. Fig. 5.5 compiles all simulated CLBEs before and after platinum deposition. From the obtained results, it is evident that the peroxide shifts are in reasonable agreement with the experimental signal, confirming the validity of peroxide formation during oxygen-plasma treatment. However, assigning the underlying facet remains challenging.

Table 5.2: PBE+U core-level binding energies (in eV) for lattice oxygen and peroxide on low-index ceria surfaces at varying peroxide coverages. The presented values correspond to average results over multiple sites, as in each case, all oxygen atoms located in the surface layer were sampled. A plot of all data points is presented in Fig. 5.4. For a coverage of 0.5 ML, two different geometric arrangements of the peroxide groups, diagonally (0.5-d) and row-wise (0.5-r) were considered.

| Surface | Species | Θ_{peroxide} / ML | | | | | |
		0.0	0.25	0.5-d	0.5-r	0.75	1.0
(111)	O^{2-}	-0.81	-0.85	-0.84	-0.85	-0.82	
	O_2^{2-}		1.59	1.67	1.64	1.68	1.70
(110)	O^{2-}	-0.86	-0.80	-0.78	-0.78	-0.74	-0.66
	O_2^{2-}		1.19	1.37	1.15	1.33	1.37
(100)	O^{2-}	-1.14	-1.23	-1.39	-1.26	-1.19	
	O_2^{2-}		1.52	1.47	1.43	1.39	1.19

Chapter 5. Theory meets experiment
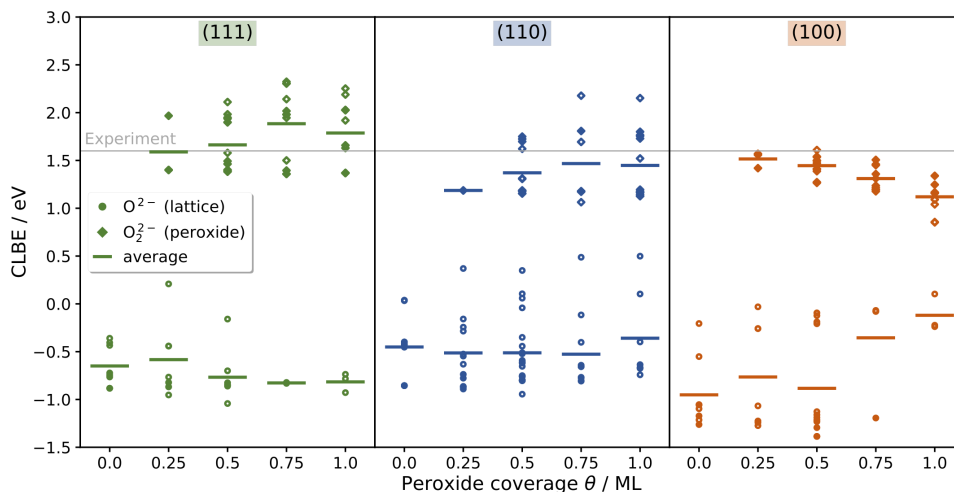
Figure 5.4: Simulated core level binding energy shifts (CLBE) for surface oxygen (round symbols) and peroxide species (diamonds) for ceria low-index surfaces without and with platinum adsorbed (filled and hollow symbols, respectively) at varying peroxide coverage. The experimentally observed shift of the novel peak compared to the main signal is indicated by the grey, horizontal line.

Having proven the presence of peroxide on the surfaces, I then evaluated its effect on the adsorption of SA platinum. The most stable optimized structures are presented in Fig. 5.5, and the computed energies listed in Table 5.3. As evident from the energies, the presence of peroxides does not tip the balance to make platinum adsorption exothermic on the low-index facets [except for two slightly exothermic, but almost thermoneutral cases on (110)]. Interestingly, though, in the case of 0.25 ML coverage, a splitting of the peroxide moiety is observed on all facets, resulting in a novel coordination motif around the platinum atom, as well as an adsorption energy lowering of $1.51\,eV$, $0.77\,eV$, and $0.17\,eV$ for (111), (110), and (100), respectively. Additionally, on the (111) facet at full ML coverage, the adsorption energy is only $0.59\,eV$, and therefore a significant $2.20\,eV$ lower than on the unmodified facet. In general, the overall changes are the largest on this surface, likely as the peroxide allows the platinum to be bonded above the rigid outermost surface layer. On the (100) surface, the dissociation of peroxide results in the common 2O coordination motif, with the other oxygen atom filling a bridging position in the neighboring row[9]. The resulting species will be highly mobile within the surface row[67], possibly available to form 3O and 4O coordination patterns, as previously discussed in Chapter 3. It is therefore easy to imagine how the dissociation of various peroxide groups on

the (100) facet can lead to the presence of sufficient mobile oxygen species to allow for the formation of square-planar 4O pockets. The dissociation of peroxide is enabled through the transfer of two electrons from the platinum atom, resulting in two O^{2-} species and the observed Pt^{2+}.

Lastly, on the reconstructed (100)-4O environment, platinum adsorption is highly favorable ($-0.85\,eV$) (as shown before) and not notably affected by the presence of peroxide (except at full coverage, which the surface cannot reasonably accommodate either way). For instance, at $0.25\,ML$ coverage, metal adsorption is exothermic $-0.59\,eV$, while at $0.5\,ML$ coverage with a diagonal arrangement of the two peroxide groups, the value ($-0.95\,eV$) is even higher than on the unmodified surface. From this, it becomes evident that the change from a lattice oxygen to a peroxide moiety does not qualitatively alter the adsorption behavior of the structure. As such, square-planar 4O environments at (111) step edges and nanoparticles (see Chapter 3) should still present the most favorable sites for SA metal stabilization. Due to the extensive amount of nanostructuring observed on the oxygen-plasma pre-treated sample, there should be plenty of such sites available on the support.

Table 5.3: Platinum adsorption energies on the low-index surfaces of ceria at different coverages, (coverages given relative to the number of surface cerium atoms). All values are in units of eV and are referenced to the energy of the pristine surface and the metal bulk energy: $\Delta E = E_{\text{total}} - E_{\text{pris}} - E_{\text{M}}$.

| Surface | Θ_{peroxide} / ML | | | | | |
	0.0	0.25	0.5–d	0.5–r	0.75	1.0
(111)	2.79	1.28	1.98	1.75	1.62	0.59
(110)	0.60	-0.17	0.75	-0.08	0.11	0.12
(100)	0.31	0.14	0.46	0.30	0.56	0.64
(100)–4O	-0.85	-0.59	-0.95	-0.24	-0.63	1.76

Dr. Wan, Prof. Beatriz Roldán Cuenya, and coworkers further prepared another nanostructured reference sample by sputtering the ceria substrate with Ar-plasma, followed by exposure to oxygen to re-oxidize the surface (further referred to as Pt/CeO_2-Ar). While no qualitative comparison of the amount of nanostructuring with the original Pt/CeO_2-plasma sample is available, XPS showed that the novel O 1s signal, is also present, albeit

---

[9]As a matter of fact, when the (100) facet is obtained via bulk cleavage, all these positions are occupied by oxygen atoms. However, to resolve the resulting surface dipole, oxygen is expelled on experimental samples, while in computational models they are usually moved to the bottom of the slab in a checkerboard fashion (further details see Section. 2.4.1). The resulting vacant positions are therefore readily available to accommodate the additional oxygen atom.

Chapter 5.   Theory meets experiment
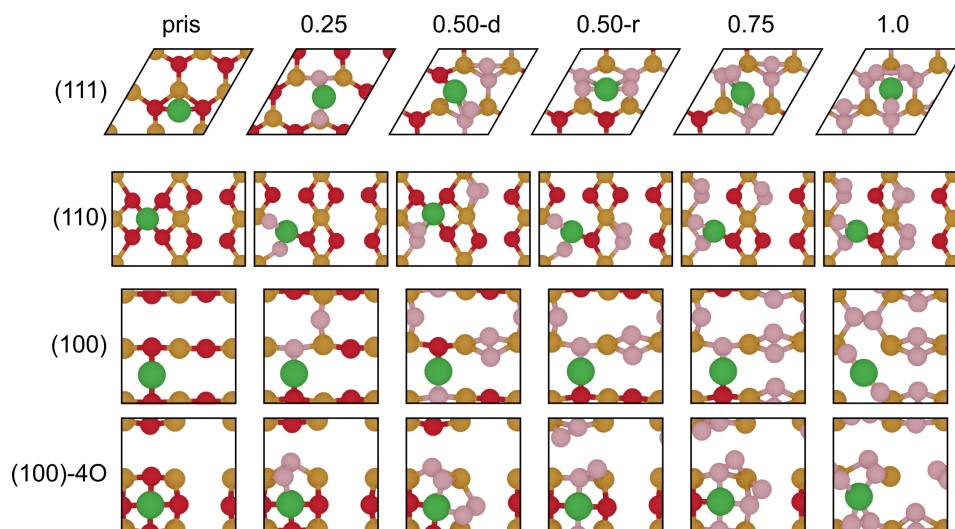
Figure 5.5: Adsorption of platinum on peroxide-precovered ceria low-index facets from 0 ML coverage (pris) up to 1.0 ML coverage. At 0.5 ML, two different local arrangements of the peroxide groups [diagonal (d) and row-wise (r)] were considered.

at markedly less pronounced intensity[43]. For one, this can be attributed to the pathway of O radical reaction with lattice oxygen being inaccessible. Furthermore, it is a known fact that on CeO_2(111), the surface does not present the most stable vacancy position, which are therefore prone to migrate into the bulk of the material[169,227]. Thus, it stands to reason that the separation of the sputtering step from the exposure to oxygen for Pt/CeO_2-Ar likely leads to a lesser amount of vacancy healing by O_2, and, consequently, formation peroxide species. Thus, when depositing the same amount of 0.2 ML platinum on this sample, in addition to the majority Pt^{2+} species, metallic NPs are also observed (on the oxygen-plasma pre-treated sample, these only form in considerable quantity in excess of 0.4 ML metal deposition). Evidently, both samples show the same qualitative behavior, however, pre-treatment with oxygen plasma allows for improved SA-Pt stabilization.

While the exact origin of the difference is not known, from the higher amount of peroxide on the Pt/CeO_2-plasma sample and the available DFT data, a few possible scenarios can be constructed. One effect could be that the breaking of peroxide on local (100) facets upon Pt-adsorption leads to an increased availability of mobile lattice O (as explained above). Hence, more favorable 4O environments could be formed on larger local (100) facets, not only at step edges or the corners of NPs where they appear naturally.

UNIVERSITAT ROVIRA I VIRGILI
CERIA-BASED SINGLE-ATOM CATALYSTS: FROM SIMPLIFIED MODELS TOWARDS REAL-WORLD COMPLEXITY
Julian Geiger

5.2. Mn_1/CeO_2 in ammonia oxidation

Furthermore, as the presence of peroxide makes adsorption of platinum on (111) and (110) more exothermic (in most cases), it might lead to longer life times of metastable Pt-species after adsorption, thus preventing the rapid agglomeration observed on pristine CeO_2(111). Moreover, in such metastable species, especially at higher peroxide coverage, the local environment around the platinum atom is often similar to the linear, gaseous PtO_2 structure that was used by Jones and coworkers to prepare one of the first ceria-based Pt-SACs[41]. Hence, while full desorption of PtO_2(g) would probably lead to a loss of metal content, partial breaking of coordinating peroxide due to electron donation from the metal might well lead to mobile PtO_x fragments on the surface, which get trapped at the stable square planar pockets. As it is likely that all ceria facets are exposed on the nanostructured sample at varying peroxide coverages, under the high-energy conditions of plasma exposure, a mixture of the aforementioned effects are likely at play.

5.2 Mn_1/CeO_2 in ammonia oxidation

5.2.1 Synthesis, performance and characterization

The second project in collaboration with experimental colleagues was focused on a ceria-based Mn-SAC which showed unprecedented activity and selectivity in the oxidation of ammonia to N_2O (Fig. 5.6). The catalyst was prepared by Ivan Surin, Prof. Javier Pérez-Ramírez, and coworkers at the ETH Zurich, who used simple incipient wetness impregnation (IWI) of manganese on a commercial ceria nanopowder to achieve a catalyst that contained isolated SA manganese at a nominal metal loading of 1 wt.%. After Mn deposition from the $Mn(NO_3)_2$ precursor solution, the sample was dried overnight in vacuum at 353 K, followed by 5 h calcination in air at 823 K.

The experimentalists also prepared various reference systems by depositing other metals on ceria, as well as manganese on alternative reducible and irreducible supports. An overview of the different synthesized systems together with their catalytic performances is presented in Fig. 5.6 a). It can be seen that Mn/CeO_2 shows a selectivity towards N_2O of about 80 %, comparable to the former state-of-the-art Au/CeO_2 system by the same group, but at almost twice the space-time yield (STY), due to its higher activity in NH_3 conversion. Astonishingly, the performance of Mn/CeO_2 even increases with time on stream (see Fig. 5.6 b),), in stark contrast to the behavior of most SACs, which usually degrade due to metal agglomeration.

To gain insight into the origin of the exceptional performance of the Mn/CeO_2 catalyst, various analytical techniques were used, as compiled

Chapter 5.   Theory meets experiment
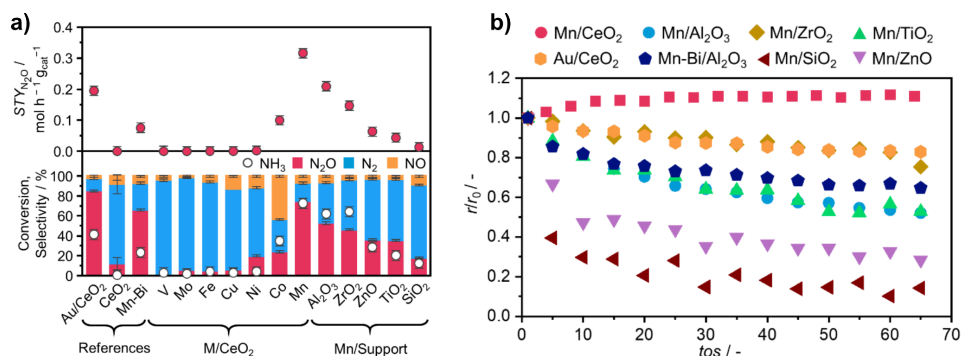
Figure 5.6: Evaluation of catalyst performances for Mn/CeO_2-SAC and reference systems in terms of, **a)** NH_3 conversion, N_2O selectivity and space-time yield (STY), and **b)** relative activity during 70 h) on stream. Figure adapted from Ref. [52].

in Fig. 5.7. Akin to the study of the plasma-functionalized Pt-SAC, the metal oxidation state (mOS) of manganese could be assigned via XPS measurements [Fig. 5.7 a)]. It was found that the metal is present mainly in a low-valent 2+ state which is retained during exposure to the reaction mixture. HAADF-STEM in conjunction with EDXS further shows the high degree of manganese dispersion [Fig. 5.7 b)]. Its single-atom nature could further be confirmed unambiguously by electron paramagnetic resonance (EPR) measurements, which show a clear and characteristic hyperfine splitting [Fig. 5.7 c)]. Furthermore, before exposure to the reaction mixture, this signal is less pronounced, and instead, a very broad signal centered at around 1800 G is observed. Hence, during the reaction manganese seems to disperse further, again in stark contrast to most SACs, which degrade via metal agglomeration. In accordance, manganese retains its low valence throughout.

In addition to the understanding of the atomistic structure obtained via the analytical techniques compiled in Fig. 5.7, more indirect techniques can provide additional insights. For instance, volumetric O_2 chemisorption at 673 K allowed for a quantification of the oxygen uptake of various supports, as well as the changes effected by manganese deposition, as presented in Fig. 5.8. Well-known for its high oxygen storage capacity (OSC), it comes as no surprise that pristine ceria shows the highest amount of oxygen uptake of all support materials. In all cases apart from ZnO and SiO_2 for which the changes were minor, manganese deposition consistently led to a significant increase in oxygen uptake of about $1\,cm^{-3}\,g^{-1}$. This result hints at the inherent capability of manganese to activate oxygen, particularly in a low-valent state. Furthermore, a direct correlation between oxygen uptake and
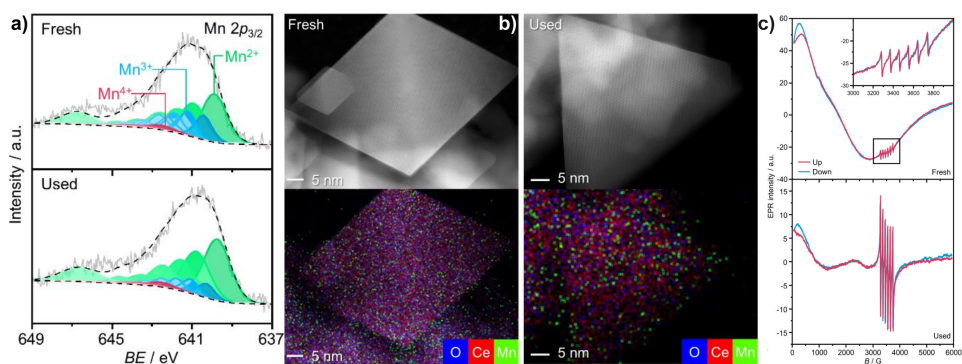
Figure 5.7: Experimental characterization of the ceria-based Mn-SAC showing the isolated nature of the metal sites before and after use in NH_3 oxidation to N_2O via **a)** XPS, **b)** electron paramagnetic resonance (EPR), as well as **c)** High-angle annular dark-field scanning transmission electron microscopy (HAADF-STEM) and energy dispersive X-ray spectroscopy (EDXS). Figure adapted from Ref. [52].

N_2O selectivity could be found, Fig. 5.8 b). Thus, sufficient availability of reactive oxygen species is likely crucial for the selective oxidation of NH_3 to N_2O. This is consistent with the necessity for dehydrogenation of NH_3 and subsequent oxidation of resulting NH_x fragments to yield nitrous oxide. On the other hand, for all manganese-based catalysts, the amount of produced NO remained low ($< 5\%$). As this product would require even further oxidation, the results indicate that the concentration of reactive oxygen species remains low enough to avoid over-oxidation.

Moreover, temporal analysis of products (TAP) experiments were also conducted to discern the role of gas-phase and lattice oxygen. Here, pulses of a 1:1:1 mixture of He, NH_3, and isotope-labeled $^{18}O_2$ were used and the order of product formation and distribution analyzed via mass spectrometry (MS). However, when evaluating TAP results, it should be kept in mind that there exists a large pressure gap between the steady-state operation of the catalyst and the conditions during TAP. Furthermore, due to the use of short pulses, participation of species might be observed, that would quickly get depleted during steady-state operation. Nonetheless, it is exactly this property that makes TAP useful, as it allows probing of the onset of the reaction. As evident from Fig. 5.8 c) and d), NO is actually observed as the main product during pulsing, in contrast to steady-state operation. This can be rationalized by a high availability of oxygen species at the catalyst surface at the beginning of the reaction, leading to highly oxidizing conditions and the formation of NO. In line with the results of steady-state operation, the relative highest selectivity towards N_2O is observed at a temperature of

Chapter 5.   Theory meets experiment

673 K. Importantly, both oxidation products mainly show the presence of ^{16}O, thus indicating direct participation of lattice oxygen. Furthermore, as seen in Fig. 5.8 d), the signals for $N_2^{16}O$ and $N_2^{18}O$ have their maximum at the same time and decline equally, indicating that the reactions occur at the same rate. Thus, lattice oxygen is likely involved in the reaction, while the resulting vacancies get quickly healed by isotope-labelled gas-phase oxygen. Lastly, lattice oxygen is also found in water, the side product formed during the initial dehydrogenation of ammonia, with the peak for $H_2^{18}O$ appearing after $H_2^{16}O$ and degrading slower after the pulse, indicating that the initial dehydrogenation likely involves lattice oxygen.
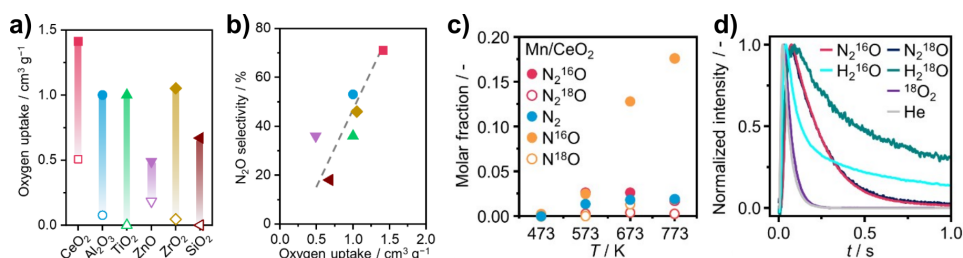
Figure 5.8: Identification of oxygen uptake as key performance descriptor. **a**) Oxygen uptake of the pristine supports and modifications due to manganese adsorption. **b**) Correlation between oxygen uptake and N_2O selectivity. **c** & **d**) Results of temporal analysis of products (TAP) experiments with isotope-labeled oxygen gas. Figure adapted from Ref. [52].

5.2.2   Constructing a catalyst library

Despite the extensive experimental investigation outlined above, knowledge of the actual atomic structure of the Mn-SAC still remained elusive. To this end, I investigated the intriguing system via computational modelling. Due to the initial absence of atomic resolution images of the catalyst surface, later obtained via high-resolution STEM (HRSTEM), I constructed a first catalyst library under consideration of all low-index facets of ceria[10]. Here, I evaluated all on-top, bridge, and hollow adsorption sites involving oxygen and/or cerium ions, as well as mixtures of both, shown in Fig. 5.9.

---

[10]Irrespective of the availability of experimental data, it is generally good practice to consider a variety of possible catalyst structures for computational exploration, as real samples are not perfect and can expose various facets, steps, and defects. Nonetheless, experimental data is indispensable in narrowing down the vast structural space. In actuality, a feedback loop between experiments and theory is often needed to establish a reliable model, particularly for complex systems such as frequently found in the SACs field.
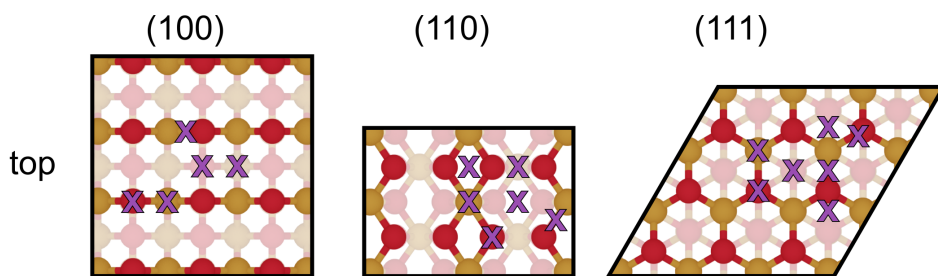
Figure 5.9: All possible considered adsorption sites on low-index ceria surfaces for the construction of the Mn-SAC library (Note: The restructured (100)-4O position (see Chapter 3) was also included as a special case, however, it is not shown here).

The most stable adsorption geometries obtained from this exploration are displayed in Fig. 5.10. mOS values ranging from 2+ to 4+ are found for the manganese atom and are correlated to the coordination number. Surprisingly, I found that in many cases, PBE+U actually over-stabilized highly oxidized metal states. This becomes especially apparent for the (111)-based systems, in which all aforementioned manganese mOS are accessible, and adsorption energy estimates with PBE+U showed a stability increase with mOS. However, when I refined the values with the HSE03–13 hybrid functional[230], based on the PBE+U optimized structures, Mn^{2+} (Mn^{3+}) appeared as the most (least) stable, and Mn^{4+} as an intermediate state. I attribute this observation to the over-stabilizing effect of the Hubbard U correction for solutions with localized electronic states[11]. Thus, Fig. 5.10 compiles adsorption energy estimates evaluated with PBE+U in gray, as well as HSE03–13, based on the PBE+U optimized structures, in bold. Energies referenced in the following text passages will therefore correspond to the values obtained with the HSE03–13 hybrid functional, as I deem them more reliable.

---

[11]HSE03–13 was chosen based on previous work of our group, in which it was shown that this hybrid functional it provides a good description of level alignment for light-harvesting semiconductors[230], and should therefore also be suitable to capture the complex electronic interactions present in ceria-based SACs (see Chapter 3).

Chapter 5. Theory meets experiment
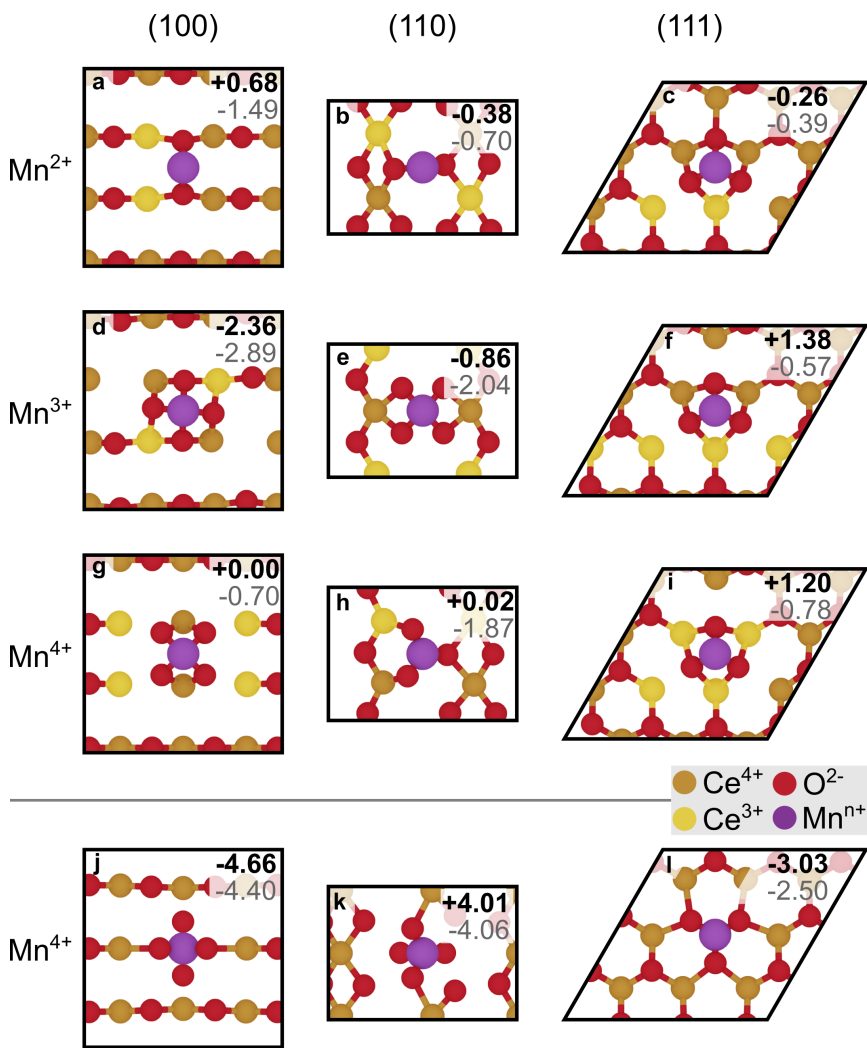
Figure 5.10: Most stable binding sites for SA-Mn on low-index ceria surfaces. Adsorption energies against the bulk metal evaluated with HSE03–13 (PBE+U) are indicated in bold (grey). Substitutional structures are shown in the bottom row.

Based on the obtained DFT data and the experimental observations, I could now gradually filter down the catalyst library to identify the most likely catalyst structure. Based on the positive adsorption energies of Mn^{4+} species on all the three low-index facets, as well as Mn^{2+} on (100) and Mn^{3+} on (111), these structures could be discarded. Mn^{3+} in the restructured (100)-4O coordination environment leads to an extremely stable catalyst structure, which likely presents a thermodynamic sink and is thus unavailable to effect further reactivity. [12]Lastly, based on the results of HRSTEM which showed that mainly the (111) facet is exposed, as well as the low-valent nature of manganese identified via XPS, I chose the (111)-based Mn^{2+} system as the most representative catalyst model.

5.2.3 Exploring the reactivity landscape

With a representative catalyst model at hand, I then turned my attention towards exploring the reactivity landscape. The total reaction of ammonia oxidation to nitrous oxide is as follows:

$$2\,NH_3 + 2\,O_2 \longrightarrow N_2O + 3\,H_2O. \tag{5.1}$$
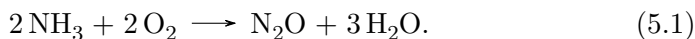
As previously proposed in the literature[52], a few key steps likely occur during the reaction sequence. These are: i) the dehydrogenation of ammonia:

$$NH_3^* + O \longrightarrow NH^* + H_2O \tag{5.2}$$

ii) the formation of an HNO (nitroxyl) intermediate

$$NH^* + O \longrightarrow HNO^*, \tag{5.3}$$

and iii) the combination of two nitrogen-containing fragments to form the N–N bond in the final product:

$$HNO^* + HNO^* \longrightarrow N_2O + H_2O. \tag{5.4}$$
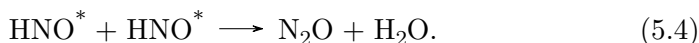
The combination of two nitroxyl fragments, as shown in Eq. 5.4 can proceed via a hyponitrous acid intermediate[231–233], followed by elimination of nitrous oxide and water. However, N–N bond formation might also occur in different

---

[12]Note the large difference in adsorption energy compared to platinum, which came out to $-0.85\,eV$ when evaluated with PBE+U (Table 5.3). While for the Pt-4O system, catalyst activation was previously proposed via reductive treatment with H_2 or CO[68], due to its exceptional stability, it remains questionable if this is possible for the equivalent Mn-4O SAC via exposure to the ammonia oxidation reaction mixture.

Chapter 5. Theory meets experiment

---

ways, involving other nitrogen-containing fragments at variable degrees of oxidation, for instance:

$$HNO^* + NH^* \longrightarrow N_2 + H_2O \tag{5.5}$$

or:

$$\begin{aligned} NH_2{}^* + NH_2{}^* &\longrightarrow N_2H_4{}^* \\ N_2H_4{}^* + O_2 &\longrightarrow N_2 + 2\,H_2O \end{aligned} \tag{5.6}$$
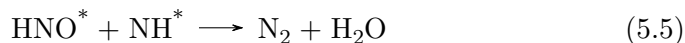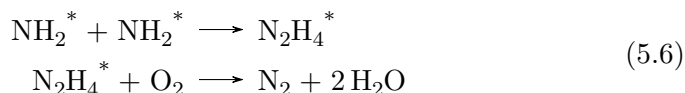
Importantly, reactions 5.5 and 5.6 proceed via less oxidized nitrogen-containing fragments and therefore prevail under more reducing conditions (e.g. on the pure ceria sample). On the other hand, strongly oxidizing conditions that provide an excess of reactive oxygen species, lead to the formation of mainly NO. Thus, the results of the TAP experiments show that the initial oxygen availability on the Mn-based catalyst is high enough to lead to over-oxidation. However, under steady state operation, the ceria-based Mn-SAC achieves exactly the right conditions to form N_2O as the main product (see Fig. 5.6). These mechanistic proposals again point to the availability of reactive oxygen species as a key descriptor for catalyst performance.

It should be noted at this point that the full network of elementary steps for the reaction at hand is far too vast to be explored exhaustively with computational methods[234]. This is especially true if the involvement of lattice oxygen (as confirmed by the TAP experiments), vacancies, acid-base equilibria with the support, and the numerous N-N bond formation routes ought to be evaluated explicitly. This is a rather common situation in the field of heterogeneous catalysis and is responsible for the fact that most chemical transformations used industrially on multi-million ton scales for decades are still poorly understood at the atomic level[235]. In addition, the need for a hybrid functional to obtain refined adsorption energy estimates increases the computational cost by one to two orders of magnitude compared to PBE+U, further complicating the situation. Thus, I shall content myself with evaluating the feasibility of the main reaction steps and intermediates *en route* to nitrous oxide formation, using three-fold coordinated low-valent Mn anchored on the majority $CeO_2(111)$ facet as representative catalyst model. The full obtained reaction scheme is presented in Fig. 5.11 and will be discussed in the following. Reaction intermediates will be referenced in bold in brackets and energy differences between important structures indicated.

When the catalyst (**1**) gets in contact with the reaction mixture, the thermodynamic driving force to bind O_2 is higher ($-1.21\,\text{eV}$) than for ammonia ($-0.98\,\text{eV}$), thus it adsorbs first on the metal center (**2**). Due to

the open and dynamic coordination motif provided by the three lattice oxygen, the Mn-SA remains available to subsequently also adsorb ammonia ($-0.79\,\text{eV}$), leading to an octahedral-like coordination sphere (**3**). With the two reactants in proximity, the dehydrogenation step can now occur, driven by the release of water molecule as side product ($0.23\,\text{eV}$), while an NH fragment and a reactive oxygen center remain bound to the manganese atom (**4**). As evident from Fig. 5.11, one bond to lattice oxygen is broken in this structure, leading to a quasi-tetrahedral coordination sphere around the metal center. Next, combination of the NH fragment and the reactive oxygen yields the nitroxyl, HNO, fragment in η^2 coordination, albeit with a rather endothermic reaction energy ($0.94\,\text{eV}$).

With the first nitroxyl formed, the number of possible pathways for the reaction is now insurmountable, thus, I assume the formation of the second fragment to occur via dehydrogenation of ammonia accordingly (**6**). Again driven by the elimination of water, the overall process is thermodynamically favorable ($-2.26\,\text{eV}$). Importantly, the low degree of coordinative saturation of the manganese atom again allows it to bind two nitroxyl fragments in a quasi-octahedral coordination sphere. These two fragments can now dimerize and form a hyponitrous acid-like ring structure (**7**), which is thermodynamically slightly uphill ($0.87\,\text{eV}$). Lastly, N_2O and H_2O can be eliminated, releasing $-1.33\,\text{eV}$ and $-1.60\,\text{eV}$, respectively, concluding the catalytic cycle. Alternatively, protonation of hyponitrous acid at the two oxygen atoms did not lead to a stable ring structure, but to the elimination of N_2. In reality, this process is likely occurring, as well, and in part responsible for the observed N_2 formation.

Chapter 5.   Theory meets experiment
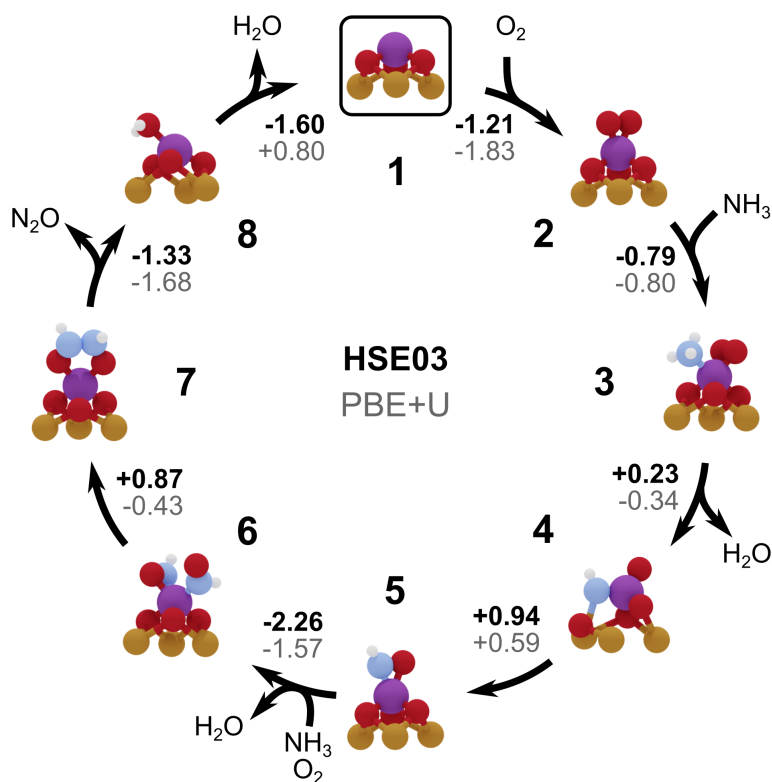
Figure 5.11: Proposed reaction scheme for ammonia oxidation to nitrous oxide on the most representative low-valent Mn-SAC on the ceria (111) majority facet. The key steps are NH_3 dehydrogenation, and the formation of a nitroxyl and hyponitrous acid-like ring intermediate. All steps are thermodynamically accessible.

It should be noted here that an alternative pathway can be constructed when ammonia is bound first and dehydrogenation is then achieved via lattice oxygen, as shown in Fig. 5.12 b). Through this process, the coordination sphere around Mn is broken in favor of integration of the NH fragment integrated ($\mathbf{3'}$). However, this step is thermodynamically significantly uphill (3.26 eV), thus some form of prior oxygen activation by the low-valent manganese atom is likely crucial. In this alternative path, oxygen adsorption is then assumed to occur after ammonia dehydrogenation ($\mathbf{4'}$, -1.06 eV), followed by oxygen splitting and N–O bond formation (-1.88 eV) to yield a nitroxyl-containing intermediate ($\mathbf{5'}$). This structure has the same composition as intermediate $\mathbf{5}$ in Fig. 5.11, and interconversion between the two proceeds almost thermoneutral (-0.14 eV). Furthermore, I also considered the elimination of water at an earlier stage in the cycle, such as from the

di-nitroxyl intermediate (**6**), as shown in Fig. 5.12 a). Here, proton transfer to one of the coordinating oxygen allows for thermoneutral (0.00 eV) elimination of H_2O_{lig}, leading to a structure in which one NO^- fragment is integrated into the coordination sphere (**7′**). In this case, ring formation to Mn-bound ONNO fragment (**8′**) is highly exothermic (−1.39 eV). Lastly, elimination of N_2O restores the 3-fold oxygen coordination, closing the catalytic cycle. Due to the formation of $N^{16}O$ and $N_2^{16}O$ observed in TAP, such a pathway with the direct participation of lattice oxygen is likely also occurring during catalyst operation.
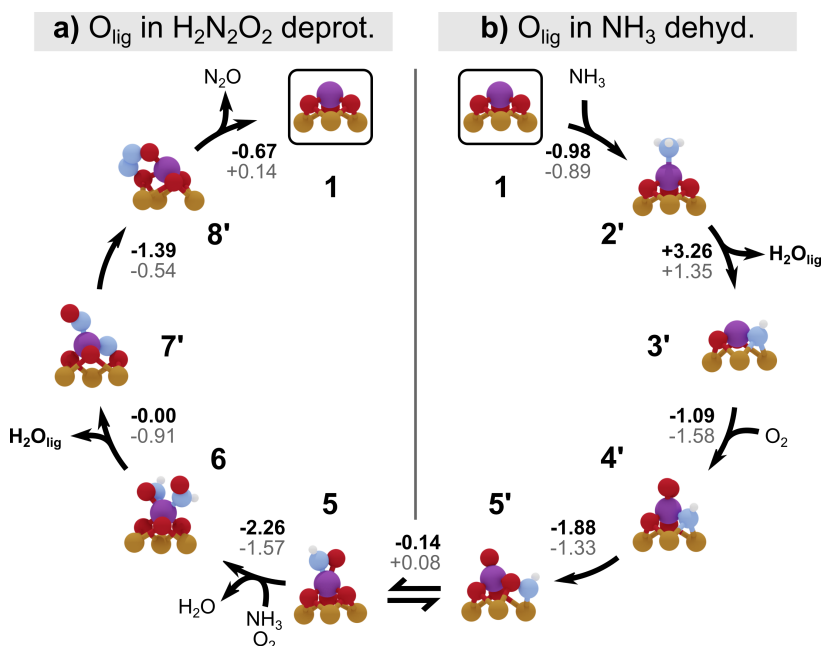
Figure 5.12: Possible deviations from the proposed reaction sequence of ammonia oxidation to N_2O on low-valent SA-Mn on ceria (111). **a)** Deprotonation of di-nitroxyl intermediate followed by elimination of H_2O_{lig} and formation of an ONNO ring intermediate. **b)** Primary adsorption of ammonia and dehydrogenation via lattice oxygen, followed by adsorption of gas-phase O_2 and isomerization to the nitroxyl intermediate.

Furthermore, I explored various acid-base equilibria at different steps of the reaction cycle, beginning with the formation of the nitroxyl intermediate (**4**). Overall, I considered proton transfer to the coordinating oxygen (O_{lig}), as well as distant lattice oxygen (O_{latt}), as shown in Fig. 5.13. Furthermore, I also investigated the elimination of water from either the di-nitroxyl (**6**) or the hyponitrous acid ring intermediate (**7**), again, under participation of either ligand or lattice oxygen. For intermediate **4**, proton transfer to a

Chapter 5.   Theory meets experiment

---

ligand oxygen is thermodynamically more accessible (0.15 eV), than transformation of the nitroxyl fragment to NO^- via the protonation of lattice oxygen (0.66 eV). Similarly, for the di-nitroxyl structure, elimination of H_2O_{lig} involving a ligand oxygen is thermoneutral (0.00 eV), while loss of a lattice oxygen is significantly endothermic (1.04 eV). This can be rationalized as in the former case the resulting NO^- fills the resulting vacancy, which is not possible in the latter case. The same applies for the hyponitrous acid-like intermediate (**7**), where elimination of H_2O_{lig} is highly exothermic (-2.26 eV), while the process is thermoneutral (0.08 eV) for H_2O_{latt}. In particular, in the former case, the fully deprotonated ONNO ring provides a structure from which elimination of N_2O perfectly restores the coordination sphere around the manganese SA (as mentioned above). Under *operando* conditions, all considered structures are likely present and involved in complex equilibria. Fully reproducing the catalytic performance would therefore require evaluation of the entire reaction network, including transition states, and coupling the results via a microkinetic model.
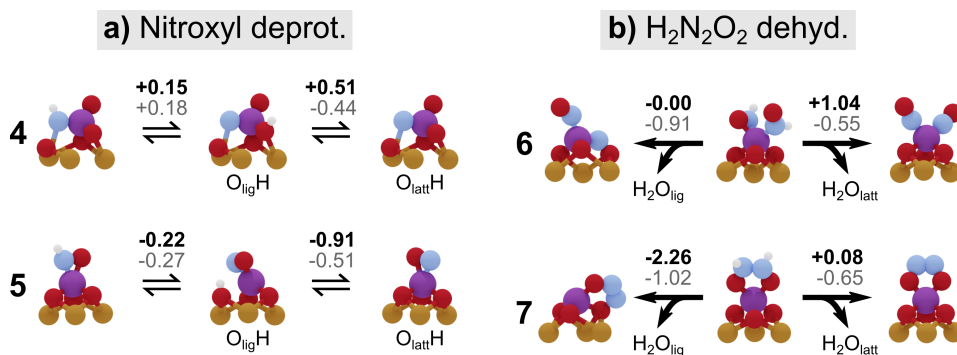
Figure 5.13: Possible acid-base equilibria between reaction intermediates and the ceria support on the (111)-based low-valent Mn-SAC. **a)** Possible proton transfer from the NH,O and nitroxyl intermediates to ligand and lattice oxygen. **b)** Possible proton transfer from the di-nitroxyl and hyponitrous acid-like intermediates to ligand (O_{lig}) and lattice oxygen (O_{latt}), leading to assumed elimination of H_2O_{lig} and H_2O_{latt}.

Lastly, as the ceria support likely also exposes small fractions of various other facets, I investigated the same mechanistic scheme obtained for the (111)-based catalyst, Fig. 5.11, for low-valent manganese anchored on the (110) and (100) surfaces (**1**), as shown in Fig. 5.14. Again, adsorption of O_2 is favorable [(110): -2.91 eV; (100): -3.47 eV] and presents the first step in the cycle (**2**). As the SA-metal is coordinated to only two surface oxygen in both structures, it can also bind ammonia in the next step (**3**). For the (100) [(110)]-based catalyst, the following NH_3 dehydrogenation is then

thermoneutral (exothermic by $-1.20\,\text{eV}$), and leads to an NH fragment that is coordinated to the metal, as well as cerium of the support in both cases (**4**). Next, rearrangement to form the nitroxyl intermediate (**5**) is thermodynamically uphill by $1.01\,\text{eV}$ ($0.81\,\text{eV}$) on (110) [(100)], thus presenting the most challenging step in the reaction sequence. This is in accordance with the reaction on (111), where the equivalent step has an energy cost of $0.94\,\text{eV}$. Formation of a second nitroxyl (**6**) is again driven by elimination of water, and followed by the formation of the hyponitrous acid-like intermediate (**7**), from which N_2O ((110): $0.71\,\text{eV}$; (100): $0.67\,\text{eV}$) and water [(110): $-0.34\,\text{eV}$; (100): $0.45\,\text{eV}$] are released (**8**) to close the catalytic cycle. Thus, the feasibility of the proposed reaction sequence obtained on all ceria low-index facets points to the inherent capability of low-valent SA-Mn to facilitate the oxidation of ammonia to nitrous oxide.
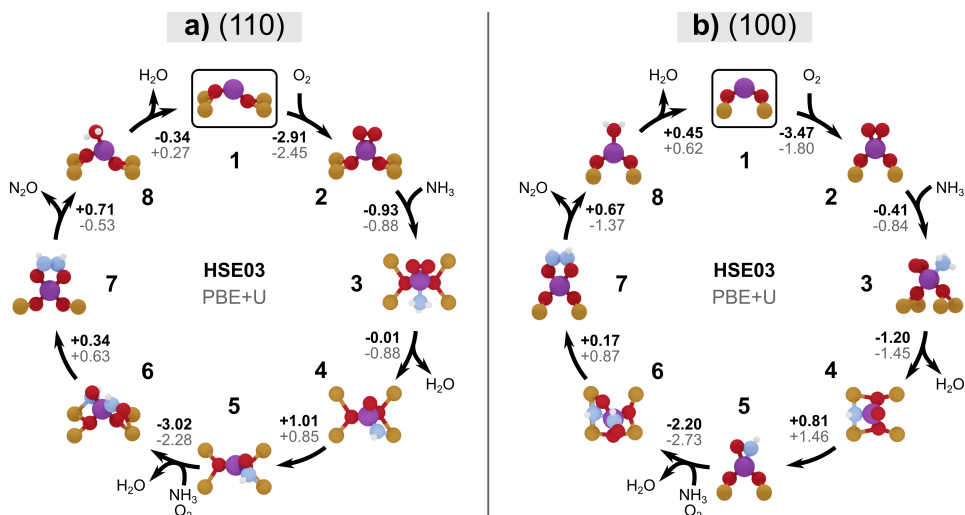
Figure 5.14: Investigation of the proposed reaction scheme of ammonia oxidation to nitrous oxide via the key steps of NH_3 dehydrogenation, and the formation of the nitroxyl and hyponitrous acid-like ring intermediates on low-valent manganese stabilized on ceria (110) and (100) facets.

To recapitulate, the key steps for obtaining a high-performing catalyst for ammonia oxidation to N_2O are i) the activation of oxygen, either from the gas phase or from the lattice, providing a sufficient concentration of reactive oxygen species for the dehydrogenation of ammonia and the oxidation of NH-fragments, and ii) the stabilization of the hyponitrous acid-like ring intermediate, facilitating N–N-bond formation. On oxidized and coordinatively saturated manganese, such as the Mn-4O motif obtained on restructured (100) and (110), the SA metal can neither sufficiently activate

Chapter 5.   Theory meets experiment

oxygen, nor bind the reactants, or form the required ring intermediates. On the other hand, as shown above, on ceria-based low-valent SA-Mn, all steps are facilitated, yielding a catalyst with unprecedented activity and selectivity.

Chapter 6

Conclusions and outlook

In this thesis, I discussed four of my works on ceria-based single-atom catalysts. Each treated different aspects of these chemically, structurally, and electronically highly complex and dynamic systems:

- In **Chapter 3**, I investigated the nature of dynamic electron transfer for ceria-based single-atom catalysts (SACs) via DFT. For the common $Pt_1/CeO_2(100)$ system, I showed that ceria reduction, modelled by introducing a surface vacancy, significantly increases the number of electronic states in the electronic ensembles. In addition to the higher number of localized polarons, this is also due to symmetry lowering. For the reduced surface, the distribution of electronic states further shifts towards lower platinum oxidation states, Pt^0/Pt^+, at the expense of Pt^{2+}, with low-energy states becoming inaccessible for the latter species. Consequently, at finite temperature (modelled via molecular dynamics simulations at $600\,K$), the ratio of total lifetimes of Pt^+ vs. Pt^{2+} shifts from 1:1 for the nondefective support, to about 7:1 for the reduced one. To further evaluate if oxidation state dynamics is an effect exclusive to platinum, I constructed models of SACs for the other group 9–11 metals, accounting for the common ceria low-index surfaces. I first investigated the question of general stability, showing that only local (100) facets, particularly in the square planar 4O reconstruction, can stabilize a wide range of different metals. I then sampled local polaron distributions to explore the electronic ensembles that comprise each system. Here, I could show that overlapping ensembles at different oxidation states, the main prerequisite for dynamic electron transfer, is present for various metals in different coordination environments, thus proving the ubiquity of the effect for ceria-based catalysts. Lastly, I again validated the results obtained by static DFT simulations via molecular dynamics, proving

Chapter 6.   Conclusions and outlook

the correspondence the two computational approaches. Importantly, the ground state structure of the static picture presents the majority state in the dynamic picture, and the directions, frequencies, and lifetimes of deviations from the ground state closely follow the energy distributions obtained through the sampling of the localized polaron distributions.

- In **Chapter 4**, I then used the previously obtained wealth of data on the energetics of local polaron distributions to construct predictive and physically insightful machine learning models. As a first step, suitable features to capture the physical interactions between the metal atoms and the support had to be constructed. The final primary feature space comprises atomic properties of the isolated metal atoms and in the given coordination environment, as well as geometric descriptors of the local polaron structure of the ceria support. Importantly, none of the features requires explicit prior evaluation with DFT, but can be looked up from literature or derived from the initial structure. Obtaining suitable descriptors for such an inhomogeneous dataset, however, brought various challenges, such as the need for the absence of empty data entries throughout. Among other methods, I could overcome these challenges by using reasonable default values and generating statistical descriptors. Then, I constructed predictive models based on the elastic net and random forest algorithms that can estimate the DFT energies. In addition to their good predictive capabilities, these models further enabled the identification of the main physical properties that are required to reproduce the energy spectra. A reduced subset of representative features could then be used in the Bayesian machine scientist symbolic regressor to obtain a closed-form mathematical formula that approximates the data. The work shows how machine learning can be used to circumvent the need for expensive ab initio simulations and augment the physical insight obtained.

- For the two projects presented in **Chapter 5**, I worked in collaboration with experimental colleagues to elucidate the origin of the high ability of oxygen plasma pretreated ceria to stabilize single-atom platinum, and to rationalize the exceptional performance of a manganese single-atom catalyst in ammonia oxidation to nitrous oxide via DFT simulations. In the first project, I could assign a previously unknown peak in the XPS spectrum of the as-prepared platinum catalyst to peroxide species. By further evaluating the effect of peroxide on the adsorption of platinum, I constructed plausible mechanisms how their presence can increase the amount of metal that can be deposited agglomeration occurs. For the Mn_1/CeO_2 catalyst of the second project,

a library of possible structures was constructed, and representative models in agreement with experiments could be identified. For various structural models, the reactivity landscape of ammonia oxidation to nitrous oxide was then explored. This could prove the crucial role of low-valent manganese in activating oxygen, either from gas phase, or the ceria lattice, necessary for the dehydrogenation of ammonia and the oxidation of nitrogen-containing fragments. It could also be shown that low-valent manganese can bind multiple such fragments and facilitate their dimerization to form a hyponitrous acid-like ring intermediate, form which the product can be evolved. A thermodynamically feasible reaction sequence could be constructed, in line with prior literature. The obtained results on the important role of low-valent manganese for the observed catalytic performance is in agreement with the available experimental data. Both projects showcase the power of the combination of computational modelling and experimentation in the field of heterogeneous catalysis.

This thesis has investigated in depth the atomic and electronic structure of ceria-based single-atom catalysts, in particular, dynamic electron transfer processes enabled by the reducible nature of the ceria support. In addition, it shows how data-driven machine learning based on computational modeling can be used to obtain accurate predictive models from which additional physical insight can be derived. Lastly, I have shown how computational modelling is invaluable to elucidate experimentally difficult or inaccessible catalyst properties. The above being said, however, there always remains work to be done, so in that spirit, I will outline few shortcomings of the presented works and provide prospective future improvements.

As discussed extensively in Section 2.4.3, the sampling of local polaron distributions is not fully complete, especially considering that mOS values up to four have been obtained. To realize a complete sampling in such cases, the use of more sophisticated tools, such as `icet`[186] or `disorder`[187,188] would be necessary, rather than the in-house scripts that were used at the time. These tools are specifically geared towards exploring configuration spaces for which a brute force approach would require the consideration of exceedingly large numbers of structures, and therefore become completely unfeasible (e.g. site-occupancy configurations of disordered structures — exceeding 10^9 in number). Thus, more advanced computational protocols could achieve a more complete sampling of polaron structures, to answer the question of oxidation state dynamicity, however, I do not deem this strictly necessary.

In addition, the inherent electronic complexity and structural variability (originating from the localized polarons) of ceria-based systems, such as the

127

Chapter 6. Conclusions and outlook

ones treated in this work, make the thorough consideration of local polaron distributions during exploration of reactivity impracticable. Thus, it could not be taken into account in depth in the collaborations with experimental colleagues, however, practical experience shows that obtained structures are typically not far from the true ground state. Moreover, the dependence of the Hubbard U-correction on the oxidation states of the considered species makes the evaluation of reaction energies with this methodology difficult. Re-evaluation with the HSE03–13 hybrid functional was applied for the study of the Mn_1/CeO_2 catalyst based on the PBE+U optimized structures, however, the desirable full structural optimization with hybrid functionals currently remains computationally inaccessible for systems of the given size.

Lastly, as evident from the predictions of the Elastic Net and Random Forest models shown in Fig. 4.6, horizontal clusters of points remain. This means that qualitatively different structures that lead to different DFT energies, could not be distinguished by the models, hinting at the fact that there remains some incompleteness in the feature space. One possible approach to tackle this problem could be via the introduction of machine learning at an earlier stage, such as in the description of the geometric structure of the local polaron distributions, as was done for example by Birschitzky, Franchini and coworkers[219].

The majority of the shortcomings and possible improvements outlined in this section originate from the unfortunate fact that our methods are just not efficient, and our computers just not powerful enough to treat systems exceeding a certain size. Feats like the computational treatment of large proteins or nanosecond molecular dynamics simulations with ab initio methods currently still remain a prospect of the future. Thus, it is the distinguished feature of the computational scientist to identify the crucial characteristics of the section of the cosmos he is trying to describe, and construct models that accurately represent reality for the given purpose.

Chapter 7

Appendix

Chapter 7. Appendix

Table 7.1: Full pool of considered primary features, to construct data-driven ML models for the interaction of group 9–11 SAs with the $CeO_2(100)$ support.

Set	Symbol	Description	Range	Unit	Ref.
	Z	Atomic number	27 − 79	-	PSE
	χ	Pauling electronegativity	1.88 − 2.54	-	220
	EA	Electron affinity	0.56 − 2.31	eV	220
	Φ_{el}	Chemical potential of the electrons in the metal	1.39 − 1.83	eV	220
	HOMO	HOMO of the isolated metal atom from DFT	-6.11 − -4.10	eV	220
	LUMO	LUMO of the isolated metal atom from DFT	-5.54 − -3.41	eV	220
	gap	HOMO-LUMO gap of the isolated metal atom	0.00 − 0.85	eV	220
1	p	Polarizability of the metal atom	26.14 − 66.00	a.u.	236
	r_p	p-orbital radius (as given by Zunger *et al.*)	1.10 − 1.47	Å	220
	r_{cov}	Empirical covalent radius	1.21 − 1.53	Å	223 pp. (9)-57
	$\Delta G^{M\text{-}O}_{mol}$	Diatomic M-O bond dissociation enthalpy	2.29 − 4.32	eV	223 pp. (9)-73
	$\Delta G^{M\text{-}O}_{bulk}$	Single M-O bond formation enthalpy derived from most stable oxide	-0.57 − -0.02	eV	223 pp. (5)-3
	$\Delta G^{M\text{-}M}_{mol}$	Metal-metal bond dissociation energy	1.32 − 3.75	eV	223 pp. (9)-73
	E_{coh}	Cohesive energy of the bulk metal	2.95 − 6.94	eV	237 p. 50
	No	Coordination number of the metal atom	2 − 4	-	†
2	mOS	Oxidation state of the metal atom	0 − 4	-	†
	IP	Cumulative ionization energy required for $M^0 \rightarrow M^{N+}$	0.00 − 51.20	eV	220
	c_{ONN}	Mean number of oxygen atoms bound to separated Ce^{3+} centers	0.00 − 3.00	-	†
	c_{OB}	Mean number of oxygen atoms bridging Ce^{3+} centers	0.00 − 1.00	-	†
	ϵ	Total mean number of oxygen atoms bound to Ce^{3+}	0.00 − 3.00	-	†
	$d_{M\text{-}Ce3}$	Mean of inverse metal-Ce^{3+} bond lengths	0.33 − 1.41	Å^{-1}	†
3	$\sum d_{M\text{-}Ce3}$	Sum of inverse metal-Ce^{3+} bond lengths	1.33 − 5.66	Å^{-1}	†
	$\delta d_{M\text{-}Ce3}$	Standard deviation of inverse metal-Ce^{3+} bond lengths	0.00 − 0.67	Å^{-1}	†
	$\min(d_{M\text{-}Ce3})$	Minimum of inverse metal-Ce^{3+} bond lengths	0.33 − 1.41	Å^{-1}	†
	$\max(d_{M\text{-}Ce3})$	Maximum of inverse metal-Ce^{3+} bond lengths	0.33 − 1.41	Å^{-1}	†
	$d_{Ce3\text{-}Ce3}$	Mean of inverse Ce^{3+}-Ce^{3+} bond lengths	0.33 − 1.00	Å^{-1}	†
	$\sum d_{Ce3\text{-}Ce3}$	Sum of inverse Ce^{3+}-Ce^{3+} bond lengths	2.00 − 5.41	Å^{-1}	†
	$\delta d_{Ce3\text{-}Ce3}$	Standard deviation of inverse Ce^{3+}-Ce^{3+} bond lengths	0.00 − 0.17	Å^{-1}	†

† Geometric properties obtained from each respective SAC structure during the sampling.

Table 7.2: Performances of the EN and RF models during Sequential Feature Selection (SFS), evaluated via K-Fold Cross-Validation (KF) and Leave-One-Group-Out Cross-Validation (LO), up to the inclusion of eight primary features.

Model	Feature	R^2	RMSE / eV	MAE / eV
EN (KF)	r_p	0.424 ± 0.001	0.507 ± 0.018	0.437 ± 0.017
	r_cov	0.614 ± 0.001	0.416 ± 0.012	0.339 ± 0.010
	N_O	0.816 ± 0.001	0.292 ± 0.008	0.231 ± 0.009
	EA	0.868 ± 0.001	0.247 ± 0.007	0.194 ± 0.007
	$d_\mathrm{Ce3\text{-}Ce3}$	0.887 ± 0.001	0.229 ± 0.012	0.181 ± 0.013
	ϵ_OB	0.898 ± 0.000	0.220 ± 0.012	0.171 ± 0.013
	$\sum d_\mathrm{M\text{-}Ce3}$	0.913 ± 0.001	0.204 ± 0.008	0.154 ± 0.006
EN (LO)	Z	0.410 ± 0.009	0.538 ± 0.080	0.451 ± 0.080
	r_cov	0.605 ± 0.009	0.452 ± 0.158	0.380 ± 0.143
	N_O	0.837 ± 0.009	0.346 ± 0.110	0.278 ± 0.094
	Φ_{el}	0.874 ± 0.004	0.291 ± 0.061	0.235 ± 0.057
	$d_\mathrm{Ce3\text{-}Ce3}$	0.888 ± 0.008	0.280 ± 0.071	0.225 ± 0.057
	$LUMO$	0.893 ± 0.009	0.267 ± 0.053	0.219 ± 0.043
	$\min(d_\mathrm{M\text{-}Ce3})$	0.899 ± 0.008	0.264 ± 0.057	0.216 ± 0.046
RF (KF)	IP	0.672 ± 0.001	0.393 ± 0.013	0.316 ± 0.012
	N_O	0.915 ± 0.002	0.213 ± 0.026	0.156 ± 0.012
	$\Delta G_\mathrm{mol}^\mathrm{M\text{-}O}$	0.928 ± 0.001	0.193 ± 0.010	0.146 ± 0.008
	ϵ_OB	0.944 ± 0.001	0.184 ± 0.004	0.134 ± 0.008
	$d_\mathrm{M\text{-}Ce3}$	0.961 ± 0.001	0.168 ± 0.007	0.119 ± 0.007
	$HOMO$	0.964 ± 0.001	0.161 ± 0.010	0.114 ± 0.010
	$LUMO$	0.963 ± 0.001	0.162 ± 0.012	0.116 ± 0.011
	ϵ	0.965 ± 0.001	0.159 ± 0.011	0.113 ± 0.010
RF (LO)	Z	0.556 ± 0.008	0.500 ± 0.072	0.435 ± 0.081
	$HOMO$	0.564 ± 0.009	0.462 ± 0.089	0.387 ± 0.087
	r_p	0.566 ± 0.010	0.454 ± 0.090	0.387 ± 0.093
	$\delta d_\mathrm{Ce3\text{-}Ce3}$	0.624 ± 0.022	0.454 ± 0.099	0.382 ± 0.099
	EA	0.625 ± 0.020	0.453 ± 0.085	0.390 ± 0.089
	$\max(d_\mathrm{M\text{-}Ce3})$	0.640 ± 0.019	0.458 ± 0.080	0.392 ± 0.085
	ϵ_OB	0.660 ± 0.022	0.458 ± 0.092	0.397 ± 0.097
	r_cov	0.660 ± 0.023	0.464 ± 0.093	0.397 ± 0.101

Chapter 7. Appendix

Table 7.3: Fitting constants used in the two BMS equations.

Term	c_1	c_2	c_3	c_4	c_5	c_6
$E_{\text{BMS}}^{\text{M}}$	$-1.06 \cdot 10^{-3}$	-5.52	0.27	$-1.26 \cdot 10^3$	0.61	$4.32 \cdot 10^6$
$E_{\text{BMS}}^{\text{Ox}}$	-27.01	0.29	$-$	$-$	$-$	$-$

Bibliography

(1) Global climate strike. *Nature Catalysis* **2019**, *2*, 831–831.

(2) How chemistry is helping to improve the environment around us `https://www.rsc.org/policy-evidence-campaigns/environmental-sustainability/global-challenges/environment/` (accessed 08/30/2023).

(3) NASA Effects — Facts – Climate Change: Vital Signs of the Planet `https://climate.nasa.gov/effects/` (accessed 08/09/2023).

(4) Effects of Climate Change - Impacts and Examples `https://www.nrdc.org/stories/what-are-effects-climate-change\#animals` (accessed 08/09/2023).

(5) How humans are driving the sixth mass extinction — Conservation — The Guardian `https://www.theguardian.com/environment/radical-conservation/2015/oct/20/the-four-horsemen-of-the-sixth-mass-extinction` (accessed 08/09/2023).

(6) What is the sixth mass extinction and what can we do about it? — Stories — WWF `https://www.worldwildlife.org/stories/what-is-the-sixth-mass-extinction-and-what-can-we-do-about-it` (accessed 08/09/2023).

(7) Castillo, M. The Scientific Method: A Need for Something Better? *Am. J. Neuroradiol.* **2013**, *34*, 1669–1671.

(8) Holt-Giménez, E. et al. We Already Grow Enough Food for 10 Billion People ... and Still Can't End Hunger. *J. Sustain. Agric.* **2012**, *36*, 595–598.

(9) Scholtz, S. et al. In *Curiosities in Medicine: Alphabetically*; Springer International Publishing: Cham, 2023, pp 181–184.

(10) Hertz's useless discovery — IOPSpark `https://spark.iop.org/hertzs-useless-discovery` (accessed 08/09/2023).

(11) Tan, S. Y.; Tatsumura, Y. Alexander Fleming (1881–1955): discoverer of penicillin. *Singapore Med. J.* **2015**, *56*, 366.

Bibliography

(12) Alexander Fleming and discovery of penicillin. How many lifes has penicillin saved? `http://www.bacteriainphotos.com/Alexander\_Fleming\_and\_penicillin.html` (accessed 08/09/2023).

(13) What are the safest and cleanest sources of energy? - Our World in Data `https://ourworldindata.org/safest-sources-of-energy` (accessed 08/09/2023).

(14) Rothenberg, G., *Catalysis: concepts and green applications*; John Wiley & Sons: 2017.

(15) Hülsey, M. J.; Lim, C. W.; Yan, N. Promoting heterogeneous catalysis beyond catalyst design. *Chem. Sci.* **2020**, *11*, 1456–1468.

(16) Sheldon, R. A.; Bode, M. L.; Akakios, S. G. Metrics of green chemistry: Waste minimization. *Curr. Opin. Green Sustain. Chem.* **2022**, *33*, 100569.

(17) Hannagan, R. T. et al. Single-Atom Alloy Catalysis. *Chem. Rev.* **2020**, *120*, 12044–12088.

(18) Qu, W. et al. Progress in metal-organic-framework-based single-atom catalysts for environmental remediation. *Coord. Chem. Rev.* **2023**, *474*, 214855.

(19) Kaiser, S. K. et al. Single-Atom Catalysts across the Periodic Table. *Chem. Rev.* **2020**, *120*, 11703–11809.

(20) Lang, R. et al. Single-Atom Catalysts Based on the Metal-Oxide Interaction. *Chem. Rev.* **2020**, *120*, 11986–12043.

(21) Asakura, K. et al. Structure and catalytic combustion activity of atomically dispersed Pt species at MgO surface. *Appl. Catal., A* **1999**, *188*, 313–324.

(22) Fu, Q.; Saltsburg, H.; Flytzani-Stephanopoulos, M. Active nonmetallic Au and Pt species on ceria-based water-gas shift catalysts. *Science* **2003**, *301*, 935–938.

(23) Single-atom catalysis of CO oxidation using Pt_1/FeO_x.

(24) Liu, L.; Corma, A. Metal Catalysts for Heterogeneous Catalysis: From Single Atoms to Nanoclusters and Nanoparticles. *Chem. Rev.* **2018**, *118*, 4981–5079.

(25) Wang, A.; Li, J.; Zhang, T. Heterogeneous single-atom catalysis. *Nat. Rev. Chem.* **2018**, *2*, 65–81.

(26) Zhang, L. et al. Single-atom catalyst: a rising star for green synthesis of fine chemicals. *Natl. Sci. Rev.* **2018**, *5*, 653–672.

UNIVERSITAT ROVIRA I VIRGILI
CERIA-BASED SINGLE-ATOM CATALYSTS: FROM SIMPLIFIED MODELS TOWARDS REAL-WORLD COMPLEXITY
Julian Geiger

Bibliography

(27) Zhang, T. Single-Atom Catalysis: Far beyond the Matter of Metal Dispersion. *Nano Lett.* **2021**, *21*, 9835–9837.

(28) Mitchell, S.; Pérez-Ramírez, J. Single atom catalysis: a decade of stunning progress and the promise for a bright future. *Nat. Commun.* **2020**, *11*, 10–12.

(29) Datye, A. K.; Guo, H. Single atom catalysis poised to transition from an academic curiosity to an industrially relevant technology. *Nat. Commun.* **2021**, *12*, 895.

(30) Zang, W. et al. Heterogeneous Single Atom Electrocatalysis, Where "Singles" Are "Married". *Adv. Energy Mater.* **2020**, *10*, 1903181.

(31) Guo, J. et al. A minireview on the synthesis of single atom catalysts. *RSC Adv.* **2022**, *12*, 9373–9394.

(32) Frei, M. S. et al. Atomic-scale engineering of indium oxide promotion by palladium for methanol production via CO_2 hydrogenation. *Nat. Commun.* **2019**, *10*, 1–11.

(33) Zhou, Y. et al. Multilayer stabilization for fabricating high-loading single-atom catalysts. *Nat. Commun.* **2020**, *11*, 1–11.

(34) Hai, X. et al. Scalable two-step annealing method for preparing ultra-high-density single-atom catalyst libraries. *Nat. Nanotechnol.* **2022**, *17*, 174–181.

(35) Tauster, S. J.; Fung, S. C.; Garten, R. L. Strong metal-support interactions. Group 8 noble metals supported on titanium dioxide. *J. Am. Chem. Soc.* **1978**, *100*, 170–175.

(36) Tauster, S. J. Strong metal-support interactions. *Acc. Chem. Res.* **1987**, *20*, 389–394.

(37) Campbell, C. T. Catalyst-support interactions: Electronic perturbations. *Nat. Chem* **2012**, *4*, 597–598.

(38) Farmer, J. A.; Campbell, C. T. Ceria maintains smaller metal catalyst particles by strong metal-support bonding. *Science* **2010**, *329*, 933–936.

(39) Bruix, A. et al. A New Type of Strong Metal-Support Interaction and the Production of H_2 through the Transformation of Water on $Pt/CeO_2(111)$ and $Pt/CeO_x/TiO_2(110)$ Catalysts. *J. Am. Chem. Soc.* **2012**, *134*, 8968–8974.

(40) Dvořák, F. et al. Creating single-atom Pt-ceria catalysts by surface step decoration. *Nat. Commun.* **2016**, *7*, 10801.

(41) Jones, J. et al. Thermally stable single-atom platinum-on-ceria catalysts via atom trapping. *Science* **2016**, *353*, 150–154.

Bibliography

(42) Neitzel, A. et al. Atomically Dispersed Pd, Ni, and Pt Species in Ceria-Based Catalysts: Principal Differences in Stability and Reactivity. *J. Phys. Chem. C* **2016**, *120*, 9852–9862.

(43) Wan, W. et al. Highly Stable and Reactive Platinum Single Atoms on Oxygen Plasma-Functionalized CeO_2 Surfaces: Nanostructuring and Peroxo Effects. *Angew. Chem. Int. Ed.* **2022**, *61*, e202112640.

(44) Qiao, B. et al. Highly Efficient Catalysis of Preferential Oxidation of CO in H_2-Rich Stream by Gold Single-Atom Catalysts. *ACS Catal.* **2015**, *5*, 6249–6254.

(45) Yu, W.-Z. et al. Construction of Active Site in a Sintered Copper–Ceria Nanorod Catalyst. *J. Am. Chem. Soc.* **2019**, *141*, 17548–17557.

(46) Khivantsev, K. et al. Economizing on Precious Metals in Three-Way Catalysts: Thermally Stable and Highly Active Single-Atom Rhodium on Ceria for NO Abatement under Dry and Industrially Relevant Conditions. *Angew. Chem. Int. Ed.* **2021**, *60*, 391–398.

(47) Surin, I. et al. Low-Valent Manganese Atoms Stabilized on Ceria for Nitrous Oxide Synthesis. *Adv. Mater* **2023**, *35*, e2211260.

(48) Crewe, A. V.; Wall, J.; Langmore, J. Visibility of Single Atoms. *Science* **1970**, *168*, 1338–1340.

(49) Liu, J. Aberration-corrected scanning transmission electron microscopy in single-atom catalysis: Probing the catalytically active centers. *Chinese J. Catal.* **2017**, *38*, 1460–1472.

(50) Song, Z. et al. Emerging Applications of Synchrotron Radiation X-Ray Techniques in Single Atomic Catalysts. *Small Methods* **2022**, *6*, 2201078.

(51) Baumann, S. et al. Electron paramagnetic resonance of individual atoms on a surface. *Science* **2015**, *350*, 417–420.

(52) Tang, Z. et al. Ceria-Supported Gold Nanoparticles as a Superior Catalyst for Nitrous Oxide Production via Ammonia Oxidation. *Angew. Chem. Int. Ed.* **2022**, *61*, e202200772.

(53) Hulva, J. et al. Unraveling CO adsorption on model single-atom catalysts. *Science* **2021**, *371*, 375–379.

(54) Freund, H.-J. et al. Bridging the pressure and materials gaps between catalysis and surface science: clean and modified oxide surfaces. *Top. Catal.* **2001**, *15*, 201–209.

(55)   Wang, Y. G. et al. Dynamic formation of single-atom catalytic active sites on ceria-supported gold nanoparticles. *Nat. Commun.* **2015**, *6*, 1–8.

(56)   Zhang, Z.; Zandkarimi, B.; Alexandrova, A. N. Ensembles of Metastable States Govern Heterogeneous Catalysis on Dynamic Interfaces. *Acc. Chem. Res.* **2020**, *53*, 447–458.

(57)   Muravev, V. et al. Interface dynamics of Pd–CeO$_2$ single-atom catalysts during CO oxidation. *Nat. Catal.* **2021**, *4*, 469–478.

(58)   Li, Y. et al. Dynamic structure of active sites in ceria-supported Pt catalysts for the water gas shift reaction. *Nat. Commun.* **2021**, *12*, 914.

(59)   Li, X. et al. In Situ/Operando Techniques for Characterization of Single-Atom Catalysts. *ACS Catal.* **2019**, *9*, 2521–2531.

(60)   Hülsey, M. J. et al. In situ spectroscopy-guided engineering of rhodium single-atom catalysts for CO oxidation. *Nat. Commun.* **2019**, *10*.

(61)   Sarma, B. B. et al. Design of Single-Atom Catalysts and Tracking Their Fate Using Operando and Advanced X-ray Spectroscopic Tools. *Chem. Rev.* **2022**, *123*, 379–444.

(62)   Chen, B. W. J.; Xu, L.; Mavrikakis, M. Computational Methods in Heterogeneous Catalysis. *Chem. Rev.* **2021**, *121*, 1007–1048.

(63)   Kraushofer, F.; Parkinson, G. S. Single-Atom Catalysis: Insights from Model Systems. *Chem. Rev.* **2022**, *122*, 14911–14939.

(64)   Lykhach, Y. et al. Counting electrons on supported nanoparticles. *Nat. Mater.* **2016**, *15*, 284–288.

(65)   Lykhach, Y. et al. Oxide-based nanomaterials for fuel cell catalysis: the interplay between supported single Pt atoms and particles. *Catal. Sci. Technol.* **2017**, *7*, 4315–4345.

(66)   Bruix, A. et al. Maximum Noble-Metal Efficiency in Catalytic Materials: Atomically Dispersed Surface Platinum. *Angew. Chem. Int. Ed.* **2014**, *53*, 10525–10530.

(67)   Capdevila-Cortada, M.; López, N. Entropic contributions enhance polarity compensation for CeO$_2$(100) surfaces. *Nat. Mater.* **2017**, *16*, 328–334.

(68)   Daelman, N.; Capdevila-Cortada, M.; López, N. Dynamic charge and oxidation state of Pt/CeO$_2$ single-atom catalysts. *Nat. Mater.* **2019**, *18*, 1215–1221.

(69)   Greeley, J. et al. Alloys of platinum and early transition metals as oxygen reduction electrocatalysts. *Nat. Chem.* **2009**, *1*, 552–556.

Bibliography

---

(70)   Bligaard, T. et al. The Brønsted–Evans–Polanyi relation and the volcano curve in heterogeneous catalysis. *J. Catal.* **2004**, *224*, 206–217.

(71)   Anand, M. et al. Scaling Relationships and Volcano Plots in Homogeneous Catalysis. *J. Phys. Chem. Lett.* **2020**, *11*, 8518–8526.

(72)   Sabatier, P La catalyse en chimie organique, Librairie Polytechnique, 1913.

(73)   Ooka, H.; Huang, J.; Exner, K. S. The Sabatier Principle in Electrocatalysis: Basics, Limitations, and Extensions. *Front. Energy Res.* **2021**, *9*, 654460.

(74)   Pérez-Ramírez, J.; López, N. Strategies to break linear scaling relationships. *Nat. Catal.* **2019**, *2*, 971–976.

(75)   Curtarolo, S. et al. The high-throughput highway to computational materials design. *Nat. Mater.* **2013**, *12*, 191–201.

(76)   Curtarolo, S. et al. AFLOWLIB.ORG: A distributed materials properties repository from high-throughput ab initio calculations. *Comput. Mat. Sci.* **2012**, *58*, 227–235.

(77)   Mounet, N. et al. Two-dimensional materials from high-throughput computational exfoliation of experimentally known compounds. *Nat. Nanotechnol.* **2018**, *13*, 246–252.

(78)   Kirklin, S. et al. The Open Quantum Materials Database (OQMD): assessing the accuracy of DFT formation energies. *npj Comput. Mater.* **2015**, *1*, 15010.

(79)   Hegde, V. I. et al. The phase stability network of all inorganic materials. *Sci. Adv.* **2020**, *6*, eaay5606.

(80)   Keith, J. A. et al. Combining Machine Learning and Computational Chemistry for Predictive Insights Into Chemical Systems. *Chem. Rev.* **2021**, *121*, 9816–9872.

(81)   Goh, G. B.; Hodas, N. O.; Vishnu, A. Deep learning for computational chemistry. *J. Comp. Chem.* **2017**, *38*, 1291–1307.

(82)   Butler, K. T. et al. Machine learning for molecular and materials science. *Nature* **2018**, *559*, 547–555.

(83)   Schleder, G. R. et al. From DFT to machine learning: Recent approaches to materials science - A review. **2019**, *2*, 032001.

(84)   Kulik, H. J. et al. Roadmap on Machine learning in electronic structure. *Electron. Struc.* **2022**, *4*, 023004.

UNIVERSITAT ROVIRA I VIRGILI
CERIA-BASED SINGLE-ATOM CATALYSTS: FROM SIMPLIFIED MODELS TOWARDS REAL-WORLD COMPLEXITY
Julian Geiger

Bibliography

(85) Tshitoyan, V. et al. Unsupervised word embeddings capture latent knowledge from materials science literature. *Nature* **2019**, *571*, 95–98.

(86) Jha, D. et al. ElemNet: Deep Learning the Chemistry of Materials From Only Elemental Composition. *Sci. Rep.* **2018**, *8*, 17593.

(87) Wang, Z. et al. Data-Driven Materials Innovation and Applications. *Adv. Mater* **2022**, *34*, 2104113.

(88) Behler, J. Four Generations of High-Dimensional Neural Network Potentials. *Chem. Rev.* **2021**, *121*, 10037–10072.

(89) Unke, O. T. et al. Machine Learning Force Fields. *Chem. Rev.* **2021**, *121*, 10142–10186.

(90) Supinski, B. R. d. et al. Billion atom molecular dynamics simulations of carbon at extreme conditions and experimental time and length scales. *Int. Conf. High Perform. Comput. Netw. Storage Anal.* **2021**, 1–12.

(91) Phuthi, M. K. et al. Accurate Surface and Finite Temperature Bulk Properties of Lithium Metal at Large Scales using Machine Learning Interaction Potentials. *arXiv* **2023**, DOI: `10.48550/arxiv.2305.06925`.

(92) Jia, W. et al. In *SC20: International conference for high performance computing, networking, storage and analysis*, 2020, pp 1–14.

(93) Musaelian, A. et al. Scaling the leading accuracy of deep equivariant models to biomolecular simulations of realistic size. *arXiv* **2023**, DOI: `10.48550/arxiv.2304.10061`.

(94) Stocker, S. et al. How robust are modern graph neural network potentials in long and hot molecular dynamics simulations? *Mach. Learn: Sci. Technol.* **2022**, *3*, 045010.

(95) Pablo-García, S. et al. Fast evaluation of the adsorption energy of organic molecules on metals via graph neural networks. *Nat. Comput. Sci.* **2023**, *3*, 433–442.

(96) Chanussot, L. et al. Open Catalyst 2020 (OC20) Dataset and Community Challenges. *ACS Catal.* **2021**, *11*, 6059–6072.

(97) Kirkpatrick, J. et al. Pushing the frontiers of density functionals by solving the fractional electron problem. *Science* **2021**, *374*, 1385–1389.

(98) Jumper, J. et al. Highly accurate protein structure prediction with AlphaFold. *Nature* **2021**, *596*, 583–589.

Bibliography

(99)   Vaswani, A. et al. Attention is all you need. *Adv. Neural Inf. Process.* **2017**, *30*.

(100)   OpenAI GPT-4 Technical Report. *arXiv* **2023**.

(101)   ChatGPT Is The Fastest Growing App In The History Of Web Applications `https://www.forbes.com/sites/cindygordon/2023/02/02/chatgpt-is-the-fastest-growing-ap-in-the-history-of-web-applications/` (accessed 08/17/2023).

(102)   Bubeck, S. et al. Sparks of Artificial General Intelligence: Early experiments with GPT-4. *arXiv* **2023**, DOI: `10.48550/arXiv.2303.12712`.

(103)   Chart: Productivity Soars, Wages Stagnate — Statista `https://www.statista.com/chart/23410/inequality-in-productivity-and-compensation/` (accessed 08/09/2023).

(104)   Sam Altman on X: "The costs of intelligence and energy are going to be on a path towards near-zero. We certainly won't get all the way there this decade, but by 2030, it will become clear that the AI revolution and renewable+nuclear energy are going to get us there." / X `https://twitter.com/sama/status/1436028668082462748` (accessed 08/17/2023).

(105)   OpenAI Unexpected $100 Trillion: Sam Altman's Vision & More `https://www.aibloggs.com/post/openai-unexpected-100-trillion` (accessed 08/14/2023).

(106)   Ramesh, A. et al. Zero-Shot Text-to-Image Generation. *arXiv* **2021**, DOI: `10.48550/arxiv.2102.12092`.

(107)   Rombach, R. et al. High-Resolution Image Synthesis with Latent Diffusion Models. *arXiv* **2021**, DOI: `10.48550/arxiv.2112.10752`.

(108)   Ramesh, A. et al. Hierarchical Text-Conditional Image Generation with CLIP Latents. *arXiv* **2022**, DOI: `10.48550/arxiv.2204.06125`.

(109)   Teale, A. M. et al. DFT exchange: sharing perspectives on the workhorse of quantum chemistry and materials science. *Phys. Chem. Chem. Phys.* **2022**, *24*, 28700–28781.

(110)   Schrödinger, E. Quantisierung als Eigenwertproblem. *Ann. Phys.* **1926**, *385*, 437–490.

(111)   Born, M.; Oppenheimer, R. Zur Quantentheorie der Molekeln. *Ann. Phys.* **1927**, *389*, 457–484.

(112)   Hohenberg, P.; Kohn, W. Inhomogeneous electron gas. *Phys. Rev.* **1964**, *136*, B864–B871.

(113)   Kohn, W.; Sham, L. J. Self-consistent equations including exchange and correlation effects. *Phys. Rev.* **1965**, *140*, A1133–A1138.

(114)   Wang, L. W. Divide-and-conquer quantum mechanical material simulations with exascale supercomputers. *Natl. Sci. Rev.* **2014**, *1*, 604–617.

(115)   Perdew, J. P. et al. Atoms, molecules, solids, and surfaces: Applications of the generalized gradient approximation for exchange and correlation. *Phys. Rev. B* **1992**, *46*, 6671–6687.

(116)   Perdew, J. P.; Burke, K.; Ernzerhof, M. Generalized gradient approximation made simple. *Phys. Rev. Lett.* **1996**, *77*, 3865–3868.

(117)   Heyd, J.; Scuseria, G. E.; Ernzerhof, M. Hybrid functionals based on a screened Coulomb potential. *The J. Chem. Phys.* **2003**, *118*, 8207–8215.

(118)   Heyd, J.; Scuseria, G. E. Efficient hybrid density functional calculations in solids: Assessment of the Heyd–Scuseria–Ernzerhof screened Coulomb hybrid functional. *The J. Chem. Phys.* **2004**, *121*, 1187–1192.

(119)   Krukau, A. V. et al. Influence of the exchange screening parameter on the performance of screened hybrid functionals. *The J. Chem. Phys.* **2006**, *125*, 224106.

(120)   Bengone, O. et al. Implementation of the projector augmented-wave LDA+U method: Application to the electronic structure of NiO. *Phys. Rev. B* **2000**, *62*, 16392–16401.

(121)   Hubbard, J Electron correlations in narrow energy bands. *Proc. Math. Phys. Eng. Sci.* **1963**, *276*, 238–257.

(122)   Capdevila-Cortada, M.; Łodziana, Z.; López, N. Performance of DFT+U approaches in the study of catalytic materials. *ACS Catal.* **2016**, *6*, 8370–8379.

(123)   Kulik, H. J. Perspective: Treating electron over-delocalization with the DFT+ U method. *The J. Chem. Phys.* **2015**, *142*, 240901.

(124)   Dudarev, S. L. et al. Electron-energy-loss spectra and the structural stability of nickel oxide: An LSDA+U study. *Phys. Rev. B* **1998**, *57*, 1505–1509.

(125)   Cococcioni, M.; de Gironcoli, S. Linear response approach to the calculation of the effective interaction parameters in the LDA + U method. *Phys. Rev. B* **2005**, *71*, 035105.

(126)   Bloch, F. Uber die Quantenmechanik der Elektronen in Kristallgittern. *Zeitschrift fur Physik* **1929**, *52*, 555–600.

Bibliography

---

(127)   Kittel, C., *Introduction to Solid State Physics*; John Wiley & Sons Inc: 2004, pp 313–314; 704 pp.

(128)   Cottenier, S. Density Functional Theory and the Family of (L)APW-methods: a step-by-step introduction. **2002-2013 (2nd edition)**.

(129)   Phillips, J. C.; Kleinman, L. New method for calculating wave functions in crystals and molecules. *Phys. Rev.* **1959**, *116*, 287–294.

(130)   Pseudopotential https://en.wikipedia.org/w/index.php?title=Pseudopotential&oldid=1148156981 (accessed 06/06/2023).

(131)   Kresse, G; Hafner, J Norm-conserving and ultrasoft pseudopotentials for first-row and transition elements. *J. Phys. Condens. Matter* **1994**, *6*, 8245.

(132)   Blöchl, P. E. Projector augmented-wave method. *Phys. Rev. B* **1994**, *50*, 17953–17979.

(133)   Joubert, D. From ultrasoft pseudopotentials to the projector augmented-wave method. *Phys. Rev. B - Condens. Matter Mater. Phys.* **1999**, *59*, 1758–1775.

(134)   Kresse, G.; Hafner, J. Ab initio molecular dynamics for liquid metals. *Phys. Rev. B* **1993**, *47*, 558–561.

(135)   Kresse, G.; Furthmüller, J. Efficiency of ab-initio total energy calculations for metals and semiconductors using a plane-wave basis set. *Comput. Mater. Sci.* **1996**, *6*, 15–50.

(136)   Kresse, G.; Furthmüller, J. Efficient iterative schemes for ab initio total-energy calculations using a plane-wave basis set. *Phys. Rev. B - Condens. Matter Mater. Phys.* **1996**, *54*, 11169–11186.

(137)   Himanen, L. et al. Data-Driven Materials Science: Status, Challenges, and Perspectives. **2019**, *6*.

(138)   Wang, H. et al. Scientific discovery in the age of artificial intelligence. *Nature* **2023**, *620*, 47–60.

(139)   Choudhary, K. et al. Recent advances and applications of deep learning methods in materials science. *npj Comput. Mater.* **2022**, *8*, 59.

(140)   Bernstein, N.; Csányi, G.; Deringer, V. L. De novo exploration and self-guided learning of potential-energy surfaces. **2019**, *5*, 1–9.

(141)   Bowman, J. M. et al. Δ-Machine Learned Potential Energy Surfaces and Force Fields. *J. Chem. Theory Comput.* **2023**, *19*, 1–17.

(142)   Unke, O. T.; Meuwly, M. Machine Learning Potential Energy Surfaces. *arXiv* **2019**, DOI: 10.48550/arxiv.1909.08027.

(143) Nagai, R.; Akashi, R.; Sugino, O. Completing density functional theory by machine learning hidden messages from molecules. *npj Comput. Mater.* **2020**, *6*, 43.

(144) Lan, J. et al. AdsorbML: Accelerating Adsorption Energy Calculations with Machine Learning. *arXiv* **2022**, DOI: `10.48550/arxiv.2211.16486`.

(145) Sorkun, M. C. et al. An artificial intelligence-aided virtual screening recipe for two-dimensional materials discovery. *npj Comput. Mater.* **2020**, *6*, 106.

(146) Gentile, F. et al. Artificial intelligence–enabled virtual screening of ultra-large chemical libraries with deep docking. *Nat. Protoc.* **2022**, *17*, 672–697.

(147) Hastie, T.; Tibshirani, R.; Friedman, J., *The Elements of Statistical Learning*; Springer New York: 2009.

(148) Guimerá, R. et al. A Bayesian machine scientist to aid in the solution of challenging scientific problems. *Sci. Adv.* **2020**, *6*, eaav6971.

(149) Fernández-Delgado, M. et al. Do we need hundreds of classifiers to solve real world classification problems? *J. Mach. Learn. Res.* **2014**, *15*, 3133–3181.

(150) Morris, V. N. et al. Lattice Constant Dependence on Particle Size for Ceria prepared from a Citrate Sol-Gel. *Journal of Physics: Conference Series* **2006**, *26*, 119.

(151) Abundance of elements in Earth's crust - Wikipedia `https://en.wikipedia.org/wiki/Abundance\_of\_elements\_in\_Earth\%27s\_crust` (accessed 08/19/2023).

(152) Trovarelli, A. et al. The utilization of ceria in industrial catalysis. *Catal. Today* **1999**, *50*, 353–367.

(153) Trovarelli, A. Catalytic Properties of Ceria and CeO_2-Containing Materials. *Catalysis Reviews* **1996**, *38*, 439–520.

(154) Trovarelli, A.; TROVARELLI, A., *Catalysis by Ceria and Related Materials*; Catalytic Science Series, 2002.

(155) Montini, T. et al. Fundamentals and Catalytic Applications of CeO_2-Based Materials. *Chem. Rev.* **2016**, *116*, 5987–6041.

(156) Rodriguez, J. A. et al. Activity of CeO_x and TiO_x Nanoparticles Grown on Au(111) in the Water-Gas Shift Reaction. *Science* **2007**, *318*, 1757–1760.

(157) Gorte, R. J. Ceria in catalysis: From automotive applications to the water–gas shift reaction. *AIChE Journal* **2010**, *56*, 1126–1135.

Bibliography

(158)   Amrute, A. P. et al. Performance, structure, and mechanism of CeO_2 in HCl oxidation to Cl2. *J. Catal.* **2012**, *286*, 287–297.

(159)   Capdevila-Cortada, M. et al. Reactivity descriptors for ceria in catalysis. *Appl. Catal.,B* **2016**, *197*, 299–312.

(160)   Liu, B. et al. Carbonate-mediated Mars-van Krevelen mechanism for CO oxidation on cobalt-doped ceria catalysts: facet-dependence and coordination-dependence. *Phys. Chem. Chem. Phys.* **2018**, *20*, 16045–16059.

(161)   Esch, F. et al. Electron Localization Determines Defect Formation on Ceria Substrates. *Science* **2005**, *309*, 752–755.

(162)   Murgida, G. E. et al. Ordering of oxygen vacancies and excess charge localization in bulk ceria: A DFT+U study. *Phys. Rev. B* **2014**, *90*, 115120.

(163)   Franchini, C. et al. Polarons in materials. *Nat. Rev. Mater.* **2021**, *6*, 560–586.

(164)   Plata, J. J.; Márquez, A. M.; Sanz, J. F. Electron mobility via polaron hopping in bulk ceria: A first-principles study. *J. Phys. Chem. C* **2013**, *117*, 14502–14509.

(165)   Mullins, D. R. The surface chemistry of cerium oxide. *Surf. Sci. Reports* **2015**, *70*, 42–85.

(166)   Geiger, J. et al. Data-driven models for ground and excited states for Single Atoms on Ceria. *npj Comput. Mater.* **2022**, *8*, 171.

(167)   Figueroba, A. et al. Towards stable single-atom catalysts: Strong binding of atomically dispersed transition metals on the surface of nanostructured ceria. *Catal. Sci. Technol.* **2016**, *6*, 6806–6813.

(168)   Zhang, D. et al. Oxygen-Vacancy Dynamics and Entanglement with Polaron Hopping at the Reduced $CeO_2(111)$ Surface. *Physical Review Letters* **2019**, *122*, 096101.

(169)   Pérez-Bailac, P.; Lustemberg, P. G.; Ganduglia-Pirovano, M. V. Facet-dependent stability of near-surface oxygen vacancies and excess charge localization at CeO_2 surfaces. *J. Phys. Condens. Matter* **2021**, *33*, 504003.

(170)   Daelman, N. et al. Quasi-degenerate states and their dynamics in oxygen deficient reducible metal oxides. *J. Chem. Phys.* **2020**, *152*, 050901.

(171)   Geiger, J.; López, N. Coupling Metal and Support Redox Terms in Single-Atom Catalysts. *J. Phys. Chem. C* **2022**, *126*, 13698–13704.

(172)   Blöchl, P. E. Projector augmented-wave method. *Phys. Rev. B* **1994**, *50*, 17953–17979.

(173)   Joubert, D. From ultrasoft pseudopotentials to the projector augmented-wave method. *Phys. Rev. B* **1999**, *59*, 1758–1775.

(174)   Fabris, S. et al. Taming multiple valency with density functionals: A case study of defective ceria. *Phys. Rev. B* **2005**, *71*, 041102.

(175)   Tang, W; Sanville, E; Henkelman, G A grid-based Bader analysis algorithm without lattice bias. *J. Phys. Condens. Matter* **2009**, *21*, 084204.

(176)   Sanville, E. et al. Improved grid-based algorithm for Bader charge allocation. *J. Comput. Chem.* **2007**, *28*, 899–908.

(177)   Henkelman, G.; Arnaldsson, A.; Jónsson, H. A fast and robust algorithm for Bader decomposition of charge density. *Comput. Mat. Sci.* **2006**, *36*, 354–360.

(178)   Yu, M.; Trinkle, D. R. Accurate and efficient algorithm for Bader charge integration. *The J. Chem. Phys.* **2011**, *134*, 064111.

(179)   Nosé, S. A molecular dynamics method for simulations in the canonical ensemble. *Molecular physics* **1984**, *52*, 255–268.

(180)   Hoover, W. G. Canonical dynamics: Equilibrium phase-space distributions. *Phys. Rev. A* **1985**, *31*, 1695.

(181)   Hay, P. J. et al. Theoretical study of CeO_2 and Ce2O3 using a screened hybrid density functional. *The J. Chem. Phys.* **2006**, *125*, 034712.

(182)   Lizzit, S. et al. Surface core-level shifts of clean and oxygen-covered Ru(0001). *Phys. Rev. B* **2001**, *63*, 205419.

(183)   Köhler, L.; Kresse, G. Density functional study of CO on Rh(111). *Phys. Rev. B* **2004**, *70*, 165405.

(184)   Bellafont, N. P. et al. Predicting core level binding energies shifts: Suitability of the projector augmented wave approach as implemented in VASP. *J. Comp. Chem.* **2017**, *38*, 518–522.

(185)   Allen, J. P.; Watson, G. W. Occupation matrix control of d- and f-electron localisations using DFT + U. *Phys. Chem. Chem. Phys.* **2014**, *16*, 21016–21031.

(186)   Ångqvist, M. et al. ICET – A Python Library for Constructing and Sampling Alloy Cluster Expansions. *Adv. Theory Simul.* **2019**, *2*, 1900015.

Bibliography

---

(187) Lian, J.-C. et al. Algorithm for generating irreducible site-occupancy configurations. *Phys. Rev. B* **2020**, *102*, 134209.

(188) Lian, J.-C. et al. Highly efficient tree search algorithm for irreducible site-occupancy configurations. *Phys. Rev. B* **2022**, *105*, 014201.

(189) Pedregosa, F. et al. Scikit-learn: Machine learning in Python. *J. Mach. Learn. Res.* **2011**, *12*, 2825–2830.

(190) Draxl, C.; Scheffler, M. NOMAD: The FAIR concept for big data-driven materials science. *MRS Bulletin* **2018**, *43*, 676–682.

(191) Code and data repository for the sampling of group 9-11 transition metal CeO_2(100)-based SACs. `https://gitlab.com/iciq-tcc/nlopez-group/ceria\_sac` (accessed 08/18/2023).

(192) Álvarez Moreno, M. et al. Managing the Computational Chemistry Big Data Problem: The ioChem-BD Platform. *J. Chem. Inf. Model.* **2015**, *55*, 95–103.

(193) GeigerJ2/sklwrap: Some wrapper functions to quickly use and evaluate sklearn predictors. `https://github.com/GeigerJ2/sklwrap` (accessed 08/18/2023).

(194) Larsen, A. H. et al. The atomic simulation environment—a Python library for working with atoms. *J. Phys. Condens. Matter* **2017**, *29*, 273002.

(195) Ong, S. P. et al. Python Materials Genomics (pymatgen): A robust, open-source python library for materials analysis. *Comput. Mat. Sci.* **2013**, *68*, 314–319.

(196) Wes McKinney In *Proceedings of the 9th Python in Science Conference*, ed. by Stéfan van der Walt; Jarrod Millman, 2010, pp 56–61.

(197) Inc., P. T. Collaborative data science `https://plot.ly`.

(198) Community, B. O. Blender - a 3D modelling and rendering package; Blender Foundation, Stichting Blender Foundation, Amsterdam, 2018.

(199) Pizzi, G. et al. AiiDA: automated interactive infrastructure and database for computational science. *Comput. Mat. Sci.* **2016**, *111*, 218–230.

(200) Huber, S. P. et al. AiiDA 1.0, a scalable computational infrastructure for automated reproducible workflows and data provenance. *Scientific Data* **2020**, *7*, 300.

(201) Uhrin, M. et al. Workflows in AiiDA: Engineering a high-throughput, event-based engine for robust and modular computational workflows. *Comput. Mat. Sci.* **2021**, *187*, 110086.

(202) Trovarelli, A., *Catalysis by ceria and related materials*; World Scientific: 2002; Vol. 2.

(203) Chorkendorff, I.; Niemantsverdriet, J. W., *Concepts of modern catalysis and kinetics*; John Wiley & Sons: 2017.

(204) Kopelent, R. et al. Catalytically Active and Spectator Ce3+ in Ceria-Supported Metal Catalysts. *Angew. Chem. Int. Ed.* **2015**, *54*, 8728–8731.

(205) Kunwar, D. et al. Stabilizing High Metal Loadings of Thermally Stable Platinum Single Atoms on an Industrial Catalyst Support. *ACS Catal.* **2019**, *9*, 3978–3990.

(206) Zhang, D. et al. Oxygen-Vacancy Dynamics and Entanglement with Polaron Hopping at the Reduced $CeO_2(111)$ Surface. *Phys. Rev. Lett.* **2019**, *122*, 096101.

(207) Turner, S. et al. High resolution mapping of surface reduction in ceria nanoparticles. **2011**, *3*, 3385–3390.

(208) Paidi, V. K. et al. Predicting NO x Catalysis by Quantifying Ce3+ from Surface and Lattice Oxygen. *ACS Appl. Mater. Interfaces* **2017**, *9*, 30670–30678.

(209) DeRita, L. et al. Structural evolution of atomically dispersed Pt catalysts dictates reactivity. **2019**, *18*, 746–751.

(210) Spezzati, G. et al. Atomically dispersed Pd-O species on $CeO_2(111)$ as highly active sites for low-temperature CO oxidation. **2017**, *7*, 6887–6891.

(211) Jeong, H. et al. Fully Dispersed Rh Ensemble Catalyst to Enhance Low-Temperature Activity. **2018**, *140*, 9558–9565.

(212) Li, Q. et al. Simultaneous Ni Doping at Atom Scale in Ceria and Assembling into Well-De fi ned Lotuslike Structure for Enhanced Catalytic Performance. **2017**.

(213) Qiao, B. et al. Highly Efficient Catalysis of Preferential Oxidation of CO in H2-Rich Stream by Gold Single-Atom Catalysts. *ACS Catal.* **2015**, *5*, 6249–6254.

(214) Schilling, C. et al. Identification of single-atom active sites in CO oxidation over oxide-supported Au catalysts. **2020**, *383*, 264–272.

(215) Yu, W.-z. et al. Construction of Active Site in a Sintered Copper - Ceria Nanorod Catalyst. **2019**.

Bibliography

(216) Khivantsev, K. et al. Pushing the Limits of Precious Metal Atom Economy for Three-Way-Catalysts (TWC): Thermally Stable and Highly Active Single Rh Atom Catalysts (Rh1/ceria) Under Both Dry and Industrially Relevant Conditions for NO Abatement. **2020**.

(217) Mai, H.-X. et al. Shape-Selective Synthesis and Oxygen Storage Behavior of Ceria Nanopolyhedra, Nanorods, and Nanocubes. *The J. Phys. Chem. B* **2005**, *109*, 24380–24385.

(218) Li, P. et al. A review on oxygen storage capacity of CeO_2-based materials: Influence factors, measurement techniques, and applications in reactions related to catalytic automotive emissions control. *Catal. Today* **2019**, *327*, 90–115.

(219) Birschitzky, V. C. et al. Machine learning for exploring small polaron configurational space. *npj Comput. Mater.* **2022**, *8*, 1–9.

(220) O'Connor, N. J. et al. Interaction trends between single metal atoms and oxide supports identified with density functional theory and statistical learning. *Nat. Catal.* **2018**, *1*, 531–539.

(221) Iyemperumal, S. K. et al. Quantifying Support Interactions and Reactivity Trends of Single Metal Atom Catalysts over TiO_2. *J. Phys. Chem. C* **2018**, *122*, 25274–25289.

(222) Tan, K. et al. Predicting Metal-Support Interactions in Oxide-Supported Single-Atom Catalysts. *Ind. Eng. Chem. Res.* **2019**, *58*, 20236–20246.

(223) Haynes, W. M., *CRC Handbook of Chemistry and Physics 97th Edition*; CRC Press LLC Florence: Taylor & Francis Group: 2016.

(224) Uhrin, M. Through the eyes of a descriptor: Constructing complete, invertible descriptions of atomic environments. *Phys. Rev. B* **2021**, *104*, 144110.

(225) Behler, J. Four Generations of High-Dimensional Neural Network Potentials. *Chem. Rev.* **2021**, *121*, 10037–10072.

(226) Harris, C. R. et al. Array programming with NumPy. *Nature* **2020**, *585*, 357–362.

(227) Yang, C. et al. O_2 Activation on Ceria Catalysts—The Importance of Substrate Crystallographic Orientation. *Angew. Chem. Int. Ed.* **2017**, *56*, 16399–16404.

(228) Ziemba, M. et al. Toward an Atomic-Level Understanding of Ceria-Based Catalysts: When Experiment and Theory Go Hand in Hand. **2021**, *9*, 2884–2893.

(229) Oswald, S. In *Encyclopedia of Anal. Chem.* John Wiley & Sons, Ltd: 2013.

Bibliography

(230) Hegner, F. S. et al. Level Alignment as Descriptor for Semiconductor/Catalyst Systems in Water Splitting: The Case of Hematite/Cobalt Hexacyanoferrate Photoanodes. *ChemSusChem* **2017**, *10*, 4552–4560.

(231) Hino, T. et al. Structural Basis of Biological N2O Generation by Bacterial Nitric Oxide Reductase. *Science* **2010**, *330*, 1666–1670.

(232) Fehling, C.; Friedrichs, G. Dimerization of HNO in Aqueous Solution: An Interplay of Solvation Effects, Fast Acid–Base Equilibria, and Intramolecular Hydrogen Bonding? *J. Am. Chem. Soc.* **2011**, *133*, 17912–17922.

(233) Ferretti, E. et al. Reductive Nitric Oxide Coupling at a Dinickel Core: Isolation of a Key cis-Hyponitrite Intermediate en route to N2O Formation. *Angew. Chem. Int. Ed.* **2019**, *58*, 1705–1709.

(234) Shrestha, K. P. et al. Detailed Kinetic Mechanism for the Oxidation of Ammonia Including the Formation and Reduction of Nitrogen Oxides. *Energy & Fuels* **2018**, *32*, 10202–10217.

(235) Jacoby, M. Hunting-hidden-chemistry-heterogeneous-catalysts `https://cen.acs.org/articles/95/i29/Hunting-hidden-chemistry-heterogeneous-catalysts.html` (accessed 08/07/2023).

(236) Schwerdtfeger, P.; Nagle, J. K. 2018 Table of static dipole polarizabilities of the neutral elements in the periodic table. *Mol. Phys.* **2019**, *117*, 1200–1225.

(237) Kittel, C., *Introduction to Solid State Physics (8th ed.)* John Wiley and Sons: 2004, pp 313–314.

Bibliography

Chapter 8

Publications

Single-Atom Catalysis

Highly Stable and Reactive Platinum Single Atoms on Oxygen Plasma-Functionalized CeO₂ Surfaces: Nanostructuring and Peroxo Effects

Weiming Wan, Julian Geiger, Nikolay Berdunov, Mauricio Lopez Luna, See Wee Chee, Nathan Daelman, Núria López,* Shamil Shaikhutdinov,* and Beatriz Roldan Cuenya*

Abstract: Atomically dispersed precious metals on oxide supports have recently become increasingly interesting catalytic materials. Nonetheless, their non-trivial preparation and limited thermal and environmental stability constitutes an issue for their potential applications. Here we demonstrate that an oxygen plasma pre-treatment of the ceria (CeO_2) surface serves to anchor Pt single atoms, making them active and resistant towards sintering in the CO oxidation reaction. Through a combination of experimental results obtained on well-defined CeO_2 films and theory, we show that the O_2 plasma causes surface nanostructuring and the formation of surface peroxo (O_2^{2-}) species, favoring the uniform and dense distribution of isolated strongly bonded Pt^{2+} atoms. The promotional effect of the plasma treatment was further demonstrated on powder Pt/CeO_2 catalysts. We believe that plasma functionalization can be applied to other metal/oxide systems to achieve tunable and stable catalysts with a high density of active sites.

Introduction

Single-atom catalysts (SACs) of precious metals have recently received great attention in the catalysis community.[1] In addition to the fact that SACs maximize the noble metal efficiency, such catalysts often show superior catalytic performance as compared to oxide-supported metal nanoparticles (NPs). Several preparation techniques have been reported in the literature, such as co-precipitation at very low metal loading,[2] strong electrostatic adsorption of metal precursors on oxide nanocrystals,[3] atom trapping,[4] atomic layer deposition,[5] magnetron co-sputtering of a noble metal and an oxide,[6] to name a few. To increase the commercial value of SACs, it is however necessary to fabricate them with relatively high metal loading. Moreover, single atoms must be resistant towards sintering under catalytically relevant conditions. To get more insight into these issues, fundamental studies employing model systems and surface sensitive techniques in combination with theoretical investigations are of high importance.

In this work, we addressed the question of how the surface structure (morphology and composition) of the oxide support affects the metal dispersion and the stability of single atoms at elevated temperatures and in a gas atmosphere. More specifically, we targeted ceria (CeO_2)-supported Pt SACs which are one of the most intensively studied systems, both experimentally and theoretically, in the CO oxidation reaction.[7] We prepared Pt/CeO_2 model catalysts by physical vapor deposition of Pt onto crystalline $CeO_2(111)$ films subjected to different pre-treatments resulting in ceria reduction and/or surface roughening. Among the ceria supports studied, Pt atoms deposited onto CeO_2 films pre-treated with O_2 plasma showed the best performance in terms of thermal stability and catalytic activity in the CO oxidation reaction. Corroborated by density functional theory (DFT), the effect is attributed to: i) a plasma-induced surface restructuring resulting in ceria clusters at the oxide surface; and ii) the formation of a significant amount of surface peroxide (O_2^{2-}) species, all favoring a dense and uniform distribution of isolated and highly stable Pt single atoms. The promotional effect of the plasma treatement was also demonstrated on the powder catalysts. These findings open a new playground for using the plasma functionalization in heterogeneous catalysis to achieve a high density of stable active sites.

Results and Discussion

Well-ordered, stoichiometric $CeO_2(111)$ films were grown on a Ru(0001) substrate as described elsewhere[8] (see the

[*] Dr. W. Wan, Dr. N. Berdunov, M. Lopez Luna, Dr. S. W. Chee, Dr. S. Shaikhutdinov, Prof. Dr. B. Roldan Cuenya
Department of Interface Science
Fritz Haber Institute
Faradayweg 4–6, 14195 Berlin (Germany)
E-mail: shaikhutdinov@fhi-berlin.mpg.de
roldan@fhi-berlin.mpg.de

J. Geiger, Dr. N. Daelman, Prof. N. López
Institute of Chemical Research of Catalonia, The Barcelona Institute of Science and Technology Institution
43007 Tarragona (Spain)
E-mail: nlopez@iciq.es

Research Articles

Angewandte
International Edition *Chemie*

Experimental Section in the Supporting Information). To examine the possible role of oxygen vacancies on the Pt adsorption, the films were annealed in ultrahigh vacuum (UHV) at high temperature resulting in ceria partial reduction (henceforth referred to as "CeO$_2$-red" films). In addition, we prepared CeO$_2$(111) films exposing a high density of monoatomic steps ("CeO$_2$-step") as described in ref. [9] in order to increase the number of low-coordinated sites at the surface. Finally, the well-ordered films were treated with a low-pressure oxygen plasma (denoted as "CeO$_2$-plasma"). Pt was deposited onto these films at low metal flux in order to minimize metal aggregation upon deposition at room temperature. The electronic structure of Pt was monitored by X-ray Photoelectron Spectroscopy (XPS) via the Pt 4f level, and the binding energy (BE) of the $4f_{7/2}$ state will only be used in the discussion.

First, we compares Pt 4f spectra obtained for 0.2 ML Pt deposited on differently prepared CeO$_2$ films (one monolayer (ML) corresponds to one Pt atom per CeO$_2$(111) surface unit cell, i.e., 8×10^{14} cm^{-2}) and measured before and after the CO oxidation reaction at 523 K at near ambient pressure. Note that all samples before the reaction were annealed in UHV at 523 K in order to discriminate solely thermal from reaction-induced effects. The full XPS data set for the Pt 4f, Ce 3d and O 1s levels are shown in Figures S1–S4. The Low Energy Electron Diffraction (LEED) patterns of the films prior to the Pt deposition are shown in Figure 1 adjacent to the spectra.

First, we discuss the results for Pt deposited onto a well-ordered stoichiometric CeO$_2$(111) film. "As deposited" Pt species are characterized by a BE of 71.8 eV (Figure S1) which is usually observed on metallic Pt clusters.[10] The peak shifts to lower BE (71.4 eV) upon UHV annealing, thus indicating particles sintering.[11] The spectrum obtained after the reaction consists of several states. Obviously, the 71.1 eV state is associated with even larger metallic NPs,

suggesting further Pt sintering under reaction conditions. Two other signals centered at 74.2 and 72.7 eV are assigned to Pt in the 4+ and 2+ oxidation states, respectively.

Analysis of the Ce 3d and O 1s spectra (Figure S1) revealed no changes after Pt deposition. The amount of Ce^{3+} slightly increases after vacuum annealing at 523 K, indicating a Pt-induced partial ceria reduction. The Ce 3d spectrum fully recovers after CO oxidation in an O$_2$-rich atmosphere. The O 1s signal at 529.3 eV showed no additional states associated with adsorbates (typically, hydroxyls and carbonates) before and after Pt deposition, since the stoichiometric CeO$_2$(111) surface is essentially inert to residual gases in the UHV background at 300 K.[12] However, a considerable signal at 531.8 eV appears after the reaction, which can be attributed to adventitious CO$_2$ (and probably water) adsorption on the bare ceria support at near ambient pressures.[8b]

The reduced ceria surface shows a complex ($\sqrt{7} \times \sqrt{7}$)-R19.1 LEED pattern, which is assigned to long-range ordering of the O vacancies at the surface.[13] In contrast to stoichiometric CeO$_2$(111), this surface readily reacts with traces of water in the UHV background causing an additional weak O 1s signal at 532.0 eV from surface hydroxyls (Figure S2).[12b] Beyond the Pt metal atoms constituting small clusters (BE at 71.6 eV), some Pt atoms on the "CeO$_2$-red" surface are in the 2+ oxidation state (at 72.8 eV). However, the Pt^{2+} signal disappears upon vacuum annealing, whereas the Pt^0 signal gains in intensity, so that the spectrum becomes virtually identical to the one observed on the stoichiometric CeO$_2$ surface (Figure 1). After CO oxidation, Pt is found almost exclusively in the 2+ state (72.8 eV), with some minor contribution of Pt^{4+} (74.2 eV) and the Pt^0 states (71.1 eV). Again, the results can be explained by the formation of relatively large Pt NPs which underwent oxidation. Concomitantly, the ceria surface became fully oxidized (no Ce^{3+} detected) in the O$_2$-rich mixture used (Figure S2).

When Pt is deposited onto CeO$_2$(111) films with an artificially increased step density ("CeO$_2$-step"), the Pt atoms are partially in the 2+ and metallic states (BEs at 72.8 and 71.9 eV, respectively, Figure S3). In contrast to the previous cases, Pt^{2+} species are thermally stable and remain at the surface in addition to small metallic clusters, which sinter upon annealing (the corresponding BE shifts from 71.9 to 71.7 eV). After the CO oxidation reaction, no metallic Pt atoms are found on the surface, which now contains only Pt^{2+} and Pt^{4+} species.

Therefore, in the above-presented systems, Pt deposits always form small metal particles upon UHV annealing. A certain amount of thermally stable Pt^{2+} species found on the "CeO$_2$-step" surface can be explained by the strong adsorption of Pt single atoms at step edges.[9] When exposed to the CO oxidation atmosphere, metal clusters become oxidized, thus giving rise to the 4+ and 2+ states, albeit their ratio depends on the initial particle size. The formation of Pt^{4+} and Pt^{2+} species on the Pt NPs in oxidizing ambient is well-documented in the literature,[14] and is commonly attributed to PtO$_2$/PtO clusters or a thin PtO$_x$ oxide film formed on the large Pt NPs.

Figure 1. Comparison of Pt 4f spectra obtained on four different 0.2 ML Pt/CeO$_2$ surfaces before and after CO oxidation reaction at 523 K (in a mixture of 10 mbar CO and 50 mbar O$_2$ balanced by He to 1 bar). Before the reaction, the samples were annealed at 523 K in UHV. LEED patterns (at 81 eV) of the ceria films prior to the Pt deposition are shown in the left panel adjacent to the spectra.

Finally, Figure 1 shows the results for the CeO_2 film exposed to oxygen plasma prior to the Pt deposition. This system substantially differs from the previous ones. Starting from the "as deposited" sample (Figure S4), Pt remains exclusively in the $2+$ state even in the CO oxidation reaction at near atmospheric pressure.

To shed light on the origin of the exceptional stability of Pt on the CeO_2-plasma films, we studied the ceria surface with STM. STM images (Figure 2a–c) revealed the formation of ceria clusters about 1 nm in size, which are randomly distributed on the surface. These STM results also explain the lack of long-range order in LEED patterns (see Figure 1). In addition, the O 1s XPS spectra (Figure 2e) revealed a prominent shoulder at 530.8 eV, which cannot be assigned to adventitious hydroxyls and/or carbonates, showing a considerably higher BE, i.e., 531.8 eV (Figure S1–S3). The signal is shifted by 1.6 eV with respect to the main peak at 529.2 eV and grows at increasing plasma exposure time. The signal gains in intensity when measured at more surface sensitive, grazing emission (Figure 2e). All these findings point to the formation of new oxygen species which are absent on other ceria surfaces studied above. Based on DFT (PBE + U) calculations of atomic O adsorption on the stoichiometric $CeO_2(111)$ surface and corresponding BE

shifts of the O 1s level (Figure 2f, see details below), we assigned the 530.8 eV signal to surface peroxides, O_2^{2-} (see also Figure S6, S7 and Table S1).

On such a disordered and very rough surface, direct visualization of metal single atoms with STM is very difficult if not impossible. In an attempt to identify Pt species formed on the CeO_2-plasma films, we employed Infrared Reflection-Absorption Spectroscopy (IRAS) using CO as a probe molecule and compared the results on the Pt/CeO_2-plasma and pristine Pt/$CeO_2(111)$ surfaces. The bare ceria surfaces did not adsorb CO under the exposure conditions studied.

Adsorption of CO (at 10^{-6} mbar) on Pt deposited onto a well-ordered $CeO_2(111)$ surface at 200 K (Figure 3a) resulted in IRAS bands centered at 2087 and 2024 cm^{-1} and a weak band as a shoulder at ~ 2060 cm^{-1}. The former two signals disappeared on the sample heated to 500 K and exposed to CO again, while the band at 2060 cm^{-1} gained in intensity. This latter band can be assigned to the stretching vibrations of CO adsorbed at the low-coordinated sites[15] on Pt NPs located primarily at the step edges, as shown by STM.[11] Accordingly, the 2087 and 2024 cm^{-1} bands observed immediately after Pt deposition belong to CO adsorbed onto Pt clusters and aggregates with ill-defined structures,[16] since their formation is affected by the limited
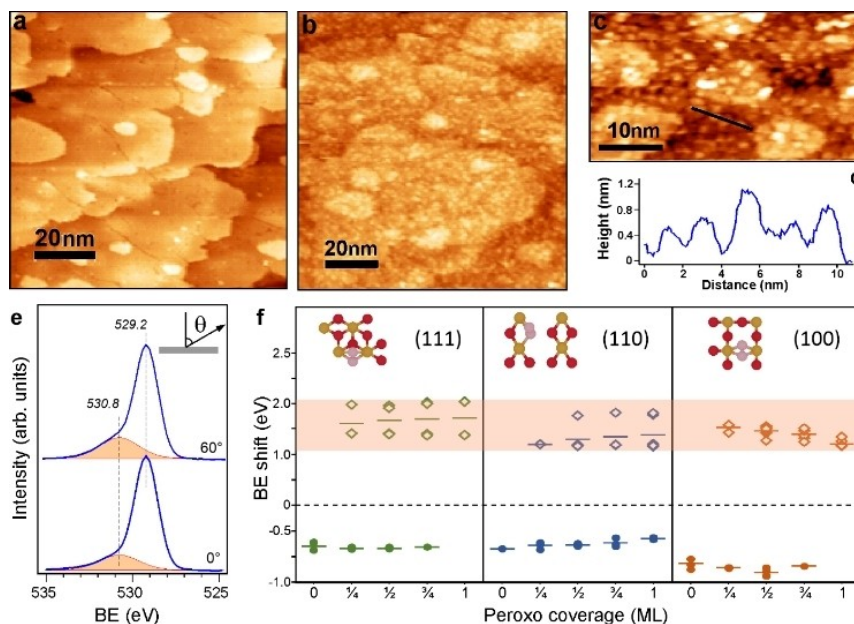
Figure 2. STM images of a) the well-ordered $CeO_2(111)$ and b, c) $CeO_2(111)$-plasma films taken in UHV at ~ 500 K. d) Topography profile along the line marked in image (c). e) O 1s XPS spectra of the $CeO_2(111)$-plasma film measured at normal and grazing emissions. f) Calculated BE shifts for the peroxo-O atoms (open symbols) and surface O atoms (filled symbols) referenced to the lattice O atoms in the bulk (set to zero). The latter are in abundance and dominate the experimental spectra. The shaded area highlights experimentally measured BE shifts. Insets show the top views of the topmost layer in DFT-optimized structures at $^1/_4$ ML peroxo coverage on (111), (110), and (100) surfaces. Color code: Ce: gold; surface O: red; peroxo O_2^{2-}: pink.
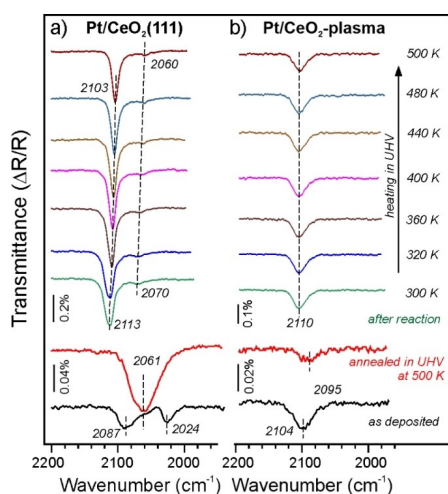
Figure 3. IRA-spectra measured in UHV on 0.2 ML Pt deposited on CeO$_2$(111) a) and CeO$_2$-plasma b) surfaces. CO was dosed at 200 K onto "as deposited" samples and after UHV annealing at 500 K for 5 min. The samples tested in the CO oxidation reaction were measured without additional CO dosage. The spectra were consecutively recorded while heating the sample in UHV to the temperatures indicated.

diffusivity of surface ad-atoms at these relatively low temperatures. In contrast, Pt species formed upon deposition onto the CeO$_2$-plasma surface showed a single band at 2104 cm^{-1}. The band is considerably reduced in intensity and red-shifted (to 2095 cm^{-1}) on the sample that was annealed in UHV at 500 K prior to the CO exposure (Figure 3b). The latter spectrum is fully reproducible after several thermal flashes to 500 K, indicating a good thermal stability of the Pt species, in full agreement with the XPS results. In principle, both the 2104 and 2095 cm^{-1} band falls in the range of those reported in the literature for powder Pt SACs proven by high resolution electron microscopy.[1f,4,5,7b] It is interesting that no CO IRAS bands were observed on the samples pre-heated to 700 K, indicating that either the Pt atoms migrate into the sub-surface region or they adsorb CO weakly. It should be noted, however, that IRAS spectra on metal-supported oxide films obey the selection rule such that only vibrations associated with dipole changes normal to the metal surface can be detected.[17] Therefore, CO molecules oriented parallel to the Ru(0001) substrate will be invisible in IRAS spectra.

We also recorded the IRAS spectra on these two systems after the CO oxidation reaction in the mixture consisting of 1% CO and 5% O$_2$ (balanced by Ar to 1 bar) in a "high-pressure" reaction cell. After 5 min of reaction at 500 K and sample cooling to room temperature, the cell was pumped out and the IRAS spectra were recorded in UHV at 300 K without additional exposure to CO. Interestingly, the spectra revealed similar bands at around 2110 cm^{-1} on both systems, but of different intensities. (A weak and broad band at

2070 cm^{-1} on Pt/CeO$_2$(111) can be assigned to traces of CO residing at the edges of metallic Pt NPs, see above). However, the spectra showed different behavior upon slow heating the sample to 500 K. On Pt/CeO$_2$(111) (Figure 3a), the band at 2113 cm^{-1} gradually shifts to a lower wavenumber (by 10 cm^{-1}), and its integral intensity slightly decreases, indicating a partial desorption of CO. These spectral changes and peak positions are characteristic for CO adsorbed on O-precovered Pt surfaces,[18] and the shift can be explained in terms of the dipole-dipole interaction between neighboring CO molecules adsorbed on the partially oxidized Pt NPs, as observed by XPS (Figure 1). The formation of relatively large Pt NPs on CeO$_2$(111) prior to the reaction can also explain the relatively high intensity of the IRAS bands due to the image charge effects. In contrast, a much weaker band at 2010 cm^{-1} observed on the Pt/CeO$_2$-plasma surface stays constant during sample heating to 500 K (Figure 3b). Although this band fully disappears upon heating to 700 K and cannot be observed upon CO exposure at room temperature, it is fully reproduced after a second CO oxidation reaction run. Based on the comparative XPS and IRAS results, we can conclude that Pt deposited onto the plasma-treated CeO$_2$ surface forms single atoms which remain stable in a reaction atmosphere, albeit its coordination to the ceria surface may be affected by the CO oxidation reaction.

Based on structural characterization of the CeO$_2$-plasma surface by LEED and STM, one may suggest that the enhanced stability of Pt originates from surface roughening that suppresses the diffusivity of the Pt ad-atoms and hence their aggregation. To examine this scenario, we prepared a rough surface by bombarding a well-ordered CeO$_2$(111) film with 1 keV Ar$^+$ ions at 300 K for 5 min, resulting in the strong attenuation of the diffraction spots in LEED and a high density of monatomic steps as previously shown by STM.[19] However, the surface becomes considerably reduced due to the preferential sputtering of lighter O atoms. To re-oxidize the ceria surface, the film was exposed to 10^{-6} mbar O$_2$ at 500 K. Subsequent deposition of 0.2 ML Pt onto this "CeO$_2$-sputter" support resulted in Pt species primarily in the 2+ state (Figure S5a), but a considerable amount of Pt was also found in the metallic state (at 71.5 eV), most likely as Pt NPs. For comparison, the latter only appeared on Pt/CeO$_2$-plasma samples at a Pt coverage about two times higher, i.e., 0.4 ML. Apparently, the plasma creates more "O-rich" sites to stabilize Pt single atoms. Indeed, a substantially higher intensity is observed for the peroxo-related 530.8 eV signal in the O 1s spectra as compared to the CeO$_2$-sputter sample (Figure S5b).

Previous studies on Pt/CeO$_2$ systems prepared by magnetron sputtering of Pt and CeO$_2$[6] and by co-deposition of Ce and Pt in an oxygen atmosphere[20] also reported exceptional stability of Pt^{2+} species, although the presence of Pt *at the surface* was not proven. DFT simulations on ceria clusters suggested a specific structural element named "nanopocket" that binds Pt^{2+} so strongly that it can withstand sintering and bulk diffusion.[16,20] In these sites, Pt is coordinated to four oxygen atoms forming a planar Pt-4O moiety. Such a coordination has also been identified on the

Research Articles

(100)-oriented surface and monoatomic step edges on the (111) surface.[9,20,21]

To get more insight into the interaction of the Pt atoms with the plasma-treated CeO_2 films, we investigated the systems at hand with DFT. First, we addressed the nature of surface oxygen species resulting from adsorption of oxygen radicals in the plasma[22] on the low Miller-index CeO_2 surfaces. The O ad-atoms readily react with lattice oxygen to form peroxo (O_2^{2-}) groups (see insets in Figure 2f, Figures S6, S7 and Tables S2–S6), in agreement with previous DFT studies of molecular O_2 adsorption on partially reduced ceria surfaces.[23] The computed BE shifts for the O_2^{2-} groups depend on the coverage, and are 1.65, 1.30, and 1.35 eV, on average, for the (111), (110) and (100) surface, respectively (Figure 2f, Table S1). These values match well the BE shifts observed experimentally (Figure 2e), which can therefore be assigned to surface peroxo species in the plasma-treated films. The above-mentioned difference and similarity of the CeO_2-sputter and CeO_2-plasma surfaces may be linked to the mechanism by which peroxides are formed on the two surfaces. For the CeO_2-sputter samples, the oxygen vacancies, initially formed during Ar^+ bombardment, react with molecular O_2 in the re-oxidation step forming the surface peroxide groups. However, oxygen vacancies on CeO_2 may also migrate into subsurface positions[23a] and hence become inaccessible to the reaction with O_2. During the plasma treatment, however, molecular oxygen that is also present in the ambient immediately quenches the O vacancies (if formed) and ultimately results in surface peroxides in addition to those formed by direct reaction with atomic oxygen species in the plasma. As such, the higher ability of the oxygen-plasma treated surface to stabilize Pt atoms could have its origin in the higher surface peroxide coverage, assuming that a similar nanostructuring is achieved with both treatments.

To understand the rationale behind the formation of ceria NPs observed by STM (Figure 2a–c) we considered a thermodynamic model[24] under the assumption that the material forming the ceria NPs stems from the top CeO_2-(111) layers of the sample (Figure S10, Note S3). Consequently, the ceria film becomes thinner, while the total number of ceria formula units remains constant during the restructuring (Ce atoms are not sputtered by the relatively light O atoms in the plasma). We approximated a ceria NP as a hemisphere that grows in registry with the underlying film and employed surface energies computed for different peroxo-covered extended surfaces (Tables S2–S6), as well as step and corner energies, using calculations of high Miller-index surfaces (Tables S9, S10). Depending on the input parameters, the computed ceria NPs were between 3 and 11 nm in diameter (Figure S11), thus larger than experimentally observed. Nonetheless, these thermodynamic considerations demonstrate that the oxygen plasma definitely promotes surface restructuring and the formation of ceria NPs on the initially flat film, in addition to the possible bombardment effects of the high-energy O atoms in the plasma. The increase in surface area leads to a larger number of local surface structures that can stabilize oxygen radicals via the peroxo groups, while the exposure of facets

other than (111) on ceria NPs simultaneously entails a more exothermic reaction energy for the formation of peroxides.

Not surprisingly, peroxo species affect the Pt adsorption on the CeO_2 surfaces (Table 1 and Figure S8). Compared to pristine CeO_2(111), a Pt atom on the peroxo-covered (111) surface is bound by 1–2 eV more strongly, albeit depending on the peroxide coverage. The effect is smaller for the (110) surface (the energy gain is about 0.6 eV, on average), while on the (100) surface, peroxo species may even weaken the Pt bonding. Among the surfaces studied, the strongest Pt adsorption is observed for (100)–4O coordination environment, in agreement with previous results.[9,20] Interestingly, the presence of peroxo groups showed no beneficial effect in terms of Pt bonding for this site. We also examined Pt adsorption on stepped surfaces (Figure S9). Even though square-planar 4O-coordination environments, particularly on the (210) and (310) surfaces, provide sites for strongly exothermic Pt adsorption (Table S7), the stepped surfaces exhibit considerably higher surface energies and are therefore thermodynamically unstable.

Next, we investigated the interaction of Pt single atoms with ceria NPs on the CeO_2(111) surface. To this end, we constructed a model system consisting of a ceria cluster anchored on an extended CeO_2(111)-(7×7) slab. The particle size was adapted to that measured experimentally (i.e., about 1 nm, see Figure 2), and the entire structure was optimized by DFT accordingly (see Figure 5a, center). Obviously, new adsorption sites for Pt atoms become available at the boundary between the NP and the surrounding (111) terrace. The computed adsorption energy of a Pt single atom E_{ads}(Pt) on these sites (0.57 eV) is substantially smaller than on clean and peroxo-covered (111) surfaces (2.80 and 1.3–1.6 eV, respectively, Table 1). However, the (100)–4O sites exposed at the vertices of the ceria NPs present the thermodynamically most favorable adsorption sites for Pt (E_{ads}(Pt) = −1.76 eV). We also note that depending on their location on the ceria NP the coordination environments for adsorbed Pt atoms are chemically different from those of their symmetrically equivalent counterparts on the extended ceria surfaces. In particular, at (100)–4O sites, the difference is substantial and amounts to 0.9 eV

Table 1: Adsorption energies (in eV) of a Pt single atom adsorbed in the most stable structure on clean and peroxide-covered CeO_2 surfaces as a function of the peroxide coverage (1 ML corresponds to one peroxo group per (1×1) surface unit cell). At 0.5 ML coverage for the (2×2) slabs used in the calculations, two peroxo groups allow for two non-equivalent geometric arrangements: 1) along the unit vectors (labelled "r" = row-wise); and 2) diagonal to the unit vectors ("d" = diagonal). The energies are referenced to the corresponding ceria surfaces and Pt bulk. Negative values indicate exothermic adsorption and unfavourable Pt aggregation (Pt–Pt bond formation).

Surface	$\Theta_{peroxide}$ (ML)					
	0.0	0.25	0.5-d	0.5-r	0.75	1.0
(111)	2.80	1.28	1.98	1.75	1.62	0.59
(110)	0.60	−0.17	0.75	−0.08	0.11	0.12
(100)	0.31	0.14	0.46	0.30	0.56	0.64
(100)-4O	−0.85	−0.59	−0.95	−0.24	−0.63	1.76

(i.e., −1.76 vs −0.85 eV, on NP vertices and the corresponding extended surface, respectively).

We further investigated the NP/terrace boundary and the square-planar "nanopocket" Pt-binding sites of this system for CO adsorption (Figure 4b, Figure S13). We found that CO does not adsorb on Pt in the $(100){-}4O$ site ($E_{ads}(CO) = 0.11$ eV), while CO adsorption is exothermic for Pt at the NP/$CeO_2(111)$ boundary ($E_{ads}(CO) = -0.86$ eV). However, on this site the CO molecule is oriented almost parallel to the metal substrate surface and will be invisible in IRAS due to the above-mentioned selection rules. Both these findings may explain the very low intensity of the IRAS bands on the "as deposited" Pt/CeO_2-plasma surface as compared to that observed for the Pt/$CeO_2(111)$ system (Figure 3). As for the latter, the calculations performed for a Pt ad-atom on the pristine $CeO_2(111)$ surface yielded $E_{ads}(CO) = -2.14$ eV and a CO frequency of 2093 cm^{-1}, which matches the 2087 cm^{-1} band observed on the "as deposited" Pt/$CeO_2(111)$ sample (Figure 3). The CO binding energy increases to −2.33 and −2.62 eV for Pt adsorbed onto 0.25 and 0.5 ML peroxo-covered $CeO_2(111)$ surfaces, and the CO frequency shifts to 2081 and 2080 cm^{-1}, respectively. Therefore, we can tentatively assign the IRAS band at 2104 cm^{-1} observed on the "as deposited" Pt/CeO_2-plasma surface to Pt single ad-atoms adsorbed on the bare and/or peroxo-covered $CeO_2(111)$ surface. Upon UHV annealing at 500 K, these atoms probably migrate to the more strongly bound boundary and nanopocket sites where they only weakly adsorb CO that leads to a considerable reduction of the signal intensity as shown in Figure 3b.

In an attempt to identify strongly bonded CO molecules remaining on the Pt/CeO_2-plasma surface after reaction, we

evaluated several structures derived from the Pt/nanopocket site by sequential removal of O atoms from the Pt-4O coordination as a result of their reaction with CO.[21] The resulting configurations, denoted Pt-3O and Pt-2O in Figure 4b, revealed exothermic CO adsorption with energies amounting to −2.00 eV and −0.82 eV, respectively. As such, the Pt-3O structure appears as likely candidate responsible for the CO IRAS band observed on the post-reacted Pt/CeO_2-plasma samples.

Now we are in position to rationalize the overall impact of the plasma treatment on the structure of the Pt/CeO_2-(111) surface as illustrated in the following Scheme.

It leads to two crucial modifications of the ceria surface: 1) morphological, as evident from the pronounced nano-structuring resulting in the formation of ceria nanoparticles; and 2) chemical, via surface peroxide formation. During Pt deposition, the metal atoms may either directly stick to the ceria NPs or adsorb onto the peroxo-covered $CeO_2(111)$ surface in-between, where they form isolated strongly bound complexes with the surface peroxide groups. This is in contrast to the pristine ceria film surface, where Pt atoms readily diffuse on the surface and ultimately agglomerate into Pt NPs. With increasing temperature, the peroxo-trapped Pt atoms on the (111) terraces may further migrate to the numerous ceria NPs around and occupy sites at the particle/terrace boundary and the nanopockets. Thus, the peroxide-covered (111) surface, firstly, prevents Pt aggregation during deposition and, secondly, acts as a reservoir for Pt single atoms on ceria NPs. Consequently, the morphological and chemical modifications of the ceria surface, as well as their synergistic interplay are critical to achieve a high density of stable Pt single atoms.

The formation of highly stable Pt single atoms on the plasma pre-treated surface shows a beneficial effect for the CO oxidation reaction. To illustrate this, Figure 5a compares steady state CO_2 production rates measured on several planar model catalysts in a high-pressure cell filled with 10 mbar of CO and 50 mbar of O_2 balanced by He to 1 bar at different sample temperatures that are increased stepwise.

Figure 4. a) Adsorption of Pt atom at several different sites on a ceria NP/film composite system ($Ce_{178}O_{356}$, shown in the middle). The adsorption energies (in eV; referenced to bulk Pt) are shown adjacent to the structures. b) Optimized geometries for CO adsorption on Pt single atoms at the NP/boundary and at sites derived from Pt in a $(100){-}4O$ "nanopocket". By removing one or two ligand oxygen atoms from the latter coordination site, other, more stable adsorption geometries for CO can be formed (termed "Pt-3O" and "Pt-2O"). CO adsorption energies (in eV) are indicated. (All the computed structures can be retrieved at DOI: 10.19061/iochem-bd-1-181)

Scheme 1. Schematic representation of the interaction of Pt atoms with pristine and oxygen plasma-treated $CeO_2(111)$ films. Upon deposition on a stoichiometric $CeO_2(111)$ surface, Pt forms small clusters which aggregate into larger Pt NPs at elevated temperatures. Plasma pre-treatment of the CeO_2 surface produces peroxo species and induces surface restructuring, resulting in small ceria NPs, which act as anchoring sites either directly upon Pt adsorption or through surface migration of peroxo-stabilized Pt single atoms. Color code: Ce: gold; O: red; Pt: green; and peroxo O_2^{2-}: pink.

Research Articles
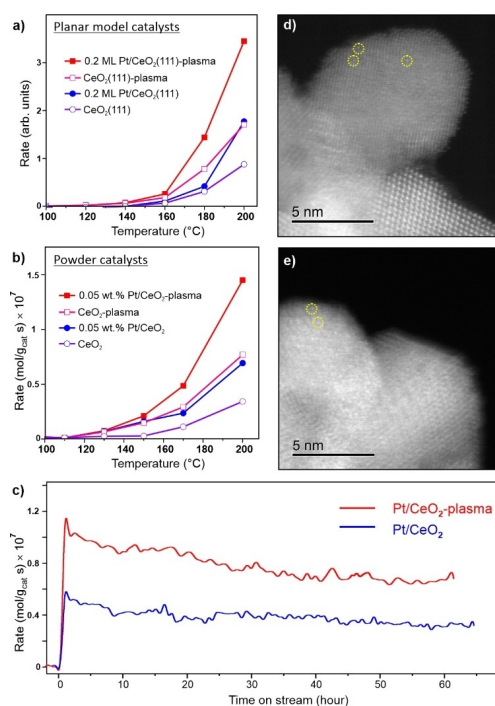
Figure 5. a, b) CO oxidation rate on model planar (a) and powder (b) Pt/CeO$_2$ catalysts measured in reaction mixtures containing 1% CO +5% O$_2$ and 1% CO+20% O$_2$, respectively, (He balanced to 1 bar) during a stepwise increase of the sample temperature. The results for Pt-free CeO$_2$ supports are shown for comparison. c) Long-term catalytic tests of "as prepared" and plasma-treated 0.05% Pt/CeO$_2$ catalysts at 200 C. Time zero corresponds to the start of heating to 200 C with the rate of 10 C min^{-1}. d, e) Aberration-corrected STEM images of 0.05 wt.% Pt/CeO$_2$-plasma catalyst before (d) and after (e) reaction at 200 C. Some of the Pt single atoms are highlighted by circles.

Among the samples studied, the Pt/CeO$_2$-plasma one showed a considerably higher rate than that of Pt/CeO$_2$-(111). It is also interesting that the CeO$_2$-plasma film itself exhibited a higher activity as compared to the pristine CeO$_2$(111) film.

To link the above-presented model studies with real catalytic systems and to demonstrate the beneficial effect of the plasma treatment also for powder catalysts, Figure 5b shows CO$_2$ production rates measured on pristine and plasma-treated CeO$_2$ and Pt/CeO$_2$ powder samples (see Experimental details in the Supporting Information). A low Pt loading (0.05 wt.%) was only used in order to compare our catalysts to "conventional" Pt/CeO$_2$ SACs reported in ref.[25] The catalytic performance of the powder catalysts revealed basically the same trend as for the planar systems (Figure 5a). The plasma-treated ceria exhibits higher activity than its pristine counterpart. Plasma treatment of the Pt/

CeO$_2$ catalyst enhances the reaction rate even further, and to a higher extent than that of observed for pure ceria, thus indicating a synergetic effect between Pt and a functionalized ceria support. The higher activity of the O$_2$-plasma treated catalysts was further confirmed by the long-term catalytic stability tests shown in Figure 5c. These data demonstrate that the beneficial effect of the plasma pretreatment is long-lasting.

On our powder samples, it was possible to directly address the peroxo formation using Raman spectroscopy.[23b] Raman spectra provided strong evidence for the enhanced formation and high stability of peroxo species on the plasma-treated samples via a characteristic Raman shift at around 835 cm^{-1} (Figure S14). Finally, we made use of aberration-corrected scanning transmission electron microscopy (STEM), which imaged Pt single atoms on plasma-treated Pt/CeO$_2$ catalysts both before and after reaction (Figure 5d,e). The STEM data demonstrate a high stability of the plasma-treated powder Pt SACs, in full agreement with the results obtained on the planar model systems. Although the promotional effect could further be optimized by tuning the plasma exposure conditions, our findings provide a strong basis for using plasma treatments in the rational design and stabilization of single atom catalysts.

Conclusion

In this work, we showed that an oxygen plasma treatment of crystalline CeO$_2$(111) films stabilizes Pt^{2+} single atoms which become resistant towards sintering in the CO oxidation reaction at near atmospheric pressures. We attribute the effect to: i) the fine roughening ("nano-roughening") of the ceria surface; and ii) the formation of peroxo species, which favor the strong interaction with Pt ultimately resulting in a uniform distribution of isolated Pt atoms and an increased single atom capacity. Such a "single-pot" fabrication of single atom coated oxide supports, which combines both surface restructuring and active oxygen enrichment is a promising approach for the rational design of new catalysts employing single atoms.

Acknowledgements

GDCh

Research Articles

Angewandte
International Edition Chemie

[1] a) J. Liu, *ACS Catal.* **2017**, *7*, 34–59; b) X.-F. Yang, A. Wang, B. Qiao, J. Li, J. Liu, T. Zhang, *Acc. Chem. Res.* **2013**, *46*, 1740–1748; c) B. C. Gates, M. Flytzani-Stephanopoulos, D. A. Dixon, A. Katz, *Catal. Sci. Technol.* **2017**, *7*, 4259–4275; d) X. Li, X. Yang, Y. Huang, T. Zhang, B. Liu, *Adv. Mater.* **2019**, *31*, 1902031; e) G. S. Parkinson, *Catal. Lett.* **2019**, *149*, 1137–1146; f) R. Lang, X. Du, Y. Huang, X. Jiang, Q. Zhang, Y. Guo, K. Liu, B. Qiao, A. Wang, T. Zhang, *Chem. Rev.* **2020**, *120*, 11986–12043.

[2] B. Qiao, A. Wang, X. Yang, L. F. Allard, Z. Jiang, Y. Cui, J. Liu, J. Li, T. Zhang, *Nat. Chem.* **2011**, *3*, 634–641.

[3] L. DeRita, S. Dai, K. Lopez-Zepeda, N. Pham, G. W. Graham, X. Pan, P. Christopher, *J. Am. Chem. Soc.* **2017**, *139*, 14150–14165.

[4] J. Jones, H. Xiong, A. T. DeLaRiva, E. J. Peterson, H. Pham, S. R. Challa, G. Qi, S. Oh, M. H. Wiebenga, X. I. Pereira Hernández, Y. Wang, A. K. Datye, *Science* **2016**, *353*, 150.

[5] X. Ye, H. Wang, Y. Lin, X. Liu, L. Cao, J. Gu, J. Lu, *Nano Res.* **2019**, *12*, 1401–1409.

[6] R. Fiala, A. Figueroba, A. Bruix, M. Vaclavu, A. Rednyk, I. Khalakhan, M. Vorokhta, J. Lavkova, F. Illas, V. Potin, I. Matolinova, K. M. Neyman, V. Matolin, *Appl. Catal. B* **2016**, *197*, 262–270.

[7] a) L. Nie, D. Mei, H. Xiong, B. Peng, Z. Ren, X. I. P. Hernandez, A. DeLaRiva, M. Wang, M. H. Engelhard, L. Kovarik, A. K. Datye, Y. Wang, *Science* **2017**, *358*, 1419; b) X. I. Pereira-Hernández, A. DeLaRiva, V. Muravev, D. Kunwar, H. Xiong, B. Sudduth, M. Engelhard, L. Kovarik, E. J. M. Hensen, Y. Wang, A. K. Datye, *Nat. Commun.* **2019**, *10*, 1358; c) H. Wang, J.-X. Liu, L. F. Allard, S. Lee, J. Liu, H. Li, J. Wang, J. Wang, S. H. Oh, W. Li, M. Flytzani-Stephanopoulos, M. Shen, B. R. Goldsmith, M. Yang, *Nat. Commun.* **2019**, *10*, 3808.

[8] a) M. Baron, O. Bondarchuk, D. Stacchiola, S. Shaikhutdinov, H. J. Freund, *J. Phys. Chem. C* **2009**, *113*, 6042–6049; b) D. R. Mullins, *Surf. Sci. Rep.* **2015**, *70*, 42–85.

[9] F. Dvořák, M. Farnesi Camellone, A. Tovt, N.-D. Tran, F. R. Negreiros, M. Vorokhta, T. Skála, I. Matolínová, J. Mysliveček, V. Matolín, S. Fabris, *Nat. Commun.* **2016**, *7*, 10801.

[10] N. Isomura, X. Wu, H. Hirata, Y. Watanabe, *J. Vac. Sci. Technol. A* **2010**, *28*, 1141–1144.

[11] Y. Zhou, J. M. Perket, J. Zhou, *J. Phys. Chem. C* **2010**, *114*, 11853–11860.

[12] a) D. R. Mullins, P. M. Albrecht, T.-L. Chen, F. C. Calaza, M. D. Biegalski, H. M. Christen, S. H. Overbury, *J. Phys. Chem. C* **2012**, *116*, 19419–19428; b) M. A. Henderson, C. L. Perkins, M. H. Engelhard, S. Thevuthasan, C. H. F. Peden, *Surf. Sci.* **2003**, *526*, 1–18.

[13] T. Duchoň, F. Dvořák, M. Aulická, V. Stetsovych, M. Vorokhta, D. Mazur, K. Veltruská, T. Skála, J. Mysliveček, I. Matolínová, V. Matolín, *J. Phys. Chem. C* **2014**, *118*, 357–365.

[14] a) S. Oh, S. Back, W. H. Doh, S. Y. Moon, J. Kim, Y. Jung, J. Y. Park, *RSC Adv.* **2017**, *7*, 45003–45009; b) T. Jin, Y. Zhou, G. J. Mains, J. M. White, *J. Phys. Chem.* **1987**, *91*, 5931–5937; c) E. M. Slavinskaya, A. I. Stadnichenko, V. V. Muravyov, T. Y. Kardash, E. A. Derevyannikova, V. I. Zaikovskii, O. A. Stonkus, I. N. Lapin, V. A. Svetlichnyi, A. I. Boronin, *ChemCatChem* **2018**, *10*, 2232–2247.

[15] M. Happel, J. Mysliveček, V. Johánek, F. Dvořák, O. Stetsovych, Y. Lykhach, V. Matolín, J. Libuda, *J. Catal.* **2012**, *289*, 118–126.

[16] H. A. Aleksandrov, K. M. Neyman, G. N. Vayssilov, *Phys. Chem. Chem. Phys.* **2015**, *17*, 14551–14560.

[17] F. M. Hoffmann, *Surf. Sci. Rep.* **1983**, *3*, 107–192.

[18] J. Yoshinobu, M. Kawai, *J. Chem. Phys.* **1995**, *103*, 3220–3229.

[19] V. Matolín, I. Matolínová, F. Dvořák, V. Johánek, J. Mysliveček, K. C. Prince, T. Skála, O. Stetsovych, N. Tsud, M. Václavů, B. Šmíd, *Catal. Today* **2012**, *181*, 124–132.

[20] A. Bruix, Y. Lykhach, I. Matolínová, A. Neitzel, T. Skála, N. Tsud, M. Vorokhta, V. Stetsovych, K. Ševčíková, J. Mysliveček, R. Fiala, M. Václavů, K. C. Prince, S. Bruyère, V. Potin, F. Illas, V. Matolín, J. Libuda, K. M. Neyman, *Angew. Chem. Int. Ed.* **2014**, *53*, 10525–10530; *Angew. Chem.* **2014**, *126*, 10693–10698.

[21] N. Daelman, M. Capdevila-Cortada, N. López, *Nat. Mater.* **2019**, *18*, 1215–1221.

[22] a) V. L. Frankland, A. Rosu-Finsen, J. Lasne, M. P. Collings, M. R. S. McCoustra, *Rev. Sci. Instrum.* **2015**, *86*, 055103; b) S. Saloum, M. Naddaf, B. Alkhaled, *Vacuum* **2010**, *85*, 439–442.

[23] a) C. Yang, X. Yu, S. Heißler, P. G. Weidler, A. Nefedov, Y. Wang, C. Wöll, T. Kropp, J. Paier, J. Sauer, *Angew. Chem. Int. Ed.* **2017**, *56*, 16399–16404; *Angew. Chem.* **2017**, *129*, 16618–16623; b) C. Schilling, M. V. Ganduglia-Pirovano, C. Hess, *J. Phys. Chem. Lett.* **2018**, *9*, 6593–6598.

[24] N. Lopez, J. K. Nørskov, T. V. W. Janssens, A. Carlsson, A. Puig-Molina, B. S. Clausen, J. D. Grunwaldt, *J. Catal.* **2004**, *225*, 86–94.

[25] J. Resasco, L. DeRita, S. Dai, J. P. Chada, M. Xu, X. Yan, J. Finzel, S. Hanukovich, A. S. Hoffman, G. W. Graham, S. R. Bare, X. Pan, P. Christopher, *J. Am. Chem. Soc.* **2020**, *142*, 169–184.

GDCh

Research Articles

Angewandte *Chemie*
International Edition

Research Articles

W. Wan, J. Geiger, N. Berdunov,
M. Lopez Luna, S. W. Chee, N. Daelman,
N. López,* S. Shaikhutdinov,*
B. Roldan Cuenya* ——————— **e202112640**

Highly Stable and Reactive Platinum Single
Atoms on Oxygen Plasma-Functionalized
CeO_2 Surfaces: Nanostructuring and Peroxo
Effects
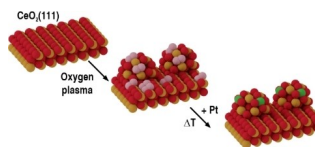
Pre-treatment of the ceria (CeO_2) surface
with oxygen plasma assists the forma-
tion of highly dense and stable Pt single
atoms resistant to sintering under CO
oxidation conditions. The effect is as-
signed to plasma-induced oxide nano-
structuring and the formation of surface
peroxo species which favor single-atom
metal adsorption. This approach can be
utilized for the preparation of stable
single-atom catalysts with a high density
of active sites.

Coupling Metal and Support Redox Terms in Single-Atom Catalysts

Julian Geiger[1,2,*] and Núria López[1,*]

[1]*Institute of Chemical Research of Catalonia (ICIQ), The Barcelona Institute of Science and Technology (BIST), Av. Països Catalans 16, 43007 Tarragona, Spain.*

[2]*Universitat Rovira i Virgili, Av. Catalunya, 35, 43002 Tarragona, Spain.*

[*]Corresponding author(s): Julian Geiger, jgeiger@iciq.es; Núria López, nlopez@iciq.es

September 1, 2023

Abstract

Single-Atom Catalysts (SACs) have emerged as a new class of materials with the best noble metal utilization. The atomic dispersion leads to strong coupling with the support, which can enable facile electron transfer between both. In the present work, we evaluate how the reducibility of the oxide matrix, in this case, ceria, affects the dynamic charge transfer for isolated gold and platinum atoms. We find that the number of accessible states in the electronic ensembles increases significantly due to oxide defects, converting them into almost continuous distributions that can expand up to $1\,\mathrm{eV}$ in magnitude. At elevated temperatures, surface reduction slows down electron transfer events involving the single-atom, thus stabilizing unusual platinum charge states. Our results demonstrate how the coupling of support electronic structure and single-atom redox states can be harvested to control the dynamic behavior of SACs.

Introduction

The utilization of noble metals as catalysts appeared as a Holy Grail in catalysis when Haruta and co. identified low-temperature CO oxidation on gold nanoparticles with sizes around $1\text{-}2\,\text{nm}$[1]. Activity was found to improve when reaching the nanoscale[2–4], and yet, the amount of noble metal can be further reduced. Ultimate atom utilization is reached when isolated single atoms (SAs) comprise the catalytically active sites[5], with the term Single-Atom Catalyst (SAC) first coined for Pt_1/FeO_x in 2011[6]. While dispersed single atoms have only recently been detected[6], their unambiguous identification is now considered (almost) routine, thanks to modern developments in microscopy[7]. Since its inception, the field has grown in an exponential manner[8,9], and with SACs reaching metal loadings as high as 23wt%, it is rapidly approaching maturity for industrial application[10–16].

Among possible support materials, reducible oxides are particularly suitable to disperse single atoms, due to their ability to form (strong) Metal-Support Interactions (MSIs)[17–19]. Ceria plays a unique role, as it combines easy surface reducibility, high oxygen-storage capacity, and the ability to supply reactive oxygen[20], leading to its widespread use in catalyzing chemical transformations[21–26]. Similarly, ceria-based SACs have shown unprecedented performance in various reactions, such as (preferential) oxidation of CO[27–29] or the Water-Gas Shift (WGS) reaction[5,30]. While the true nature of the active site is often unknown[18], for isolated platinum atoms, square-planar (100)-like coordination environments that allow stabilization up to temperatures of $800\,\text{K}$ were unambiguously identified[10,28,31,32]. The particular sites are found on (111) step edges, nanoparticles/nanoislands[16,28,31–33], and can be formed on extended (100) via dynamic restructuring of the oxide sublattice[34,35].

It was for the $Pt_1/CeO_2(100)$ system, for which we recently discovered dynamic redox coupling between the isolated platinum atom and the ceria support[36], adding an additional electronic degree of freedom. The effect is possible due to the alignment of the metal and oxide electronic states, which can become close enough so that electron transfer from the metal to the semiconductor support occurs. On ceria, the electrons localize on Ce^{4+} centers

and cause local lattice distortions which effectively screen the charge. The coupling of an excess electron with the local phonon cloud results in a quasiparticle denoted as a polaron. Lastly, the existence of various polaron distributions within the ceria support can give rise to quasi-degenerate electronic ensembles at varying metal oxidation states (mOS)[37]. Preliminary evidence suggests that the phenomenon also occurs for other platinum-group metals and reducible semiconductor oxides[36], rendering the assignment of a single mOS an exceedingly simplistic approximation[38]. In addition, experimentally prepared oxide supports are usually oxygen-depleted and rich with vacancies due to the thermal treatments employed in their synthesis. However, the effect of surface reduction and inherent polaronic fine structure of the support[39], on the mOS dynamics of dispersed single metal atoms has not been investigated.

In this work, we address the role of intrinsic oxide polarons when coupling with the metal states by sampling electronic ensembles of SA gold and platinum on two typical (100)-like coordination environments of ceria. We identify a rich interplay between the redox states of the metal and the inherent electronic fine structure of the support. The limited capacity to accommodate increasing amounts of polarons leads to the stabilization of platinum in unusual charge states. Thus, we expect control of surface reduction to present a viable strategy for reducible oxide-based SACs to target more reduced metal states, ultimately improving catalyst performances[40].

Computational Details

Density Functional Theory simulations were performed using the Vienna Ab Initio Simulation Package (VASP; version 5.4.4)[41] and the Perdew–Burke–Ernzerhof (PBE) functional[42]. To achieve electron localization, we further applied the Hubbard U correction[43] to the cerium centers[44]. Here, we use an effective U_{eff} of 4.5 eV, following suggested values in the literature[36,45]. Core electrons were treated with the Projector Augmented Wave (PAW)

163

method[46,47], while valence electrons were expanded in plane waves with a kinetic energy cut-off of $500\,\mathrm{eV}$. If not indicated otherwise, total energies were evaluated at the Gamma point (a comparison to a 3x3x1 k-point sampling for the pristine surfaces is provided in Figs. S1 and S2). Electronic convergence was set to $1\times10^{-6}\,\mathrm{eV}$ and atomic positions were converged until residual forces fell below $0.015\,\mathrm{eV\,\mathring{A}^{-1}}$. Throughout, we assigned discrete mOS states by the localized magnetic moments of cerium atoms, with an applied threshold of $0.8\,\mu_B$. Through an extensive validation of the overall methodology in our previous works[36,48], we found this to be the best proxy for the SA oxidation state and preferred over the evaluation of Bader charges or metal magnetization. Molecular Dynamics (MD) simulations were conducted within the canonical NVT ensemble (constant number of particles, N, volume, V, and temperature, T), using the Nosé-Hoover thermostat[49] at an average temperature of $600\,\mathrm{K}$. Data was collected for a total of $12\,\mathrm{ps}$ and at a time step of $3\,\mathrm{fs}$, with a relaxed electronic convergence criterion of $1\times10^{-5}\,\mathrm{eV}$ applied at each ionic step.

Slab models were built as p(3x3) supercells[50] based on optimized ceria bulk (theoretical lattice parameter: $5.491\,\mathring{A}$). They extend nine atomic layers along the z-direction, of which the bottom three were kept fixed at the optimized bulk positions. Around $15\,\mathring{A}$ of vacuum were added on top of the surfaces. To resolve the dipole of oxygen-terminated $CeO_2(100)$ after bulk cleavage, we moved half of the surface oxygen atoms to the bottom of the slab in a chequerboard-like manner. Vacancy formation energies ("vac"; for the pristine surfaces) and metal adsorption energies ("ads") were calculated as follows:

$$E_{vac} = E_{total} - E_{surf} + \frac{1}{2}E_{ox} \tag{1}$$

$$E_{ads} = E_{total} - E_{surf} - E_M^{bulk} \tag{2}$$

$$E_{ads}^{vac} = E_{total} - E_{surf} - E_M^{bulk} \tag{3}$$

$$E_{ads}^{O} = E_{total} - E_{surf} - E_M^{bulk} - \frac{1}{2}E_{ox} \tag{4}$$

where E_{total} denotes the DFT energy of the optimized system, E_{surf} the energy of the respective pristine surface (in the case of E_{ads}^{vac} the defective surface at its ground state polaron distribution), E_{ox} the energy of diatomic oxygen, and E_M^{bulk} the energy of the metal atom in bulk.

Results and discussion

To investigate the influence of support reduction on the coupling of surface and metal redox terms, we studied ceria-based Pt and Au-SACs on two coordination environments of $CeO_2(100)$, termed "2O" and "4O". Based on the nondefective support, Fig. 1a and **d**, we introduced a surface vacancy adjacent to the metal, Fig. 1b and **e**, implying a surface vacancy concentration of around 11% (in addition to the removal of 50% of the oxygen atoms from the polar surface via reconstruction; see Computational Details). Vacancy introduction leads to two excess electrons in the lattice, which reduce Ce^{4+} to Ce^{3+} centers. To decouple electronic from geometric effects, we further investigated the effect of a bulk vacancy for the Pt-2O system, Fig. 1g, implying a vacancy concentration of around 6% in the corresponding oxygen layer. For these structures, we then sampled all possible surface polaron distributions with up to two (four) Ce^{3+} centers in the absence (presence) of the respective vacancy. Lastly, we investigated the effect of an electron-withdrawing group on the distributions by applying the same sampling with up to two initial Ce^{3+} for structures with an additional oxygen atom added to the surface, Fig. 1c and f.
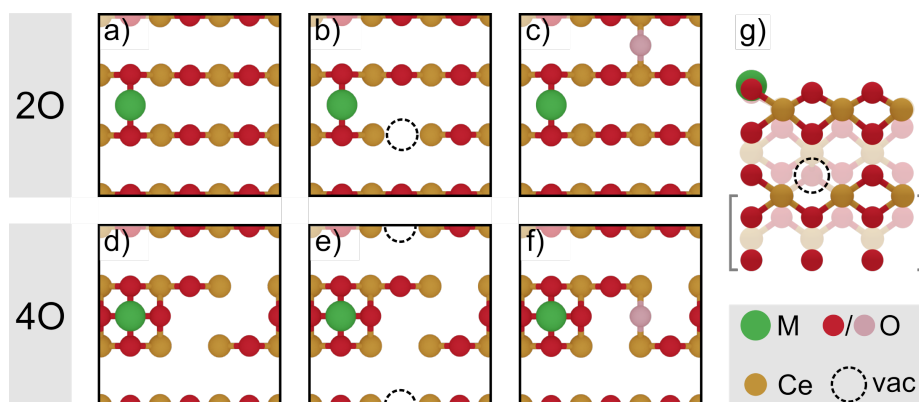
Fig. 1: a - f) Surface layer top views of the investigated SACs in the 2O and 4O coordination environments of $CeO_2(100)$ in our p(3x3) supercells, presented in the top and bottom row, respectively. **a, d)** SACs based on the unmodified ceria surfaces, **b, e)** SACs based on the defective ceria surfaces, and **c, f)** SACs with an extra oxygen atom (shown in pink), added as electron-withdrawing group. **g)** Side-view of the employed slab model, extending nine atomic layers along the z-direction. The location of the investigated bulk vacancy and the fixed bottom layers are indicated. Background atoms are shown with reduced opacity. Color code (bottom right): green = metal (M); orange = cerium (Ce); red/pink = lattice/added oxygen (O); dashed circle = oxygen vacancy (vac).

Local polaron structure of defective $CeO_2(100)$

While vacancy formation was extensively studied on the most stable (111) surface[51–53], research on the (100) facet is more scarce[54–56]. We therefore first outline the influence of local polaron structure on the bare $CeO_2(100)$ supports, as shown in Fig. S1 and S2. The stabilities of the defective surfaces, and thus vacancy formation energies, are determined by several geometric properties[56], which can be summarized as follows: i) the ability of the lattice to adjust for the more spacious, reduced Ce^{3+} centers, ii) the accommodation of oxygen distortions towards the newly formed empty site, and lastly, iii) the repulsion between the Ce^{3+} centers. These effects were used to rationalize the global minimum structure for defective (100), reported as a surface vacancy with two surface polarons located at the NN positions to the vacancy[56,57].

By considering all symmetry-inequivalent distributions of two surface polarons on de-

fective, unreconstructed $CeO_2(100)$ in our p(3x3) supercell, we obtain vacancy formation energies of 1.40 - 2.30 eV, in line with previously reported results[20,50,56,58]. The significant influence of the computational setup on the ordering of individual states should be noted[56,59] and is further discussed in Note S1. Nonetheless, low-energy structures are generally closely spaced within the energy spectrum and therefore easily accessible at typical operating temperatures. Excess electron localization in the subsurface layer, see Fig. S1, is more endothermic (1.80 - 2.09 eV) as the cerium ions are more highly coordinated and their reduction therefore incurs greater lattice strain.

For defective $CeO_2(100)$-4O, we placed the vacancy in the Ce-O-Ce row unaffected by the reconstruction, see Fig. S2, such that the energy trends can be primarily attributed to local polaron structure. Vacancy formation energies span a similar range of 1.37 - 2.15 eV, but as the reconstruction renders all cerium centers symmetry-inequivalent, the ensemble is composed of a higher number of more closely-spaced states, see Fig. S2. Excess electrons again preferably localize at low-coordinated surface cerium centers, however, due to the more open nature of reconstructed $CeO_2(100)$-4O, subsurface sites are more easily populated (1.60 - 2.53 eV) than for defective $CeO_2(100)$-2O, see Fig. S1. Overall, the large energy ranges of around 1 eV obtained for both surfaces are indicative of the significant influence of the local polaron structure. Its consideration is therefore crucial to fully characterize ceria-based SACs.

Static coupling of support and metal states

Upon adsorption of SA-Pt on nondefective, unreconstructed $CeO_2(100)$-2O, the metal atom adapts oxidation states of 0, +1 and +2[36], with ground state adsorption energies of 0.28 eV, 0.02 eV and 0.09 eV, respectively, see Fig. 2a. As the Pt^+ and Pt^{2+} ensembles span energy ranges of 0.15 eV and 0.40 eV, they are significantly overlapping. This energy overlap was shown to give rise to dynamic mOS behavior at elevated temperatures and improve low-temperature CO oxidation activity of the SAC[36]. In contrast, Au-2O is found exclusively

in a +1 state, with adsorption energies ranging from –0.28 to -0.13 eV. When anchored in the square-planar environment available on reconstructed $CeO_2(100)$-4O, the dynamicity trends of the two metals are inverted. Owed to the higher coordination number, Au^{3+} species are now accessible and represent the ground state species at an adsorption energy of -0.17 eV, while formation of Au^+, is endothermic by at least 0.10 eV, see Fig. 2c. As such, we expect dynamic transformations between the two species via two-electron transfers, albeit the high energy difference of 0.27 eV between the ensemble ground states should be noted. For Pt-4O, on the other hand, the platinum atom is found exclusively in highly stable (-1.02 to -0.34 eV) Pt^{2+} states, in line with experiments[28,32]. Thus, the two metals provide a unique opportunity to investigate the influence of support reduction on mOS dynamics in both coordination environments provided by $CeO_2(100)$.

Overall, we find that the introduction of a surface vacancy (denoted "vac" in Fig. 2) does not alter the accessible mOS, or ground state species for any of the systems. Instead, as the larger number of surface polarons allows for more possible distributions, and therefore accessible excited states, the energy spans of the ensembles are expanded upwards. This is evident, for instance, in Au-2O (Fig. 2b), where the span grows from 0.15 to 0.76 eV, while the ground state energy remains largely unchanged at around -0.30 eV. For Pt^0, a single state on nondefective $CeO_2(100)$-2O, an ensemble of eleven closely-spaced states spanning an energy range of 0.34 eV emerges, while for Pt-4O, the ensemble reaches a magnitude of 1.39 eV. The whole set is listed in Table S3.

In addition, ground state energies of highly charged species in the dynamic systems, Pt-2O and Au-4O, get shifted upwards upon vacancy formation, while they remain largely unchanged for the static systems, Pt-4O and Au-2O. Pt^{2+} will serve as an example to rationalize this difference: Since 2+ is the only accessible mOS in Pt-4O, it is retained in the presence of the vacancy. The resulting energy spectrum, see Fig. 2d, therefore resembles a near-continuum distribution of states with an almost unchanged ground state energy of around -1 eV. For nondefective Pt-2O, on the other hand, structures with lower mOS val-

ues of 0 and +1 are easily accessible, see Fig. 2a. Hence, in the presence of the vacancy, more reduced metal states get populated at the expense of otherwise accessible (highly) charged states. Here, the interplay of two opposing forces is decisive: i) the tendency of the SA-metal to adapt particular mOS states within given chemical environments, following rules derived from ligand field theory, and ii) the minimization of surface strain through a decrease in the number of localized excess electrons via metal reduction. Furthermore, we note that the inter-conversion of states during optimization points to the fundamental uncertainty of the completeness of the sampling, see Note S2 and Table S4. In conjunction with the combinatorial explosion of the number of distributions (Fig. 2 compiles the energies of 582 converged structures), this makes the full characterization of the dynamic ensembles a challenging problem. By circumventing the need for explicit DFT evaluation, Machine Learning techniques hold the promise to aid future efforts of exploring such complex polaron spaces[60].

Lastly, when positioning the vacancy in the bulk of the slab of Pt-2O, while retaining polarons in the surface layer, we observe the same qualitative alterations of the ensembles, see Fig. 1g and Fig. S3, thus confirming the origin of the alterations in the local surface polaron structure. In contrast to surface reduction, the presence of a strongly electron-withdrawing group like oxygen, see Fig. 1c and f, causes the depletion of electrons from the SA metals, yielding only highly oxidized metal species, see Fig. S4).
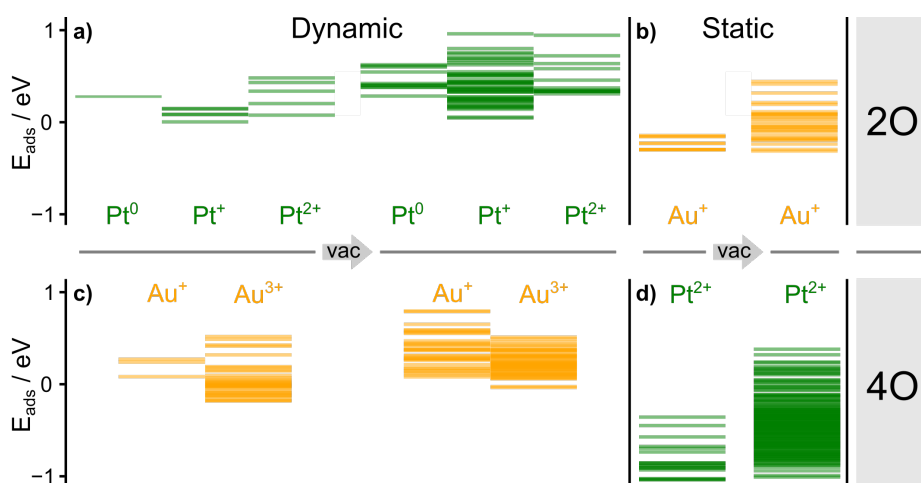
Fig. 2: Ground and excited states composing the electronic ensembles of Pt- and Au-SACs on nondefective and defective ("vac") on: **a, b)** $CeO_2(100)$-2O and **c, d)** $CeO_2(100)$-4O supports. Pt-2O and Au-4O present overlapping ensembles at varying metal oxidation states (mOS) of $0/+1/+2$, and $+1/+3$, respectively, while for Au-2O and Pt-4O only fixed mOS of $+1$ and $+2$ are obtained. Individual states are shown with decreased opacity, such that their overlap in high-density regions is indicated by higher color saturation.

Dynamic coupling of support and metal states

To probe the influence of surface reduction and local polaron structure on the dynamic behavior at elevated temperatures, we performed 12 ps ab initio Molecular Dynamics (AIMD) simulations at 600 K for the nondefective and defective Pt-2O SACs in our p(3x3) supercells (see Computational Details). The results are presented in Fig. 3, while additional information is provided in Note S3. Overall, we find nondefective Pt-2O in a Pt^+ (Pt^{2+}) state for 5.7 ps (6.2 ps), that is, 48% (52%) of the full trajectory, and only one short-lived ($\approx$ 100 fs) Pt^0 species. Excess electrons are exclusively localized at the NN positions to the metal, and, in the case of Pt^{2+} mainly diagonal to each other, see Supplementary Video 1. In total, we count approximately 48 polaron hopping events and 40 mOS changes (see Note S3).

In the presence of the surface vacancy, the relative abundances of the different platinum species are significantly altered, see Fig. 3g. With 10.2 ps, or 86% of the full trajectory, the metal now resides overwhelmingly as Pt^+, while Pt^{2+} states account for a total of just 1.6 ps, or 13%. Again, only a single, short-lived Pt^0 state is formed. While we count an increased number of around 54 electron transfer events, mOS changes of the SA-Pt occur less frequently ($\approx$ 19 times) than for the nondefective support, see Supplementary Video 2.

As outlined above for the static sampling, the presence of two additional electrons in the surface leads to a higher number of possible polaron distributions, see Table S4. Hence, there exist more potential electron transfer channels within the ceria support, resulting in the observed statistically higher frequency of these events. However, the influence of surface reduction on the formation of Pt^{2+} is inverted: On one hand, electron injection from the metal to the support is thermodynamically disfavored due to the higher number of localized excess electrons and thus surface strain, stabilizing Pt^+ in favor of Pt^{2+}. On the other hand, as otherwise reducible Ce^{4+} centers are more likely to already be reduced, available electron transfer channels from the metal to the support are blocked, making the formation of highly charged platinum species kinetically hindered. A purely static representation, as shown in Fig. 2, therefore cannot capture the full picture, highlighting the importance of entropic

contributions to dynamic catalyst behavior[61].
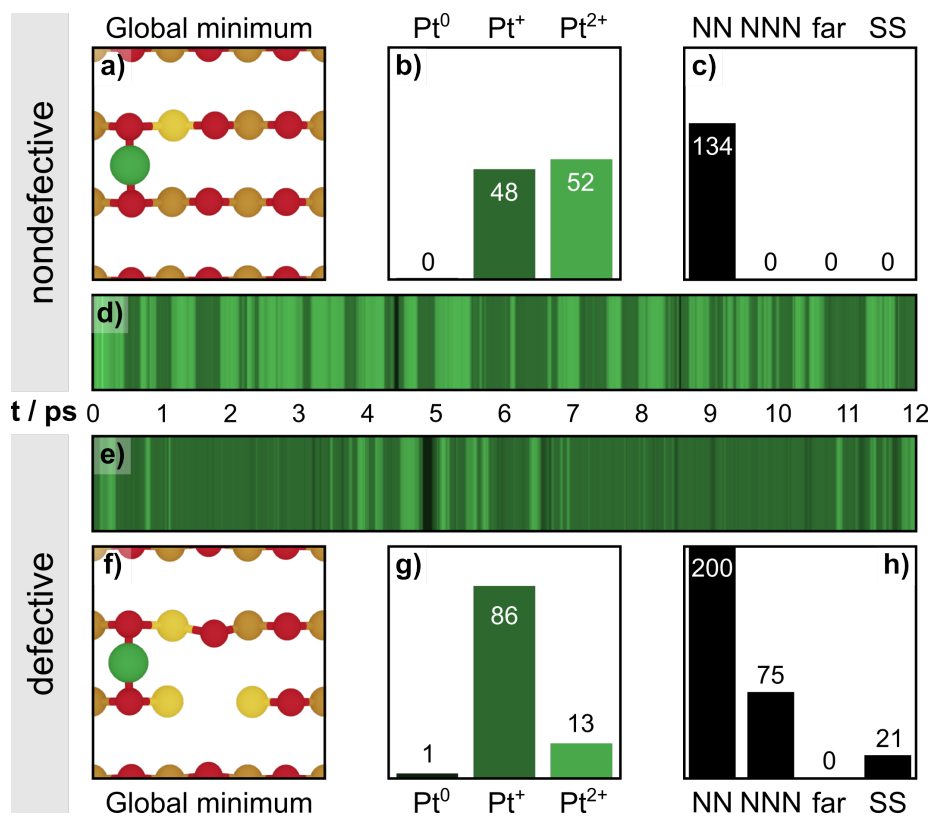
Fig. 3: Ab initio Molecular Dynamics simulations of the Pt-2O SAC on nondefective and defective ceria supports at $600\,\mathrm{K}$. **a, f)**; Global minimum structures obtained from the static DFT sampling presented in Fig. 2. Color code: Pt, green; Ce^{4+}, orange; Ce^{3+}, yellow; O^{2-}, red. **b, g)**; Retention times (in % of the $12\,\mathrm{ps}$ trajectories) of the platinum atom in the different mOS states, and **c, h)**; of the polarons in nearest neighbor (NN), next-nearest neighbor (NNN), and more distant positions (far) relative to the metal atom, as well as in the subsurface (SS) layer of the slab (values above $100\,\%$ are due to the presence of multiple polarons). **d, e)**; Visual representation of the trajectories of the platinum mOS, following the same color coding used in panels **b)** and **g)**.

Conclusions

We have identified a rich interplay between metal redox terms and support electronic structure for ceria-based SACs. Increased surface polaron concentrations due to surface reduction lead to a significant expansion of electronic ensembles composed of low-lying excited states, spanning energy ranges of over $1\,\mathrm{eV}$. The adoption of favorable metal oxidation states in given coordination environments is counteracted by the inclination of the support to decrease surface strain. As we demonstrated for platinum, the balancing of these opposing forces can drive the dynamic equilibrium of single metal atoms towards unusual charge states. We therefore expect control of the degree of surface reduction to allow for a fine-tuning of the metal electronic state, ultimately paving the way toward future performance improvements of reducible oxide-based SACs.

Associated Content

Supporting Information The Supporting Information is available free of charge on the ACS Publications website at DOI: `doi`.

It contains an in-depth discussion of the employed methodology for the static sampling of local polaron distributions and ab initio Molecular Dynamics simulations, including the influence of supercell size, symmetry, k-point sampling, and a comparison to literature. It further provides captions for the Supplementary Videos. Selected local polaron distributions of the pristine, defective slabs are shown and compared to a 3x3x1 k-point sampling. The influence of a bulk vacancy, as well as an electron-withdrawing additional surface oxygen atom, are presented. Lastly, individual energies of local polaron distributions of the pristine, defective surfaces, and energy ranges of the ensembles composing each SAC are tabulated.

Data availability DFT optimized structures and Molecular Dynamics trajectories are available in the ioChem-BD database[62]: `https://doi.org/10.19061/iochem-bd-1-246`

Author Information

Corresponding Author

*E-mail: jgeiger@iciq.es, nlopez@iciq.es

ORCID

Julian Geiger: 0000-0003-0023-1960

Núria López: 0000-0001-9150-5941

Notes

The authors declare no competing financial interest.

Acknowledgments

References

(1) Haruta, M.; Kobayashi, T.; Sano, H.; Yamada, N. Novel Gold Catalysts for the Oxidation of Carbon Monoxide at a Temperature far Below 0 °C. *Chem. Lett.* **1987**, *16*, 405–408.

(2) Lopez, N.; Janssens, T. V.; Clausen, B. S.; Xu, Y.; Mavrikakis, M.; Bligaard, T.; Nørskov, J. K. On the origin of the catalytic activity of gold nanoparticles for low-temperature CO oxidation. *J. Catal.* **2004**, *223*, 232–235.

(3) Min, B. K.; Friend, C. M. Heterogeneous gold-based catalysis for green chemistry: Low-temperature CO oxidation and propene oxidation. *Chem. Rev.* **2007**, *107*, 2709–2724.

(4) Wittstock, A.; Zielasek, V.; Biener, J.; Friend, C.; Bäumer, M. Nanoporous gold catalysts for selective gas-phase oxidative coupling of methanol at low temperature. *Science* **2010**, *327*, 319–322.

(5) Fu, Q.; Saltsburg, H.; Flytzani-Stephanopoulos, M. Active nonmetallic Au and Pt species on ceria-based water-gas shift catalysts. *Science* **2003**, *301*, 935–938.

(6) Qiao, B.; Wang, A.; Yang, X.; Allard, L. F.; Jiang, Z.; Cui, Y.; Liu, J.; Li, J.; Zhang, T. Single-atom catalysis of CO oxidation using Pt_1/FeO_x. *Nat. Chem.* **2011**, *3*, 634–641.

(7) Mitchell, S.; Par, F.; Akl, D. F.; Collins, S. M.; Kepaptsoglou, D. M.; Ramasse, Q. M.; Garcia-gasulla, D.; Javier, P. Automated Image Analysis for Single-Atom Detection in Catalytic Materials by Transmission Electron Microscopy. *J. Am. Chem. Soc.* **2022**, *18*, 8018–8029.

(8) Wang, A.; Li, J.; Zhang, T. Heterogeneous single-atom catalysis. *Nat. Rev. Chem.* **2018**, *2*, 65–81.

(9) Liu, J. Catalysis by Supported Single Metal Atoms. *ACS Catal.* **2017**, *7*, 34–59.

(10) Kunwar, D.; Zhou, S.; Delariva, A.; Peterson, E. J.; Xiong, H.; Pereira-Hernández, X. I.; Purdy, S. C.; Ter Veen, R.; Brongersma, H. H.; Miller, J. T. et al. Stabilizing High Metal Loadings of Thermally Stable Platinum Single Atoms on an Industrial Catalyst Support. *ACS Catal.* **2019**, *9*, 3978–3990.

(11) Beniya, A.; Higashi, S. Towards dense single-atom catalysts for future automotive applications. *Nat. Catal.* **2019**, *2*, 590–602.

(12) Xiong, Y.; Sun, W.; Han, Y.; Xin, P.; Zheng, X.; Yan, W.; Dong, J.; Zhang, J.; Wang, D.; Li, Y. Cobalt single atom site catalysts with ultrahigh metal loading for enhanced aerobic oxidation of ethylbenzene. *Nano Res.* **2021**, *14*, 2418–2423.

(13) Datye, A. K.; Guo, H. Single atom catalysis poised to transition from an academic curiosity to an industrially relevant technology. *Nat. Commun.* **2021**, *12*, 895.

(14) Hai, X.; Xi, S.; Mitchell, S.; Harrath, K.; Xu, H.; Akl, D. F.; Kong, D.; Li, J.; Li, Z.; Sun, T. et al. Scalable two-step annealing method for preparing ultra-high-density single-atom catalyst libraries. *Nat. Nanotechnol.* **2022**, *17*, 174–181.

(15) Yang, J.; Li, W.; Tan, S.; Xu, K.; Wang, Y.; Wang, D.; Li, Y. The Electronic Metal–Support Interaction Directing the Design of Single Atomic Site Catalysts: Achieving High Efficiency Towards Hydrogen Evolution. *Angew. Chem. Int. Ed.* **2021**, *60*, 19085–19091.

(16) Wan, W.; Geiger, J.; Berdunov, N.; Lopez Luna, M.; Chee, S. W.; Daelman, N.; López, N.; Shaikhutdinov, S.; Roldan Cuenya, B. Highly Stable and Reactive Platinum Single Atoms on Oxygen Plasma-Functionalized CeO_2 Surfaces: Nanostructuring and Peroxo Effects. *Angew. Chem. Int. Ed.* **2022**, *61*, e202112640.

(17) Tauster, S.; Fung, S.; Garten, R. L. Strong Metal-Support Interactions. Group 8 Noble Metals Supported on TiO_2. *J. Am. Chem. Soc.* **1978**, *100*, 170–175.

(18) Lang, R.; Du, X.; Huang, Y.; Jiang, X.; Zhang, Q.; Guo, Y.; Liu, K.; Qiao, B.; Wang, A.; Zhang, T. Single-atom catalysts based on the metal-oxide interaction. *Chem. Rev.* **2020**, *120*, 11986–12043.

(19) Hulva, J.; Meier, M.; Bliem, R.; Jakub, Z.; Kraushofer, F.; Schmid, M.; Diebold, U.; Franchini, C.; Parkinson, G. S. Unraveling CO adsorption on model single-atom catalysts. *Science* **2021**, *371*, 375–379.

(20) Capdevila-Cortada, M.; Vilé, G.; Teschner, D.; Pérez-Ramírez, J.; López, N. Reactivity descriptors for ceria in catalysis. *Appl. Catal. B* **2016**, *197*, 299–312.

(21) Trovarelli, A. *Catalysis by ceria and related materials*; World Scientific, 2002; Vol. 2.

(22) Amrute, A. P.; Mondelli, C.; Moser, M.; Novell-Leruth, G.; López, N.; Rosenthal, D.; Farra, R.; Schuster, M. E.; Teschner, D.; Schmidt, T. et al. Performance, structure, and mechanism of CeO_2 in HCl oxidation to Cl_2. *J. Catal.* **2012**, *286*, 287–297.

(23) Capdevila-Cortada, M.; García-Melchor, M.; López, N. Unraveling the structure sensitivity in methanol conversion on CeO_2: A DFT+*U* study. *J. Catal.* **2015**, *327*, 58–64.

(24) McCabe, R. W.; Trovarelli, A. Forty years of catalysis by ceria: a success story. *Appl. Catal. B* **2016**, *197*, 1.

(25) Scharfe, M.; Capdevila-Cortada, M.; Kondratenko, V. A.; Kondratenko, E. V.; Colussi, S.; Trovarelli, A.; López, N.; Pérez-Ramírez, J. Mechanism of Ethylene Oxychlorination on Ceria. *ACS Catal.* **2018**, *8*, 2651–2663.

(26) Puértolas, B.; Rellán-Piñeiro, M.; Núñez-Rico, J. L.; Amrute, A. P.; Vidal-Ferran, A.; López, N.; Pérez-Ramírez, J.; Wershofen, S.; Rella, M.; Nu, L. et al. Mechanistic Insights into the Ceria-Catalyzed Synthesis of Carbamates as Polyurethane Precursors. *ACS Catal.* **2019**, *9*, 7708–7720.

(27) Qiao, B.; Liu, J.; Wang, Y.-G.; Lin, Q.; Liu, X.; Wang, A.; Li, J.; Zhang, T.; Liu, J. Highly Efficient Catalysis of Preferential Oxidation of CO in H_2-Rich Stream by Gold Single-Atom Catalysts. *ACS Catal.* **2015**, *5*, 6249–6254.

(28) Jones, J.; Xiong, H.; DeLaRiva, A. T.; Peterson, E. J.; Pham, H.; Challa, S. R.; Qi, G.; Oh, S.; Wiebenga, M. H.; Hernández, X. I. P. et al. Thermally stable single-atom platinum-on-ceria catalysts via atom trapping. *Science* **2016**, *353*, 150–154.

(29) Nie, L.; Mei, D.; Xiong, H.; Peng, B.; Ren, Z.; Hernandez, X. I. P.; DeLaRiva, A.; Wang, M.; Engelhard, M. H.; Kovarik, L. et al. Activation of surface lattice oxygen in single-atom Pt/CeO_2 for low-temperature CO oxidation. *Science* **2017**, *358*, 1419–1423.

(30) Li, Y.; Kottwitz, M.; Vincent, J. L.; Enright, M. J.; Liu, Z.; Zhang, L.; Huang, J.; Senanayake, S. D.; Yang, W. C. D.; Crozier, P. A. et al. Dynamic structure of active sites in ceria-supported Pt catalysts for the water gas shift reaction. *Nat. Commun.* **2021**, *12*, 914.

(31) Bruix, A.; Lykhach, Y.; Matolínová, I.; Neitzel, A.; Skála, T.; Tsud, N.; Vorokhta, M.; Stetsovych, V.; Ševčíková, K.; Mysliveček, J. et al. Maximum Noble-Metal Efficiency in Catalytic Materials: Atomically Dispersed Surface Platinum. *Angew. Chem. Int. Ed.* **2014**, *53*, 10525–10530.

(32) Dvořák, F.; Camellone, M. F.; Tovt, A.; Tran, N. D.; Negreiros, F. R.; Vorokhta, M.; Skála, T.; Matolínová, I.; Mysliveček, J.; Matolín, V. et al. Creating single-atom Pt-ceria catalysts by surface step decoration. *Nat. Commun.* **2016**, *7*, 10801.

(33) Figueroba, A.; Kovács, G.; Bruix, A.; Neyman, K. M. Towards stable single-atom catalysts: strong binding of atomically dispersed transition metals on the surface of nanostructured ceria. *Catal. Sci. Technol.* **2016**, *6*, 6806–6813.

(34) Capdevila-Cortada, M.; López, N. Entropic contributions enhance polarity compensation for $CeO_2(100)$ surfaces. *Nat. Mater.* **2017**, *16*, 328–334.

(35) Yang, C.; Capdevila-Cortada, M.; Dong, C.; Zhou, Y.; Wang, J.; Yu, X.; Nefedov, A.; Heißler, S.; López, N.; Shen, W. et al. Surface Refaceting Mechanism on Cubic Ceria. *J. Phys. Chem. Lett* **2020**, *11*, 7925–7931.

(36) Daelman, N.; Capdevila-Cortada, M.; López, N. Dynamic charge and oxidation state of Pt/CeO_2 single-atom catalysts. *Nat. Mater.* **2019**, *18*, 1215–1221.

(37) Daelman, N.; Hegner, F. S.; Rellán-Piñeiro, M.; Capdevila-Cortada, M.; García-Muelas, R.; López, N. Quasi-degenerate states and their dynamics in oxygen deficient reducible metal oxides. *J. Chem. Phys.* **2020**, *152*, 050901.

(38) Lykhach, Y.; Kozlov, S. M.; Skála, T.; Tovt, A.; Stetsovych, V.; Tsud, N.; Dvořák, F.; Johánek, V.; Neitzel, A.; Mysliveček, J. et al. Counting electrons on supported nanoparticles. *Nat. Mater.* **2016**, *15*, 284–288.

(39) Murgida, G. E.; Ferrari, V.; Ganduglia-Pirovano, M. V.; Llois, A. M. Ordering of oxygen vacancies and excess charge localization in bulk ceria: A DFT+U study. *Phys. Rev. B* **2014**, *90*, 115120.

(40) Cheng, X.; Xiao, B.; Chen, Y.; Wang, Y.; Zheng, L.; Lu, Y.; Li, H.; Chen, G. Ligand Charge Donation–Acquisition Balance: A Unique Strategy to Boost Single Pt Atom Catalyst Mass Activity toward the Hydrogen Evolution Reaction. *ACS Catal.* **2022**, *12*, 5970–5978.

(41) Kresse, G.; Furthmüller, J. Efficiency of ab-initio total energy calculations for metals and semiconductors using a plane-wave basis set. *Comput. Mater. Sci.* **1996**, *6*, 15–50.

(42) Perdew, J. P.; Burke, K.; Ernzerhof, M. Generalized Gradient Approximation Made Simple. *Phys. Rev. Lett.* **1996**, *77*, 3865–3868.

(43) Hubbard, J. Electron correlations in narrow energy bands. *Proc. R. Soc. A: Math. Phys. Eng. Sci.* **1963**, *276*, 238–257.

(44) Fabris, S.; Gironcoli, S. D.; Baroni, S.; Vicario, G.; Balducci, G. Taming multiple valency with density functionals: A case study of defective ceria. *Phys. Rev. B* **2005**, *71*, 041102.

(45) Capdevila-Cortada, M.; Łodziana, Z.; López, N. Performance of DFT+U approaches in the study of catalytic materials. *ACS Catal.* **2016**, *6*, 8370–8379.

(46) Blöchl, P. E. Projector augmented-wave method. *Phys. Rev. B* **1994**, *50*, 17953–17979.

(47) Joubert, D. From ultrasoft pseudopotentials to the projector augmented-wave method. *Phys. Rev. B* **1999**, *59*, 1758–1775.

(48) Schäfer, T.; Daelman, N.; López, N. Cerium Oxides without U: The Role of Many-Electron Correlation. *J. Phys. Chem. Lett* **2021**, *12*, 6277–6283.

(49) Hoover, W. G. Canonical dynamics: Equilibrium phase-space distributions. *Phys. Rev. A* **1985**, *31*, 1695–1697.

(50) Kropp, T.; Paier, J. Activity versus Selectivity of the Methanol Oxidation at Ceria Surfaces: A Comparative First-Principles Study. *J. Phys. Chem. C* **2015**, *119*, 23021–23031.

(51) Esch, F.; Fabris, S.; Zhou, L.; Montini, T.; Africh, C.; Fornasiero, P.; Comelli, G.; Rosei, R. Electron Localization Determines Defect Formation on Ceria Substrates. *Science* **2005**, *309*, 752–755.

(52) Jerratsch, J. F.; Shao, X.; Nilius, N.; Freund, H. J.; Popa, C.; Ganduglia-Pirovano, M. V.; Burow, A. M.; Sauer, J. Electron Localization in Defective Ceria Films: A Study with Scanning-Tunneling Microscopy and Density-Functional Theory. *Phys. Rev. Lett.* **2011**, *106*, 246801.

(53) Zhang, D.; Han, Z. K.; Murgida, G. E.; Ganduglia-Pirovano, M. V.; Gao, Y. Oxygen-Vacancy Dynamics and Entanglement with Polaron Hopping at the Reduced $CeO_2(111)$ Surface. *Phys. Rev. Lett.* **2019**, *122*, 096101.

(54) Nolan, M.; Grigoleit, S.; Sayle, D. C.; Parker, S. C.; Watson, G. W. Density functional theory studies of the structure and electronic structure of pure and defective low index surfaces of ceria. *Surf. Sci.* **2005**, *576*, 217–229.

(55) Nolan, M. Hybrid density functional theory description of oxygen vacancies in the $CeO_2(110)$ and (100) surfaces. *Chem. Phys. Lett.* **2010**, *499*, 126–130.

(56) Pérez-Bailac, P.; Lustemberg, P. G.; Ganduglia-Pirovano, M. V. Facet-dependent stability of near-surface oxygen vacancies and excess charge localization at CeO_2 surfaces. *J. Phys.: Condens. Matter* **2021**, *33*, 504003.

(57) Ji, W.; Wang, N.; Li, Q.; Zhu, H.; Lin, K.; Deng, J.; Chen, J.; Zhang, H.; Xing, X. Oxygen vacancy distributions and electron localization in a $CeO_2(100)$ nanocube. *Inorg. Chem. Front.* **2022**, *9*, 275–283.

(58) Nolan, M.; Fearon, J. E.; Watson, G. W. Oxygen vacancy formation and migration in ceria. *Solid State Ion.* **2006**, *177*, 3069–3074.

(59) Kullgren, J.; Hermansson, K.; Castleton, C. Many competing ceria (110) oxygen vacancy structures: From small to large supercells. *J. Chem. Phys.* **2012**, *137*, 044705.

(60) Birschitzky, V. C.; Ellinger, F.; Diebold, U.; Reticcioli, M.; Franchini, C. Machine learning for exploring small polaron configurational space. *npj Comput. Mater.* **2022**, *8*, 1–9.

(61) Teschner, D.; Novell-Leruth, G.; Farra, R.; Knop-Gericke, A.; SchlÖgl, R.; Szentmiklósi, L.; Hevia, M. G.; Soerijanto, H.; Schomäcker, R.; Pérez-Ramírez, J. et al.

In situ surface coverage analysis of RuO_2-catalysed HCl oxidation reveals the entropic origin of compensation in heterogeneous catalysis. *Nat. Chem.* **2012**, *4*, 739–745.

(62) Álvarez-Moreno, M.; De Graaf, C.; López, N.; Maseras, F.; Poblet, J. M.; Bo, C. Managing the Computational Chemistry Big Data Problem: The ioChem-BD Platform. *J. Chem. Inf. Model.* **2015**, *55*, 95–103.

TOC Graphic

Check for updates

ARTICLE   OPEN
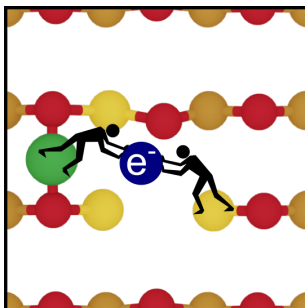
Data-driven models for ground and excited states for Single Atoms on Ceria

Julian Geiger[1,2], Albert Sabadell-Rendón[1,2], Nathan Daelman [1] and Núria López [1 ✉]

Ceria-based single-atom catalysts present complex electronic structures due to the dynamic electron transfer between the metal atoms and the semiconductor oxide support. Understanding these materials implies retrieving all states in these electronic ensembles, which can be limiting if done via density functional theory. Here, we propose a data-driven approach to obtain a parsimonious model identifying the appearance of dynamic charge transfer for the single atoms (SAs). We first constructed a database of (701) electronic configurations for the group 9–11 metals on $CeO_2(100)$. Feature Selection based on predictive Elastic Net and Random Forest models highlights eight fundamental variables: atomic number, ionization potential, size, and metal coordination, metal–oxygen bond strengths, surface strain, and Coulomb interactions. With these variables a Bayesian algorithm yields an expression for the adsorption energies of SAs in ground and low-lying excited states. Our work paves the way towards understanding electronic structure complexity in metal/oxide interfaces.

INTRODUCTION

Single-atom catalysts (SACs) are a promising class of materials that provide the ultimate miniaturization of the active site[1–5]. They present the best utilization of expensive metal atoms, given they can be prepared in high concentrations and defined speciation[6,7]. Various supports have been used to fabricate stable SACs, including other metals, (doped) carbons, metal-organic frameworks, and most commonly oxides, for which the definition was coined[1,3,8]. Stabilization of single atoms (SAs) on oxides is often attributed to a strong metal-support interaction (SMSI), in which electron density is donated from the metal to the support, thus making reducible oxides particularly suitable host materials[3,9]. However, the reverse electron transfer (from the oxide to metal nanoparticles) is also possible[10]. Dispersing metals up to single atoms is very efficient in oxygen-rich environments of Fe_3O_4 and ceria, and stable SAs of rhodium, palladium, platinum and gold[8,11–14] have been characterized.

Owed to their isolated nature, SAs exhibit unusual electronic properties. For instance, in an AgCu single-atom alloy catalyst, free-atom like states of copper were reported[15], while strong electronic coupling in a Pd_1/Fe_2O_3 SAC resulted in improved alkyne semi-hydrogenation performance[16]. Moreover, the oxidation state of the isolated platinum atom in Pt_1/CeO_2 dynamically changes due to the electronic coupling of the metal and ceria support[17]. For ceria, this process results in localized Ce^{3+} centers (polarons). The electron transfer process is assisted by lattice phonons and was therefore coined as phonon-assisted metal-support interaction (PAMSI)[17]. A Born–Haber model was devised to understand the origin of the dynamic behavior of the Pt_1/CeO_2 system that retrieved the energy difference between the adsorbed Pt in its neutral and charged state with concomitant reduction of the oxide. To compensate for the ionization potential of the metal atom, as well as the reduction and distortion of the oxide, covalent Pt–O interactions contribute, and large favorable changes in Coulomb interactions tip the balance.

The dynamic nature of the metal oxidation state (mOS) in Pt_1/CeO_2 challenges the classical assignment of a static charge to SACs[9], thus limiting the applicability of traditional structure-activity relationships. Consequently, Pt_1/CeO_2 needs to be represented as an electronic ensemble with similar geometric structures, but significantly different electron density distributions. Highly active metastable states, which are easily populated under operando conditions, can considerably influence material properties and catalytic reactivities, as has been shown for geometric ensembles[18]. The dynamic effect significantly increases structural and electronic complexity, thus requiring sophisticated multiscale modeling approaches[19]. Similarly, assessing the properties of multiple low-lying electronic states is a non-trivial task. As seen for Pt, these states are closely spaced within the energy spectrum, and the number of possible distributions grows rapidly with the number of electrons exchanged by the isolated metal and the oxide.

Thus, the prediction of dynamic behavior is challenging and we lack a model that provides a physical expression for the interaction between the SAs and the reducible oxide support. Machine-learning (ML) techniques applied to materials modeling hold promise to overcome these hurdles[20–22]. Data-driven models based on readily available physical properties have proven to simplify the analysis of complex configurational spaces. For instance, a Gaussian Process Regression model was used to augment first-principles estimates of the reduction temperatures of 38 metal oxides[23]. ML methods further predicted adsorption energies of SACs on various oxides[24], shed light on the influence of surface modifications on MgO(100) supports[25], and identified aggregation trends compromising SA stability[26]. A Least Absolute Shrinkage and Selection Operator (LASSO) model was used to single out the 75 most representative descriptors out of 300k candidates governing the adsorption of transition metals (TMs) on oxide supports[27]. Many of these exploratory efforts have resulted in robust models, but require large feature spaces and offer limited explainability.

[1]Institute of Chemical Research of Catalonia (ICIQ), The Barcelona Institute of Science and Technology (BIST), Avinguda Països Catalans 16, 43007 Tarragona, Spain. [2]Universitat Rovira i Virgili, Avinguda Catalunya, 35, 43002 Tarragona, Spain. ✉email: nlopez@iciq.es

npj

npj

2

J. Geiger et al.
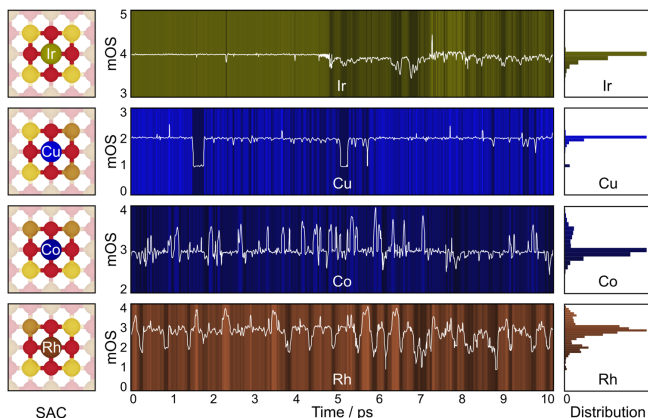
Fig. 1 Molecular Dynamics of selected CeO$_2$(100)-4O-based SACs investigated for metal oxidation state (mOS) dynamics at typical working temperature (600 K). The left panels show top views of the initial, unoptimized SAC structures, with ground state Ce^{3+} distributions indicated. colour code: O^{2-}, red; Ce^{4+}, orange; Ce^{3+}, yellow (metal species annotated; one subsurface polaron for Co-4O). The center panels depict the continuous mOS progressions during the 10 ps trajectories, indicated via the white lines and background colour gradients, where brighter (darker) colour corresponds to higher (lower) mOS values. Distributions of states at mOS increments of 0.1 are shown in the right panels. The full trajectories of the BOMD simulations can be seen in the Supplementary Videos 1–4.

In this work, we employed a data-driven approach to augment the simple representation of a physics-based two-state Born–Haber model, constructed for Pt$_1$/CeO$_2$[17]. To this end, we have created an extensive database of (701) ground and low-lying excited states for CeO$_2$(100)-based SACs of the group 9–11 metals, accounting for their rich and varied redox chemistry, adapting up to five distinct metal charge states, as well as alternative coordination environments of the ceria support. We applied a toolbox of ML techniques to reproduce the energies of ground and excited states for all SACs. Predominant features were then used to construct a parsimonious, interpretable model that predicts the appearance of dynamic electron transfer and rationalizes main contributions.

RESULTS AND DISCUSSION
Metal adsorption on CeO$_2$ surfaces

To analyze the stability of single metal atoms on the low-energy facets of ceria (see Supplementary Fig. 1 and Supplementary Note 1), we evaluated their adsorption energies by means of DFT (PBE+U) via: $E_{Ads} = E_{total} - E_{surface} - E_{bulk\ metal}$, where E_{total} denotes the energy of the SAC, $E_{surface}$ that of the unreconstructed oxide surface and $E_{bulk\ metal}$ the metal cohesive energy per atom (Supplementary Tables 1 and 2). Exothermic (endothermic) adsorption indicates favorable dispersion in the form of single atoms (nanoparticles). On the lowest energy facet (111), as well as on (110), adsorption is always endothermic with respect to the bulk metal, the only exceptions being cobalt and nickel on (110).

In contrast, adsorption on unreconstructed (2O) CeO$_2$(100) is exothermic for cobalt, nickel, copper, silver and gold. Moreover, lattice oxygen atoms in CeO$_2$(100) easily diffuse and rearrange to form oxygen-rich domains[28]. These modified coordination environments involve three or four surface oxygen atoms, denoted 3O and 4O, respectively. 3O-sites stabilize the first-row TMs cobalt, nickel and copper, while adsorption on square-planar (100)-4O is exothermic for all metals (except for Au and Ag), rendering them as stable SACs. These coordination motifs are very common on

ceria as they appear at CeO$_2$(111) step edges[29] and the corners of cuboctahedral ceria nanoparticles[30], agreeing with experimental observations[29,31]. Upon adsorption, electrons from the deposited metal atoms can be transferred to the ceria support and localize at Ce^{4+} centers, forming Ce^{3+} polarons. Thus, counting reduced cerium centers can be used as a proxy for the metal oxidation state, mOS[30], avoiding difficulties in charge assignment[32]. Particularly, for Pt$_1$/CeO$_2$(100) dynamic electron exchange between the metal atom and the support was found at around 500 K according to our previous ab initio Born-Oppenheimer Molecular Dynamics (BOMD)[17].

Dynamic behavior of M$_1$/CeO$_2$(100) SACs

To assess if the dynamic charge transfer is common to other metals, we performed 10 ps BOMD simulations of the stable CeO$_2$(100)-4O SACs for cobalt, rhodium, iridium and copper (Supplementary Note 2). Figure 1 shows the continuous mOS progressions and frequency distributions during the BOMD trajectories for each system. Interestingly, the very redox active metal iridium remains in a charge state of 4+ throughout, with 3+ states persisting for less than 30 fs and charge transfer events being limited to the oxide (i.e., polaron hopping; see Supplementary Fig. 2). On the other hand, copper presents a 2+ ground state and forms two long-lived (about 200 fs) Cu$^+$ species, while cobalt fluctuates between mOS values of 2+ and 4+, transitioning through the 3+ ground state. Co^{2+} states are short-lived (< 10 fs) and precede transitions to 4+ states, which are stable for up to 70 fs. Rhodium shows the most dynamic behavior and adapts mOS values ranging from 1+ to 4+. The longest lifetime of this system in its 3+ ground state is below 600 fs, while 2+ (4+) states last up to 200 fs (150 fs), and also short-lived (<50 fs) 1+ states are accessible. Overall, for copper, cobalt and rhodium, we identify ~7, 27, and 65 states at varying mOS that persist for more than 30 fs, respectively.

Thus, the BOMD trajectories show that all SACs except Ir$_1$/CeO$_2$ present a dynamic mOS, albeit to varying extents. It is therefore challenging to predict mOS dynamics ad-hoc, since a poor redox
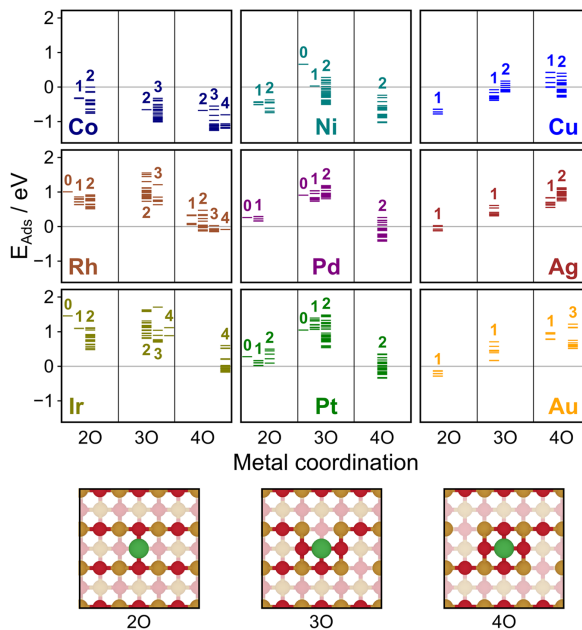
Fig. 2 Adsorption energies for ground and accessible excited states of the investigated CeO$_2$(100)-based transition metal (TM) SACs. The individual values were obtained via: $E_{Ads} = E_{total} - E_{2O\ surface} - E_{bulk\ metal}$. Each TM is represented by one panel. The different coordination environments (illustrated in the bottom row) are separated horizontally within each panel. Metal oxidation states, mOS, are annotated above/below the respective energy distributions.

active metal such as copper does present the effect, while a highly multivalent metal like iridium does not. However, an extended investigation with BOMD for other metals, coordination environments and longer timescales necessary to ascertain ground states and dynamicity is computationally not possible.

Sampling of SAC electronic ensembles

Alternatively, the dynamic properties of CeO$_2$(100)-based SACs at typical working temperatures can be inferred from a static investigation of ground and excited states[17]. Thus, we performed a systematic exploration of electronic ensembles for the group 9–11 transition metals (M = cobalt, rhodium, iridium, nickel, palladium, platinum, copper, silver, gold), surface oxygen coordinations (N_O), metal oxidation states (mOS), and Ce^{3+} distributions resulting from electron transfer to the different cerium centers in the surface. By considering all possible Ce^{3+} configurations up to an mOS of 2+, we have created 1242 initial structures, see Supplementary Note 3, that converged to a dataset of 701 distinct optimized geometries, as presented in Fig. 2.

We find that each metal can be stabilized by at least one oxygen coordination environment on the CeO$_2$(100) surface. However, there is great variability throughout the set: while for the group 9 and 10 metals, square-planar 4O coordination presents the ground, 2O an intermediate and 3O a metastable state, for group 11, adsorption energies become more endothermic with increasing valency of the metal atom. Moreover, the ground state mOS largely depends on the coordination number,

where, higher valency generally leads to more highly charged metal species. In numerous cases, SACs at a given coordination and charge state show the presence of low-lying excited states that cover energy ranges up to 1 eV in magnitude, see Supplementary Table 3. Thus, the electronic ensembles for different mOS frequently overlap, indicative of dynamic behavior at finite temperatures. The ground states deduced from the static sampling reproduce the majority species observed in the BOMD simulations (Fig. 1), and the frequencies and lifetimes of dynamic mOS deviations closely follow the energy distributions of the ensembles. For instance, in addition to its 3+ ground state, Co$_1$/CeO$_2$(100)-4O mainly occupies 4+ states, as expected from the small energy difference between the two ensembles, see Fig. 2. Similarly, the static mOS behavior of Ir$_1$/CeO$_2$(100)-4O relates to the lack of accessible states with a charge other than 4+.

Feature space construction

To investigate the main contributions ruling the dynamic charge transfer, we built data-driven ML models that reproduce the adsorption energies of ground and accessible low-lying excited states of the SACs. Our initial pool of atomic metal descriptors is based on the set proposed by O'Connor et al.[27], containing among others: the atomic number (Z), the cumulative ionization potential (IP), electronegativity, (χ), and orbital levels/radii, amounting to a total of nine features. Following previous ML models for the prediction of ground state adsorption energies of SAs on oxide supports[24,27,33], we added thermodynamic data for metal–metal
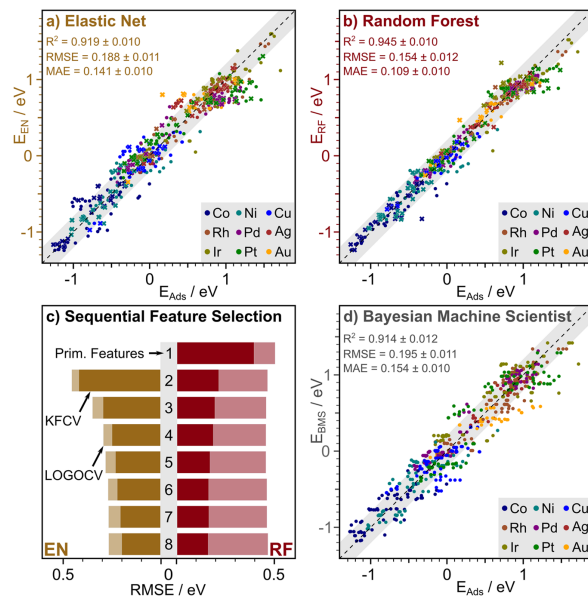
Fig. 3 Predictive ML models constructed from the DFT dataset of adsorption energies (E_{Ads}) of ground and excited states of ceria-based group 9–11 transition metal (TM) SACs. Predictions by the best-performing Elastic Net (EN), Random Forest (RF), and Bayesian Machine Scientist (BMS) models are shown in the panels **a**, **b**, and **d**, with training (testing) data points indicated as circles (crosses). The gray areas mark a region with a deviation of up to 0.2 eV. Panel **c** shows the courses of RMSE values for the EN and RF models during sequential feature selection (SFS), evaluated via K-fold cross-validation (KFCV; opaque bars) and leave-one-group-out cross-validation (LOGOCV; transparent bars). The use of secondary features for Elastic Net (see main text) requires a minimum of two descriptors in the reduced primary space. The actual error values and selected primary features obtained during SFS, panel **c**, are listed in Supplementary Table 6.

and metal–oxygen interactions[34]. Specifically, we evaluated the bond enthalpies of the metal–metal, ΔG^{M-M}, and metal–oxygen bonds, ΔG^{M-O}, both for the diatomic molecules and for the bulk systems, see Supplementary Table 4.

Among the oxide descriptors, studies on oxygen defects on ceria demonstrate that the geometric properties of local Ce^{3+} distributions crucially affect the relative stability of vacancies[35]. Thus, we augmented the feature space with topological descriptors of the oxide: (i) the average number of surface oxygen bound to the Ce^{3+} centers, denoted ϵ, indicative of surface strain[35]; and (ii) the M-Ce^{3+} and Ce^{3+}-Ce^{3+} distances, accounting for Coulomb interactions between these centers. To remove the need for explicit DFT optimizations, the distances are expressed in units of primitive cell vectors. Owing to the inhomogeneity of the dataset, we used statistical measures (i.e., the sum, minimum, mean, maximum and standard deviation) of the respective distance sets as ML features, instead of the individual values, see Supplementary Note 4 and Supplementary Fig. 4.

Predictive ML models

In Fig. 3, we present a summary of the predictive ML models. In all cases, we employed K-fold cross-validation (KFCV) using a 5-fold data split and show predictions obtained by the best-performing model, with mean errors and standard deviations indicated. Linear regression (LR) with metal-only descriptors led to a convoluted description, proving that host descriptors are crucial to untangle the

metal clusters, see Supplementary Fig. 5. However, as fully linear models cannot capture the physics of the metal–oxide interaction, predictions stay poor (Supplementary Table 5).

In a next step, nonlinearity was introduced via a secondary feature space of second-order products and ratios of all combinations of primary descriptors[27] (871 in total), making regularization essential to combat overfitting. Hence, we use the Elastic Net (EN) method[36], as it combines l1-and l2-regularization and therefore achieves feature subset selection and robust predictions, even in the presence of correlated variables, see Supplementary Note 5 and Supplementary Figs. 4 and 6. With the secondary feature space, the EN model achieves an excellent predictive performance of 0.19 eV (RMSE) and 0.14 eV (MAE), see Fig. 3a. Complementary, a nonlinear Random Forest (RF) model, see Supplementary Note 6, provides similar predictive performance of 0.15 eV (RMSE) and 0.11 eV (MAE) with the primary feature space, see Fig. 3b. Thus, our models confirm that nonlinearity is crucial to reproduce the energy distributions of the electronic ensembles for each SAC, and validate the suitability of our descriptor pool. However, the large number (86) of convoluted features retained by EN and the poor interpretability of RF make it difficult to readily derive physical insight.

Feature space reduction

To identify the most representative descriptors, we then applied sequential feature selection (SFS), while evaluating model performances with KFCV, as well as leave-one-group-out cross-validation
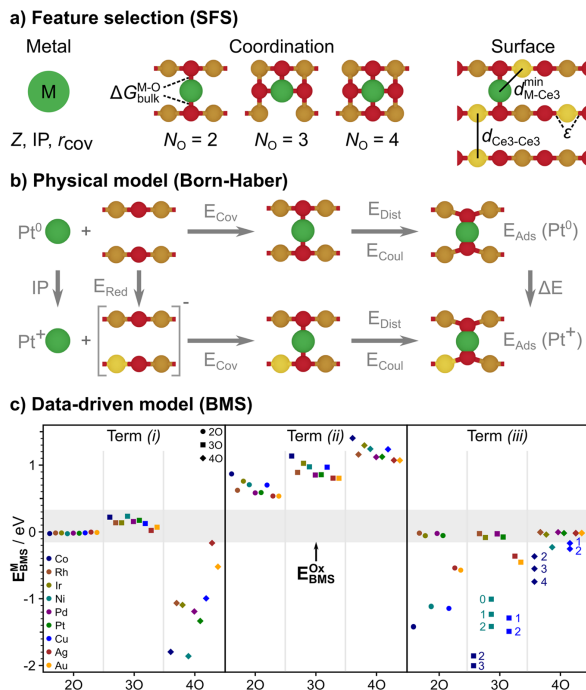
Fig. 4 Schematic of the data-driven construction of a closed-form model for the interaction of single metal atoms with the CeO$_2$(100) support, obtained by the Bayesian Machine Scientist (BMS). a Representative features selected via sequential feature selection (SFS) from predictive ML models. **b** Physical Born–Haber model previously used to describe the metal-support interaction of a Pt$_1$/CeO$_2$(100) SAC at fixed coordination and two charge states (energy terms: Red = Reduction; Cov = Covalent; Dist = Distortion; Coul = Coulomb; Ads = Adsorption). **c** Energy contributions given by each individual term of E$_{BMS}^M$. The range of energy contribution due to the support, E$_{BMS}^{Ox}$, is indicated as gray background. Relevant mOS values for term *(iii)* are annotated.

(LOGOCV), see Supplementary Note 7). Figure 3c) shows the RMSE values of the Elastic Net and Random Forest models during SFS up to the inclusion of eight primary features, while the full data is presented in Supplementary Table 6. The use of Random Forest with LOGOCV leads to considerable errors throughout, which we attribute to the poor extrapolation capabilities of the method. On the other hand, the EN model converges to low errors of around 0.20 eV, irrespective of the applied data partitioning. Predictions by the Elastic Net model during leave-one-group-out cross-validation are presented in Supplementary Fig. 8.

Importantly, as feature subsets are expanded during SFS, the errors of both models quickly converge. Thus, a reduced set of representative physical descriptors is sufficient to capture the complex interactions governing metal adsorption energies of ceria-based SACs. As the actual feature sets obtained from SFS vary with model choice and validation procedure, see Supplementary Table 6, we instead identified frequently occurring feature classes that directly map to distinct physical properties of the systems, see Fig. 4a. These properties, and corresponding representative features, are (i) the metal species, Z; (ii) its charge state, IP (cumulative up to mOS); (iii) its size, r_{cov}; (iv) the coordination environment, N_O; (v) the covalent contribution of

the metal–oxygen bonds, ΔG_{bulk}^{M-O}; (vi) surface strain and distortion, ϵ; (vii) Coulomb interactions between the metal and the support, $min(d_{M-Ce3})$; and lastly (viii) Coulomb interactions between Ce^{3+} centers, $d_{Ce3-Ce3}$. Notably, this reduced space of eight representative features contains all contributions earlier suggested in the Born–Haber model[17], as well as relevant geometric properties of the ceria support identified by Murgida et al.[35].

Search for a closed-form model

Based on the reduced set of representative features, we then searched for a closed-form model for the metal–oxide interaction that generalizes the two-state Born–Haber cycle (Fig. 4b), to all considered metals, coordination environments, oxidation states, and surface electron distributions. Such a model has the advantage that mathematical analysis of the obtained functional form can provide additional physical insight. We employed the Bayesian Machine Scientist (BMS)[37], which samples the space of possible functional forms that fit the training data (further details are provided in the Methods Section). During preliminary runs with all eight features (Supplementary Table 7), BMS only retained dissimilar, reduced subsets, see Supplementary Note 8. Due to the

npj

6

greater energy differences between the metal ensembles, compared to within the individual distributions, BMS mostly retained metal features, while oxide variables were discarded. Therefore, initial models (Supplementary Eqs. 7 to 9) had low predictive power and were elusive to physical interpretation.

Consequently, we decomposed the adsorption energies, E_{Ads}, into a predominant metal and a separate oxide contribution. Training the first BMS model with only the five metal features (see above) gives an approximate positioning of each metal ensemble in the appropriate region of the energy spectrum, E_{BMS}^M. To retrieve the remaining oxide contributions, approximated by E_{BMS}^{Ox}, we then subtracted E_{BMS}^M from the DFT adsorption energies and trained a second BMS model on the residuals, using the remaining three host descriptors. Following this approach, we obtained consistent and interpretable functional forms for both contributions, as presented in Eqs. (1) to (3). The full, additive model gives accurate adsorption energy predictions (RMSE = 0.20 eV and MAE = 0.15 eV), as shown in Fig. 3d. Relevant fitting constants are reported in Supplementary Table 8.

$$E_{Ads} = E_{Ads}^M + E_{Ads}^{Ox} \approx E_{BMS}^M + E_{BMS}^{Ox} = E_{BMS}. \tag{1}$$

$$E_{BMS}^M = \overbrace{N_O c_1 (\Delta G_{bulk}^{M-O} + c_2)^{N_O} \cos(r_{cov})}^{(i)} + \overbrace{N_O c_3 + \Delta G_{bulk}^{M-O2}}^{(ii)}$$
$$- \underbrace{\frac{N_O r_{cov}^2 (IP + Z)^{-c_2 - N_O}}{c_4 (\Delta G_{bulk}^{M-O} + c_5)^2 \left(\Delta G_{bulk}^{M-O} \cdot (IP + Z)^{-c_2 - N_O} + c_4 \right) \left(r_{cov} + \cos\left(\frac{c_5 r_{cov}}{c_4}\right) \right)^2}}_{(iii)} \tag{2}$$

$$E_{BMS}^{Ox} = \frac{1}{c_1} \left(d_{Ce^{3}-Ce^{3}} + \frac{\min(d_{M-Ce^{3}})}{c_2^2 \min(d_{M-Ce^{3}}) - c_2 d_{Ce^{3}-Ce^{3}}} \cos(c_1(c_1\epsilon(c_1+c_2)+\epsilon^2)) \right) \tag{3}$$

Deriving physical insight from the closed-form model

For better interpretability, we evaluated each of the three constituent terms of E_{BMS}^M (Eq. (2), see above), denoted (i), (ii), and (iii), separately, while their individual energy contributions are presented in Fig. 4c. Term (i) spans from –1.86 to 0.24 eV and attributes the greatest stability to highly coordinated (small) metals that form strong bonds with oxygen. Thus, it accounts for metal–oxygen bonding in the different coordination environments, and predicts the following stability trends: $N_O = 4$ (exothermic) > $N_O = 2$ (thermoneutral) > $N_O = 3$ (endothermic), in agreement with expectations derived from coordination chemistry. Thus, term (i) correctly reproduces the dependence of the adsorption energies on the coordination number for the group 10 metals (Ni, Pd, Pt), Rh, and to some extent, Ir (see Fig. 2). However, it provides a poor approximation for the group 11 metals (Cu, Ag, Au), as they do not follow the same energy trends.

Term (ii) is endothermic, spanning from 0.54 to 1.40 eV, and only depends on ΔG_{bulk}^{M-O} and N_O. Contrary to term (i), it particularly destabilizes high coordination and strong metal–oxygen bonds, thus we mainly attribute it to distortion. Term (ii) provides a first correction to the estimates of term (i), and further distinguishes the different metals and coordination environments in the energy spectrum.

Lastly, term (iii) is given by a fraction that involves all five metal features and spans from –2.00 to 0.00 eV. It therefore introduces a distinction by the mOS. The contribution of term (iii) is exothermic for the first-row metals cobalt, nickel, and copper, particularly at lower coordination $N_O = 2$ and 3. In the limit of large atomic numbers and covalent radii, that is, for the second and third row TMs, term (iii) approaches zero, therefore leaving these metals almost unaffected. Owing to their weak metal–oxygen bond strength, the effect is somewhat mitigated for silver and gold, for

which term (iii) slightly stabilizes low coordinations. Overall, the influence of term (iii) is highly dependent on the specific metal atom and mOS state, thus providing a final refinement of the estimates given by terms (i) and (ii).

The remaining oxide contributions, approximated by E_{BMS}^{Ox} and illustrated as gray background in Fig. 4c, are mainly attributed to Coulomb interactions (within the support, and between the metal and Ce^{3+} centers), as well as lattice strain induced by the oxygen-rearrangements and surface polarons. E_{BMS}^{Ox} particularly penalizes configurations with increased lattice strain, which span from –0.15 to 0.33 eV, and are therefore of the same magnitude as polaron hopping barriers in ceria (0.40 eV)[38], or the reconstruction energy from 2O to 3O (0.30 eV, see Supplementary Note 1).

The investigated ML models (EN, RF, and BMS) all provide similar predictive accuracy. However, as outlined above, the closed functional expression obtained with BMS is physically interpretable. Supplementary Fig. 9 presents the BMS predictions in direct comparison to the original data of Fig. 2. Overall, deviations for ground states are within the range of the PBE+U inherent error for the ceria reduction energy (up to 0.4 eV)[39]. In certain cases, ground state mOS for a given metal and coordination are not correctly identified by the BMS. We attribute these discrepancies to the inherently small energy differences for these systems. For instance, DFT adsorption energies of Co-4O in its 3+ and 4+ charge states differ by only 0.06 eV, see Fig. 2. On the other hand, highly excited states are generally less well-reproduced, causing a contraction of the energy spans of the individual distributions. Nonetheless, the BMS model correctly reproduces ensemble overlaps, and thus mOS dynamicity.

Owing to its compact nature, we can compare the generalized model obtained from BMS to the phenomenological Born–Haber (BH) cycle, which only provided the energy difference for two states (Pt and Pt$^+$), in a fixed coordination environment (2O). While the BH model is derived from physical insights, BMS functional forms are data-driven. The BH is based on seven local variables, including the IP, surface distortion/reduction, a covalent contribution, and Coulomb interactions, which were evaluated using explicit DFT distances and Bader charges. Instead, the BMS accounts for nine metals, three coordination environments, and up to five different oxidation states, while using only eight variables, none of which require explicit DFT. Owing to its significant contribution, the IP appears in both models. The covalent term, E_{Cov} in BH was approximated by the Pt(H$_2$O)$_2$-binding energy. In the BMS, it is replaced by the more general metal–oxygen bond-formation enthalpy, ΔG_{bulk}^{M-O}. As a bulk property, ΔG_{bulk}^{M-O}, also contains non-local ionic interactions that were approximated via the Coulomb term in the BH model (see Supplementary Note 4). The remaining contributions in the BH cycle are the reduction and surface distortion of ceria, both of which are rather small, as no additional oxygen-rearrangements were considered. In BMS, these effects are condensed in the surface term, E_{BMS}^{Ox}, which further accounts for long-range repulsion and elastic properties of the surface due to the localized polarons.

Finally, to provide an outlook on the expected generalization capabilities of our BMS model, we consider the impact of different metals and reducible oxide supports. Retaining the same functional form and atomic descriptors, the adsorption energies of other SA metals can be predicted by fine tuning the coefficients, as evaluated for our set of metals through leave-one-group-out cross-validation, see Supplementary Table 9. As for the oxides, the surface contributions account for local strain and polaron structure, and can thus be adapted to other reducible oxide supports using equivalent descriptors. Accounting for defects, such as oxygen vacancies, will require future extensions of the method[40].

In summary, we have shown that the dynamic charge transfer between isolated single-metal atoms and ceria supports is ubiquitous and can be predicted via an interpretable, parsimonious

mathematical expression for the metal-support interactions. Our data-driven model employs a set of eight variables, including metal properties like the atomic number, covalent radius, ionization potentials, metal–oxygen bond strengths, and the coordination number, as well as oxide contributions, accounting for surface strain and Coulomb interaction. It generalizes a previous, physical Born–Haber model and reproduces the adsorption energies for ground and low-lying excited states for a variety of $CeO_2(100)$-based SACs. The proposed methodology of augmenting physics-based models with data-driven machine-learning techniques allows for a generalization of dynamic electron transfer in metal-support interactions and paves the way towards the introduction of complex electronic structure contributions in the modeling of single atoms for heterogeneous catalysis.

METHODS

Density functional theory

DFT simulations were performed with the Vienna Ab Initio Simulation Package (VASP; version 5.4.4)[41] and the Perdew–Burke–Ernzerhof (PBE) functional[42]. For the cerium atoms, an additional Hubbard U correction[43], with an effective U_{eff} value (Dudarev's approach[44]) of 4.5 eV was applied[45]. Core electrons were treated with the projector augmented wave (PAW) method[46,47] using the appropriate PAW-PBE pseudopotentials, while valence electrons were expanded with plane waves up to a basis set cutoff of 500 eV. Total energies were evaluated at the Gamma point, and validated by comparison to (3 x 3 x 1) k-point sampling, see Supplementary Fig. 3. Electronic convergence was set to 10^{-6} eV and atomic positions were converged until residual forces fell below 0.01 eV Å^{-1}.

Slab models for the (111) and (100) surfaces were constructed as (3 x 3), and for the (110) surface as (2 x 2) supercells, based on optimized ceria bulk (theoretical lattice parameter: 5.491 Å). They extend nine, nine, and six atomic layers along the vertical direction, with the bottom three, four, and three layers fixed at the optimized bulk positions, respectively. At least 10 Å of vacuum were added on top of the surfaces to avoid non-physical interactions between periodic images. Ce^{3+} centers, and consequently discrete mOS states, were assigned through the localized magnetic moments of cerium atoms, where we applied a threshold of 0.8 μ_B, based on previous work[17].

For the Born-Oppenheimer Molecular Dynamics (BOMD) simulations, we used reduced (2 x 2) supercells of $CeO_2(100)$. They were conducted within the canonical NVT ensemble (constant number of particles, volume and temperature), using the Nosé-Hoover thermostat[48] at an average temperature of 600 K. Data was collected for 10 ps trajectories, with a time-step of 1 fs. For the MD simulations, we lowered the electronic convergence threshold to 10^{-5} eV. Continuous mOS progressions along the MD trajectories (center panels of Fig. 1) were obtained by summing up the absolute magnetic moments of all surface and subsurface cerium atoms, without the application of a magnetization threshold. The distributions shown in the right panels of Fig. 1 represent states at discrete mOS values at increments of 0.1 μ_B.

Statistical modeling

All the data follows FAIR principles (findable, accessible, interoperable, and reusable) according to the guidelines outlined by Artrith et al.[22]. Predictive models (LR, RF, EN)[36] were evaluated using KFCV with a 5-fold data split, and LOGOCV procedures, see Supplementary Table 6. Data centering and standardization were applied when necessary. Reported error measures (R^2, RMSE, MAE) were averaged over the different train-test splits, with standard deviations indicated. Presented energy predictions correspond to the best-performing models, as identified during the respective cross-validation procedure. Hyperparameter tuning for the EN and RF models is provided in Supplementary Figs. 6 and 7. For the final EN model, we used values of $a = 1 \times 10^{-3}$ and `l1-ratio` = 0.999 throughout (low total amount of regularization, high fraction of l1). The RF was constructed as an ensemble of 128 trees, which were grown to a maximum depth of eight. At each split, randomly selected features amounting to 60% of the given pool were evaluated. Training was performed on bootstrapped data sets. For data visualization, we made extensive use of the Plotly Python library[49].

The symbolic equation search was performed via the Bayesian Machine Scientist (BMS)[37], which samples the space of possible functional forms that fit the training data using using Markov Chain Monte-Carlo. As the

space of mathematical functions to be explored by BMS grows exponentially with the number of variables, the method requires a simplified descriptor space[50]. We limited the number of steps to 10,000, of which the first 1000 were discarded. The maximum depth was set to 100 iterations per step. At each step, we examined the following BMS outputs: (i) the current function and its complexity, (ii) the Bayesian Information Criterion (BIC), (iii) the sum of squared errors (SSE), and (iv) the values of all the fitting constants. Functions were evaluated by mathematical analysis, focusing on accuracy and simplicity. For the separate metal (oxide) models we used six (three) fitting constants, and suitable priors accordingly. BMS allows continuous, as well as discrete variables as inputs. In our setup, the latter are given by the metal features and the coordination number, both of which separate distinct classes of data. In practice, BMS frequently achieves separation of data classes and approximation of polynomial terms by the use of trigonometric functions, as their compact nature lowers the applied penalty on model complexity.

REFERENCES

1. Qiao, B. et al. Single-atom catalysis of CO oxidation using Pt$_1$/FeO$_x$. Nat. Chem. 3, 634–641 (2011).
2. Wang, A., Li, J. & Zhang, T. Heterogeneous single-atom catalysis. Nat. Rev. Chem. 2, 65–81 (2018).
3. Lang, R. et al. Single-Atom Catalysts Based on the Metal−Oxide Interaction. Chem. Rev. 120, 11986−12043 (2020).
4. Hai, X. et al. Scalable two-step annealing method for preparing ultra-high-density single-atom catalyst libraries. Nat. Nanotechnol. 17, 174–181 (2022).
5. Datye, A. K. & Guo, H. Single atom catalysis poised to transition from an academic curiosity to an industrially relevant technology. Nat. Commun. 12, 895 (2021).
6. Resasco, J. et al. Uniformity is Key in Defining Structure−Function Relationships for Atomically Dispersed Metal Catalysts: The Case of Pt/CeO₂. J. Am. Chem. Soc. 142, 169−184 (2020).
7. Xu, Y. et al. Revealing the Correlation between Catalytic Selectivity and the Local Coordination Environment of Pt Single Atom. Nano Lett. 18, 6865−6872 (2020).
8. Hulva, J. et al. Unraveling CO adsorption on model single-atom catalysts. Science 371, 375–379 (2021).
9. Lykhach, Y. et al. Counting electrons on supported nanoparticles. Nat. Mater. 15, 284–288 (2016).
10. Cho, Y. et al. Disordered-Layer-Mediated Reverse Metal−Oxide Interactions for Enhanced Photocatalytic Water Splitting. Nano Lett. 21, 5247–5253 (2021).
11. Jones, J. et al. Thermally stable single-atom platinum-on-ceria catalysts via atom trapping. Science 353, 150–154 (2016).
12. Qiao, B. et al. Highly Efficient Catalysis of Preferential Oxidation of CO in H₂-Rich Stream by Gold Single-Atom Catalysts. ACS Catal. 5, 6249–6254 (2015).
13. Khivantsev, K. et al. Economizing on Precious Metals in Three-Way Catalysts: Thermally Stable and Highly Active Single-Atom Rhodium on Ceria for NO Abatement under Dry and Industrially Relevant Conditions. Angew. Chem. Int. Ed. 60, 391–398 (2021).
14. Muravev, V. et al. Interface dynamics of Pd-CeO₂ single-atom catalysts during CO oxidation. Nat. Catal. 4, 469–478 (2021).
15. Greiner, M. T. et al. Free-atom-like d states in single-atom alloy catalysts. Nat. Chem. 10, 1008–1015 (2018).
16. Gao, R. et al. Pd/Fe₂O₃ with Electronic Coupling Single-Site Pd−Fe Pair Sites for Low-Temperature Semihydrogenation of Alkynes. J. Am. Chem. Soc. 144, 573–581 (2022).
17. Daelman, N., Capdevila-Cortada, M. & López, N. Dynamic charge and oxidation state of Pt/CeO₂ single-atom catalysts. Nat. Mater. 18, 1215–1221 (2019).
18. Zhang, Z., Zandkarimi, B. & Alexandrova, A. N. Ensembles of Metastable States Govern Heterogeneous Catalysis on Dynamic Interfaces. Acc. Chem. Res. 53, 447–458 (2020).

npj

8

19. Wang, Y., Kalscheur, J., Su, Y. Q., Hensen, E. J. M. & Vlachos, D. G. Real-time dynamics and structures of supported subnanometer catalysts via multiscale simulations. *Nat. Commun.* **12**, 5430 (2021).

20. Butler, K. T., Davies, D. W., Cartwright, H., Isayev, O. & Walsh, A. Machine learning for molecular and materials science. *Nature* **559**, 547–555 (2018).

21. Keith, J. A. et al. Combining Machine Learning and Computational Chemistry for Predictive Insights Into Chemical Systems. *Chem. Rev.* **121**, 9816–9872 (2021).

22. Artrith, N. et al. Best practices in machine learning for chemistry. *Nat. Chem.* **13**, 505–508 (2021).

23. Garrido Torres, J. A. et al. Augmenting zero-Kelvin quantum mechanics with machine learning for the prediction of chemical reactions at high temperatures. *Nat. Commun.* **12**, 7012 (2021).

24. Tan, K., Dixit, M., Dean, J. & Mpourmpakis, G. Predicting Metal−Support Interactions in Oxide-Supported Single-Atom Catalysts. *Ind. Eng. Chem. Res.* **58**, 20236–20246 (2019).

25. Liu, C. Y., Zhang, S., Martinez, D., Li, M. & Senftle, T. P. Using statistical learning to predict interactions between single metal atoms and modified MgO(100) supports. *NPJ Comput. Mater.* **6**, 102 (2020).

26. Su, Y. Q. et al. Stability of heterogeneous single-atom catalysts: a scaling law mapping thermodynamics to kinetics. *NPJ Comput. Mater.* **6**, 144 (2020).

27. O'Connor, N. J., Jonayat, A. S., Janik, M. J. & Senftle, T. P. Interaction trends between single metal atoms and oxide supports identified with density functional theory and statistical learning. *Nat. Catal.* **1**, 531–539 (2018).

28. Capdevila-Cortada, M. & López, N. Entropic contributions enhance polarity compensation for CeO$_2$(100) surfaces. *Nat. Mater.* **16**, 328–334 (2017).

29. Dvořák, F. et al. Creating single-atom Pt-ceria catalysts by surface step decoration. *Nat. Commun.* **7**, 10801 (2016).

30. Figueroba, A., Kovács, G., Bruix, A. & Neyman, K. M. Towards stable single-atom catalysts: Strong binding of atomically dispersed transition metals on the surface of nanostructured ceria. *Catal. Sci. Technol.* **6**, 6806–6813 (2016).

31. Kunwar, D. et al. Stabilizing High Metal Loadings of Thermally Stable Platinum Single Atoms on an Industrial Catalyst Support. *ACS Catal.* **9**, 3978–3990 (2019).

32. Walsh, A., Sokol, A. A., Buckeridge, J., Scanlon, D. O. & Catlow, C. R. A. Oxidation states and ionicity. *Nat. Mater.* **17**, 958–964 (2018).

33. Iyemperumal, S. K., Pham, T. D., Bauer, J. & Deskins, N. A. Quantifying Support Interactions and Reactivity Trends of Single Metal Atom Catalysts over TiO$_2$. *J. Phys. Chem. C.* **122**, 25274–25289 (2018).

34. Haynes, W. M. *CRC Handbook of Chemistry and Physics 97th Edition* (CRC Press LLC Florence, Taylor & Francis Group, 2016).

35. Murgida, G. E., Ferrari, V., Ganduglia-Pirovano, M. V. & Llois, A. M. Ordering of oxygen vacancies and excess charge localization in bulk ceria: A DFT+U study. *Phys. Rev. B* **90**, 115120 (2014).

36. Hastie, T., Tibshirani, R. & Friedman, J. *The Elements of Statistical Learning: Data Mining, Inference, and Prediction* (Springer, New York, 2009).

37. Guimerà, R. et al. A Bayesian machine scientist to aid in the solution of challenging scientific problems. *Sci. Adv.* **6**, eaav6971 (2020).

38. Plata, J. J., Márquez, A. M. & Sanz, J. F. Electron Mobility via Polaron Hopping in Bulk Ceria: A First-Principles Study. *J. Phys. Chem. C.* **117**, 14502–14509 (2013).

39. Capdevila-Cortada, M., Łodziana, Z. & López, N. Performance of DFT+U Approaches in the Study of Catalytic Materials. *ACS Catal.* **6**, 8370–8379 (2016).

40. Geiger, J. & López, N. Coupling Metal and Support Redox Terms in Single-Atom Catalysts. *J. Phys. Chem. C* https://doi.org/10.1021/acs.jpcc.2c03710 (2022).

41. Kresse, G. & Furthmüller, J. Efficiency of ab-initio total energy calculations for metals and semiconductors using a plane-wave basis set. *Comput. Mater. Sci.* **6**, 15–50 (1996).

42. Perdew, J. P., Burke, K. & Ernzerhof, M. Generalized Gradient Approximation Made Simple. *Phys. Rev. Lett.* **77**, 3865–3868 (1996).

43. Hubbard, J. Electron correlations in narrow energy bands. *Proc. Math. Phys. Eng. Sci.* **276**, 238–257 (1963).

44. Dudarev, S. & Botton, G. Electron-energy-loss spectra and the structural stability of nickel oxide: An LSDA+U study. *Phys. Rev. B* **57**, 1505–1509 (1998).

45. Fabris, S., Gironcoli, S. D., Baroni, S., Vicario, G. & Balducci, G. Taming multiple valency with density functionals: A case study of defective ceria. *Phys. Rev. B* **71**, 041102 (2005).

46. Blöchl, P. E. Projector augmented-wave method. *Phys. Rev. B* **50**, 17953–17979 (1994).

47. Kresse, G. & Joubert, D. From ultrasoft pseudopotentials to the projector augmented-wave method. *Phys. Rev. B* **59**, 1758–1775 (1999).

48. Hoover, W. G. Canonical dynamics: Equilibrium phase-space distributions. *Phys. Rev. A* **31**, 1695 (1985).

49. Plotly Technologies Inc. *Collaborative Data Science* (Plotly Technologies Inc, 2015). https://plot.ly.

50. Pablo-García, S., García-Muelas, R., Sabadell-Rendón, A. & López, N. Dimensionality reduction of complex reaction networks in heterogeneous catalysis: From linear-scaling relationships to statistical learning techniques. *WIREs Comput. Mol. Sci.* **11**, e1540 (2021).

51. Álvarez-Moreno, M. et al. Managing the Computational Chemistry Big Data Problem: The ioChem-BD Platform. *J. Chem. Inf. Model.* **55**, 95–103 (2015).

ACKNOWLEDGEMENTS

AUTHOR CONTRIBUTIONS

J.G. performed the calculations. J.G., A.S.-R., and N.D. carried out the data analysis and constructed the machine-learning models. J.G., A.S.-R., N.D., and N.L. prepared the manuscript.

COMPETING INTERESTS

The authors declare no competing interests.

ADDITIONAL INFORMATION

Supplementary information The online version contains supplementary material available at https://doi.org/10.1038/s41524-022-00852-1.

Correspondence and requests for materials should be addressed to Núria López.

Reprints and permission information is available at http://www.nature.com/reprints

Publisher's note Springer Nature remains neutral with regard to jurisdictional claims in published maps and institutional affiliations.

npj Computational Materials (2022) 171   Published in partnership with the Shanghai Institute of Ceramics of the Chinese Academy of Sciences

192

RESEARCH ARTICLE

ADVANCED MATERIALS
www.advmat.de

Low-Valent Manganese Atoms Stabilized on Ceria for Nitrous Oxide Synthesis

Ivan Surin, Zhenchen Tang, Julian Geiger, Suyash Damir, Henrik Eliasson, Mikhail Agrachev, Frank Krumeich, Sharon Mitchell, Vita A. Kondratenko, Evgenii V. Kondratenko, Gunnar Jeschke, Rolf Erni, Núria López, and Javier Pérez-Ramírez*

Nitrous oxide, N_2O, exhibits unique reactivity in oxidation catalysis, but the high manufacturing costs limit its prospective uses. Direct oxidation of ammonia, NH_3, to N_2O can ameliorate this issue but its implementation is thwarted by suboptimal catalyst selectivity and stability, and the lack of established structure–performance relationships. Systematic and controlled material nanostructuring offers an innovative approach for advancement in catalyst design. Herein low-valent manganese atoms stabilized on ceria, CeO_2, are discovered as the first stable catalyst for NH_3 oxidation to N_2O, exhibiting two-fold higher productivity than the state-of-the-art. Detailed mechanistic, computational and kinetic studies reveal CeO_2 as the mediator of oxygen supply, while undercoordinated manganese species activate O_2 and facilitate N_2O evolution via N—N bond formation between nitroxyl, HNO, intermediates. Synthesis via simple impregnation of a small metal quantity (1 wt%) predominantly generates isolated manganese sites, while full atomic dispersion is achieved upon redispersion of sporadic oxide nanoparticles during reaction, as confirmed by advanced microscopic analysis and electron paramagnetic resonance spectroscopy. Subsequently, manganese speciation is maintained, and no deactivation is observed over 70 h on stream. CeO_2-supported isolated transition metals emerge as a novel class of materials for N_2O production, encouraging future studies to evaluate their potential in selective catalytic oxidations at large.

1. Introduction

In view of the growing demand for green and sustainable technologies in the chemical industry, performing atom-efficient and selective oxidation reactions represents a key challenge.[1–5] Nitrous oxide, N_2O, stands to play an important role in addressing this issue. While it is a well-established specialty chemical, primarily known for its use as an anesthetic, in the 1980s it has started to attract significant attention as a selective oxidizing agent. Owing to its ability to donate a single oxygen atom, it avoids the risk of over-oxidation and, notably, generates ecologically benign N_2 as the only by-product, positioning it as a green alternative to many conventional oxidizing agents.[6–8] In the following years, N_2O has been shown to unlock unique pathways for the one-step oxidation of benzene to phenol or methane to methanol.[9,10] The highly selective and facile nature of the former led to the implementation of the AlphOx process in the late 1990s. Therein, the Boreskov Institute

I. Surin, Z. Tang, S. Damir, S. Mitchell, J. Pérez-Ramírez
Institute for Chemical and Bioengineering
Department of Chemistry and Applied Biosciences
ETH Zürich
Vladimir-Prelog-Weg 1, Zürich 8093, Switzerland
E-mail: jpr@chem.ethz.ch
J. Geiger, N. López
Institute of Chemical Research of Catalonia (ICIQ)
The Barcelona Institute of Science and Technology
Av. Països Catalans 16, Tarragona 43007, Spain

H. Eliasson, R. Erni
Electron Microscopy Center
Empa – Swiss Federal Laboratories for Materials Science
and Technology
Überlandstrasse 129, Dübendorf 8600, Switzerland
M. Agrachev, G. Jeschke
Laboratory of Physical Chemistry
Department of Chemistry and Applied Biosciences
ETH Zürich
Vladimir-Prelog-Weg 1, Zürich 8093, Switzerland
F. Krumeich
Laboratory of Inorganic Chemistry
Department of Chemistry and Applied Biosciences
ETH Zürich
Vladimir-Prelog-Weg 1, Zürich 8093, Switzerland
V. A. Kondratenko, E. V. Kondratenko
Department of Catalysis Discovery and Reaction Engineering
Leibniz-Institut für Katalyse
Albert-Einstein-Straße 29a, 18059 Rostock, Germany

of Catalysis (BIC) and Solutia Inc. launched a pilot plant utilizing waste N_2O generated during manufacture of adipic acid, achieving 98% yield of phenol.[6,7] Despite the success of the technology, no significant advances in the commercialization of N_2O-mediated processes have been made in the past two decades. The main reason for this is the lack of affordable N_2O. On the one hand, the existing N_2O streams (i.e., by-product of adipic acid production) contain only 30-40% N_2O and require extensive purification (removal of NO_x, CO_x, and,O_2), entailing large capital and operational costs.[11] On the other hand, almost all of the deliberately synthesized N_2O currently comes from thermal decomposition of ammonium nitrate, resulting in a prohibitively high price ($\approx$ 4000$ t^{-1}).[12] This is reflected in the limited scale of N_2O production, estimated to be $\approx$ 0.2–0.3 Mt year^{-1} and expected to increase at the rate of only around 7% annually.[13] The reason for this is the high cost of ammonium nitrate itself, which is a product of a complex and multi-stage manufacturing route, comprised of ammonia, NH_3, oxidation to NO, its subsequent transformation into nitric acid, acid-base reaction with NH_3 and, finally, crystallization into a salt. Crucially, N_2O also forms as a minor by-product during the first stage of this process.[14,15] Thus, by designing a suitable catalytic material and adapting the reaction conditions, the process of NH_3 oxidation can be tuned to yield N_2O as the main product, significantly reducing its price ($\approx$ 600$ t^{-1}) and eliminating the need for downstream purification and allowing its application in existing or new selective oxidation reactions.[12] Recent advances in the field of blue and green NH_3 production make this approach even more appealing, as they hold the potential to transform NH_3 oxidation to N_2O into a fully sustainable process, starting at the stage of feedstock procurement and ending with the ultimate product application.[16,17]

In an effort to design catalysts for NH_3 oxidation to N_2O, reducible metal oxides have been studied most extensively, owing to their inherent activity in redox reactions,[18,19] with manganese-based systems being the most prominent.[20,21] An important milestone was reached in 1998, with the identification of Mn-Bi-O/α-Al$_2$O$_3$, the state-of-the-art catalyst at the time.[22] This system, comprised of nm-sized particles of oxides of manganese, bismuth, and mixtures thereof and with a total metal content of 20 wt%, showed the highest N_2O selectivity ($\approx$ 83%) to date at nearly complete conversion of NH_3.[23,24] This result prompted the construction of a pilot plant by Solutia Inc. in collaboration with the BIC. However, despite the reported success of the test, the catalyst was never industrially implemented. The apparent reason for this was that Mn-Bi-O system performed optimally under an excess of O_2, requiring its removal downstream and significantly increasing the costs. In contrast, the use of stoichiometric reactant amounts would likely have had a negative effect on the catalyst stability, as transition metal-based catalysts are known to suffer from deactivation due to over-reduction of the active phase[15,24–27] — a key limitation of this class of materials.

In the following years, little advancement in the field of direct NH_3 oxidation to N_2O has been made. However, recently the topic experienced a revival, when our group reported small Au nanoparticles (2–3 nm) supported on ceria, CeO_2, to be a highly selective and active material, far outperforming the

Mn-Bi-O system and setting a new benchmark for N_2O productivity.[12] Remarkably, CeO_2 assumed the role of a co-catalyst, serving as the mediator of oxygen supply for the reaction, which proceeded via a Mars-van Krevelen-type mechanism at the interface between the support and Au. However, the catalyst suffered from deactivation due to agglomeration of Au nanoparticles. Furthermore, despite the superior activity of Au, the global trend toward making the chemical industry more sustainable demands a reduction in the use of precious metals. Thus, we adopted a new approach toward catalyst design, leveraging the newly gained understanding of the unique redox capabilities of CeO_2, while utilizing well-established manganese as the active phase. Beyond simply using a cheaper and more abundant metal, this strategy aims to combine the specific redox properties of both phases, making it possible to engineer the active site at the atomic level, which can often give rise to new materials with unprecedented catalytic properties.[28–30] Thereby, the long-standing problem of control over the nanostructure of NH_3 oxidation catalysts can be addressed.

Following this approach, we identify isolated, low-valent manganese atoms stabilized on CeO_2 as an outstanding catalyst for NH_3 oxidation to N_2O, outperforming Au nanoparticles in terms of selectivity, activity, and stability. The oxygen buffer ability of CeO_2 is found to be essential for the attainment of high N_2O productivity, providing abundant O species for the reaction. This is complemented by the ability of undercoordinated Mn^{2+} species on the surface of the support to effectively activate gas-phase O_2 and facilitate N—N bond formation, as evidenced by atomistic simulations. Furthermore, in contrast to the previously reported manganese-based systems, the high catalytic activity is attained with the total metal content of only 1 wt%. Atomic dispersion of the majority of manganese atoms is achieved during synthesis, proceeding via a simple impregnation method, while the few sporadic manganese oxide particles redisperse into single atoms over the course of the reaction. The resultant material remains subsequently unchanged, showing no loss of catalytic activity over 70 h on stream — an unprecedented result for an NH_3 oxidation catalyst to N_2O. Moreover, the remarkable oxidative properties of CeO_2-supported atomically-dispersed transition metals presented here can extend beyond oxidation of NH_3 and find application in a range of other oxidation reactions. Thus, these findings are of significant relevance to the field of catalytic oxidations not only as an advancement in the production of an affordable and efficient oxidant, N_2O, but also as a demonstration of a novel type of material for selective oxidations at large.

2. Results and Discussion

2.1. Platform of Materials

To verify that manganese represents the most promising earth-abundant transition metal for NH_3 oxidation, a series of CeO_2-supported transition metal catalysts were synthesized by incipient wetness impregnation (IWI) with a nominal metal content of 1 wt%. The reference catalysts were prepared following the synthetic procedures described in the respective studies.[12,23] The catalytic performance of the derived materials
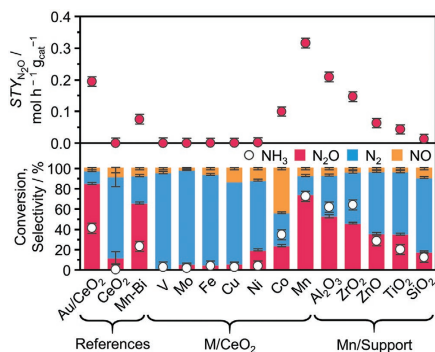
Figure 1. Catalytic performance in NH_3 oxidation of CeO_2 support and reference catalysts (References), transition metals supported on CeO_2 (M/CeO_2) and manganese supported on different carriers (Mn/Support), represented by the space-time yield (STY) of N_2O (top), NH_3 conversion and product selectivity patterns (bottom). Data presented as mean ± 95% confidence interval ($n = 2$). Reaction conditions: $T_{bed} = 673$ K; $m_{cat} = 0.04$ g; $GHSV = 375000$ cm^3 h^{-1} g$_{cat}^{-1}$; Feed = 8 vol.% NH_3, 8 vol.% O_2, 4 vol.% Ar, 80 vol.% He; $P = 1$ bar. Au/CeO_2 and Mn-Bi were evaluated at 573 K and 623 K, respectively.

was subsequently evaluated in NH_3 oxidation. Reference systems showed performance metrics consistent with previous reports, thus providing a valid benchmark, while transition metal catalysts exhibited varying levels of NH_3 conversion and product selectivity (**Figure 1**). The majority showed very low activity and primarily formed N_2, while Co/CeO_2 achieved appreciable NH_3 conversion, but also produced a much larger amount of NO ($S_{NO} > 20\%$). Accordingly, the poor catalytic performance of these systems disqualified them from further consideration in this work. However, in line with our expectations, manganese-based system achieved the highest N_2O selectivity, even rivaling that of the state-of-the-art Au/CeO_2. In fact, Mn/CeO_2 exceeded the NH_3 conversion of the latter by a significant margin (73% vs 41%), thereby reaching a higher space-time yield of N_2O (STY_{N2O}) than any previously reported material. Interestingly, the Mn-Bi/Al_2O_3 reference catalyst displayed an order of magnitude lower STY value, despite significantly larger manganese content (1 wt% vs 8.4 wt%). This suggests that manganese does appear to possess an inherent ability to catalyze the formation of N_2O from NH_3, in accordance with previous reports. However, there remain other aspects of catalyst design, most prominently the choice of the support and the nanostructure of the active phase, which can have a profound effect on the catalytic footprint.

Accordingly, a platform of manganese catalysts on a selection of different carriers was synthesized by analogy with Mn/CeO_2. Following the rationale of redox-active properties, supports ranging from non-reducible (i.e., Al_2O_3, SiO_2) to partially-reducible (i.e., ZrO_2, TiO_2) and reducible (ZnO) oxides were chosen. The resultant materials were then thoroughly characterized prior to testing. High-angle annular dark-field scanning

transmission electron microscopy (HAADF-STEM) coupled with energy dispersive X-ray spectroscopy (EDXS) revealed manganese to be highly dispersed on the surface of all supports except ZnO, where nanoparticles of MnO_x (≈ 21 nm) were observed (Figure 4 and Figure S4, Supporting Information). Additionally, powder X-ray diffraction (XRD) analysis of the materials prior to and after manganese deposition showed identical reflection patterns (Figure S5, Supporting Information). This served as a further indication that the majority of manganese is likely present in the form of a largely amorphous MnO_x phase, and even the nanoparticles visible on ZnO are likely too small and too few in number (metal content = 1 wt%) to produce sufficiently sharp reflections. Temperature-programmed reduction with hydrogen (H_2-TPR) analysis also complemented this notion, generally showing several ill-defined reduction peaks appearing over a wide range of temperatures, characteristic of a highly dispersed nature and heterogeneous speciation of manganese (Figure S6, Supporting Information).[31] In the case of Mn/CeO_2, the assignment of individual peaks to specific transformations of the active phase was further complicated by the redox-active nature of CeO_2. Accordingly, surface reduction of CeO_2 strongly contributed to the superposition of peaks visible between 360 and 700 K.[32] Furthermore, it appears that manganese deposition led to the onset of surface reduction at a lower temperature, which likely occurred due to a strong interaction between the metal and the lattice oxygen species, a well-documented phenomenon for CeO_2-based catalysts.[32–34] Conversely, Mn/ZnO showed a strong reduction peaks at 625 K, which can be attributed to transformations of $Mn_2O_3 \rightarrow MnO$.[35] Such behavior is consistent with the presence of nanoparticles seen by EDXS mapping. Finally, X-ray photoelectron spectroscopy (XPS) analysis of Mn $2p_{3/2}$ revealed a diverse electronic structure of manganese in all samples, with metal oxidation state ranging from Mn^{2+} to Mn^{4+} present in varying amounts (Figure S8, Supporting Information). Remarkably, in Mn/CeO_2 low-valent manganese (i.e., Mn^{2+}) was most abundant, which is in line with previous reports on the ability of CeO_2 to strip oxygen from manganese at temperatures above 700 K.[36] This process likely occurred during sample calcination ($T = 823$ K), resulting in manganese being primarily stabilized in the reduced form. This point is further corroborated by the position of the peak being shifted towards lower binding energy values (640.9 eV) relative to other catalysts and the presence of a prominent satellite feature at ≈ 647 eV, characteristic of Mn^{2+}.[37]

With structural differences and commonalities between the catalysts established, their performance in NH_3 oxidation was assessed and differences in activity and N_2O selectivity could be observed, with the CeO_2-supported system outpacing its counterparts (Figure 1). Still, the catalysts do share some common features, such as the fact that N_2O selectivity is generally maximized at 673 K (Figure S2, Supporting Information) and increases alongside NH_3 conversion (Figure S3, Supporting Information). This is an important practical consideration, as it enables operation under optimal conditions without the need to recycle unreacted NH_3. This trend also suggests that there is likely to be a specific material property, which could serve as a descriptor of both activity and selectivity, and thus guide the rational design of a superior material.

2211260 (3 of 14)

2.2. Structure–Performance Relations

In order to understand the origin of the diverging behavior of manganese-based catalysts and identify relevant structure-performance relationships, we first considered the ability of the catalysts to interact with gas-phase O_2 as a necessary factor for attaining high catalytic activity. Namely, by performing volumetric O_2 chemisorption at 673 K, the quantity of adsorbed oxygen, herein referred to as the oxygen uptake, could be quantified. Notably, this property clearly depends on both the redox properties of the support, as evidenced by negligible oxygen uptake values of all pristine carriers except CeO_2, and the manganese speciation, as is evident from the correlation with the valence of manganese, determined by XPS (**Figure 2**a,b). This observation was rationalized by considering manganese valence as a degree of oxygen saturation, and thus low-valent surface manganese species can accommodate more oxygen ligands. In this regard, it must be noted a significant increase in the oxygen uptake of CeO_2 would also be expected upon doping with a heteroatom,[12] which could happen if manganese substituted cerium atoms during calcination. However, penetration of manganese into even the surface layer of CeO_2 would entail manganese assuming a higher oxidation state (vide infra), which was not reflected by the XPS analysis, therefore suggesting that undercoordinated manganese is indeed present on the catalyst surface. Additionally, the quantities of O_2 adsorbed either physically or chemically can be easily differentiated

using this technique, where the latter represents the amount of oxygen that forms a bond with the catalyst surface. This value was used for quantification of the oxygen uptake. It must also be emphasized that the measurements were carried out at 673 K, that is, the temperature of the reaction. Hence, the determined values of oxygen uptake are representative of a material's ability to activate O_2 under the reaction conditions, and thus can be related to the observed catalytic performance. In this respect, a correlation between the oxygen uptake of different catalysts and their corresponding selectivity to N_2O and STY_{N2O} could be identified (Figure 2c,d). Accordingly, the principal role of oxygen uptake here can be interpreted on the basis of the reaction mechanism, which must comprise oxidative dehydrogenation of NH_3, followed by oxidation of NH_x fragments to ultimately yield N_2O. As all manganese catalysts exhibited modest NO selectivity (< 5%) due to the relatively low reaction temperature, the main discrepancy between them consisted in the relative quantities of N_2 and N_2O produced. As the latter contains a more oxidized form of nitrogen, it stands to reason that oxygen availability is of central importance to the ability of a material to promote N_2O formation.

To further validate this hypothesis, kinetic analysis of the catalyst platform was performed. Namely, by systematically varying the reaction temperature or the partial pressure of a given reactant, the apparent activation energy and the reaction orders with respect to each reactant were derived (Figure S7, Supporting Information). The latter reflects how the respective
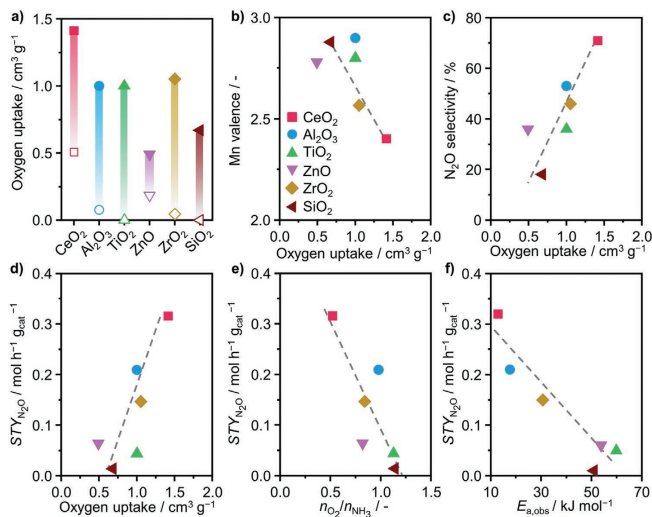
Figure 2. Performance descriptors of Mn/Support catalysts. a) Oxygen uptake of bare supports (open symbols) and after depositing manganese (solid symbols), determined by volumetric O_2 chemisorption; b) Mn valence, determined by XPS, and c) N_2O selectivity as a function of oxygen uptake; STY_{N2O} as a function of d) oxygen uptake, e) the ratio of O_2 and NH_3 reaction orders; and f) the apparent activation energy. Reaction conditions: T_{bed} = 673 K; m_{cat} = 0.04 g; $GHSV$ = 375 000 cm^3 h^{-1} g_{cat}^{-1}; Feed = 8 vol% NH_3, 8 vol% O_2, 4 vol% Ar, 80 vol% He; P = 1 bar.

concentrations of the reactants affect the observed rate of reaction. Given that both reactants must be adsorbed on the catalyst surface for the reaction to occur, the difference in the reaction orders can give an indication of the relative abundance of each species on the catalyst surface under typical reaction conditions. For instance, if $n(O_2)$ is larger than $n(NH_3)$, we can interpret this in terms of the availability of NH_3 for the reaction exceeding that of O_2, and hence the rate of reaction is more strongly affected by a change in O_2 partial pressure. Furthermore, as the stoichiometry of NH_3 oxidation toward N_2, N_2O, and NO varies, with each product requiring progressively larger quantity of O_2, we can expect that the selectivity profile of a catalyst will depend on the relative ratio of the two reaction orders as well. Following this rationale, the ratio of $n(O_2)/n(NH_3)$ was calculated and plotted against STY_{N2O} (Figure 2e) for each manganese catalyst. In agreement with our expectation, a good correlation was obtained, suggesting that the ability of a catalyst to activate O_2 plays a decisive role in determining its activity and selectivity to N_2O. This is also in accordance with the previously established relation between STY_{N2O} and oxygen uptake, further validating it as a performance descriptor. Finally, the apparent activation energy of the reaction could also be correlated with STY_{N2O}, leading to the conclusion that oxygen activation is likely to be the rate-limiting step of the reaction as well (Figure 2f).

2.3. Mn/CeO$_2$ Catalyst for N$_2$O Synthesis

Having established the underlying reason for the observed differences in catalytic activity and selectivity, catalyst stability in NH_3 oxidation was also evaluated for 70 h on stream. The resultant profiles showed significant variations in terms of both the rate of the initial activity loss and the overall drop in STY_{N2O} during the test (**Figure 3**a). Accordingly, Mn/SiO$_2$ and Mn/ZnO rapidly deactivated during the first 10 h of the reaction, losing over 50% of their initial activity. At the same time, most of the remaining catalysts experienced a gradual drop in STY_{N2O}. Mn/CeO$_2$ stands in contrast to all other materials, as it actually underwent an induction period during the initial ≈ 20 h of the reaction, during which a minor increase in selectivity and activity was observed (Figure S9, Supporting Information). Subsequently, a stable mode of operation was achieved and maintained throughout the entire duration of the test. This is a remarkable result, as both reference catalysts showed significant deactivation under identical reaction conditions, thus setting Mn/CeO$_2$ apart as not only a highly productive, but also a robust catalyst. It must also be noted that the conditions of the stability test, namely the gas-hourly space velocity (GHSV), were much harsher than the typical values reported in the literature.[38,39] Therefore, the apparently relatively short duration of the test (70 h) nevertheless allows for a valid assessment of catalytic stability.

To gain insights into the structural changes that underpin the observed stability trends, HAADF–STEM, EDXS, and XPS analyses of the material after 70 h on stream were carried out. The acquired microscopy images and elemental maps clearly evidenced manganese agglomeration in all samples except Mn/CeO$_2$ and Mn/ZrO$_2$ (**Figure 4** and Figure S10, Supporting
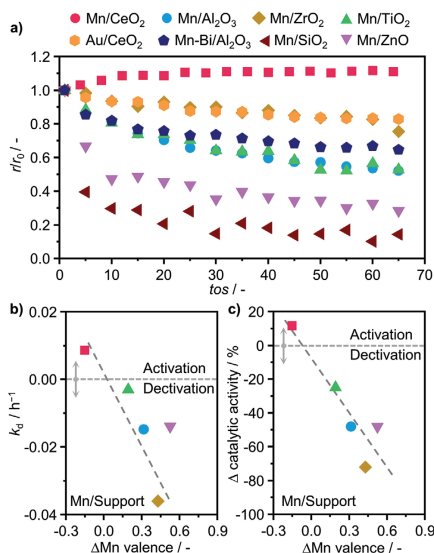
Figure 3. a) Stability test of selected catalysts. While all other systems exhibit varying rates of deactivation, Mn/CeO$_2$ undergoes an induction period, gaining activity and subsequently stabilizing; b) deactivation constant k_d and c) loss of catalytic activity of supported Mn catalysts as a function of change of Mn valence after 70 h on stream. Reaction conditions: T_{bed} = 673 K; m_{cat} = 0.04 g; GHSV = 375 000 cm^3 h^{-1} g$_{cat}^{-1}$; Feed 8 vol% NH$_3$, 8 vol% O$_2$, 4 vol% Ar, 80 vol% He; P = 1 bar.

Information). The latter two appeared to maintain the high degree of manganese dispersion, despite Mn/ZrO$_2$ still deactivating, albeit to a lesser extent than others. Mn 2p$_{3/2}$ XPS analysis of the used catalysts led to a rather unexpected result, revealing that manganese in nearly all samples was oxidized (Figure S8, Supporting Information). In fact, the only catalyst which experienced a decrease in manganese valence is Mn/CeO$_2$, which consistently enhanced the activity. This is in direct opposition to the commonly accepted notion that transition metal-based catalysts primarily suffer from deactivation due to reduction under the reaction conditions. Still, in view of the observed changes of manganese nuclearity, it is possible that the overall increase in manganese valence was inextricably linked to the agglomeration process. Nevertheless, the importance of maintaining manganese in the low-valent state is evident—a clear correlation between both the rate of the initial deactivation and the overall decrease in catalytic activity with the change in the average oxidation state was found (Figure 3b,c). We can therefore conclude that preserving the highly dispersed nature of manganese is advantageous from the standpoint of both atomic efficiency, and as a way of maintaining the optimal metal speciation. Consequently, Mn/CeO$_2$ warranted a more detailed investigation, as its stability not only positions it as a
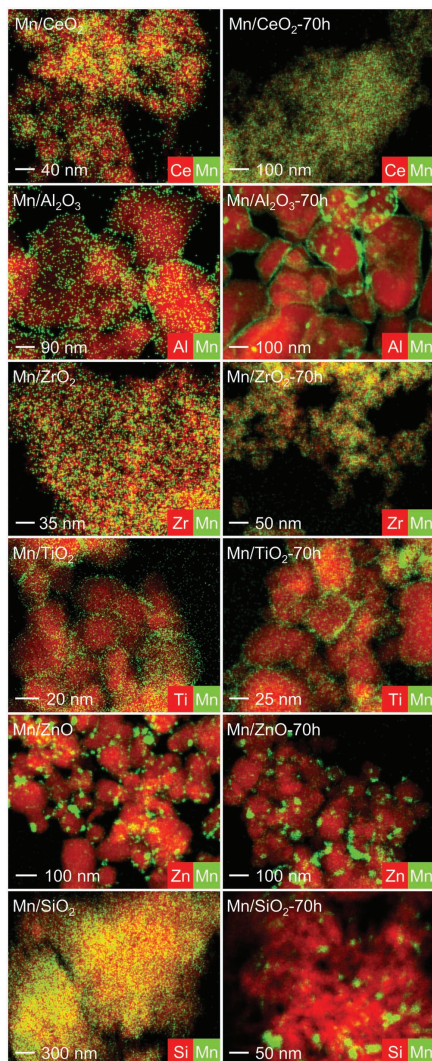
Figure 4. STEM-EDX maps of as-prepared and used Mn/Support catalysts.

2.4. Manganese Speciation in Mn/CeO$_2$

While the highly distributed nature of manganese was apparent based on the elemental mappings shown in Figure 4, the exact nanostructure of the metal could not be fully discerned. Accordingly, a more detailed microscopic analysis of both the fresh and the used sample was conducted, comprising high-resolution STEM (HRSTEM) and EDXS mapping (**Figure 5**a,b). An extensive HRSTEM search was carried out looking at the surface and edges of well-defined CeO$_2$ flakes, but no manganese particles were found. Single manganese atoms and clusters of a few atoms are not visible in the HAADF images due to the much higher atomic mass of cerium. Still, the presence of manganese was confirmed by the integrated EDXS spectra (Figure S11, Supporting Information). By analyzing the corresponding elemental maps, the manganese signals appeared to be evenly scattered across the entire surface of CeO$_2$, which, given the scale of the images, suggested that manganese could be present in the form of isolated atoms.

To further substantiate the claim of atomic dispersion of manganese in Mn/CeO$_2$, electron paramagnetic resonance (EPR) spectroscopy was employed as a means of probing the degree to which EPR-active species (i.e., Mn^{2+} and Mn^{4+}) are magnetically, and hence spatially, isolated. Accordingly, the EPR spectrum of as-prepared Mn/CeO$_2$ was measured at room temperature and showed a very broad (with a linewidth of almost 3000 G) signal centered at around 1800 G (Figure 5d). Contrary to the expectations, such broad, anisotropic, and low-field-centered signals are typical for magnetically ordered systems with strongly exchange-coupled paramagnetic ions. This is confirmed by the change of the spectrum observed after changing the sweep direction (i.e., up: from low to high field, down: from high to low field). This magnetic hysteresis clearly indicates that the signal can be attributed to the presence of ferro/antiferromagnetic particles. In order to identify the latter, a series of additional measurements were performed at different temperatures (Figure S13, Supporting Information). A clear decrease of the signal intensity was observed with lower temperatures, which is characteristic of antiferromagnetic systems. By plotting the reciprocal of the peak-to-peak amplitude, which roughly estimates the magnetic susceptibility, a Néel temperature (i.e., temperature at which antiferromagnetic ordering takes place) of ≥ 130 K was determined. This leads to the conclusion that this signal stems from nm-sized MnO nanoparticles, in which Mn^{2+} ions are antiferromagnetically coupled.[40,41] Nevertheless, an additional signal was observed at around 3500 G (g factor g = 2.006), consisting of six lines of almost equal intensity, split by about 92 G. This signal is typical for magnetically-diluted Mn^{2+}, with the splitting due to the hyperfine interaction between electron and nuclear spin (S = 5/2, I = 5/2, respectively). The signal can therefore be attributed to atomically-dispersed Mn^{2+} on the surface of CeO$_2$. The narrow lines indicate that the dipole–dipole interactions between Mn^{2+} are relatively weak, which indicates that a significant fraction of manganese is still highly dispersed, despite the presence of some amount of MnO.

The spectrum of the used sample acquired at room temperature also showed the two manganese-related components. However, in contrast to the as-prepared material, the MnO

practically relevant system for potential commercialization, but also as one of fundamental interest, offering a platform to study the nature of the active site.
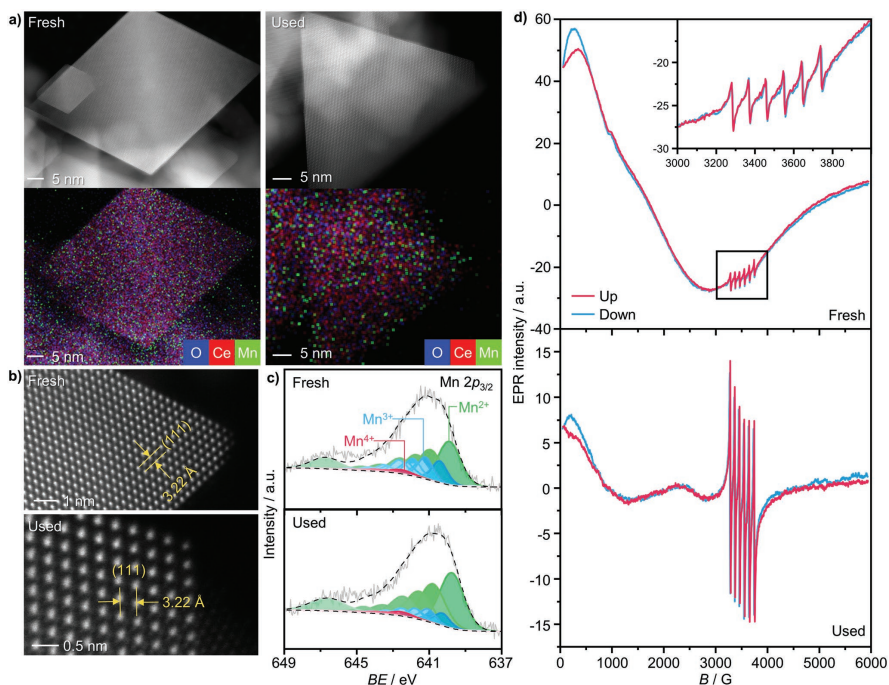
Figure 5. Characterization of as-prepared Mn/CeO$_2$ and after 70 h on stream. a) HAADF-STEM micrographs with EDX maps, b) HRSTEM images, and c) Mn $2p_{3/2}$ XPS spectra demonstrate that the highly dispersed low-valent nature of manganese is maintained during the reaction. d) Both EPR spectra evidence hyperfine splitting, characteristic of large quantities of isolated Mn^{2+} species. Disappearance of the broad signal, characteristic of bulk MnO, after the reaction suggests that redispersion occurred and full atomic dispersion was achieved.

signal practically disappeared, while the signal of isolated Mn^{2+} species became much stronger. Such changes in the intensity of the signals may arise either from redox processes between paramagnetic (i.e., EPR-active) and diamagnetic (i.e., EPR-silent) states or from nuclearity changes, which can lead to interconversion between paramagnetic (isolated sites) and antiferromagnetic (particles) signals. From Mn $2p_{3/2}$ XPS analysis it is evident that manganese undergoes reduction during the reaction (Figure 5c). Therefore, if we only consider the redox processes, they would lead to an increase of the MnO signal. However, the opposite was observed, which instead suggests that redispersion of MnO into isolated Mn^{2+} species took place. This is also the likely origin of the observed induction period during the stability test. Additionally, the increase of the Mn^{2+} signal could be attributed not only to redispersion of MnO, but also to the transformation of isolated Mn^{3+} species into Mn^{2+}.

To further validate these conclusions, EPR spectra of Mn/Al$_2$O$_3$ at room temperature were also acquired (Figure S14,

Supporting Information). The as-prepared sample showed a very similar, but significantly stronger MnO signal. No Mn^{2+} signal was observed in this case. This indicates a lower dispersion degree, compared to Mn/CeO$_2$. After the reaction, the MnO signal decreased, but its intensity was still quite strong. However, as evidenced by Mn $2p_{3/2}$ analysis, in contrast to Mn/CeO$_2$, Mn/Al$_2$O$_3$ gets significantly more oxidized with time on stream. Therefore, in this case, the decrease in the intensity of the MnO signal could be attributed to the transformation of Mn^{2+} into Mn^{3+}. Indeed, this is more consistent with the microscopy analysis, which shows significant agglomeration of manganese (Figure 4 and Figure S10, Supporting Information). In addition, a narrow, unstructured line appears at $g = 2.006$ after the reaction, which can be attributed to Mn^{2+} species still present on the surface of Al$_2$O$_3$. Unlike in Mn/CeO$_2$, however, the hyperfine splitting here is completely unresolved because the lines are significantly broader. This is due to stronger Mn^{2+}–Mn^{2+} dipolar interactions and indicates that the degree of spatial isolation is lower than in Mn/CeO$_2$.

On the basis of the acquired spectroscopic and microscopic insights, we affirm that Mn/CeO_2 constitutes a single-atom catalyst (SAC), being the first material of this class for NH_3 oxidation to N_2O. After synthesis, the as-prepared sample still has a small degree of nanostructure heterogeneity, exhibiting sporadic MnO nanoparticles, albeit so few in number that they could not be detected in any of the micrographs. However, upon exposure to the reaction conditions, full atomic dispersion was achieved, ultimately giving rise to a distribution of Mn^{2+} and Mn^{3+} stabilized on the surface of the catalyst. Furthermore, in view of the catalytic inertness of CeO_2 alone, and the observed induction period during the stability test, attributed to in situ redispersion, we propose that isolated manganese atoms act as the active sites of the reaction. Therefore, having established the likely structure of the latter, we were presented with a unique opportunity to also study the mechanism of the reaction, which could potentially reveal new guidelines for catalyst design and optimization.

2.5. Mechanistic Insights

It is generally accepted that the mechanism of low-temperature NH_3 oxidation must involve two key steps, namely the oxidative dehydrogenation of NH_3 (Equations (1) and (2)) and subsequent oxidation of the NH_x fragments to a nitroxyl intermediate, HNO (Equation (3)).[24,42–45] The latter has long been postulated to be central in the formation of N_2O, which proceeds via the recombination of two HNO species (Equation (4)).

$$NH_3^* + O \rightarrow NH^* + H_2O \tag{1}$$

$$NH_3^* + O \rightarrow NH_2^* + OH \tag{2}$$

$$NH^* + O \rightarrow HNO^* \tag{3}$$

$$HNO^* + HNO^* \rightarrow N_2O + H_2O \tag{4}$$

Conversely, if oxygen supply is insufficient, NH_x fragments may proceed to react with each other or HNO, thereby forming N_2 as the main product (Equations (5)–(7)).

$$HNO^* + NH^* \rightarrow N_2 + H_2O \tag{5}$$

$$NH_2^* + NH_2^* \rightarrow N_2H_4^* \tag{6}$$

$$N_2H_4^* + 2O \rightarrow N_2 + H_2O \tag{7}$$

While only limited experimental or computational evidence exists to support this scheme, it is nevertheless in good agreement with the observation that the catalyst's ability to provide active oxygen species results in the superior capacity to selectively generate N_2O.[12] Thus, we adopted this reaction sequence as a starting point for the investigation of the mechanism over isolated manganese sites, using density functional theory (DFT).

For this purpose, we first evaluated all possible adsorption sites for manganese atoms on the low-index (100), (110), and (111) facets of CeO_2, considering on-top, bridge, and hollow adsorption sites (Figure S15, Supporting Information), as well as substitutional lattice positions. Structural optimizations for these 20 possible catalyst structures were done with the Perdew–Burke–Ernzerhof (PBE) functional, using a Hubbard U-correction

for the cerium cations.[46] Overall, we find that on all facets, feasible coordination motifs for the stabilization of single-atom Mn exist (Figure S16, Table S5, Supporting Information). We then assigned formal manganese oxidation states (OS) by counting reduced Ce^{3+} centers (polarons) in the support, revealing the strong correlation between the number of oxygen ligands and the manganese oxidation state (Figure S16, Supporting Information). Formal OS assignments were further verified by Bader charges and simulated XPS shifts (Figure S17, Supporting Information).[47–49] However, we found that Mn/CeO_2 presents a highly complex electronic structure, due to the charge transfer between manganese and CeO_2 that leads to a variable oxidation state of the former and a variable number (and distribution) of reduced Ce^{3+} centers in the support. Therefore, while for many applications the PBE+U method offers balanced cost-efficiency performance, a more sophisticated method including exact exchange (i.e., hybrid method) is required to assess the energies for the Mn/CeO_2 interface. This comes at a price of at least one order of magnitude higher computational cost and the impossibility to re-optimize the structures, thus limiting our investigation to a thermodynamic assessment of the reaction mechanism. Thus, we further refined adsorption energy estimates with the HSE03-13 hybrid functional based on the PBE+U optimized structures.[50–53] Importantly, we find that highly oxidized manganese states are overstabilized when using PBE+U (Table S5, Supporting Information). For instance, on $CeO_2(111)$, the exothermicity of single-atom adsorption increases with the formal Mn-OS. This is in contrast to HSE03-13, which yields Mn^{2+} as the only stable structure on this facet. It should further be noted that the discrepancies for the substitutional catalyst models are less severe as they do not contain reduced Ce^{3+} centers. Thus, we deem energy differences for structures with a fixed numbers of Ce^{3+} centers to be reliable, even at the PBE+U level.

From the retained potential catalyst structures (Figure S16, Supporting Information), we then turned our attention to the investigating of possible reaction pathways towards the formation of N_2O. Although manganese is likely a mixture of various species, XPS points to manganese being mainly present in a low-valent state, particularly after stabilization on stream (Figure 5c). Thus, we selected Mn^{2+} on all three low-index facets, as well as the two lowest-energy Mn^{3+} structures on (110) and (100) (models a–e in Figure S16, Supporting Information and **Figure 6**a) as representative reaction sites. This reduced set of five possible Mn-SAC structures encompasses all low-index ceria surfaces, as well as coordination patterns ranging from two to four oxygen atoms, and was then used to investigate adsorption of the reactants, O_2 and NH_3, as well as the proposed HNO intermediate. Additionally, the stability of a hyponitrous acid, $H_2N_2O_2$, cyclic intermediate was investigated. It is the protonated form of a hyponitrite, $N_2O_2^{2-}$, ion, commonly accepted to form during NO coupling in nitric oxide reductase (NOR) enzymes, followed by decomposition into N_2O.[54–56] Given the single-atom nature of the catalyst, the manganese site could potentially act in an analogous fashion to the enzymatic metal center of an enzyme and promote the combination of HNO species to yield N_2O.

Adsorption energies were evaluated both with PBE+U and refined at the higher level HSE03-13 hybrid functional and
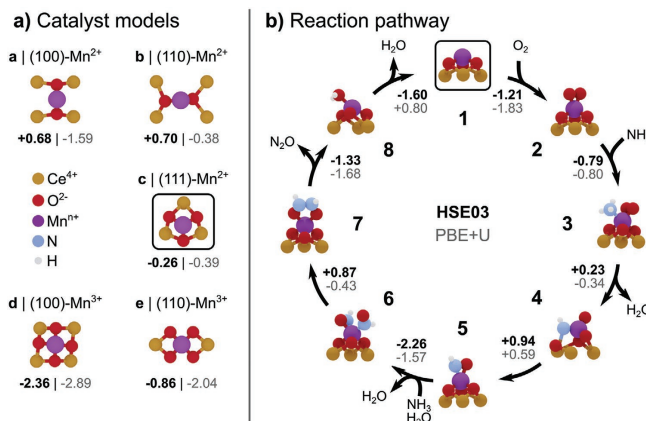
Figure 6. Computational exploration of the reactivity landscape. a) Representative Mn-SAC structures on low-index ceria facets, encompassing varied coordination motifs and manganese oxidation states. b) Proposed reaction pathway proceeding via nitroxyl, HNO, and *cis*-hyponitrous acid, $H_2N_2O_2$ intermediates for the most stable Mn^{2+} catalyst structure on the most abundant exposed (111) facet. Single-atom adsorption energies and reaction energies between intermediates along the reaction sequence are indicated. All energies are given in eV.

are summarized in Table S7, Supporting Information. First, we note that both molecular and dissociative O_2 adsorption on low-valent Mn is highly exothermic for all three ceria facets (Figure S18a, Supporting Information), proving its inherent ability activate gas-phase O_2, and to provide reactive oxygen species necessary for the reaction. Second, we find that low-coordinated Mn^{2+} (models a–c in Figure 6a) allows for the stabilization of a cis-hyponitrous acid intermediate via the formation of a κ^2-coordinated ring structure. This is a crucial step for N—N bond formation en route to the main observed products, N_2O, and N_2.[57–59] On the four-fold coordinated Mn^{3+} (models d-e in Figure 6a), on the other hand, this process is hindered by the saturated coordination of the manganese to the support.

Finally, from the wealth of the obtained data, we could construct a thermodynamically plausible reaction pathway for the full selective catalytic cycle, schematically shown for Mn^{2+} on (111), (structure 1 in Figure 6b). It should be noted that the arrows along the cyclic reaction path do not denote elementary steps, but rather serve to connect key intermediates used to evaluate thermodynamic viability. Importantly, the reaction sequence proceeds via previously proposed HNO and $H_2N_2O_2$, intermediates, and indeed follows a similar route as the formation of N_2O by nitric oxide reductase (NOR) enzymes. First, exothermic adsorption (−1.21 eV) and activation of gas-phase O_2 leads to intermediate 2 (Figure 6b). The low-valent nature of manganese allows for co-adsorption of NH_3, which completes its octahedral coordination sphere. Subsequently, NH_3 dehydrogenation is facilitated by the activated nature of O_2 (Figure S18a, Supporting Information) and driven by H_2O elimination. In the resulting intermediate 3, the NH fragment is stabilized by coordination to an adjacent cerium center of the support, while one reactive oxygen atom remains bound to manganese. The

formation a first η^2-coordinated HNO fragment, intermediate 5, requires the endothermic (+0.94 eV) formation of the N—O bond.

We then assume the formation of another HNO proceeding in a similar fashion, consuming another NH_3 and O_2 pair, while eliminating H_2O, and finally resulting in intermediate 6. In this structure, asymmetric coordination of the two HNO moieties again leads to octahedral coordination around the manganese atom. Crucially, the simultaneous coordination of two HNO fragments to low-valent manganese brings them in proximity to facilitate N—N bond formation (+0.87 eV), which results in the *cis*-hyponitrous acid intermediate 7. Interestingly, in this structure, one of the Mn—O bonds to the ceria support is significantly elongated (2.41 Å) such that the coordination around the manganese atom can best be described as square planar. Evidently, the dynamic coordination to the $CeO_2(111)$ support allows the manganese atom to adapt its geometry during the reaction sequence. Lastly, from the cis-hyponitrous acid fragment, intermediate 7, N_2O can be released (intermediate 8), with elimination of H_2O recovering the catalyst in its initial state.

It should be noted that along the proposed reaction sequence (Figure 6b) different acid-base equilibria for the intermediates 5 to 7, involving ligand and/or lattice oxygen, are likely to influence the rate. Similarly, under operating conditions, the direct participation of reactive lattice oxygen originating from CeO_2 in a surface Mars-van Krevelen type mechanism is likely (Figure S19, Supporting Information). While we have evaluated some alternative structures, presented in Figures S18b,c, Supporting Information, these processes open up an intractable number of additional reaction pathways, far exceeding the scope of the present work, and warranting separate, dedicated investigations.

Lastly, we could also obtain analogous, thermodynamically, feasible reaction pathways (Figure S20, Supporting Information) for Mn^{2+} catalysts on the (100) and (110) facets (models a and b in Figure 6a), hinting at the inherent capability of low-valent single-atom Mn to facilitate N_2O formation.

To experimentally investigate the role of lattice oxygen of CeO_2 in the course of NH_3 oxidation to N_2O, a suitable method to monitor the onset of the reaction under relevant conditions was required. As oxidation of NH_3 proceeds very quickly and evolves a large amount of heat, temporal analysis of products (TAP) was chosen as a suitable tool to study the interactions of the reactants and the product formation under isothermal conditions.[60,61] A further advantage of TAP is the ability to pulse small quantities of the reactants (in the order of 10^{-9} mol), thereby making it possible to monitor the initial catalytic behavior of a material and potentially observe the most prominent involvement of oxygen species from CeO_2. To this end, an equimolar mixture of He, NH_3, and $^{18}O_2$ was pulsed over Mn/CeO_2 in the temperature window of 473–773 K. Despite the quantitative difference in product distribution between steady-state and TAP experiments, likely arising as a result of the large pressure gap, the general selectivity trends were consistent, with the highest quantity of N_2O formed at 673 K, while the amount of NO produced steadily increased with reaction temperature (**Figure 7**a). Remarkably, the quantity of ^{16}O-containing products, that is, $N^{16}O$ and $N_2^{16}O$, significantly exceeded that of $N_2^{18}O$ and $N^{18}O$, indicating that direct participation of oxygen originating from CeO_2 took place. Furthermore, the identical shape of the signals for products containing labelled and non-labelled oxygen indicate that their formation proceeds at the same rate. This implies that $^{18}O_2$ likely healed the oxygen vacancy formed when lattice oxygen of CeO_2 participated in NH_3 oxidation, and was incorporated into another

N_2O molecule as a lattice specie upon subsequent reaction. We also observed two distinct signals at mass to charge ratio (m/z) of 18 and 20, which could be attributed to $H_2^{16}O$ and $H_2^{18}O$ molecules, respectively (Figure 7b). Despite $^{18}O_2$ contributing to the signal at m/z 18 as doubly ionized ion, the different shapes of the responses related to m/z 36 and 18 prove that $H_2^{16}O$ is formed. Thus, lattice oxygen species of CeO_2 also participated in oxidative dehydrogenation of NH_3. However, it should be noted that the origin of labelled and non-labelled oxygen in the H_2O molecules is different. As the peak of $H_2^{18}O$ appears after that of $H_2^{16}O$, the formation of the former proceeds slower. This suggests that $^{18}O_2$ participates in the initial dehydrogenation of NH_3 as adsorbed and not lattice species, albeit to a lesser degree, as can be inferred from the relatively noisier signal of $H_2^{18}O$.

Given the presence of sporadic MnO particles in the fresh sample of Mn/CeO_2, it also had to be verified that it is indeed the lattice of CeO_2 that acts as the source of ^{16}O atoms. Accordingly, we have conducted analogous TAP pulse experiments on Mn/Al_2O_3. Interestingly, in this case we have also observed an appreciable amount of ^{16}O-containing products, however, it is still significantly lower than that found in Mn/CeO_2, particularly at higher temperature (Figure 7c). In view of the non-reducible nature of Al_2O_3, the non-labelled oxygen atoms must have originated from the supported manganese oxide phase. Notably, participation of lattice O in NH_3 oxidation has also been reported for a TiO_2-supported manganese catalyst.[62] Therefore, we cannot exclude that MnO particles found in Mn/CeO_2 also contribute to the product formation via a Mars-van Krevelen mechanism. However, given the significantly higher intensity of manganese oxide signal in the EPR spectrum of Mn/Al_2O_3 as compared to Mn/CeO_2 (Figure 5, S 14), and the smaller amount of ^{16}O-containing products formed over the former, we can deduce that CeO_2 is still the primary origin of oxygen species for NH_3 oxidation over Mn/CeO_2. On the basis of these findings, we can conclude that the process of N_2O formation over Mn/CeO_2 proceeds via a surface Mars-van Krevelen-type mechanism. This observation is in line with our previous findings on Au/CeO_2, serving as another example of atomically dispersed metal species activating surface lattice oxygen of the support for catalytic oxidations,[63,64] and highlighting the role of CeO_2 as an integral component of the catalyst.

Notably, the observation that oxygen species of manganese oxide can be involved in the product formation potentially offers interesting insights into the previously mentioned redispersion of manganese oxide particles in Mn/CeO_2. Strategies for the redispersion of metallic nanoparticles through alternating reducing and oxidizing treatments are well-established in the literature.[65,66] These typically describe a "strain" model, where oxidation of the outer layer of a metallic nanoparticle induces metal strain energy, prompting the fragmentation of the large particle into smaller species which then undergo dispersion through interactions with the carrier. Although in the case of Mn/CeO_2 the particles are not metallic, it is possible that the inversion of the mechanism described above could be the reason for the observed redispersion. Namely, through the removal of oxygen atoms from the outer layer of the manganese nanoparticle via NH_3 oxidation, the outer layer is reduced, resulting in generation of strain. This, coupled to the high exo-
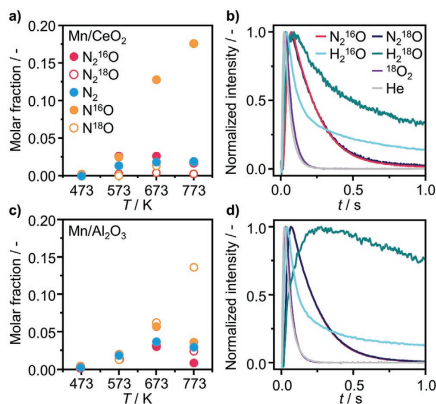
Figure 7. Temporal analysis of products (TAP) of NH_3 oxidation over Mn/CeO_2 and Mn/Al_2O_3. a,c) Product distribution as a function of temperature and b,d) transient response at 673 K after pulsing of 1:1:1 NH_3:$^{18}O_2$:He mixture.

2211260 (10 of 14)

thermicity of NH_3 oxidation, and previously established ability of CeO_2 to effectively stabilize manganese atoms, could serve as the impetus for particle fragmentation and subsequent anchoring of isolated manganese species, leading to redispersion. However, extensive experimental validation of the proposed mechanism would be required and remains a subject for a separate, dedicated investigation.

2.6. Catalyst Design Guidelines

The main elements that distinguish Mn/CeO_2 as a remarkable catalytic material are summarized in **Figure 8**. At the foundation of its design lies the ability of CeO_2 to stabilize isolated atoms of manganese, as demonstrated by the combination of microscopy and EPR analyses. These can be formed by simple impregnation, using a small amount of metal (1 wt%). While CeO_2 is known as a support for single-atom catalysts,[28,67] to our knowledge there have not been previous reports of surface-stabilized manganese. Indeed, the anchoring sites of the carrier appear to be sufficiently strong to prevent agglomeration during the reaction, resulting in a robust metal nanostructure and stable catalytic performance. The surface nature of the manganese species also allows them to remain in a low-valent, undercoordinated state, which in turn translates into the exceptional ability to activate gas-phase O_2 and facilitate N–N bond formation, as shown by the kinetic analysis and DFT modeling. This complements the inherent oxygen transfer ability of the support and enables the attainment of high N_2O selectivity and activity. Additionally, we found the active oxygen species to originate from the lattice of CeO_2, while O_2 in the feed appears to primarily replenish their reserves. The involvement of lattice oxygen in both the initial dehydrogenation of NH_3 and the ulti-

mate formation of N_2O has been demonstrated by TAP experiments. Furthermore, the DFT simulations show cerium atoms adjacent to the isolated manganese sites to participate in stabilization of dehydrogenated NH_x intermediates, emphasizing the multifaceted role of CeO_2. With this, we have gained both practical and fundamental insights into the structure and function of Mn/CeO_2, revealing a novel class of CeO_2-supported atomically-dispersed transition metal-based catalysts for N_2O formation via NH_3 oxidation. In fact, the combination of properties pertaining to the generation and supply of active oxygen species, which emerge as a result of the catalyst's unique nanostructure, are of relevance to selective catalytic oxidations in general and encourage future investigations for a range of other applications.

3. Conclusion

In summary, low-valent manganese atoms stabilized on CeO_2 are revealed as the first stable catalyst for NH_3 oxidation to N_2O, rivaling state-of-the-art Au/CeO_2 in terms of selectivity and reaching a two-fold higher N_2O productivity. The isolated manganese sites are primarily generated during synthesis via a simple impregnation, while in situ redispersion of few scattered MnO particles results in full atomic dispersion. The resultant material shows no structural changes or loss of catalytic activity over 70 h on stream. The oxygen transfer ability of CeO_2 is unveiled to be a fundamental property which promotes N_2O selectivity, setting CeO_2 apart from other redox-inactive carriers. Furthermore, the reaction is found to proceed with the direct participation of lattice oxygen of CeO_2. Accordingly, low-valent manganese sites effectively activate gas-phase O_2, thereby healing the vacancies and allowing the abundant supply of active oxygen species to be maintained. Furthermore, the isolated manganese species can facilitate the N–N bond formation between HNO intermediates via a cyclic intermediate closely related to NOR enzymes, ultimately leading to selective evolution of N_2O. The adjacent Ce atoms, in turn, aid in stabilizing dehydrogenated NH_x intermediates. This work sets an important milestone in the design and understanding of catalysts for NH_3 oxidation to N_2O, establishing CeO_2-supported SACs as a highly promising class of materials for this application, as well as a range of other selective oxidation reactions.

Figure 8. Summary of the key structural and catalytic properties of Mn/CeO_2.

4. Experimental Section

Catalyst Synthesis: Supported metal catalysts were synthesized by an IWI method. Metal precursors were dissolved in deionized water and the obtained solutions were added dropwise to the support. After impregnation, the samples were dried under vacuum at 353 K overnight and then calcined in static air at 673 or 823 K (heating rate = 3 K min^{-1}, hold time = 5 h). Au/CeO_2 was prepared by deposition precipitation with urea method, following the protocol described elsewhere.[12] Additional details of the catalyst synthesis are provided in the Supporting Information.

Catalyst Characterization: Numerous techniques were employed to characterize the catalysts in fresh form and after use in NH_3 oxidation. Namely, the composition of the catalyst, metal speciation and dispersion were determined by X-ray fluorescence (XRF), XPS, EPR, H_2-TPR, and HAADF-STEM. The specific surface area was determined by N_2 sorption

at 77 K. The interactions of the catalysts with O_2 were studied by static volumetric O_2 chemisorption at the reaction temperature (673 K). Details of all characterization techniques and procedures are provided in the Supporting Information.

Catalyst Evaluation: Evaluation of catalytic performance in continuous-flow NH_3 oxidation was conducted in a fixed-bed reactor set-up (depicted in Figure S1, Supporting Information and further described in the Supporting Information). In a typical test, the catalyst (particle size 0.15–0.4 mm, m_{cat} = 0.004–0.5 g for catalytic activity tests, and 0.04 g for kinetic and stability tests; for tests at elevated *GHSV* (> 32 000 cm^3 h^{-1} g_{cat}^{-1}) the catalyst bed was diluted with SiC (particle size 0.5–0.6 mm) to avoid the formation of hot spots) was loaded into a quartz micro-reactor and activated in a He flow (T_{bed} = 473 K, F_T = 40 cm^3 min^{-1}) for 30 min prior to the measurement. Subsequently, the reactor was heated to the desired temperature (T_{bed} = 473–723 K) and allowed to stabilize for at least 30 min before the reaction mixture (8 vol% NH_3, 8 vol% O_2, 4 vol% Ar, 80 vol% He) was fed at a total volumetric flow of F_T = 16-250 cm^3 min^{-1}. The relevant performance metrics, including the NH_3 conversion, product selectivities, material balances, and criteria for the presence of mass and heat transfer limitations were quantified according to the protocols detailed in the Supporting Information.

Transient Mechanistic Studies: NH_3 oxidation was investigated in the temporal analysis of products (TAP-2) reactor operating in pulse mode. The catalyst ($\approx$ 70 mg, particle size 0.2–0.4 mm) was packed between two layers of quartz particles (particle size 0.25–0.35 mm) in the isothermal zone of an in-house developed quartz reactor. After the exposure of the reactor to $\approx$ 10^{-5} Pa, $^{18}O_2$:NH_3:He = 1:1:1 mixture was pulsed (pulse size = $1.5 \times 10^{15} – 5 \times 10^{16}$ molecules) in the temperature range of 473–773 K with a 100 K step. The pulses were repeated ten times and averaged to improve the signal-to-noise ratio. The feed components and the reaction products were quantified by an online quadrupole mass spectrometer with a time resolution of $\approx$ 100 μs. The contribution of the compounds to the respective m/z values was estimated using standard fragmentation patterns determined in separate experiments. Additional details are provided in the Supporting Information.

Computational Details: To gain insights into the possible structural configurations of isolated manganese atoms on different surfaces of CeO_2, and their corresponding reactivity, DFT modelling was conducted with the Vienna Ab Initio Simulation Package (VASP 5.4.4),[68] using the PBE functional,[50] and the HSE03 hybrid functional with 13% exact exchange (HSE03-13).[50,69] The valence electrons were extended in plane waves with a basis set cutoff of 500 eV.[70,71] PBE+U framework was employed to carry out the structural relaxations. For cerium atoms, an additional Hubbard *U* term (U_{eff} = 4.5 V) was applied, following previous literature reports.[52,72,73] Projector Augmented Wave (PAW) method was applied to the core electron, utilizing appropriate PAW–PBE pseudopotentials. Simulations were performed spin unrestricted, applying dipole corrections, where appropriate. The threshold for electronic convergence was set at 1×10^{-6} eV and the positions of atoms were relaxed until residual forces reached 0.015 eV $Å^{-1}$. For selected structures, HSE03-13 hybrid functional was also used to refine the energies, fixing the atomic coordinates at the PBE+U optimized positions. In view of the significantly higher computational cost of HSE03-13, the threshold for electronic convergence was lowered to 1×10^{-4} eV. Total energies of slab models were evaluated at the Gamma point throughout. Relative XPS shifts (core level binding energies) were calculated in the final state approximation[74] and referenced to manganese in a 29-atom supercell of α-Mn. The code developed by Henkelman et al. was used for Bader charge analysis.[75—78]

For the (111), (110), and (100) facets of CeO_2 slab models were constructed as (3 × 3), (2 × 2), and (3 × 3) supercells, extending 9, 6, and 9 atomic layers along the z-direction, of which the bottom 4, 3, and 4 layers were fixed at the optimized bulk positions, respectively. At least 10 Å of vacuum was added on top of the surfaces to minimize interactions of vertically repeated slab images under periodic boundary conditions. Formal oxidation states of manganese single-atoms were assigned using the localized magnetic moments of reduced Ce^{3+} centers, where a threshold of 0.8 μ_B was applied.[48] Single-atom manganese adsorption

and substitution energies were calculated following Equations (8) and (9), where E_{SAC}^{ads} and E_{SAC}^{sub} are the energies of the respective single-atom catalysts (SACs), E_{pris} is the energy of the corresponding pristine ceria slab, E_{Mn} is the energy of single-atom manganese, using α-Mn as reference (E_{coh} = −8.98 eV $atom^{-1}$), and E_{Ce} is the energy of the substituted cerium atom, evaluated via Equation (10). Adsorption energies of reactants and reaction intermediates were evaluated using Equation (8), accordingly.

$$E_{ads} = E_{SAC}^{ads} - E_{pris} - E_{Mn} \tag{8}$$

$$E_{sub} = E_{SAC}^{sub} - E_{pris} - E_{Mn} + E_{Ce} \tag{9}$$

$$E_{Ce} = E_{CeO_2} - E_{O_2} \tag{10}$$

Statistical Analysis: All catalytic data (i.e., conversion, selectivity, *STY*) are presented as arithmetic mean ± 95% confidence interval, based on at least two repeated measurements under the specified conditions. Source data obtained from selected characterization techniques (i.e., H_2-TPR, XRD, EPR) were plotted as received without further manipulation. O_2 chemisorption values (i.e., oxygen uptake) were acquired based on Sinfelt analysis method of the corresponding isotherms, performed on the 3Flex software (V 5.01, Micromeritics Instrument Corp., US). Specific surface area values were acquired based on Brunauer–Emmett–Teller analysis method, performed on TriStar II 3020 software (V 3.02, Micromeritics Instrument Corp., US). Metal content based on XRF analysis was determined using the built-in quantitative analysis tool of ORBIS Vision software (V 2.148, EDAX Inc. US). The particle size distribution presented in Figure S4 and S10 were determined through analysis of > 100 particles identified on the HAADF-STEM micrographs and elemental mappings, using ImageJ software (V 1.52a, National Institute of Health, US). The corresponding plots were created using OriginPro 2019 software (V 9.6.0.172, OriginLab Corp., US), assuming a normal distribution of particle size. XPS spectra were subject to charge correction based on the C 1s photoemission of adventitious carbon, set at 284.8 eV, prior to the fitting. The fitting was performed using CasaXPS software (V 2.3.23PR1.0, Casa Software Ltd., UK), as described in the respective section of the Supporting Information.

Supporting Information

Supporting Information is available from the Wiley Online Library or from the author.

Conflict of Interest

The authors declare no conflict of interest.

Data Availability Statement

The data that support the findings of this study are openly available in Zenodo at https://doi.org/10.5281/zenodo.7380563, reference number 7380563, and ioChem-BD at http://dx.doi.org/10.19061/iochem-bd-1-262.

[1] Z. Guo, B. Liu, Q. Zhang, W. Deng, Y. Wang, Y. Yang, *Chem. Soc. Rev.* **2014**, *43*, 3480.

[2] I. Hermans, E. S. Spier, U. Neuenschwander, N. Turrà, A. Baiker, *Top. Catal.* **2009**, *52*, 1162.

[3] J. Pérez-Ramírez, C. Mondelli, T. Schmidt, O. F. K. Schlüter, A. Wolf, L. Mleczko, T. Dreier, *Energy Environ. Sci.* **2011**, *4*, 4786.

[4] F. Cavani, *Catal. Today* **2010**, *8*, 157.

[5] S. Siankevich, G. Savoglidis, Z. Fei, G. Laurenczy, D. T. L. Alexander, N. Yan, P. J. Dyson, *J. Catal.* **2014**, *315*, 67.

[6] V. N. Parmon, G. I. Panov, A. Uriarte, A. S. Noskov, *Catal. Today* **2005**, *100*, 115.

[7] A. K. Uriarte, *Stud. Surf. Sci. Catal.* **2000**, *130*, 743.

[8] G. I. Panov, K. A. Dubkov, A. S. Kharitonov, in *Modern Heterogeneous Oxidation Catalysis* (Ed: N. Mizuno), Wiley VCH, Hoboken, NJ **2009**.

[9] L. V. Pirutko, V. S. Chernyavsky, A. K. Uriarte, G. I. Panov, *Appl. Catal. A Gen* **2002**, *227*, 143.

[10] M. V. Parfenov, E. V. Starokon, L. V. Pirutko, G. I. Panov, *J. Catal.* **2014**, *318*, 14.

[11] Office of Air Quality Planning and Standards, *AP42 Background Report. Adipic Acid Production*, U. S. Environmental Protection Agency, Research Triangle Park, NC, **1997**.

[12] Z. Tang, I. Surin, A. Rasmussen, F. Krumeich, E. V. Kondratenko, V. A. Kondratenko, J. Pérez-Ramírez, *Angew. Chem., Int. Ed.* **2022**, *61*, e202200772.

[13] Grand View Research, Nitrous Oxide Market Size & Share, Global Industry Report, 2018-2025, grandviewresearch.com/insustry-analysis/nitrous-oxide-market, accessed: September, 2022 .

[14] J. Pérez-Ramírez, E. V. Kondratenko, V. A. Kondratenko, M. Baerns, *J. Catal.* **2004**, *227*, 90.

[15] V. A. Sadykov, L. A. Isupova, I. A. Zolotarskii, L. N. Bobrova, A. S. Noskov, V. N. Parmon, E. A. Brushtein, T. V. Telyatnikova, V. I. Chernyshev, V. V. Lunin, *Appl. Catal. A Gen.* **2000**, *204*, 59.

[16] S. Ghavam, M. Vahdati, I. A. G. Wilson, P. Styring, *Front. Energy Res.* **2021**, *9*, 580808.

[17] C. Smith, A. K. Hill, L. Torrente-Murciano, *Energy Environ. Sci.* **2020**, *13*, 331.

[18] C. D. Chang, S. A. Stevenson, J. C. Vartuli (ExxonMobil Oil Corporation US), USOO6312657B1, **2001**.

[19] N. Ilchenko, *J. Catal.* **1975**, *39*, 73.

[20] K. Fujiwara, H. Kato, K. Wakimura, H. Nakamura, S. Yoshinaga (Mitsui Toatsu Chemicals Inc. JP), EP0799792A1, **1997**.

[21] J. Ludvíková, M. Jabłońska, K. Jirátová, L. Chmielarz, J. Balabánová, F. Kovanda, L. Obalová, *Res. Chem. Intermed.* **2016**, *42*, 2669.

[22] V. V. Mokrinskii, E. M. Slavinskaya, A. S. Noskov, I. A. Zolotarskii (SOLUTIA Inc. US), WO98/25698, **1998**.

[23] A. S. Ivanova, E. M. Slavinskaya, V. V. Mokrinskii, I. A. Polukhina, S. V. Tsybulya, I. P. Prosvirin, V. I. Bukhtiyarov, V. A. Rogov, V. I. Zaikovskii, A. S. Noskov, *J. Catal.* **2004**, *221*, 213.

[24] E. M. Slavinskaya, S. A. Veniaminov, P. Notté, A. S. Ivanova, A. I. Boronin, Y. A. Chesalov, I. A. Polukhina, A. S. Noskov, *J. Catal.* **2004**, *222*, 129.

[25] A. Wollner, F. Lange, H. Schmelz, H. Knozinger, *Appl. Catal. A Gen.* **1993**, *94*, 181.

[26] S. Hinokuma, H. Shimanoe, Y. Kawabata, S. Kiritoshi, K. Araki, M. Machida, *Catal. Commun.* **2018**, *105*, 48.

[27] J. Petryk, E. Kołakowska, *Appl. Catal. B* **2000**, *24*, 121.

[28] R. Lang, X. Du, Y. Huang, X. Jiang, Q. Zhang, Y. Guo, K. Liu, B. Qiao, A. Wang, T. Zhang, *Chem. Rev.* **2020**, *120*, 11986.

[29] S. K. Kaiser, Z. Chen, D. Faust Akl, S. Mitchell, J. Pérez-Ramírez, *Chem. Rev.* **2020**, *120*, 11703.

[30] S. Mitchell, R. Qin, N. Zheng, J. Pérez-Ramírez, *Nat. Nanotechnol.* **2021**, *16*, 129.

[31] F. Kapteijn, A. D. Vanlangeveld, J. A. Moulijn, A. Andreini, M. A. Vuurman, A. M. Turek, J. M. Jehng, I. E. Wachs, *J. Catal.* **1994**, *150*, 94.

[32] A. Trovarelli, *Catal. Rev. Sci. Eng.* **1996**, *38*, 439.

[33] H. Wang, J. X. Liu, L. F. Allard, S. Lee, J. Liu, H. Li, J. Wang, J. Wang, S. H. Oh, W. Li, M. Flytzani-Stephanopoulos, M. Shen, B. R. Goldsmith, M. Yang, *Nat. Commun.* **2019**, *10*, 3808.

[34] K. Ma, W. Liao, W. Shi, F. Xu, Y. Zhou, C. Tang, J. Lu, W. Shen, Z. Zhang, *J. Catal.* **2022**, *407*, 104.

[35] A. Sultana, M. Sasaki, H. Hamada, *Catal. Today* **2012**, *185*, 284.

[36] S. Imamura, M. Shono, N. Okamoto, A. Hamada, S. Ishida, *Appl. Catal. A Gen.* **1996**, *142*, 279.

[37] E. S. Ilton, J. E. Post, P. J. Heaney, F. T. Ling, S. N. Kerisit, *Appl. Surf. Sci.* **2016**, *366*, 475.

[38] A. S. Ivanova, E. M. Slavinskaya, V. V. Mokrinskii, I. A. Polukhina, S. V. Tsybulya, I. P. Prosvirin, V. I. Bukhtiyarov, V. A. Rogov, V. I. Zaikovskii, A. S. Noskov, *J. Catal.* **2004**, *221*, 213.

[39] A. S. Noskov, I. A. Zolotarskii, S. A. Pokrovskaya, V. N. Korotkikh, E. M. Slavinskaya, V. V. Mokrinskii, V. N. Kashkin, *Chem. Eng. J.* **2003**, *91*, 235.

[40] L. D. Bogomolova, Y. G. Tepliakov, F. Caccavale, *J. Non-Cryst. Solids* **1996**, *194*, 291.

[41] I. Ardelean, M. Flora, *J. Mater. Sci.: Mater. Electron.* **2002**, *13*, 357.

[42] J. Zawadzki, *Discuss. Faraday Soc.* **1950**, *8*, 140.

[43] K. Otto, M. Shelef, J. T. Kummer, *J. Phys. Chem.* **1970**, *74*, 2690.

[44] O. N. Sil'chenkova, V. N. Korchak, V. A. Matyshak, *Kinet. Catal.* **2002**, *43*, 363.

[45] E. M. Slavinskaya, Y. A. Chesalov, A. I. Boronin, I. A. Polukhina, A. S. Noskov, *Kinet. Catal.* **2005**, *46*, 555.

[46] M. Capdevila-Cortada, Z. Łodziana, N. López, *ACS Catal.* **2016**, *6*, 8370.

[47] A. Walsh, A. A. Sokol, J. Buckeridge, D. O. Scanlon, C. R. A. Catlow, *Nat. Mater.* **2018**, *17*, 958.

[48] N. Daelman, M. Capdevila-Cortada, N. Lopez, *Nat. Mater.* **2019**, *18*, 1215.

[49] J. Geiger, N. López, *J. Phys. Chem. C* **2022**, *126*, 13698.

[50] J. P. Perdew, K. Burke, M. Ernzerhof, *Phys. Rev. Lett.* **1996**, *77*, 3865.

[51] J. Hubbard, *Proc. Math. Phys. Eng. Sci.* **1963**, *276*, 238.

[52] S. L. Dudarev, G. A. Botton, S. Y. Savrasov, C. J. Humphreys, A. P. Sutton, *Phys. Rev. B* **1998**, *57*, 1505.

[53] F. S. Hegner, D. Cardenas-Morcoso, S. Gimenez, N. López, J. R. Galan-Mascaros, *ChemSusChem* **2017**, *10*, 4552.

[54] T. Hino, Y. Matsumoto, S. Nagano, H. Sugimoto, Y. Fukumori, T. Murata, S. Iwata, Y. Shiro, *Science* **2010**, *330*, 1666.

[55] E. Ferretti, S. Dechert, S. Demeshko, M. C. Holthausen, F. Meyer, *Angew. Chem. Int. Ed. Engl.* **2019**, *58*, 1705.

[56] A. M. Wright, T. W. Hayton, *Inorg. Chem.* **2015**, *54*, 9330.

[57] J. Jover, C. K. Brozek, M. Dincă, N. López, *Chem. Mater.* **2019**, *31*, 8875.

[58] F. Schreiber, P. Wunderlin, K. M. Udert, G. F. Wells, *Front. Microbiol.* **2012**, *3*, 372.

[59] C. Fehling, G. Friedrichs, *J. Am. Chem. Soc.* **2011**, *133*, 17912.

2211260 (13 of 14)

ADVANCED SCIENCE NEWS
www.advancedsciencenews.com

ADVANCED MATERIALS
www.advmat.de

[60] J. Pérez-Ramírez, E. V. Kondratenko, *Catal. Today* **2007**, *121*, 160.
[61] K. Morgan, N. Maguire, R. Fushimi, J. T. Gleaves, A. Goguet, M. P. Harold, E. V. Kondratenko, U. Menon, Y. Schuurman, G. S. Yablonsky, *Catal. Sci. Technol.* **2017**, *7*, 2416.
[62] D. Wang, Q. Yao, C. Mou, S. Hui, Y. Niu, *Fuel* **2019**, *254*, 115719.
[63] L. Nie, D. Mei, H. Xiong, B. Peng, Z. Ren, X. I. Pereira-Hernandez, A. DeLaRiva, M. Wang, M. H. Engelhard, L. Kovarik, A. K. Datye, Y. Wang, *Science* **2017**, *358*, 1419.
[64] E. J. Peterson, A. T. DeLaRiva, S. Lin, R. S. Johnson, H. Guo, J. T. Miller, J. Hun Kwak, C. H. Peden, B. Kiefer, L. F. Allard, F. H. Ribeiro, A. K. Datye, *Nat. Commun.* **2014**, *5*, 4885.
[65] V. Giulimondi, S. K. Kaiser, M. Agrachev, F. Krumeich, A. H. Clark, S. Mitchell, G. Jeschke, J. Pérez-Ramírez, *J. Mater. Chem. A* **2022**, *10*, 5953.
[66] K. Morgan, A. Goguet, C. Hardacre, *ACS Catal.* **2015**, *5*, 3430.
[67] J. Jones, H. Xiong, A. T. DeLaRiva, E. J. Peterson, H. Pham, S. R. Challa, G. Qi, S. Oh, M. H. Wiebenga, X. I. Pereira-Hernandez, Y. Wang, A. K. Datye, *Science* **2016**, *353*, 150.
[68] G. Kresse, J. Furthmüller, *Comput. Mater. Sci.* **1996**, *6*, 15.

[69] F. S. Hegner, I. Herraiz-Cardona, D. Cardenas-Morcoso, N. López, J. R. Galan-Mascaros, S. Gimenez, *ACS Appl. Mater. Interfaces* **2017**, *9*, 37671.
[70] G. Kresse, D. Joubert, *Phys. Rev. B* **1999**, *59*, 1758.
[71] P. E. Blochl, *Phys. Rev. B* **1994**, *50*, 17953.
[72] J. Hubbard, *Proc. Math. Phys. Eng. Sci.* **1997**, *276*, 238.
[73] S. Fabris, S. de Gironcoli, S. Baroni, G. Vicario, G. Balducci, *Phys. Rev. B* **2005**, *71*, 041102.
[74] N. Pueyo Bellafont, F. Vines, W. Hieringer, F. Illas, *J. Comput. Chem.* **2017**, *38*, 518.
[75] W. Tang, E. Sanville, G. Henkelman, *J. Phys. Condens. Matter* **2009**, *21*, 084204.
[76] E. Sanville, S. D. Kenny, R. Smith, G. Henkelman, *J. Comput. Chem.* **2007**, *28*, 899.
[77] G. Henkelman, A. Arnaldsson, H. Jónsson, *Comput. Mater. Sci.* **2006**, *36*, 354.
[78] M. Yu, D. R. Trinkle, *J. Chem. Phys.* **2011**, *134*, 064111.
[79] M. Alvarez-Moreno, C. de Graaf, N. López, F. Maseras, J. M. Poblet, C. Bo, *J. Chem. Inf. Model.* **2015**, *55*, 95.

206

UNIVERSITAT
ROVIRA i VIRGILI